DORIN LELEA
Digitally signed by DORIN LELEA
T=Director Scoala Doctorala, C=RO, S=TIMIS, L=Timisoara, O=UNIVERSITATEA POLITEHNICA DIN TIMISOARA, E=dorin.lelea@upt.ro, SERIALNUMBER=201104209 DL10, G=DORIN, SN=LELEA, CN=DORIN LELEA
Atest integritatea acestui document
Computerul meu
2023.06.15 15:22

IMPROVED INDUCTION MACHINE TORQUE OBSERVERS AND VIRTUAL LOADING IN INDUSTRIAL APPLICATIONS, BASED ON REAL-TIME EMBEDDED CONTROLLERS

A Thesis Submitted for obtaining
the Scientific Title of PhD in Engineering
from
Politehnica University Timișoara
in the Field of Electrical Engineering
by

ing. Adrian Daniel MARTIN

PhD Committee Chair:	Prof. Univ. Ph.D. Nicolae MUNTEAN Lect. Univ. Ph.D. Ciprian SORANDARU Lect. Univ. Ph.D. Octavian CORNEA
PhD Supervisor:	Prof. Univ. Ph.D. Lucian TUTELEA
Scientific Reviewers:	Prof. Univ. Ph.D. Prof. Univ. Ph.D. Prof. Univ. Ph.D.

Date of the PhD Thesis Defense:

BUPT

The PhD thesis series of UPT are:

1.Automation
2.Chemistry
3.Energetics
4.Chemical Engineering
5.Civil Engineering
6.Electrical Engineering
7.Electronic Engineering and Telecommunications
8.Industrial Engineering
9.Mechanical Engineering
10.Computer Science and Information Technology
11.Science and Material Engineering
12.Systems Engineering
13.Energy Engineering
14.Computers and Information Technology
15.Materials Engineering
16.Engineering and Management
17.Architecture
18.Civil Engineering and Installations
19.Electronics, Telecommunications and Information Technologies

Politehnica University Timișoara, Romania, initiated the above series to disseminate the expertise, knowledge and results of the research carried out within the doctoral school of the university. According to the Decision of the Executive Office of the University Senate No. 14/14.07.2006, the series includes the doctoral theses defended in the university since October 1, 2006.

Copyright © Editura Politehnica – Timișoara, Romania, 2021

This publication is subject to copyright law. The multiplication of this publication, in whole or in part, the translation, printing, reuse of illustrations, exhibit, broadcasting, reproduction on microfilm or any other form is allowed only in compliance with the provisions of the Romanian Copyright Law in force and permission for use obtained in writing from the Politehnica University Timișoara, Romania. The violations of these rights are under the penalties of the Romanian Copyright Law.

Romania, 300223 Timișoara, Bd. Vasile Pârvan no. 2B
Tel./fax +40-(0)256 404677
e-mail: editura@upt.ro

BUPT

Acknowledgement

This thesis has been developed in collaboration with industry during five and a half years in the Department of Electrical Engineering of the Politehnica University Timisoara

First of all, I want to thank and to express my sincere gratitude to my supervisor Professor Lucian Tutelea for the kindness, patience, and empathy he showed for this long period. I want to thank him for all the discussions and dedicated time.

A special thanks to Professor Nicolae Muntean, for all the care and attention which he granted me, and thanks to whom I choose this honorable career.

I am truly grateful that in addition to the sustained and unwavering technical help of Academician Professor Ion Boldea, I would like to thank him again for the daily moral and ethical education lessons he taught me throughout these years.

Furthermore, I want to thank all representatives and colleagues from SC Beespeed Automatizari SRL, especially to Mr. Radu Babau, who initiated this Ph.D. program's basic idea and offered me all the financial support I needed.

I want to thank Associate Professor Cornea Octavian for the friendship advice he always had time to give me.

I want to thank Associate Professor Lascu Cristian for the time given to constructive discussions.

I truly appreciate the relationship with my department colleagues and friends with whom I went through this life experience; I especially want to thank Dani for his true and strong friendship.

Finally, and most importantly, I want to thank my beloved wife, who had the courage to go through all these hard years with me, for her support and patience to endure the shortcomings of these periods, and for her precious dedicated time to our little boy.

To my parents for their love, especially my mother, for her encouragement and motivation she always gave me to continue.

I want to thank my parents-in-law for all the trust they had in me.

I want to thank my brother and his family for all the parental support they have given to me.

I will always be grateful for all your support during all these difficult years.

"And whatever you ask in prayer, you will receive, if you have faith."
Mattew 21:22

Timişoara, April, 2023 Adrian Daniel Martin

BUPT

MARTIN, Adrian Daniel

IMPROVED INDUCTION MACHINE TORQUE OBSERVERS AND VIRTUAL LOADING IN INDUSTRIAL APPLICATIONS, BASED ON REAL-TIME EMBEDDED CONTROLLERS

PhD theses of UPT, Series X, No. YY, Editura Politehnica, 200Z, 219 pages, 184 figures, 10 tables.

ISSN:
ISBN:

Keywords
Industrial equipment, Real-time embedded controller, Induction machine, Variable frequency converter, Torque estimator, Online data processing, Artificial loading, Torque pulsation reduction

Abstract

This thesis presents an extension of the use of standard industrial command and control equipment in different applications.

Three types of programmable logic controllers (PLC) are investigated as the main controller for electrical machine torque estimation and also for frequency spectrum analysis. The major drawback of the investigated low-cost PLCs related to this topic is highlighted.

With high applicability in condition monitoring and fault detection, three types of electrical machines' electromagnetic torque estimators are presented, simulated, and experimentally tested on a high-speed data acquisition and control platform based on cRIO-9086 chassis. Online and offline-obtained results are given in the context of steady-state and dynamic load opperation.

An artificial loading method for electrical machines is given and investigated as a niche application of the standard low-cost equipment. Two identical induction machines without mechanical coupling driven by two identical dc link-connected variable frequency drives are artificially loaded at phase-rated RMS current. A low-cost PLC is used for command and control. A simple open-loop method with different loading reference types validates the synthetic loading principle. A closed-loop control method is successfully used for automatized thermal testing of both machines. Frequency spectrum analysis presents the inverters and the machine windings' connection influences. Comprehensive acceptable results related to the loss equivalency are obtained from simulation.

A high-speed data acquisition and control system is used as a torque estimator for online and offline analysis of a novel active torque pulsation reduction method for rotary electromechanical systems with position-dependent loading torques. A mathematical two-step method used for preliminary total system inertia and loading torque detection is presented in detail and experimentally validated.

BUPT

Table of contents

BUPT

BUPT

BUPT

Nomenclature

Abbreviations

IACS – industrial automation and control systems
SCADA – supervisory control and data acquisition
HMI -human machine interface
PLC – programmable logic controller
RTU – remote terminal unit
DCS – distributed control system
VFC – variable frequency converter
P – proportional – type controller
PI – integral, proportional-type controller
PID – derivative, integral, proportional- type controller
RT – real time
OBO – output-based observer
IBO – input-based observer
IOBO – input and output based observer
PIO – proportional-integral observer
NLO – basic nonlinear observer
KF – Kalman filter
EKF – extended Kalman filter
DE – disturbance estimator
DO – disturbance observer
UIO – unknown input observer
PO – perturbation observer
ESO – extended state observer
CESO – cascade extended state observer
AI – artificial inteligence
DL – deep learning
ANN – artificial neural network
IPMSM – interior permanent magnet synchronous machine
FPGA – field programmable gate array
FEA – finit element analysis
IRFOC – indirect rotor-field oriented control
PMSM – permanent magnet synchronous machine
RMS – root mean square
AVC – active vibration control
PZT – piezoelectric
ANC – active noise canceling
ILC – iterative learning control
RC – repetitive control
IMP – internal model principle
RESS – recuperative energy storage system
FISG – flywheel-integrated starter generator
API – american petroleum institute

IM – induction machine
DFT – discrete Fourier Transform
CPU – central processing unit
MCM&PHM - machine condition monitoring and predictive health monitoring
FFT – fast Fourier transform
RHC – relative harmonic content
DIT – decimation in time
DIF – decimation in frequency
GCIM – grid-connected induction machine
DMA – direct memory access
FIFO – first in first out
MM – main motor
ELM – emulated load machine
DTC – direct torque control
DC – direct current
AC – alternating current
EMF – electromotive force
HPF – high pass filter
LPF – low pass filter
PLL – phase lock loop
RC – resistive - capacitive
PC – personal computer
RTD – resistance temperature detector
AO – analog output
PWM – pulse width modulation
PM – permanent magnet
ATPRM – active torque pulsation reduction method
ICE – internal combustion engine
TCP/IP – transmission control protocol / internet protocol
AM – auxiliary machine
TTL – transistor-transistor logic

Symbols

$E_{rr_{t1}}$ – error between any two channels – test 1

Err_{t2} - error between any two channels – test 2

ch_m - channle „m” from PLC

ch_n - channle „n” from PLC

f_{PLC} - PLC acquisition frequency

f_{SG} - generator signal frequency

$A_{P_{ct}}$ - average cyclic time of the processor

C_{Pct} - configured processor speed

$\Delta t(\%)$ - difference between two successive program cycles relative to the setpoint

$\bar{T}_{Et}(ms)$ - average of the PLC actual execution time

$f(t)$ - periodic function

a_0 - constant value for periodic signal

a_k - amplitude of the „cos” component of a periodic function

b_k - amplitude of the „sin” component of a periodic function

$X(F)$ - frequency-domain function

$x(t)$ - time-domain function

X_k - discrete Fourier transform

W_N^k - twiddle factor

X_{2r} - even entries array

$X_{(2\cdot r+1)}$ - odd entries array

$V_{L_{sc}}$ - line voltage during short-circuit test

$V_{ph_{sc}}$ - phase voltage during short-circuit test

P_{sc} - absorbed power during short-circuit test

I_{sc} - phase current during short-circuit test

P_0 - absorbed no-load power

$P_{in}, P_{co1}, P_{co2}, P_{iron}, P_{add}, P_{mech}$ - input power and stator and rotor copper losses, iron, additional and mechanical losses

$\dot{\Psi}_{\alpha s}, \dot{\Psi}_{\beta s}, \dot{\Psi}_{\alpha r}, \dot{\Psi}_{\beta r}$ - stator and rotor α, β -axis time derivatives of orthogonal flux components

$\Psi_{\alpha s}, \Psi_{\alpha r}, \Psi_{\beta s}, \Psi_{\beta r}$ - stator and rotor α, β -axis fluxes

$R_s, R_r, R_{m_{prl}}$ - stator, rotor, and magnetizing resistance

L_m, L_s, L_r - magnetizing, stator and rotor inductances

$I_{\alpha s}, I_{\beta s}, I_{\alpha r}, I_{\beta r}$ - stator and rotor α, β -axis estimated current components

ω - estimated shaft speed

p - number of pole pairs

$a_{11}, a_{12}, a_{21}, a_{22}, c_1, c_2, c_3, \sigma, k_{add}$ - coefficients

ω_r - shaft (rotor) speed

ω_1 - synchronous speed

T_{elm}, T_{load} - electromagnetic and load torques

ω_c - cutoff frequency of the low pass filter

s - induction machine’s slip

η - efficiency

$R_{m_{srs}}, X_{m_{srs}}$ - core resistance and reactance in series connection of the equivalent circuit

$R_{m_{prl}}, X_{m_{prl}}$ - core resistance and reactance in parallel connection of the equivalent circuit

$R'_{m_{prl}}$ - core resistance in parallel connection of the equivalent circuit, without taking into account the voltage drop on the phase reactance

Z_0, R_0, X_0 - total impedance, total resistance and total reactance of the induction machine no-load equivalent circuit

Z_{sc}, R_{sc}, X_{sc} - total impedance, total resistance and total reactance of the induction machine short-circuit equivalent circuit

X_s, X_m - stator and magnetizing reactance of the induction machine's equivalent circuit

$RHC_{3^{rd}H}, RHC_{5^{rd}H}, RHC_{7^{rd}H}, RHC_{9^{rd}H}, RHC_{11^{rd}H}, RHC_{Total}$ - total and individual relative harmonic content

$v_{ph1}, v_{ph2}, v_{ph3}$ - momentary simulated three-phase voltages

$V_{ph1}, V_{ph2}, V_{ph3}$ - maximum values of each momentary voltage

$\varphi_{ph1}, \varphi_{ph2}, \varphi_{ph3}$ - phase shifts used for ideal voltages

$v_{ph1_{rc}}, v_{ph2_{rc}}, v_{ph3_{rc}}$ - ideal three-phase voltage system after the real characteristics (real-measured relative harmonic content and the inverse component influences) were added

$V_{(ph1)_k}, V_{(ph2)_k}, V_{(ph3)_k}$ - amplitudes of the harmonics based on the relative harmonic content

$\omega_{(ph1)_i}, \omega_{(ph2)_i}, \omega_{(ph3)_i}$ - frequency of each harmonic

$\varphi_{(ph1)_i}, \varphi_{(ph2)_i}, \varphi_{(ph3)_i}$ - initial phase of each harmonic

k_{ic} - coeficient that characterize the influence of the inverse component on the three-phase voltage system

$\hat{\Psi}_s, \hat{\Psi}_r$ - stator and rotor fluxes

u_s, i_s, R_s - stator voltages, currents, and phase resistance

$i_{s\alpha}, i_{s\beta}$ - stator and rotor α, β -axis measured currents

$\hat{i}_{s\alpha}, \hat{i}_{s\beta}$ - stator and rotor α, β -axis estimated currents

T_{elm}, T_k, T - electromagnetic torque, maximum torque and actual torque

V_a, V_b, V_c - stator phase voltages in abc – axis.

V_α, V_β - stator α, β -axis voltages

I_α, I_β - stator α, β -axis currents

ω_1 - synchronous speed

s_k, s - maximum slip and the slip for which the induction machine produces the maximum torque

k_1, k_2, k_3, k_4 - slopes in different points from integration interval for RK4

y_n, y_{n-1} - desired function used for RK4

$VFC1^*_{speed\_ref}, VFC2^*_{speed\_ref}$ - speed reference given to the inverters for artificial loading

DC_{off} - the speed reference dc offset used for inverters for artificial loading

$I_{RMS_{PLC}}$ - Induction machine RMS phase current determined inside the PLC based on IM RMS phase current read from VFC

$I_{RMS_{VFC}}$ - induction machine RMS current read from VFC

$Phase\_shift$ - the total phase shift between speed references used for artificial loading

$cp_{nbs} \cdot ct$ - PLC total number of cyclic programs (ct ms) uses for shifting and the duration of a program cycle

I^*_{ref} - prescribed induction machine RMS current

H_{lim}, L_{lim} - high and low limit necessary for variables limitation for closed-loop control method for artificial loading

c.v. - intermediate variable

$I_{RMS_{ac\_source}}$ - RMS value of the ac source current

P_{IM} - the induction machine power

η_{IM}, η_{VFC} - IM's and VFC's efficiency

ω_{IM}, ω_b, ω_{fw} - induction machine's rotor speed, the IM's base speed, and the speed after the flux weakening,

Ψ^*_r - flux weakening after the base speed,

$I_{\alpha\beta}, I_{abc}, I_{dq}$ represent the $\alpha\beta, abc, dq$ reference frame current, I^*_{dq} represents the dq reference current

T_r - rotor time constant

$H(s)$ - transfer function used for I_d determination

T^* - torque reference obtaine from Speed and torque regulator block

p - number of pole pairs

ω^*_2. - reference rotor speed

θ - rotor angle

V^*_{dq} - reference voltage in dq frame

$V_{dc\_real}, V_{dc\_ideal}$ represents the real voltage obtained based on VFCs loading and the ideal dc voltage

C, L represent the total dc-link capacitance and the total inductances

$I_{ac\_source}, I_{dc1}, I_{dc2}$ represents the ac source current and the VFCs dc currents

T^*_{EL} represents the torque reference given to the emulated loading machine

I_{1m}, I_{2m}, I_{3m} represent the GCIM read phase currents

ω_m - system measured speed

ω_2^*, pp - represent the rotor reference speed and the number of the pole pair

L_r, T^*, T_r, ω_b - rotor inductances, reference prescribed torque, rotor time constant and base speed used for flux weakening

$\hat{U}_d^*, \hat{U}_q^*$ - d, q components of the estimated voltage references

$\hat{U}_\alpha^*, \hat{U}_\beta^*$ - α, β components of the estimated voltage references

J, J_{total} - system moment of inertia

T_{diff}, B - resulting torque on the system, and total friction coefficient

$d\omega / dt$ - time derivative component of the speed

$\hat{T}_{Ampl}, \hat{T}_{GCIM}$ - Grid-connected induction machine determined torque amplitude

$\hat{T}_{Aux}$ - auxiliary machine determined torque amplitude

$\sin_{\hat{T}}, \cos_{\hat{T}}$ - sine and cosine component of the Grid-connected induction machine determined torque amplitude

$\bar{T}_{load}, \bar{T}_{obs1}, \bar{T}_{obs2}, \bar{T}_{aux}$ - complex number of loading machine torque, observer torque determined from Step 1 and Step 2, torque and auxiliary machine torque

$\bar{T}_{aux_\measuredangle}, \bar{T}_{aux_{ampl}}$ - angle and amplitude of the auxiliary machine torque

$\bar{\Omega}_1, \bar{\Omega}_2$ - complex number of measured speed from Step 1 and Step 2

θ_{ideal} - ideal angle based on the elapsed time from simulation

Ω_0 - mean speed on the interest interval

$\Omega(t)$ - momentary speed

$\Omega_{1_{real}}, \Omega_{1_{imag}}$ - real and imaginary part of the complex speed

$T_{obs1_{real_h}}, T_{obs1_{imag_h}}$ - real and imaginary part of the observer 1 torque for h harmonic

$\bar{T}_{load_c}$ - final computed form of the loading torque

T_{C_1}, T_{C_2} - torque transmitted through mechanical couplings

T_{IM}, T_{AM} - GCIM and AM torque

J_{IM}, J_{AM} - inertia moment of the GCIM and AM

List of Figures

BUPT

BUPT

BUPT

List of Tables

BUPT

Motivation

The motivation behind this thesis is based on the current worldwide trend regarding the use of industrial equipment in all automation applications and not only. In recent years, the expansion of the Internet of Things concept in the industrial sectors led to the emergence of a new sector called the Industrial Internet of Things (IIoT). These types of equipment are about to become part of the latest technology that focuses primarily on machine-to-machine communication. In the near future, smart industrial equipment will replace classic equipment.

Expanding the primary role of using this standard equipment and their integration into new types of applications can represent the link between classic and future smart applications.

Playing a key role in process control and industrial automation, PLCs are also a main element in standard nowadays applications and in future smart systems. Starting from the basic operating principle of executing sequential and repetitive tasks, the PLCs continuously expand their range of use in the context of the IIoT.

With a high demand for controllability, industrial automation processes have been developed with the advent of centralized supervision, control, and data acquisition systems (SCADA systems). The strong relationship between SCADA systems and PLCs represents another impulse for studying and expanding the industrial equipment limitations.

Starting from small production lines to large power plants, predictive maintenance and fault diagnostics are getting a lot of attention. Industrial plant condition monitoring represents a global trend for total system downtime cost reduction. For rotary electromechanical systems, online torque monitoring can be used to predict and prevent potential system faults. In special conditions, the standard, already mounted PLCs can also be used to perform an online electrical machine's torque estimation besides their classical purpose with small changes.

For existing industrial applications, extending the motor drives' role can reduce the human resources cost leading to time and money savings.

For rotary mechanical systems with position-dependent loading torques, torque pulsations represent one of the main factors that can lead to system failures. Torque pulsation smoothening for pulsating loads is still being investigated, especially for large power machines.

This thesis concisely presents several applications with industrial command and control equipment as an extension to their traditional roles with applicability in the fields of online electrical machine torque estimation and frequency spectrum analyses, electrical machine-rated power, and thermal testing, and torque pulsation reduction methods.

BUPT

Thesis outline

This thesis is divided into six chapters. The first one represents an overview of all discussed methods and applications, and the next four focus on several applications with industrial equipment. The last chapter presents the general conclusion, original contributions, and future work.

Chapter 1 aims to perform a state-of-the-art of the general trend of industrial applications, highlighting the main scope of expanding classic automation solutions toward smart systems with multiple functions. The transition to such systems involves expanding the possibilities of using classic industrial types of equipment beyond their classic purpose. This chapter gives a comprehensive overview diagram for a better understanding of where the industrial equipment is placed in the studied topics.

An overview of the most used state and torque observers with their particular characteristics is presented.

A survey of last century's most used electrical machines' artificial (virtual) loading procedures is presented, together with the proposed solution.

Finally, the chapter briefly describes the active pulsation reduction methods for electromechanical systems driven by electrical machines. The most used literature solutions and the thesis approach to this subject are given in terms of high-torque pulsating loads.

Chapter 2 presents the possibility of using the classical low-cost programmable logic controllers (PLC) beyond their standard repetitive and sequential character. The PLCs are being investigated to be used as main controllers for electrical machines' electromagnetic torque observers. Three preliminary tests are given to validate the controllers' performances for this application. It is presented that for three different types of low-cost PLCs, the real measured operating cyclic times have both different mean values than the setpoint and also an inconsistent variation of the program cycle time at each iteration.

In the second part of the chapter, a well-known Discrete Fourier Transform procedure is successfully implemented on the low-cost PLC for frequency spectrum analysis. Experimental validation is given.

Chapter 3 focuses on simulation and experimental validation for three different induction machine torque estimators. The chapter starts with a well-known induction machine parameters identification procedure, information that is used later (including in the other chapters) to simulate, as accurately as possible, the real 11kW, three pole-pair induction machine's (IM) operation. The investigated IM's mathematical model and Simulink diagram are given with performance results, both for ideal and real simulated voltages. The real simulated voltages are reconstructed based on a frequency spectrum analysis of the real on-site grid voltages. The direct electromagnetic torque computation method, dynamic model, and the Luenberger flux observer method are simulated and experimentally validated online on an industrial high-performance platform (cRIO-9068).

Chapter 4 presents a novel artificial (synthetic) loading method for induction machines without mechanical coupling, driven by two dc-link - connected standard industrial variable frequency converters (VFC), using a low-cost PLC for command and control. An open-loop and closed-loop control methods are

BUPT

presented. Three control references are investigated for the closed-loop method to limit the VFCs' grid-absorbed current.

It is proved that an automatic test procedure can successfully perform the thermal test of both induction machines, considering the grid power limitations. The frequency spectrum of the grid, machines', and VFCs' currents are investigated.

Comprehensive Matlab&Simulink simulations are given for ac-source current and machine power loss validation. Finally, the tested induction machine's electromagnetic torque is estimated online during the artificial loading procedure.

Chapter 5 deals with the possibility of actively reducing the torque pulsations in an electromechanical system with position-depended loads driven by a grid-connected induction machine with an auxiliary connected variable frequency converter-driven machine. The here presented novel idea relies on the well-known Active Vibration Control technique that requires an external force added to the system in an opposite manner than the perturbance. A closed-loop method using two torque observers is proposed to actively reduce the torque pulsations. The proposed idea is open-loop validated both in simulation and experiment.

In the second part of the chapter, a novel two-step mathematical tool for system inertia and loading torque preliminary detection is simulated and experimentally validated. The two-step method is tested both for fundamental-only frequency-based torque and also for more complex loading torques.

Chapter 6 presents the general conclusions of this work, highlights the author's contribution, and finally presents the future work needed for this subject.

BUPT

Thesis objectives

The thesis's main objectives are presented as follows:

- To perform an overview of the state and flux observers, present the most popular electrical machine virtual loading procedures, and offer the existing methods for torque pulsation reduction in electromechanical systems.
- To study the possibility of extending the traditional role of the low-cost industrial command and control equipment (PLC).
- To examine and compare different types of electrical machine torque estimators/observers.
- To create an easy-to-use online torque estimator for grid-connected and variable frequency-driven induction machines.
- To analyze the influence of the industrial sites' real grid voltage over the grid-connected induction machines' operation.
- To develop a new synthetic loading procedure for induction machines based on standard industrial equipment.
- To implement an automated thermal test procedure considering the lab power limitation.
- To develop a new active torque pulsations reduction method for electromechanical systems driven by grid-connected induction machines.
- To propose a new mathematical tool for the system moment of inertia and loading torque preliminary detection.
- To simulate as accurately as possible the theoretical assumptions.
- To experimentally validate the theoretical and simulated solutions.
- To create experimental setups needed for operating principle validation.

BUPT

1. Introduction

Abstract

The chapter aims to perform an essential and simplified introduction to the most important thesis aspects.

It begins with a short state-of-the-art regarding the industrial equipment's present status and future direction. Next, a brief classification and description of the most important observers are presented, followed by the presentation of the electrical machine artificial loading historical and nowadays procedures.

The chapter ends with a survey of the common issues and possible solutions for torque pulsation reduction in position-dependent loading machines.

1.1. Industrial trends – the need for industrial equipment

Nowadays, industrial equipment plays a crucial role in all industries. From measuring sensors to the most advanced control and supervisor complex systems, industrial equipment represents the foundation in all kinds of applications, from very small applications (such as small pumping groups, fans, machine condition, etc.) to very large applications (such as petroleum stations, the chemical industries, naval and aerospace factories, etc.).

The aims of this chapter are dedicated mainly to justifying the need to utilize industrial equipment on a larger scale in as many industrial applications as possible and the expansion of their classical role with the development of processing capacities.

The global digitization trend forces the industrialization of all manufacturing, transformation, and transportation processes.

One of nowadays revolutions is represented by the possibility of creating a world full of communicating, interconnected electronic devices and sensors. From smart devices to smart cities or regions, high power efficiency, and not only could be implemented only through effective communication between the producer, transformer, transporter, and consumer.

The Internet of Things (IoT) represents the communication features and processes between all electronic devices. With exponential growth in the last years, the IoT revolution impacts all past, current, and future business plans and strategies in all kinds of potential domains such as Smart Cities, Energy (and Power management), Medicine, Transportation, Automotive (Smart cars), Agriculture, Security, Stock Markets, etc. [1]

The need for high response time, low downtime, reduced costs, and the possibility of scheduled maintenance represents some major industrial processes' requirements.

Besides smart electronic devices and systems, the Internet of Things has increasingly found its place in industrial processes, thus representing the highest level of Industrial Automation and Control Systems (IACS). There are many

BUPT

definitions and explanations about SCADA systems, some of them being given here [2], [3].

Nowadays, many questions are regarding the possibility that the Internet of Things concept would take place in the near future in front of the Supervisory Control and Data Acquisition (SCADA) systems.

Besides the primary role of this real-time signals collection and monitoring system, in recent years, the need for a SCADA system also came as a requirement to increase efficiency, reduce system downtime, record errors, to facilitate communication with other equipment (pumps, sensors, fans, complex equipment, Human Machine Interfaces (HMI), etc.) and to actively participate in smart decisions [3]–[6].

With a high possibility of performance and scalability, SCADA systems have reached new functionalities recently regarding their role in industrial processes.

Fig. 1.1 presents a basic diagram of a SCADA system. The lower level is represented by the I/O Field, in which all the measurements and actions take place. The read information and data setpoints are sent to/from the I/O Field through standard Process Automation Protocols (such as Modbus, Profibus, Profinet, Interbus, etc.). In the first step, the send/receive data goes through the programmable logical controllers (PLCs) and remote terminal units (RTUs) to the higher level of the hierarchy. Both equipment (PLC and RTU) play a key role in a Distributed Control System (DCS).

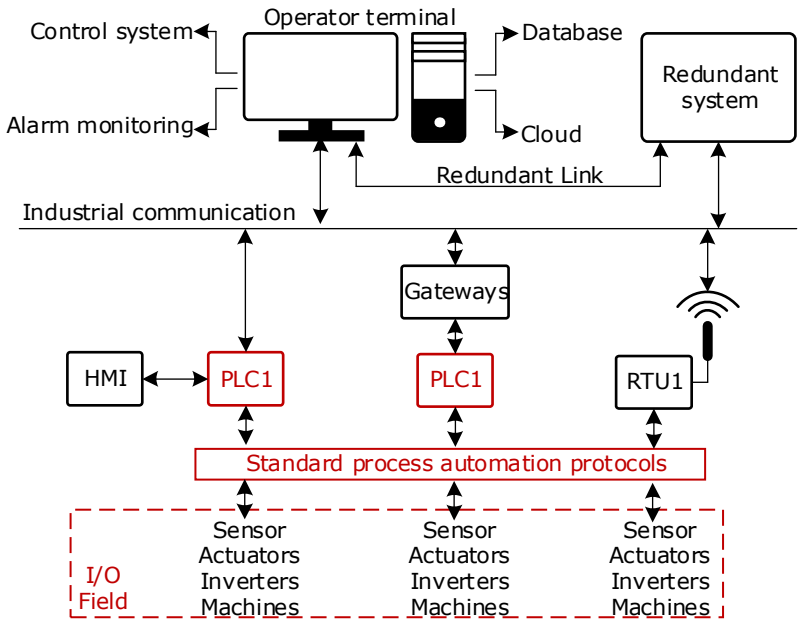

Fig. 1.1 Basic SCADA system diagram

In Industrial Automation and Control Systems, the I/O field can be represented by all the sensors, actuators, and process equipment. For example, in the case of power electronics applications, these input/output signals can be given by the electrical machines' Variable Frequency Converters (VFC).

BUPT

All the field data are processed, analyzed and stored in higher SCADA levels. The redundancy feature of a SCADA system is mainly performed at the server level (but not limited to), which in many cases is transparent to the operator (user).

With high computing capability, the PLCs represent a crucial component of SCADA systems. They are worldwide spread and used due to their characteristics: they are stable against vibration, temperature, and dust and require low human resources for maintenance. Nowadays, PLCs can run complex tasks using dedicated functions, either integrated into SCADA systems or individually. As the main controller, the PLCs can have a complex centralized or decentralized structure [7], [8]. Nowadays, PLCs represent a central element of all industrial automation and have become an essential part of more and more applications.

Starting from standard, well-known control techniques such as P, PI, and PID regulators [9], [10], more complex fuzzy control-based algorithms are subjected to the PLCs applications.

The ease of programming and PLC integration into existing or new control systems and the system scalability characteristic determine an expansion of the range of use of standard or special (high-performance) PLCs. Thus, various relatively new applications with PLCs can be found in the literature, such as the control of charging stations for electric or hybrid vehicles or the control of intelligent microgrid systems up to smart and intelligent applications or image processing [11]–[14]. In addition, the PLC can be, for example, the main controller in various fuzzy applications [15]–[18].

The current global trend of digitalization will connect industrial processes and their components in a way that has never been before. The PLC based and the DCS-based systems represent two basic architectures in many industries (i.e., [19] in the petrochemical industry). The global trend involves transitioning all these "conventional" systems to newer IoT-based systems. At the moment, in the literature, you can find mature applications based on PLC integration in IoT [20]–[24]. The expansion of the IoT range in industrial sectors is called the Industrial Internet of Things (IIoT) [25].

A comprehensive relationship between IoT, IIoT, and SCADA is given in Fig. 1.2: IIoT represents a small part of IoT. The link between the Internet of Things concept and SCADA (or DCS) systems is represented by the Industrial Internet of Things.

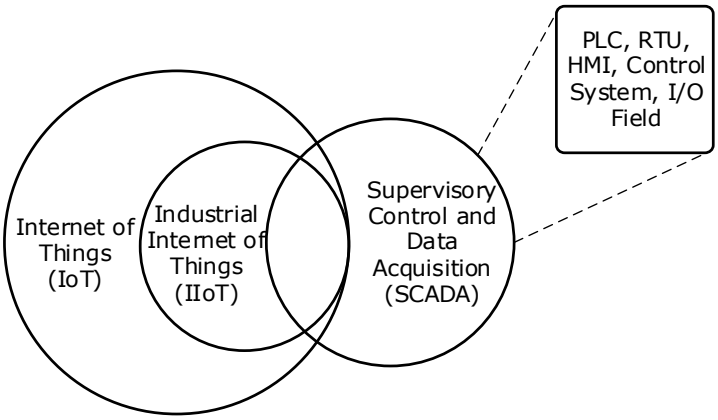

Fig. 1.2 IoT, IIoT, and SCADA interaction

BUPT

1.2. Industrial equipment in the studied topics

The global trend of IIoT represented the central core of studying the possibility of integrating standard industrial equipment in niche applications. All factory processes are based on industrial equipment and their integration into more complex systems.

Next, the standard industrial equipment (PLC, VFC, Encoders, etc.) are studied to their limits to extend their application range.

The main concept of this thesis is related to industrial equipment control and system integration according to specific tasks and requirements. In Fig. 1.3, the simplified structured diagram of the thesis

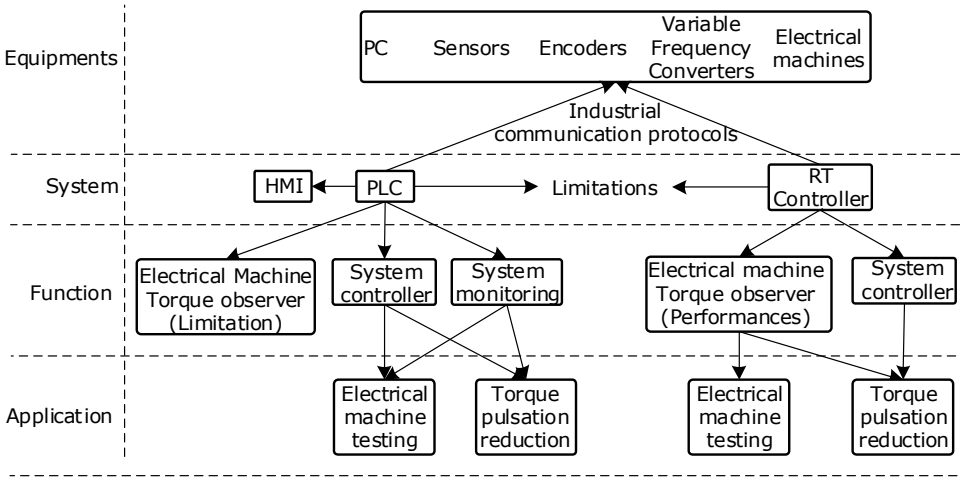

Fig. 1.3 Thesis outline – structured diagram

The structured diagram of the thesis is presented in 4 distinct layers.

The System layer is represented by all the Process controllers used in the following chapters. The first chapter investigates the PLCs and Real-Time controllers as induction machine torque observers. Their drawbacks are studied in all the chapters, with more attention to the PLCs' limitations described in the second chapter. Compared to the RT (real time) Controller, the PLC-based system communicates with an HMI.

The Function layer describes how the system controllers are used in each application. Several functions are given to both systems (PLC-based and Real-time controller-based systems).

In the second chapter, the performances of 3 low-cost industrial PLCs are studied, and the main disadvantage is presented, for which they cannot be used as electric machines' torque estimators.

On the other hand, three torque estimators are successfully implemented in the Real-Time controller-based industrial system. The online obtained experimental results for each estimator at variable torque load are compared with those obtained from simulation.

The most suitable electromagnetic torque observer or combination of multiple torque observers is then used on RT Controller in several applications. The PLC-based system commands variable frequency drives used both for electric

BUPT

machines testing procedure presented in Ch. 3 and for the torque pulsation reduction method presented in Ch. 4. Both systems are used as system controllers.

As a system controller, the RT Controller is used only on the torque pulsation reduction method as a real-time calculation processor for various control parameters.

The PLC-based controller is also used as an online monitoring system for both testing electrical machines procedure and torque pulsation reduction method.

The Application layer of the here presented thesis represents the industrial-specific applications studied in the following chapters.

The electric machine testing procedure is presented in detail in chapter 3. Two identical induction machines without mechanical coupling are virtually loaded at phase-rated currents. Both machines are driven by two identical variable frequency converters with a common dc link. The inverters a controlled and monitored by a PLC-based system. The RT controller online estimates the induction machine torque.

The virtual loading procedure assumes that both induction machines run at a constant speed (represented by the dc component of a sinusoidal speed reference). An alternating sinusoidal speed reference is overlapped with the dc component. The speed reference is given so that when one induction machine accelerates, the other decelerates.

The power generated from the induction machine, which decelerates (generator mode), goes through the standard inverters dc link to the accelerating induction machine (motor mode). The lack of mechanical coupling significantly impacts the total human resources cost of the here-presented virtual loading testing procedure. It is proven that the test bench power source could be substantially diminished due to the regenerative character of the virtual loading procedure.

The induction machines' phase currents are modified by the speed reference parameters: the amplitude and frequency of the sinusoidal reference.

Several speed references and their results from the induction machine testing are investigated. An open loop and a closed loop control technique are given. The automated test procedure and the thermal test are presented using the closed-loop control method.

The artificial loading test procedure is investigated in terms of influence on the test bench power source. The ac source currents are measured and analyzed.

Two simulations are presented and studied for ac source currents investigation and induction machines power loss validation.

Finally, two online observers (presented in Chapter 4) are studied. Their online obtained results are compared with the variable frequency converter's estimated torque and with that obtained from simulation.

The fifth chapter is related to the possibility of using standard command and control industrial equipment to actively reduce the torque pulsation in electromechanical systems driven by grid-connected induction machines. In this case, the torque pulsation source is represented by position-dependent loads (such as crankshaft-based loads). The here presented method is based on an auxiliary machine mounted on the same shaft as the motor and loading machine (on the loading machine side).

The concept of this method is first simulated and then experimentally validated. The test bench consists of 3 induction machines, two back-to-back power converters, and two encoders, a PLC based and an RT controller-based system. The loading torque is emulated by a 30kW, 4-pole pairs induction machine driven by a 25kVA inverter. The motor is represented by an 11kW, three pole pairs grid-connected induction machine.

BUPT

The auxiliary machine is represented by a 15kW, two-pole pairs induction machine driven by a 16kVA back-to-back variable frequency converter.

The active torque pulsation reduction method proposes that the auxiliary machine compensates for total or partial position-dependent loading torque spikes. The online torque observer gives the auxiliary machine torque reference, which estimates the grid-connected induction machine electromagnetic torque. No torque transducer is used for this method.

A fully operational method for system moment of inertia and loading torque profile detection is simulated and experimentally validated. The results reveal the importance of the loading torque phase and amplitude and confirm the method's performances.

1.3. Observers design – a survey

In many industries, sensorless control represents a valuable achievement thanks to its potential benefits. More than that, in safety-critical applications, the redundant character is often achieved through multiple "parallel" connected sensors. In the last decades, the trend has been to replace at least one of those sensors with a sensorless monitoring device.

Fig. 1.4 presents a simplified structured diagram of the state observers used over the years. Based on the literature, the diagram represents the author's point of view regarding the most used state observers or design methods for the state observers in internal Plant uncertainties and external disturbances conditions for linear and non-linear systems.

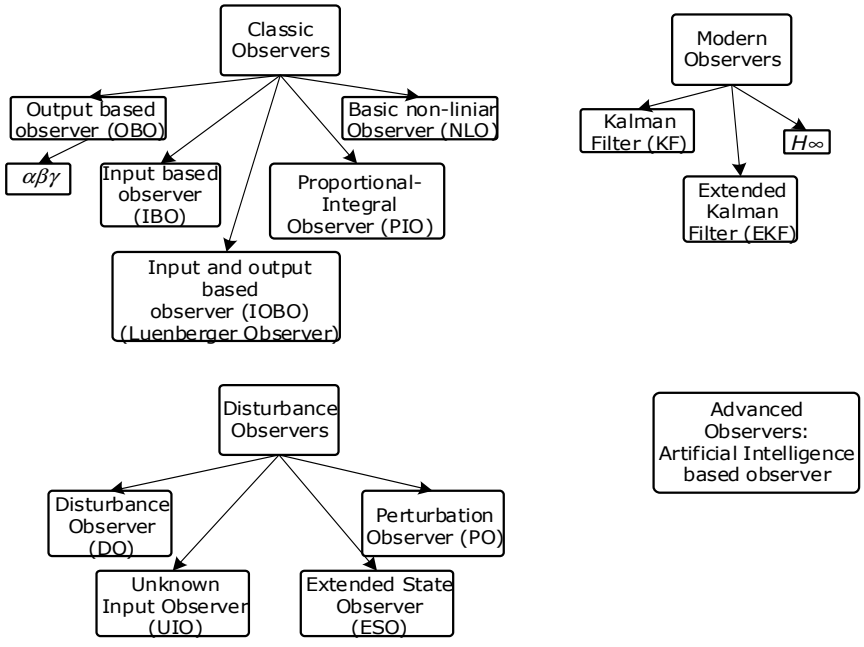

Fig. 1.4 State-of-the-art structured diagram of state observers (estimators/filters) [26]

BUPT

Sensorless monitoring methods were extensively investigated in all domains in response to the need for cost reduction.

In electrical machine control, the electrical machine state could be monitored by sensors (such as encoders or torque transducers) or by speed or torque estimators (observers/filters).

Recently, many electrical machines' torque and speed observers have been proposed. Some are also used for machine and system condition monitoring and fault detection [27].

In response to the market requirements, the robot and medical industry path rely on torque and speed observers. Based on these requirements, a lot of torque observers for high-precision applications (robot manipulation, medical applications and aerospace) can be found in the literature [28]–[30].

1.3.1. Classic observers

The first system observers are considered classic observers, where the basic idea was to extract unmeasurable parameters of the system from the input, output, and internal system dynamics.

a) Output-based Observer (OBO)

One of the basic and used estimator types is based on the output information of a system. In other words, the system output is used for the parameter or state estimation, using only the generated system output. Based on its principle, the first Observer is called an Output-based Observer (OBO) [31]. Several such applications can be considered to be low-pass filters or approximate differentiators. In Fig. 1.5, a system structure of an output-based observer is presented.

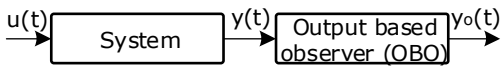

Fig. 1.5 Output-based Observer (OBO) diagram

More complex observers can be achieved starting from OBO by considering advanced techniques for system output filtering or processing [32].

b) $\alpha\beta\gamma$ observer ($\alpha\beta\gamma$)

The $\alpha\beta\gamma$ Observer can be considered a particular case of the output-based observer structure as long as the monitored system output represents the observer input. An interesting comparison (with experiments) between the Alpha-Beta-Gamma observer and two other observer types is given in [33], where the Observer is used for a parallel manipulator application. Another simple approach of $\alpha\beta\gamma$ observers is given in [34], where a simple Alpha-Beta filter algorithm is presented with different learning models.

c) Input-based Observer (IBO)

In contrast with the output-based Observer, where the system output values were used for estimation, the input-based Observer (IBO) is represented by a copy

BUPT

of the real system, producing the same result as the system. In other words, the IBO rebuilds the system functionality based on the system's inputs.

The correctness of the observer results depends on the Observer's capability to replicate the system performance. The input-based observer diagram is presented in Fig. 1.6.

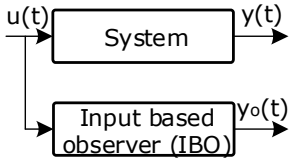

Fig. 1.6 Input-based Observer (IBO) diagram

d) Input and output-based Observer (IOBO) – Luenberger Observer (LO)

The Input and Output based Observer, also called the Luenberger Observer, represents a combination of the OBO and IBO. Compared with the previously presented observers, the Luenberger Observers use the system input and output for increased performances [35].

The Luenberger Observer principle relies on the possibility of actively finding the errors -as precise as possible- between the real system and the system replica. In Fig. 1.7, the errors between the system and Observer are continuously modified in the "Error weighting" block and then used as a correction for the observer input.

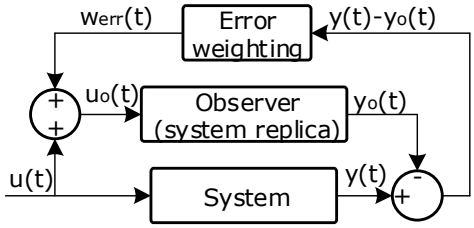

Fig. 1.7 Basic diagram of Luenberger Observer (after [35])

e) Proportional Integral Observer (PIO)

The Proportional-Integral Observer represents an improvement of the Luenberger observers, in which the estimation error is reduced by using an integral gain [36], [37].

In this case, the Observer can estimate the system uncertainties and external disturbances. Based on estimations, the controller can modify the system state according to overall perturbation.

The PI loop improves observer performances, thus reducing the cumulative error over time. The PIO's gain improves the observer performances but at the cost of increased measured noise.

In Fig. 1.8, the PI observer's structure can be seen. Compared to other observers, in this case, the proportional and integral coefficients are the subjects of a careful selection process.

BUPT

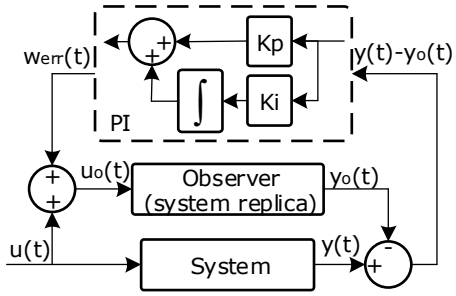

Fig. 1.8 Proportional Integral Observer (PIO) – an improvement of Lunberger observer (after [36])

f) Basic non-linear Observer (NLO) – Non-linear Luenberger observer (NLO)

A set of non-linear equations can express a non-linear system. Such filters can be used for state observation, but they are limited by the system's nonlinearity knowledge [38], [39].

In non-linear systems, the Observer can either be designed directly based on the non-linear equations or perform a system linearization and then uses a linear observer.

1.3.2. Modern observers

With a greater need for computational resources, modern observers have been developed more recently than classic observers. In contrast with classic observers, the modern ones are designed considering the perturbance from the beginning. Three different such observers are summarily presented in the following.

a) Kalman Filter (KF)

The Kalman filter can be interpreted, basically, as a state observer. Thanks to their robustness, the KFs are extensively used in many mechatronics systems, and not only. It was extensively used

The Kalman Filter is represented by a recursive data processing algorithm for linear dynamic systems with relatively low demand for data resources. In real-time systems, the KF requires a high speed of the data processing loop with a constant sampling rate.

In Fig. 1.9, a Kalman filter recursive algorithm is given according to [40].

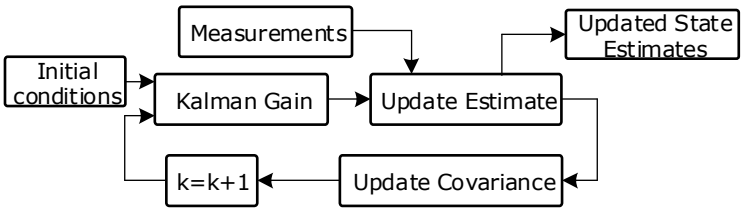

Fig. 1.9 Kalman filter recursive procedure – schematic diagram (after [40])

To estimate the system state, the algorithm requires a well-known system model and the total error influence in the measurements and system [41]. The KF

BUPT

was extensively used for minimizing the measurements errors and even for future system state estimation [42].

b) Extended Kalman Filter (EKF)

The Extended Kalman Filter is represented as the Kalman Filter for non-linear systems. Its principle of work relies on the linearization of the non-linear system [43] based on multivariate Taylor series expansions.

Even if the EKF is considered to be a significant improvement compared to KF, one of its major drawbacks is that if the initial system state is wrong estimated, the entire modeled filter will rapidly diverge. More, similar unwanted results will be achieved if the modeled process is slightly incorrect

As in the case of KF, the filter follows an undesirable path with accordingly negative results if the Gaussian white noise does not represent the modeling error. Higher order of EKFs gives better performance results in smaller noise conditions [44].

Similar to KF, the EKF is represented by a recursive algorithm. For example, in [45], the authors use the EKF to monitor and improve the state of charge for lithium-ion batteries.

c) H∞ Estimator (H∞)

Considered to be more of a design method for the controller, instead of an estimator, the H∞ is being used to perform an optimization that "hides behind" a control problem. Being a linear robust control method, the H∞ is considered to be a mathematically complex tool.

It is characterized by a high-gain functionality which is considered necessary to be able to reject any unwanted situation encountered in the system.

A standard robust control problem based on H∞ can be represented in Fig. 1.10, where the system consists of a transfer function with two inputs, one of which (w) represents the reference signal together with the disturbance and the other one (u) represents the manipulated variable. Also, the system has two outputs: the error that must be minimized by control (z), and the measurable variable that represents the controller's input [46]. In other words, the controller has to be able to minimize the influences of the disturbance (from w) over the system by modifying its output value (u) based on the measurable output of the system (v).

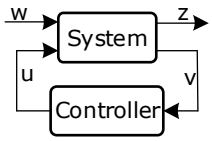

Fig. 1.10 Standard configuration for H∞-based robust control [47]

1.3.3. Disturbance estimators

Compared to previously presented estimators, which were able to detect the true state of a system as much as possible, the perturbance estimator aims to detect and reject the potential system perturbations. Considering "measurable" perturbances, a relatively simple strategy could be implemented to reject it. In most cases, the external disturbances can not be measured.

BUPT

Starting from this idea, the Disturbance Estimators (DE) are used to estimate the disturbances and use this information in a feedback control strategy to compensate for disturbance influences. Several such applications and comparisons based on DE are given in [48], [49].

a) Disturbance observer (DO)

The DO consists of a feedback-based controller as an inner loop which increases the general controller robustness by rejecting the external measured disturbances.

In Fig. 1.11, the basic diagram of a DO is given. The Disturbance Observer contains the System model, which also considers the external noise. The inner loop feedback can be filtered, although in some cases, the filters can be applied directly to the signal subtracted from Disturbance Observer (γ).

In [50], the design of a disturbance observer for non-linear systems is presented.

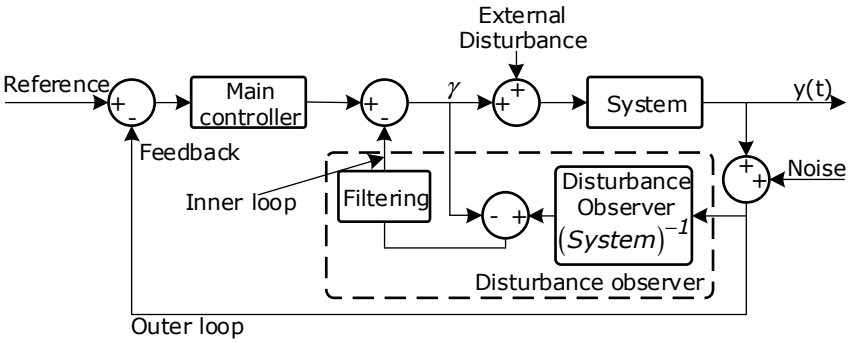

Fig. 1.11 Basic diagram of a Disturbance Observer

b) Unknown Input Observer (UIO)

As a practical improvement of the Disturbance Estimator, the capability to simultaneously estimate both the disturbance and system state was newly added in Unknown Input Observers.

In Fig. 1.12, a simplified structure of UIO is presented without representing the observed system.

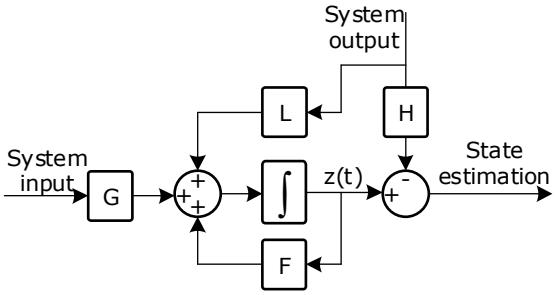

Fig. 1.12 Simplified unknown input observer structure diagram [51]

BUPT

The System input and output measurements are respected by the system. The H, L, F, and G are matrices with appropriate dimensions.

Moreover, the UIO can estimate the system state even if not all inputs are known. The first UIO report for known and unknown inputs was mentioned in 1975 by Wang [52].

In other words, the UIO is designed so that the disturbances do not influence the estimation error. A practical example of observer design for linear time-variant systems with numerical examples is given in [53].

c) Perturbation observer (PO)

In this type of Observer, the system uncertainty and the measurement error (disturbances) are estimated in the time domain.

Being mathematically simpler than other observers, the PO is extendedly applied to motion control systems. In addition to the DO, the PO also considers the system dynamics. More than that, the observer-obtained results depend on the system model and the type of low-pass filter used for input noise filtering [54]. The so-called Q-filter (the low pass filter) represents a key factor for controller performance and robustness.

In [55], the author proposed a discrete perturbation observer for linear systems in motion control applications. The paper comprehensively analyses perturbation observer performances for different low-pass filters, system inertia, and sampling frequency.

d) Extended state observer (ESO)

Standard ESO is very susceptible to measured high-frequency disturbances amplification due to its high-gain nature. This leads to an increase in the difficulty of choosing the gain, considering, on the one hand, the accuracy of the Observer and on the other hand the sensitivity to high-frequency noise [62].

A less noise amplification UES is presented in [63], where a Cascade Extended State Observer (CESO - Fig. 1.13) is given to improve the total estimation process. The Extended State Observer is considered an essential part of the uncertain non-linear systems [61] because it requires less information about the system.

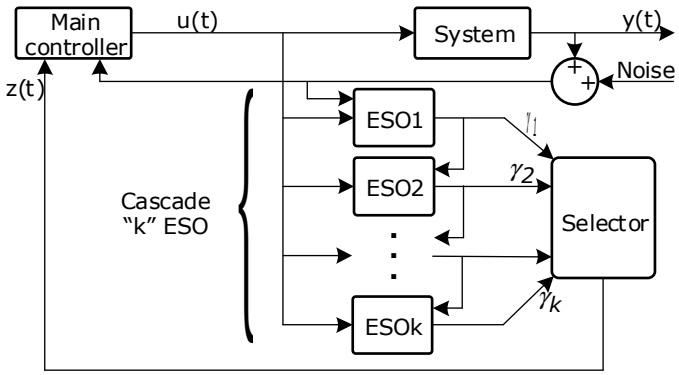

Fig. 1.13 Cascade Extended State Observer – simplified diagram [56]

BUPT

The performances are achieved, basically by small gain values, which thus limits the disturbances amplification.

1.3.4. Advanced observers – Artificial Intelligence based Observer

As a nowadays great interest subject, in other words, as an essential part of the new technological revolution (Industry 4.0), Artificial Intelligence finds its place in as many applications as possible. Deep Learning (DL) and machine learning (ML) can be considered core technology in AI (Artificial inteligence). With a wide range of applicability, DL technologies come from Artificial Neural Networks (ANN) [57].

In [58], the authors present state-of-the-art ANN-based controllers and observers for electric drive applications. One of the significant changes can be considered in how new modern ANN-based controllers replace the classical PI or PID controllers. In this context, the author describes the concept of an Induction machine drive based on ANN with two controllers for the rotor speed and stator currents.

Fig. 1.14 presents a basic simplified diagram of an electrical machine control technique with system feedback given by an ANN-based torque observer.

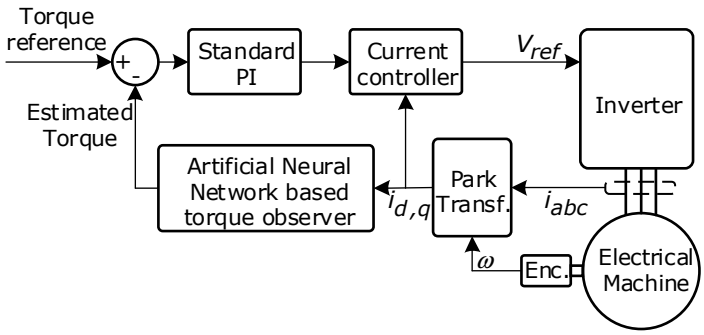

Fig. 1.14 Artificial Neural Network – based torque observer - its place in a standard and simplified control scheme

As experimentally presented in [59], the AI technique can be successfully used (root mean square error less than 1% of the estimated torque related to the rated torque) for electrical machine torque estimation. More than that, the authors train the neural network using only the measured torque and does not request the estimated flux.

1.4. Electrical machine virtual testing

Electrical machine testing is required for preliminary design checks and batch performance validation. Moreover, the electrical machine thermal testing represents a validation of the ventilation system and the insulation quality and confirms the machine's performance.

With the development of power electronics, electric motors' "standard" regenerative testing procedure was mainly done in a back-to-back configuration. In Fig. 1.15, a basic schematic diagram of the back-to-back configuration for electrical machine testing is presented for fixed speed with one machine directly connected to

BUPT

the grid (a), and with the possibility for dynamic testing with two variable frequency converters (b).

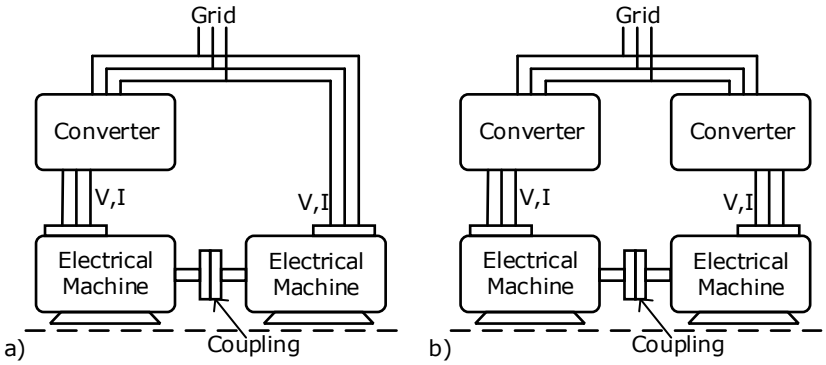

Fig. 1.15 Electrical machine testing regenerative setup in the back-to-back configuration: a) single converter, fixed-testing speed, b) two converters, dynamic testing

In many cases, the classical approach of electrical machine testing can be a high-time-demanding procedure not only due to the testing procedure but rather because of the need for mechanical coupling between the machines. In the case of large or vertical-mounted shaft machines, the shaft loading procedure can be very expensive or even impossible.

1.4.1. Superposition equivalent loading method

As part of standard electrical machine testing procedures, the superposition equivalent loading method for induction machines involves replacing the classical electrical machine rated-power shaft loading for thermal testing with a test procedure that does not require the actual machine loading at rated power. This method presents a major potential interest for large machine testing, where the rated-loading test can be challenging.

In [60], the authors present (based on this method) experimental results for small and medium machines. Their work clarifies the IEEE 112-2017 standard [61], where the superposition equivalent loading method is presented for polyphase induction motors.

As a response to these limitations, in the literature, many virtual loading procedures have been used for electrical machine loading over the last decade. These virtual (synthetic) loading procedures imply an artificial rise in the machine temperature without needing mechanical couplings.

Several methods of virtual electric machine testing procedures are given and explained in the literature. Some of them claim the reduction of the test human resources cost, the improvement of the loss estimation, and the achievement of a shorter test completion time.

The virtual loading procedure for electrical machines presents a high demand in all industries (electrical machine design, production, and system integration), especially where the mechanical or electrical conditions require special needs.

Next, a short state-of-the-art of the most commonly used electrical machine testing procedures is presented.

BUPT

1.4.2. Mixed frequency loading method

Some of the artificial loading methods presented below are relatively old methods. For example, the mixed frequency method, introduced by Ytterberg ("two-frequency method" has been around for more than one decade (since 1921). One of its literature mentions is given by the A. Meyer and H.W. Lorenzen in 1979 ([62]). His virtual loading method was based on two series-connected generators which fed a test machine without shaft loading. The generators provide two different three-phase voltage systems with different amplitudes and frequencies. In other words, two magnetic fields would appear in the machine that would rotate at different speeds.

1.4.3. Current harmonic injection method

An improved synthetic loading procedure is presented in [63] for in-wheel motors (IWMs) with current harmonic injection. The proposed method reduces human resources costs, thus eliminating mechanical coupling. Testing method results are given in contrast with the classical back-to-back artificial loading method.

1.4.4. Dynamic thermal loading

Another synthetic loading method can be considered when it performs a fast change of the machine regime (from the motor to the generator and vice versa). Fast machine acceleration and deceleration (with the direction reversal – but not always necessarily) can lead to similar dynamic effects on the machine, such as shaft loading.

In Fig. 1.16, a possible setup configuration for electrical machine synthetic loading is presented, with one machine driven by a 4-quadrant variable frequency converter. The back-to-back converter is required (in case of small inside dc capacitance) to inject into the grid the machine-generated pulsating power. In this case, the inside-converter dc capacitor has a significant role during the test. When testing, the grid may be subject to pollution due to the test nature (during the motor/generator mode, the power is absorbed/generated from/to the grid). The total system inertia (machine + inertia J), the dc capacitor, and the speed and control techniques are critical factors for test performances and grid pollution. When the machine rotor inertia is considered sufficient for test dynamics, the external moment of inertia J can be missing.

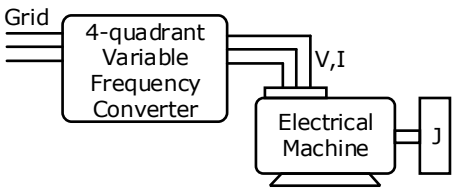

Fig. 1.16 Possible experimental setup for electrical machine dynamic loading

In one of the author's scientific papers [64], the influences of a dynamically controlled induction machine on the dc voltage of the used inverter (2-quadrant inverter), for two dc capacitance values are presented. It is clearly shown that the

BUPT

voltage pulsations are smaller for doubled dc capacitance. It is also presented how the ac-source current (grid-absorbed current) looks during the artificial loading test.

Another synthetic loading with performance analysis for an Interior Permanent Magnet Synchronous Machine (IPMSM) is presented in [65], where the author uses a Field Programmable Gate Array (FPGA) for direct measurements of the electrical machine converter's output voltages. No torque transducer or loading machine is required. The virtually-loaded machine is accelerated and decelerated rapidly, thus being considered a dynamic loading method. The results obtained from experiments are compared with Finite Element Analysis (FEA) results.

1.4.5. Multiphase machine artificial loading

The multiphase machines tend to become a promising alternative for more and more applications thanks to their capability "to split" the power and their robustness and redundant character. From Electrical Vehicles (EVs) to aerospace applications, multiphase machines are increasingly used [66].

Several such electrical machine synthetics loading examples are next presented based on literature.

Fig. 1.17 presents an example of a multiphase electrical machine in an artificial loading connection. Two controlled converters are used to send the energy from one winding to another.

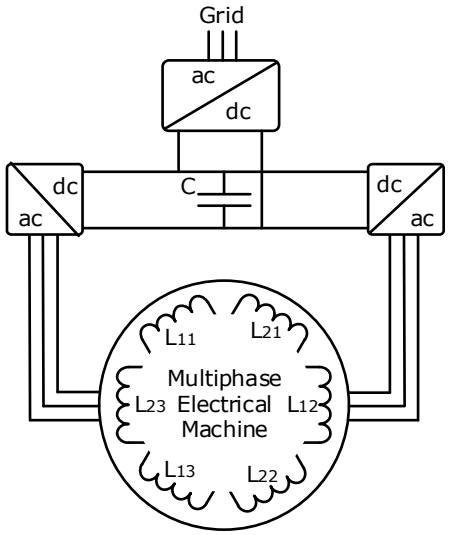

Fig. 1.17 example of artificial loading for multiphase electrical machine

For instance, an Indirect Rotor-Field Oriented Control (IRFOC) technique is utilized in [67] and [68] for a synthetic loading procedure for multiphase symmetrical or asymmetrical winding machines. The authors presented the thermal testing for a two-three-phase and for a three three-phase machine in both papers.

In [69], the authors propose a synthetic loading procedure for an electrical machine with multiple three-phase windings. Compared to other virtual loading techniques, here, the authors presented a 150kW Permanent Magnet Synchronous Machine (PMSM) with double three-phase winding loading, when one three-phase winding is used as a motor and the second one is used as a generator. The authors

BUPT

claim that the testing system losses represent only absorbed grid power. Experimental validations are given.

1.4.6. Proposed solution

In addition to all previously mentioned information related to artificial loading methods, the author proposes a new electrical machine synthetic loading method, which is extended and described in Chapter 4.

Twin induction machines without mechanical coupling driven by two dc-connected variable frequency converters are presented as the main parts of the new artificial loading method [64].

The solution allows machine testing for up to 120% of RMS phase current, with a power source twice smaller than the power source used for one single induction machine artificial testing. It is presented that the ac source current spikes are due to induction machines' losses. Two comprehensive simulations are being used for experimental validation.

The proposed solution uses only industrial types of equipment for command and control. A mechanized solution is given for automated thermal testing with various speed references.

1.5. Active torque pulsation reduction techniques in pulsating loads

In Chapter 5, the presented and discussed topic is related to pulsating loading torque, especially position-dependent pulsating loading torque (such as crankshaft-based loads).

The solution applied there relies on a well-known, worldwide spread and used control technique called: Active Vibration Control.

1.5.1. Active vibration control – short intro

Active Vibration Control (AVC) represents a well-known in-literature technique used in many domains, from seismic compensation to marine ships and noise canceling.

The AVC principle relies on a simple assumption that by adding force into the system in the opposite manner, equal or smaller in amplitude than the perturbance force, the sum of both forces (perturbance and newly added one) should have a smaller overall influence on the system than the disturbance alone.

In the sound domain, the idea of the active control of the unwanted system perturbation by adding the same perturbation but in the opposite manner is discussed in [77]. The author mentioned that, presumably, the first discussion about the principle of sound superposition was made by Lord Rayleigh in 1878.

The AVC principle is extensively used in construction sectors, where tall buildings (in general) are secured against winds and small earthquakes. Passive or active solutions minimize the unwanted effects of external forces.

In Fig. 1.18, the basic principle of the well-known AVC technique is given (a) in comparison with no active vibration compensation (b). The input force represents the external force that creates the unwanted system behavior. The added force represents the newly added force into the system.

BUPT

The amplitude and the phase of the added force represent key factors for AVC efficiency (more work related to this topic is presented in Ch. 4). The resulting force, theoretically, no longer affects the system. This performance (with a total compensation level) cannot be achieved practically.

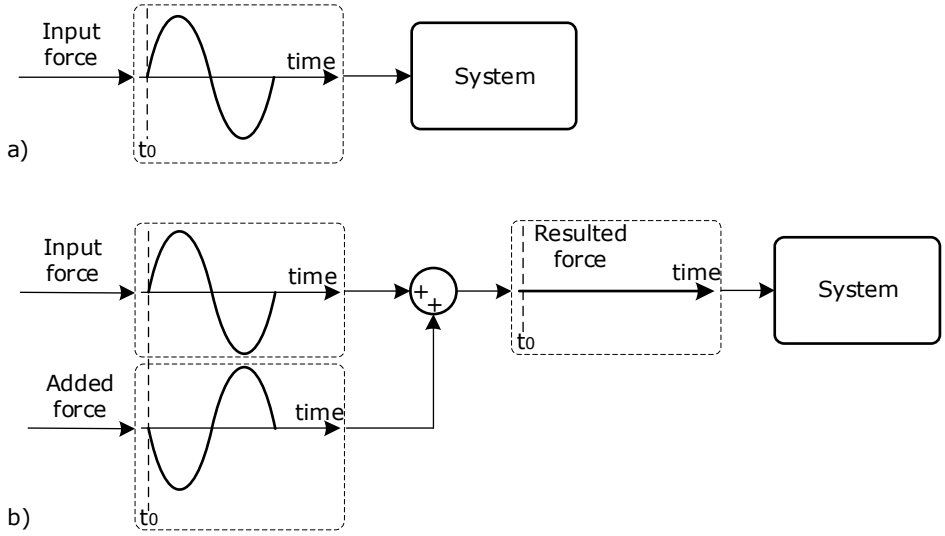

Fig. 1.18 Active Vibration Control principle: a) without AVC, b) with AVC

Three different active or semi-active solutions for AVC in tall buildings (with experiments) are presented [70] 20 years ago. The author's described solution for strong winds is represented by a hybrid mass damper system installed on the roof of the forty-three stories. Another explanation for severe earthquakes is represented by an unbonded brace damper installed at the top of a fifteen-story building, used as an energy absorber. Modern such applications are still being investigated nowadays [71].

Inspired by a catastrophic situation, in [72], the author designed a controllable spring as a vibration dampener with the possibility to change the spring stiffness during a seismic movement. Numerical simulations are given.

Another AVC practical approach can be implemented based on piezoelectric (PZT) actuators thanks to their cost, weight, and control simplicity characteristics. In many cases, the PZT is also used as a sensor and an actuator. A practical PZT-based AVC application with a solid theoretical background is given in [73].

Several other such applications can be found in the literature. For example, in [74], the author proposes an AVC PZT based on wind turbines for increased safety against blade vibrations. In [75], [76], and [77], examples of the PZT-based AVC technique applied in structures and buildings safety with applications from 1997 until now are given. Another domain with a high demand for vibration control is represented by aeronautics. In [78] is presented a practical need for PZD actuators in helicopter applications to reduce the blades' vibration influences over the fuselage actively.

A particular application of the AVC technique is found in Active Noise Canceling (ANC). The basic idea is the same as in AVC. Still, in ANC, the superimposed added signal is represented by a sound signal, not by a mechanical

BUPT

force, not to reduce de vibrations but to eliminate the effect of an unwanted frequency (or noise).

In the last decades, the ANC control easily found its place in all industries (appliances, industrial, automotive, transportation, etc.). Some of the ANC control techniques can be found in the [79], which can be considered a reference paper of the last two decades in this field.

As a general system controller topology used in all applications that require active compensation of force or noise, in Fig. 1.19, three commonly used structures are presented.

In some cases, u(t) (which is the system input containing the perturbance) can be directly measured and used by the controller in a "raw" form or filtered by the H filter for compensation.

In that case, the controller directly receives the measurable input and uses it to create the superimposed added force (n(t)). y(t) represents the system output responding to the disturbing input.

The system feedback is not measured in the open-loop structure (a). In this case, the control relies only on the system input. As a response to system safety, the controller output could be limited.

In the feedback structure (b), the newly added force, which is overlapped with the input force, is obtained by the controller for the system output. In this case, there is now needed of the controller output limitation. But in this case, the added force is generated from the system's response to the disturbing input.

One of the most used structures is represented by a feedback closed-loop controller with an additional feedforward loop for improved results (c). In this case, the system output and the measured input disturbed signal are both considered for the superimposed new force.

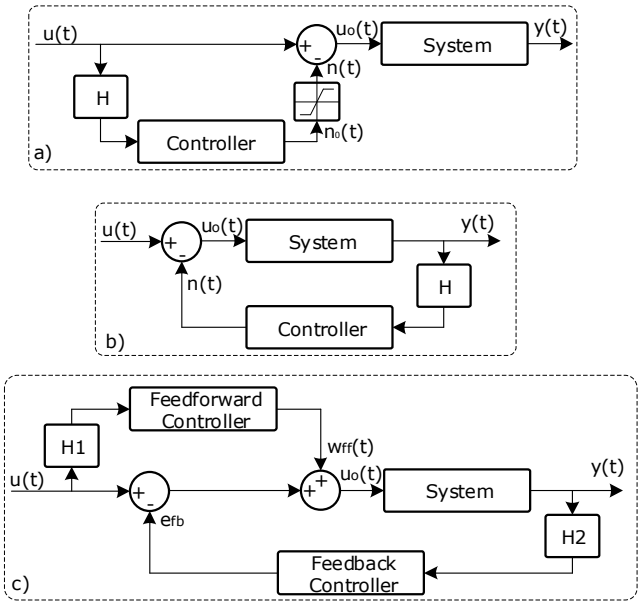

Fig. 1.19 The most commonly used controller approaches applied for active control in a) open-loop structure, b) closed-loop feedback structure and c) closed-loop with feedback and feedforward structure

BUPT

1.5.2. Active pulsation reduction method

In practice, there are different sources and types of torque pulsations in electric machines or electromechanical systems driven by electric machines. Regardless of the torque pulsation source, vibrations, noise, faulty positioning, and even mechanical failure are counted among their negative effects.

In electrical machines, the torque pulsations can be represented by the cogging torque. With a high impact over the speed, the cogging torque pulsation reduction methods are addressed in many applications in several electrical machine types.

Even from the design stage, the literature can be found many procedures for cogging torque reduction. Various such applications can be found concerning the reduction procedures for cogging torque and torque ripple in different types of electrical machines (Permanent magnet synchronous machine [80], Permanent magnet motor with Auxiliary Salient Poles [81], Brushless DC claw-pole [82], Interior Permanent Magnet Synchronous Machine [83]).

For already in-use machines, the designing methods can't be applied any longer. However, several control techniques are presented in the literature to suppress unwanted repetitive disturbances (such as cogging torque or torque ripple). This way, the torque pulsations are diminished using the power electronics-based equipment used for machine control.

There are several techniques in the literature for controlling an arbitrary periodic disturbance. For instance, Iterative Learning Control (ILC) can improve the system performance if it is subjected to an in-time repetition. Its performance drops drastically with the increase of the perturbance non-repetitively character. Such an example can be found in [84], where the author used a Robust ILC for torque ripple minimization in PMSM.

In Fig. 1.20, a basic schematic diagram of an ILC is given, used for an existing closed-loop system. Based on the error between the setpoint reference and the current system state (e(t)), the H filter computes the value that is being added to the last value of the ILC to obtain the new value for the ILC input, which is then filtered by a robustness filter (Q filter) [85].

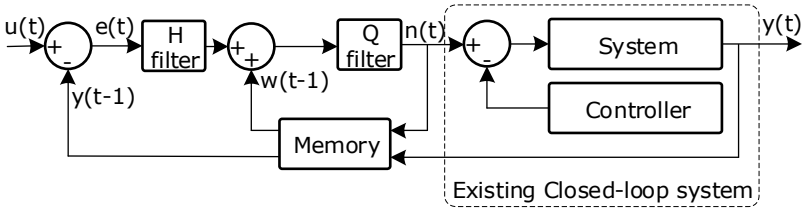

Fig. 1.20 Iterative Learning Controller (ILC) schematic diagram

Another intensively used technique to eliminate unwanted repetitive disturbances is related to Repetitive Control (RC). In [86], the authors mentioned the first report (1981 by Inoue et al.) on the Repetitive Control technique.

The RC theory is based on the Internal Model Principle (IMP). The concept is based on tracking a repetitive reference using a delay model in the feedback loop. The controller uses a model of the input reference to obtain zero error asymptotically. For unknown inputs, it is mandatory that at least the signal period be known so that a positive feedback delay will be applied. In Fig. 1.21, a simple

BUPT

structure diagram of the repetitive control is given. The Q(s) is a low-pass filter. Repetitive control designing methods and their applications can be found, for example, in [87], [88]. In [89], the author proposes a practical, robust repetitive control of a linear oscillating motor loaded by a pump. The author treated the load individually on its Fourier components and compensated for the model uncertainties.

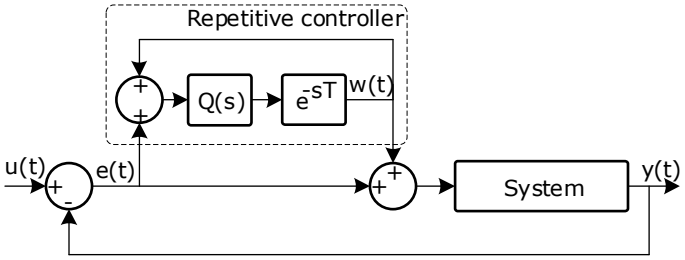

Fig. 1.21 Repetitive control general simplified schematic diagram

Several such applications with periodically repetitive external influences in the system can be considered position-dependent loads (commonly used examples consists of, but are not limited to, crankshaft-based loads). In Fig. 1.22, a general position-dependent loading torque example is given.

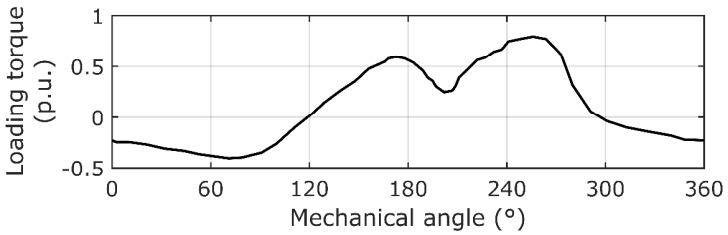

Fig. 1.22 example of position-dependent loading torque for rotary mechanical system

The torque pulsation of a system represents one of the leading factors for mechanical system failure.

Torque smoothening is highly recommended in pulsating torque applications. Among the load torque filtering methods (thus reducing the created vibrations and other negative influences), passive smoothening methods are related to the utilization of the high mass inertias mounted on the same shaft as the load.

One of the most used practical applications of high-mass flywheels is given in low-frequency recuperative energy storage systems (RESS).

As a significant difference between the on-shaft flywheel-based methods, the RESS requires a more complex system based on power converters (with large dc storing capacitors) and special mechanical topologies.

In this case, the pulsating torque frequency is limited by the amount of energy that can be rapidly stored in the flywheel. A similar application can be found in [90], where the authors proposed a flywheel storage system for a welding current source.

In Fig. 1.23, two different schematic diagrams related to pulsation reduction methods are presented, a) passive solution, where the torque pulsations are filtered by a high-mass flywheel, or b) where power pulsations are filtered by a regenerative system.

BUPT

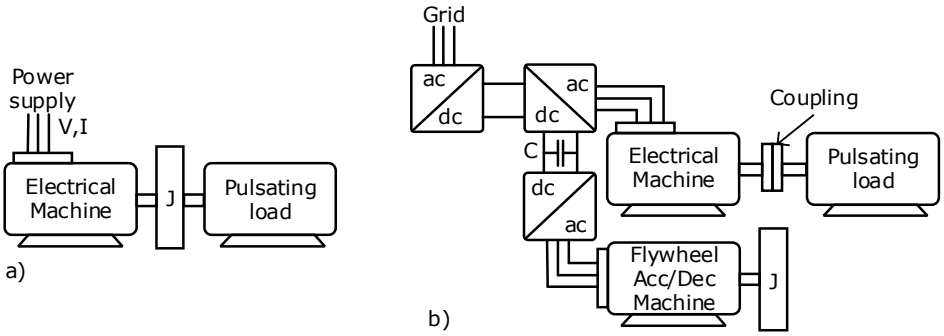

Fig. 1.23 Pulsating torque filtering: a) passive flywheel mounted on the same shaft, b) regenerative storage system

Pulsation reduction methods are also intensively used in refrigerator applications, where, due to the nature of the compressor's operation, the efficiency and life span of the system decreases. Similar to refrigerators, a current controller for linear reciprocating vapor compressors is presented in [91]. The author gave a hybrid current controller for a linear motor as a combination of a PI controller and a B-spline neural network. The B-spline neural network is online in real-time trained. Simulation and experimental results are given for a prototype linear compressor.

In electromechanical systems, the torque pulsations directly reflect into the system speed.

A speed fluctuation regulation application can be found in the automotive industry, where a flywheel-integrated starter generator (FISG - motor starter mounted directly on the engine crankshaft) is used for torque (speed) filtering. A passive solution contains flywheels or torsional dampers. In this paper [92], the author monitored the engine torque through a torque observer, which directly controls the FISG. The torque observer is based on the dual-lumped-mass system.

In electromechanical systems affected by vibrations, international standards (API 618 - Standards) regulate the level of vibrations accepted in different cases (power, speed, vibration amplitude, etc.). Such situations are often encountered in piston-based compressors (reciprocating compressors).

The pulsating loading torque interacts with the electrical machine's electromagnetic torque in the electromechanical system. In other words, considering the entire system, the machine air-gap produced torque has to be considered for a more-precise system dynamic state estimation. A comparative study between a classical lumped model of reciprocating compressor trains driven by an induction motor with a more advanced model is presented in [93].

The last chapter of here presented work is related to a novel pulsation reduction method applied in the electromechanical system with position-dependent loads is presented.

Compared to literature solutions, this method is based on a position-dependent load driven by a grid-connected induction machine with an additional on-shaft small power machine driven by a variable frequency converter.

Based only on three currents and three voltages, an electromagnetic torque estimator is used for online real-time grid-connected induction machine torque estimation. The theoretical solution implies that the additional machine counteracts the pulsating load according to the system speed, using only information from the grid-connected induction machine that drives the load. Based on that value, the additional machine's drive is being controlled.

BUPT

The practical solution is based on industrial equipment with standard industrial communication protocols. The presented solution offers a two-step method for pulsating torque and system inertia detection.

Simulations and experimental results are given.

1.6. Conclusion

In the first part of this chapter, an overview of the basic concepts of the further covered subjects is presented. The industrial equipment trend in the present and future industries is discussed. A short state-of-the-art of the nowadays technologies is given in terms of standard industrial equipment. The need for industrial equipment is well-defined in the Industrial Internet of Things.

A state observer's basic structure is presented with a summary of the most used state estimators. Advantages and disadvantages, as well as comparisons between the observers, are mentioned with literature examples. A comprehensive base structure of observers is given for classic, modern, disturbance, and advanced observers based on artificial intelligence.

Three observers are treated for two different applications. State-of-the-art virtual loading machine technique is given. Differences between the author's method for artificial loading and the literature presented methods are provided.

In the last part of the chapter, the author presented a summary of the most affected applications by torque pulsations. Several active or passive torque-damping approaches were given.

BUPT

2. Standard low-cost industrial equipment – scope broadening

Abstract

This chapter presents clear information on low-cost industrial programmable logic controllers (PLCs) limitations. It highlights why this equipment cannot be used effectively in real-time induction machine (IM) torque estimation.

Moreover, a theoretical and practical approach is given for frequency spectrum analysis in the discrete-time domain based on the Fast Fourier Transform (Discrete Fourier Transform (DFT) implemented into the PLC. The experimental result is presented and discussed.

2.1. Preliminary aspects

Over the last few years, one of the industry's significant trends was integrating compact industrial equipment into all applications. From research and education processes to safety and hardware-in-the-loop applications, PLCs have found their place in all industries: health and medical, wastewater treatment, construction sector, power generation, and management [94]–[97].

In general, suitable control devices should be used depending on the application type (critical application, health application, etc) and application specification (time response, acquisition frequency, output update time, etc.).

A higher degree of performance, as it is known, comes with higher production costs. For example, unlike processes with relatively high time constants (water flow, heating, etc.), the controller performance increases significantly in the case of high-frequency response control.

In more complex applications, where the PLC unit represents the main control core, special and dedicated devices are mainly used in sub-applications that require special running conditions [98]. In electric drive systems, the maintenance process is a key factor for saving time and money.

Real-time monitoring of system health status is an essential factor in all applications [99]–[102].

The author presented in [103] how a low-cost PLC structure can be used with certain limitations for online grid-connected induction machine torque estimation.

2.2. Low-cost industrial equipment - limitations

Periodic (uniform/equidistant) sampling represents one of the world's most used sampling/acquisition methods. This means that the intervals between two read data are equal.

BUPT

In case of variable (random) sample frequency it is mandatory that each action was taken in one interval to be computed based on the time interval since the last sample. In signal processing and analyzing, this issue represents one of the standard problems.

In literature, as the most straightforward way (which requires a minimum computation effort), it is recommended to interpolate the non-uniformed sampled signal and then "resample" at a constant frequency rate.

For non-real-time applications, considering a high performances control unit, using this method could be a practical solution. But on the other hand, in real-time applications, with output updates every program cycle, the interpolation/resample process cannot be successfully implemented

Moreover, for IMs electromagnetic torque estimation, unchanged read data are mandatory to increase time response and estimator's performances [104]–[108].

Below are presented three preliminary tests that the author recommends to be performed before using the PLC as an electromagnetic torque estimator for a grid-connected induction machine.

First, some low-cost industrial programmable logic controllers (PLC) were investigated to find suitable equipment to implement the torque estimators.

Generally, the basic and reduced structure of the investigated industrial equipment is composed of a centralized or a decentralized system (Fig. 2.1) where the processor, the communication (Profibus) module, and the digital input and output modules are directly or indirectly connected with the analog input module.

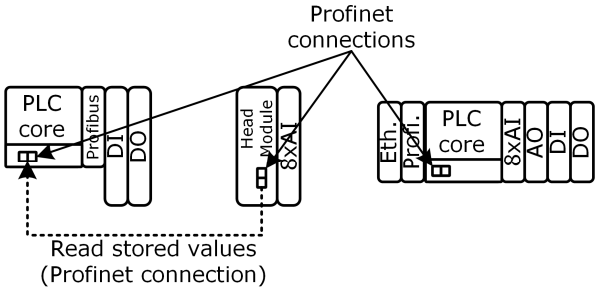

Fig. 2.1 An example of the general basic and reduced structures of the investigated PLC systems: a) decentralized system, b) centralized system

The Profinet interface could be built-in in into the processor, while the Profibus module has a right or left-side connection to the main processor (but not necessarily)

Three preliminary tests, which highlight - depending on the type of application - the suitability of the equipment to the related applications, are further presented briefly in Table 2.1. These initial tests are meant to demonstrate the PLC's correctness of the data-read process as well as the PLC processing capability.

To perform the tests, all the analog input channels were supplied with the same alternating voltage from a signal generator. The generator signal frequency is $f_{SG}[Hz]$, and the industrial equipment (in this case, a PLC) acquisition frequency is $f_{PLC}[Hz]$.

BUPT

At each time, all channels were read at once, and the values were stored in the PLC.

To check the tests, Table 2.1 has to be completed with the data stored in the PLC's memory.

Table 2.1 Test 1 and Test 2 structure for an 8AI PLC

Test 1 Test 2		Read Channels							
		Ch1	Ch2	Ch3	Ch4	Ch5	Ch6	Ch7	Ch8
Time	t1	X1.1	X1.2	X1.3	X1.4	X1.5	X1.6	X1.7	X1.8
	t2	X2.1	X2.2	X2.3	X2.4	X2.5	X2.6	X2.7	X2.8
	t3	X3.1	X3.2	X3.3	X3.4	X3.5	X3.6	X3.7	X3.8
	t4	X4.1	X4.2	X4.3	X4.4	X4.5	X4.6	X4.7	X4.8
	⋮	⋮	⋮	⋮	⋮	⋮	⋮	⋮	⋮
	t(j)	Xj.1	Xj.2	Xj.3	Xj.4	Xj.5	Xj.6	Xj.7	Xj.8
	⋮	⋮	⋮	⋮	⋮	⋮	⋮	⋮	⋮
	t(pk)	X(pk).1	X(pk).2	X(pk).3	X(pk).4	X(pk).5	X(pk).6	X(pk).7	X(pk).8

a) Test 1 – Momentary deviation between the channels

The test has to be performed on k full input signal periods (k – an integer that represents the total number of full periods of the generator signal). Based on (2.1) the first test consists of finding the maximum difference between any two channels.

$$Err_{t1} = \frac{max\left(\left|ch_m(i) - ch_n(i)\right|\right)}{Input\ signal\ amplitude} \cdot 100[\%] \tag{2.1}$$

Where:

i – represents the read data index: $i \in \left[1..pk\right]$;

p – represents the total number of read data;

k – represents the number of points from one period:

$$k = \frac{f_{PLC}}{f_{SG}} \tag{2.2}$$

m, n – represent the total number of read channels: $m \in \left[1..8\right]$ $n \in \left[1..8\right]$, $m \neq n$

The first test provides information about the read module conversion limitations. These are largely part of the processing capabilities of the analog-to-digital converter (ADC). The processor must be chosen so that the acquisition error of the related module is within limits imposed by the application.

b) Test 2 – The in-time channels synchronization

The second test deals with the evolution of the program cycle average. This means that, in the case of the low-cost PLCs, the average cyclic time of the

BUPT

processor (A_{Pct})could be slightly different than the configured processor speed (C_{Pct}).

$$Err_{t2} = ch_n(j) - ch_n(j+k) \tag{2.3}$$

where j represents the j^{th} number of cyclic program, and k is defined by (2.2).

Depending on the Err_{t2} actual (average) speed of the program cycle may be higher or lower than the set speed.

$$\begin{cases} A_{Pct} > C_{Pct}, & Err_{t2} < 0; \\ A_{Pct} > C_{Pct}, & Err_{t2} > 0; \end{cases} \tag{2.4}$$

c) Test 3 – The sampling frequency (synchronous cycle) variation test

The standard low-cost PLCs have system-dependent fluctuations. This means that depending on high-priority operations or during communication activities, the program cycle can be triggered at different intervals.

The communication between the peripheral systems and the central unit represents another significant influence on execution time. Depending on the data volume to be exchanged, the program cycle execution is subject to considerable time deviations [109]–[111].

Fig. 2.2 shows a practical example of time variation in PLC. Even if the execution time setpoint is set to 1 ms, the following figure shows an execution time average of 0.9086 ms. More than that, in this case, the maximum deviation time between two successive executions represents almost 19% of the execution setpoint.

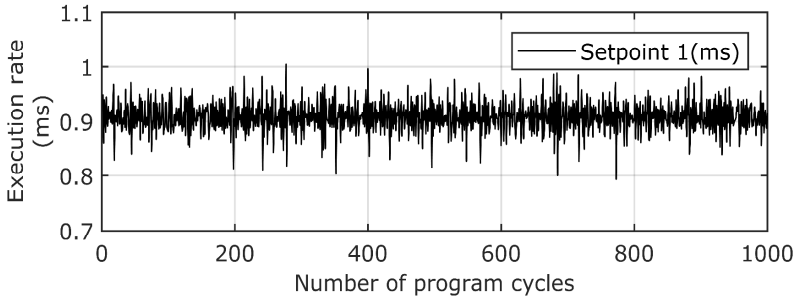

Fig. 2.2 Example of execution rate variations for one low-cost PLC 1ms execution rate setpoint

A practical example of acquisition time problems can be seen in Table 2.2, where 3 PLCs were investigated according to the last presented test.

All the PLCs were tested at 1ms, 10ms, and 100ms program cycles (although 10ms and 100ms are not helpful for torque calculation, they were presented only to highlight the variation of the program cycle).

Max $\Delta t(\%)$ represents the maximum percentage difference between two successive program cycles relative to the setpoint. These were calculated by calling the internal clock of the PLC at each program cycle.

$\bar{T}_{Et}(ms)$ is the average of the actual execution time performed by the PLC - it must be taken into account that the PLC had no computational loading.

BUPT

To highlight the negative impact of the variation of the acquisition time over the IM torque estimation, in Chapter 3 (Fig. 3.19) is presented the IM electromagnetic torque briefly, when there is no time variation in acquisition frequency and then when the acquisition frequency varies with 1% and 3% of its time limit.

Table 2.2 The maximum time difference between two successive programs and the PLC average execution time for different execution setpoints

	PLC1		PLC2		PLC3	
Execution Setpoint	Max $\Delta t(\%)$	$\bar{T}_{Et}(ms)$	Max $\Delta t(\%)$	$\bar{T}_{Et}(ms)$	Max $\Delta t(\%)$	$\bar{T}_{Et}(ms)$
1(ms)	18.8	0.9086	17.29	1.0006	6.84	0.994
10(ms)	2.42	9.897	1.45	9.997	0.81	9.996
100(ms)	0.219	99.896	0.129	99.994	0.079	100.018

As presented in Fig. 2.2 and Table 2.2, the inconsistent time variations and their appearance uncertainty make PLCs challenging for high-speed real-time, high-performance torque estimation applications. Some improvements can be achieved by measuring the elapsed time between two successive calculus and using it as a variable "*dt*" in the integral structures. The triggered time function produces an even greater central processing unit (CPU) loading.

2.3. Frequency spectrum analysis

Besides the previous investigation that proves that a low-cost PLC can not be used as a high-performance induction machine torque estimator due to the inconsistencies in acquisition and processing rate, next, the fundamental theory, as well as the experimental results, are given to use a standard low-cost PLC for frequency spectrum analysis based on well-known Fast Fourier Transform [112] for discrete-time (Discrete Fourier Transform DFT) [113], [114].

All the time-domain signals can also be represented in the frequency domain. A clear picture of a signal's structure and pattern can be determined using frequency spectrum analysis [115].

In machine condition monitoring and predictive health monitoring (MCM&PHM) systems, the presence or absence of a specific frequency from the frequency spectrum of a measured signal (voltage, current, vibration, speed, etc.) could represent the presence of a faulty part in the system.The need for frequency spectrum analysis for system fault detection could represent a time and money-saving practice. An initial spectrum analysis could lead to preventive maintenance, thus reducing system downtime.

Generally, the frequency spectrum analysis can be done online with specialized equipment or by measuring signals and offline process data with dedicated software. An application that would require a continuous frequency spectrum analysis is described in Chapter 5, where a system affected by high pulsating loading torques is subjected to a novel active torque pulsation reduction method. Next, the possibility of using a low-cost industrial PLC as a frequency spectrum analyzer without dedicated functions is presented.

BUPT

Next, a well-known algorithm for frequency spectrum analysis is theoretically presented and implemented into a low-cost PLC.

2.3.1. Fast Fourier Transform – short intro

As a fundamental, a periodic function $f(t)$ can be expressed as a series of sines and cosines functions.

In continuous time this function can be expressed as:

$$f(t) = \frac{1}{2} \cdot a_0 + \sum_{k=1}^{\infty} a_k \cdot cos(2 \cdot \pi \cdot k \cdot t) + \sum_{k=1}^{\infty} b_k \cdot sin(2 \cdot \pi \cdot k \cdot t) \tag{2.5}$$

Where: a_0 represents a constant value and $k = \{1,2,3,...\}$ represents the frequency.

The Fourier transform realizes the frequency spectrum analysis in the continuous time domain. Image processing, military industry [116], equation solver, malfunction identification, communication (wired and wireless), and medical [117], [118] represent some of the applications that are developed based on the Fourier transform.

The Fast Fourier Transform represents an improved time-saving procedure with a reduced number of calculus.

For a signal consisting of N samples, we have:

N^2 calculus – for Fourier Transform;

$N \cdot log_2 N$ calculus – for Fast Fourier Transform (FFT);

Taking into account the Euler formula:

$$e^{\theta i} = cos(\theta) + i \cdot sin(\theta) \tag{2.6}$$

Where: θ represents the angle;

We obtain the forward Fourier Transform, which transforms a function of time into a function of frequency. The previous continuous-time Fourier forme can be expressed as:

$$Time \rightarrow Frequency : X(F) = \int_{-\infty}^{\infty} x(t) \cdot e^{-j \cdot 2 \cdot \pi \cdot F \cdot t} dt \tag{2.7}$$

Where: $X(F)$ represents the frequency-domain function, $x(t)$ represents the time-domain function, j represents the complex number, F represents the frequency, and t represents the time.

If the function and the analyzing function are similar, they'll multiply and sum to a larger coefficient. In other words, that means that if the signal is compared with a lot of sinusoids, the most significant obtained coefficient will be between my signal and the sinusoid with the same frequency.

The inverse Fourier transform transforms a function of frequency into a function of time:

$$Frequency \rightarrow Time : x(t) = \int_{-\infty}^{\infty} X(F) \cdot e^{-j \cdot 2 \cdot \pi \cdot F \cdot t} dF \tag{2.8}$$

BUPT

This subchapter presents the conversion between the time and frequency-domain representation for a discrete signal.

For applications where the signal is sampled at a specific sample rate, the Discrete Fourier Transform (DFT) is used.

In this thesis, the PLC performs data acquisition and processing. The DFT algorithm is related to the PLC's performance.

The DFT is based on a finite amount of elements (N elements). If we note:

$$\frac{k}{N} \triangleq F,\ n \triangleq t \tag{2.9}$$

We obtain the direct discrete Fourier transform:

$$X_k = \sum_{n=0}^{N-1} x_n \cdot e^{-\frac{j \cdot 2 \cdot \pi \cdot k \cdot n}{N}} = \sum_{n=0}^{N-1} x_n \cdot W_N^{k \cdot n} \tag{2.10}$$

Were W_N^k represented by the twiddle factor, which is explained further.

$$\left.\begin{aligned} W_N^k &\triangleq e^{-\frac{j \cdot 2 \cdot \pi \cdot k}{N}} = \cos\frac{2 \cdot \pi \cdot k}{N} - j \cdot \sin\frac{2 \cdot \pi \cdot k}{N} \\ n &= \{0,1,2,..,N\} \\ k &= \{0,1,2,..,N\} \end{aligned}\right\} \tag{2.11}$$

2.3.2. Cooley-Tukey Algorithm for DFT implementation

The Cooley-Tukey algorithm represents one of the most popular Fast Fourier Transform in discrete time. Because it requires low data resources and it consists of non-complex data operations, the Cooley-Tukey algorithm is widely used for DFT implementation.

There are a lot of Cooley-Tukey's algorithm versions based on different approaches to data processing. The method is used for data arrays with complex elements of lengths equal to the powers of 2 for maximizing the method's efficiency [119], [120]. This method divides the input data array into two equal parts. The method consists of combining these two equal parts taking the elements two-by-two and then multiplying them with the appropriate unit root, which also represents the twiddle factor. There are two possibilities below presented to perform DFT [121], [122].

Starting from the equation (2.10), the Decimation-in-Time (DIT) and Decimation-in-Frequency (DIF) algorithms are briefly presented below. Both algorithms perform $N \cdot log_2 N$ calculus.

2.3.2.1. Decimation-in-time (DIT) algorithm

In the Decimation-in-Time algorithm, the output is represented in a natural order, while the input is in a bit-reversed order. This method split the analyzed array of size N into two interleaved arrays of $N/2$ size. This method of Radix-2 DIT is one of the simplest methods used for DFT.

BUPT

The general formula of the Discrete Fourier Transform is given in (2.12)

$$X_k = \sum_{n=0}^{N-1} x_n \cdot e^{-\frac{j \cdot 2 \cdot \pi \cdot k \cdot n}{N}} = \sum_{n=0}^{N-1} x_n \cdot W_N^{k \cdot n} \tag{2.12}$$

First, the algorithm split the array into the even-indexed input subarray and odd-indexed input subarray:

$$X_k = \sum_{n_{even}=2r} x_{n_{even}} \cdot W_N^{k \cdot n_{even}} + \sum_{n_{odd}=2r+1} x_{n_{odd}} \cdot W_N^{k \cdot n_{odd}} \tag{2.13}$$

$$X_k = \sum_{r=0}^{\frac{N}{2}-1} x_{(2 \cdot r)} \cdot W_N^{k \cdot 2 \cdot r} + \sum_{r=0}^{\frac{N}{2}-1} x_{(2 \cdot r+1)} \cdot W_N^{k \cdot (2 \cdot r+1)} \tag{2.14}$$

$$X_k = \sum_{r=0}^{\frac{N}{2}-1} x_{(2 \cdot r)} \cdot \left(W_N^2\right)^{r \cdot k} + W_N^k \sum_{r=0}^{\frac{N}{2}-1} x_{(2 \cdot r+1)} \left(W_N^2\right)^{r \cdot k} \tag{2.15}$$

Where:

$\sum_{r=0}^{\frac{N}{2}-1} x_{(2 \cdot r)} \cdot \left(W_N^2\right)^{r \cdot k}$ represents the $\frac{N}{2}$ length of DFT even entries and

$W_N^k \sum_{r=0}^{\frac{N}{2}-1} x_{(2 \cdot r+1)} \left(W_N^2\right)^{r \cdot k}$ represents the $\frac{N}{2}$ length of DFT odd entries.

So, considering the periodicity characteristics of the complex exponent, a simplified version of the previous equation can be rewritten as:

$$\Rightarrow \begin{cases} X\left[k_{(1)}\right] = G[k] + H[k] \cdot W_N^k \\ X\left[k_{(2)}\right] = G[k] - H[k] \cdot W_N^k \end{cases} \tag{2.16}$$

A graphical representation of the Radix2 Butterfly structure of the Decimation-in-Time Algorithm can be observed in Fig. 2.3.

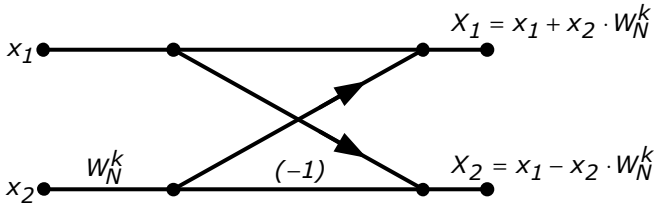

Fig. 2.3 Radix 2 Butterfly structure - Decimation-in-Time Algorithm (according to [122])

BUPT

2.3.2.2. Decimation-in-Frequency (DIF) algorithm

Compared with the DIT algorithm, in the DIF, the input is represented in a natural order while the output is in bit-reversed order.

Again, starting from the general DFT formula:

$$X_k = \sum_{n=0}^{N-1} x_n \cdot e^{-\frac{j \cdot 2 \cdot n \cdot k \cdot n}{N}} = \sum_{n=0}^{N-1} x_n \cdot W_N^{k \cdot n} \tag{2.17}$$

- The even entries array is compound below:

$$X_k = \sum_{r=0}^{N-1} x_n \cdot W_N^{2 \cdot r \cdot n} \tag{2.18}$$

$$X_{2r} = \sum_{n=0}^{\frac{N}{2}-1} x_n \cdot W_N^{2 \cdot r \cdot n} + \sum_{n=\frac{N}{2}}^{N-1} x_n \cdot W_N^{2 \cdot r \cdot n} \tag{2.19}$$

$$X_{2r} = \sum_{n=0}^{\frac{N}{2}-1} x_n \cdot W_N^{2 \cdot r \cdot n} + \sum_{n=0}^{\frac{N}{2}-1} x_{\left(n+\frac{N}{2}\right)} \cdot W_N^{2 \cdot r \cdot \left(n+\frac{N}{2}\right)} \tag{2.20}$$

$$X_{2r} = \sum_{n=0}^{\frac{N}{2}-1} \left(x_n + x_{\left(n+\frac{N}{2}\right)} \right) \cdot W_{\frac{N}{2}}^{r \cdot n} \tag{2.21}$$

- The odd entries array is compound as presented next:

$$X_{(2 \cdot r+1)} = \sum_{n=0}^{N-1} x_n \cdot W_n^{(2 \cdot r+1) \cdot n} \tag{2.22}$$

$$X_{(2 \cdot r+1)} = \sum_{n=0}^{\frac{N}{2}-1} \left(x_n \cdot W_N^{(2 \cdot r+1) \cdot n} + W_N^{\frac{N}{2}} \cdot x_{\left(n+\frac{N}{2}\right)} \cdot W_n^{(2 \cdot r+1) \cdot n} \right) \tag{2.23}$$

$$X_{(2 \cdot r+1)} = \sum_{n=0}^{\frac{N}{2}-1} \left(x_n + W_N^{\frac{N}{2}} \cdot x_{\left(n+\frac{N}{2}\right)} \right) \cdot W_N^{(2 \cdot r+1) \cdot n} \tag{2.24}$$

$$X_{(2 \cdot r+1)} = \sum_{n=0}^{\frac{N}{2}-1} \left(\left(x_n - x_{\left(n+\frac{N}{2}\right)} \right) \cdot W_N^n \right) \cdot W_{\frac{N}{2}}^{r \cdot n} \tag{2.25}$$

BUPT

So, as was previously stated at DIT, considering the periodicity characteristics of the complex exponent, the previous equation for DIF can be rewritten as:

$$\Rightarrow \begin{cases} X\left[k_{(1)}\right] = G[k] + H[k] \\ X\left[k_{(2)}\right] = \left(G[k] - H[k]\right) \cdot W_N^k \end{cases} \tag{2.26}$$

In Fig. 2.4, similarly to Fig. 2.3, a graphical representation of the Radix 2 Butterfly structure of the Decimation-in-Frequency Algorithm is given:

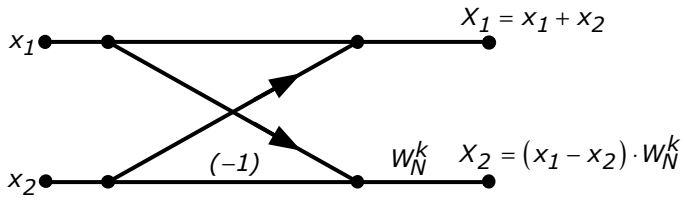

Fig. 2.4 Radix 2 Butterfly structure - Decimation-in-Frequency Algorithm (according to [122])

2.3.2.3. Twiddle factor calculation

From the previous subchapter, it was observed that the Cooley-Tukey algorithm, DIT, and DIF use the roots of unity: W_N^k, which is periodic with a period N. This twiddle factor is a multiplicative constant used to reduce the computational complexity in this algorithm [123]. If we consider the following notation:

$$W_N^k = e^{-j\frac{2 \cdot \pi}{N}k} \tag{2.27}$$

We can assume that:

$$\left(W_N^k\right)^N = 1 \tag{2.28}$$

For any $k = \{1, 2, 3, .., N-1\}$, where k represents the frequency index, and n represents the time index.

From the periodicity point of view, the twiddle factor repeats at every certain number of cycles. In the space vector, the twiddle factor is a rotating vector.

Next is presented how the twiddle factor and DFT work for a signal of different lengths.

a) N=2;

In Fig. 2.5 the roots of unity are represented graphically for a signal of two elements.

BUPT

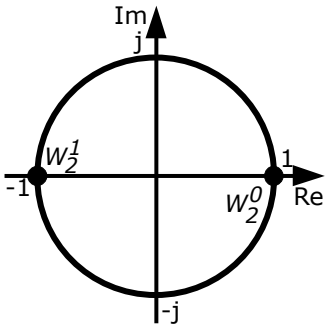

Fig. 2.5 Roots of unity for a signal of N=2 elements

In this case, the output data can be written as:

$$W_N^k = e^{-j\frac{2\cdot\pi}{N}k},(N=2,k-negligible) \Rightarrow W_2 = e^{-j\frac{2\cdot\pi}{2}} \tag{2.29}$$

$$\Rightarrow W_2 = e^{-j\cdot\pi} = cos(-\pi) + j\cdot sin(-\pi) = -1 \tag{2.30}$$

$$\Rightarrow X_k = \sum_{n=0}^{1} (-1)^{k\cdot n}\cdot x_n = (-1)^{k\cdot 0}\cdot x_0 + (-1)^{k\cdot 1}\cdot x_1 \tag{2.31}$$

Finally:

$$\left.\begin{aligned} X_0 &= x_0 + x_1 \\ X_1 &= x_0 - x_1 \end{aligned}\right\} \tag{2.32}$$

A more complex calculation example for a signal with 8 inputs is presented below.

b) N=8

Fig. 2.6 presents the roots of unity for a signal of 8 elements.

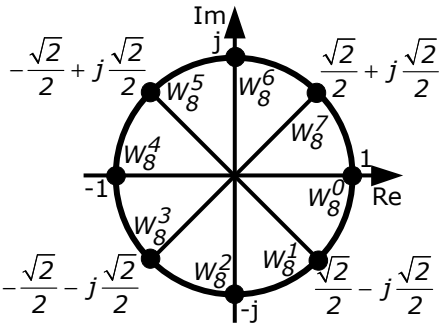

Fig. 2.6 Roots of unity for a signal of N=8 elements

So, for an 8-point DFT, we have:

BUPT

$$W_N^k = e^{-j\frac{2\cdot\pi}{N}k},\ (N=8, k-negligible) \Rightarrow W_8 = e^{-j\frac{2\cdot\pi}{8}} \tag{2.33}$$

$$\Rightarrow W_4 = e^{-j\frac{\pi}{4}} = cos\left(-\frac{\pi}{4}\right) + j\cdot sin\left(-\frac{\pi}{4}\right) = \frac{\sqrt{2}}{2} - j\cdot\frac{\sqrt{2}}{2} \tag{2.34}$$

For simplicity, we consider the: $\sigma = \frac{\sqrt{2}}{2} - j\cdot\frac{\sqrt{2}}{2}$;

$$\Rightarrow X_k = \sum_{n=0}^{7} (\sigma)^{k\cdot n}\cdot x_n = \sigma^{k\cdot 0}\cdot x_0 + \sigma^{k\cdot 1}\cdot x_1 + \sigma^{k\cdot 2}\cdot x_2 + \sigma^{k\cdot 3}\cdot x_3 + \sigma^{k\cdot 4}\cdot x_4 + \sigma^{k\cdot 5}\cdot x_5 + \sigma^{k\cdot 6}\cdot x_6 + \sigma^{k\cdot 7}\cdot x_7 \tag{2.35}$$

So, it results in the output vector as:

$$\left.\begin{aligned}
X_0 &= x_0 + x_1 + x_2 + x_3 + x_4 + x_5 + x_6 + x_7\\
X_1 &= x_0 + \sigma x_1 + \sigma^2 x_2 + \sigma^3 x_3 + \sigma^4 x_4 + \sigma^5 x_5 + \sigma^6 x_6 + \sigma^7 x_7\\
X_2 &= x_0 + \sigma^2 x_1 + \sigma^4 x_2 + \sigma^6 x_3 + \sigma^8 x_4 + \sigma^{10} x_5 + \sigma^{12} x_6 + \sigma^{14} x_7\\
X_3 &= x_0 + \sigma^3 x_1 + \sigma^6 x_2 + \sigma^9 x_3 + \sigma^{12}\cdot_4 + \sigma^{15} x_5 + \sigma^{18} x_6 + \sigma^{21} x_7\\
X_4 &= x_0 + \sigma^4 x_1 + \sigma^8 x_2 + \sigma^{12} x_3 + \sigma^{16} x_4 + \sigma^{20} x_5 + \sigma^{24} x_6 + \sigma^{28} x_7\\
X_5 &= x_0 + \sigma^5 x_1 + \sigma^{10} x_2 + \sigma^{15} x_3 + \sigma^{20} x_4 + \sigma^{25} x_5 + \sigma^{30} x_6 + \sigma^{35} x_7\\
X_6 &= x_0 + \sigma^6 x_1 + \sigma^{12} x_2 + \sigma^{18} x_3 + \sigma^{24} x_4 + \sigma^{30} x_5 + \sigma^{36} x_6 + \sigma^{42} x_7\\
X_7 &= x_0 + \sigma^7 x_1 + \sigma^{14} x_2 + \sigma^{21} x_3 + \sigma^{28} x_4 + \sigma^{35} x_5 + \sigma^{42} x_6 + \sigma^{49} x_7
\end{aligned}\right\} \tag{2.36}$$

2.4. PLC implementation of the DFT algorithm

Next, the DFT based on the Cooley-Tukey Radix 2 method is being implemented on the low-cost PLC. The input read data has 32(2^5) values. In Fig. 2.7, the read filtered speed and phase current are presented. For both signals, the Discrete Fourier Transform is performed.

The measurements are performed on an electromechanical system consisting of a three-pole pair 11kW grid-connected induction machine (GCIM) loading by a two-pole pair 15kW induction machine driven by a 15kVA variable frequency drive (VFC).

The loading machine is Direct Torque Controlled by the drive. The VFC loading reference consists of 50% of the GCIM-rated torque dc components overlapped with a 50% torque amplitude sinusoidal reference. The sinusoidal reference has the GCIM frequency. (3 pole pairs resulting in 1000rpm>16.6Hz).

BUPT

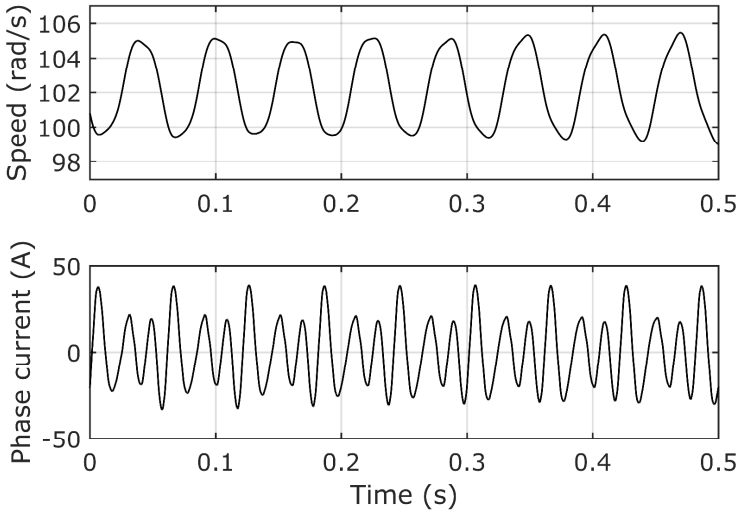

Fig. 2.7 Filtered speed and unfiltered phase current read from PLC

The measurements are performed using the PLC analog modules and an absolute encoder.

In Fig. 2.8, the results are given when the 32 inputs vector is read on one full rotation ($16.6Hz \rightarrow 0.06s$). The resulting frequency bin is 16.65(Hz).

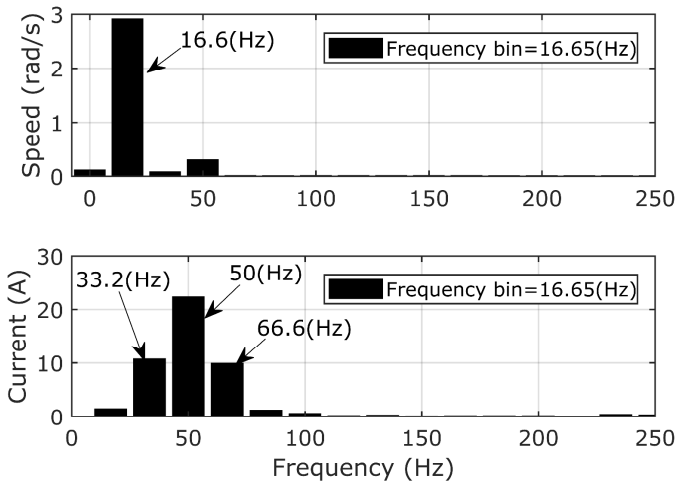

Fig. 2.8 Discrete Fourier Transform based on Cooley-Tukey Radix 2 algorithm for 32 input data on measured speed and phase current for one period (0.06s) of sinusoidal loading torque at 16.6Hz- PLC implementation

The results presented below are related to the PLC capacity to perform the Discrete Fourier Transform based on the Cooley-Tukey Radix-2 algorithm.

Similarly, in Fig. 2.9, the results are given when the 32 input vector is obtained on three full turns ($16.6Hz \rightarrow 0.18s$). In this case, the frequency bin is 5.56Hz.

BUPT

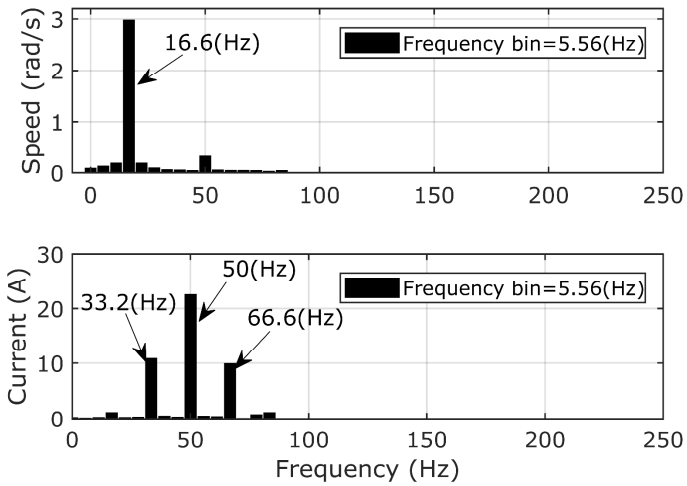

Fig. 2.9 Discrete Fourier Transform based on Cooley-Tukey Radix 2 algorithm for 32 input data on measured speed and phase current for three periods (0.18s) of sinusoidal loading torque at 16.6Hz- PLC implementation

The experiments are computed offline: the PLC reads the data and then computes the calculus.

The PLC acquisition frequency was chosen according to the frequency of the signal that is being acquired. Depending on each PLC and the programming language, different acquisition frequencies can be set through the execution time of the used function.

The speed dc component was rejected. The 16.6Hz fundamental is presented in both figures (Fig. 2.8, Fig. 2.9)

On the other hand, the phase current frequency spectrum is composed of a mix of two frequencies: the grid-absorbed current frequency 50Hz and the pulsating current frequency (16.6Hz) caused by the loading. More details about this effect are presented in Chapter 5.

A similar procedure was implemented on MATLAB software. For the same set of input data, the results are the same also for PLC, Matlab (DFT procedure), and Matlab (with the dedicated "FFT" function).

Because of the PLC software used for programming - the software has multiple declaration areas with graphical programming - in Appendix 1, the Matlab version of the DFT Cooley-Tukey algorithm was given.

2.5. Conclusion

Although programmable logic controllers (PLCs) are widely spread and used nowadays, their limitations make them rather suitable for applications with considerable time constants, where the variation of the acquisition cycle becomes insignificant with the increase of the program cycle. Because the standard industrial equipment (PLC, RTU, VFC, etc.) represents one of the most important existing layers in all the present and future industrial applications, in this chapter, a study

BUPT

related to the possibility of extending the classical range of utilization of low-cost PLCs was investigated.

In the first part, three simple tests are given to briefly check the PLC capability to perform calculus at a fixed sampling rate. Often, the problem does not occur due to the analog input module sampling rate but rather because of the CPU, which cannot maintain a constant program cycle.

Even though the performance of the equipment was not discussed in accordance with their prices, in this chapter, it was demonstrated that with industrial equipment, the electromagnetic torque of induction machines is difficult to estimate, especially with high precision.

The first part of this chapter presents how the PLC's acquisition frequency inconsistency directly affects the integration process and why this type of limitation is unacceptable.

In the second part of the chapter, the author presents the in-literature well-known Discrete Fourier Transform based on Cooley-Tukey, Radix-2 algorithm and the results obtained by implementing this method for 32 inputs in a low-cost PLC.

The experimental result proves that for a 1000rpm synchronous speed electromechanical system (16.6Hz), a low-cost PLC can be used successfully for spectral analysis in low-frequency areas. System speed and induction machine phase current were investigated.

BUPT

3. Industrial equipment-based line-start IM torque estimation with experiments

Abstract

This chapter starts with the induction machine losses identification and its modeling in Matlab Simulink. The performance of the simulated induction machine is compared with the performance of the real one.

The negative impact of the real industrial platforms' voltage components over the induction machine operation and their importance in the correctness of the simulations are given.

Next, starting from one of the simplest voltage-model-based flux estimators, another three different approaches for electromagnetic torque estimation are investigated, both in simulation and experimentally. The real voltage characteristic's influences on the estimator's performances are highlighted.

Both the Host (RT) and the Target (FPGA) softwares are given and presented. A practical approach to how the data is being transferred from Target to Host using a high-speed DMA FIFO is given in detail. Finally, the Labview-based software for cRio-9068 programming in FPGA mode is shown.

3.1. Preliminary aspects

Over the last few years, one of the industry's major trends was integrating compact industrial equipment into all types of applications. From research and education processes to safety and hardware-in-the-loop applications, PLCs have found their place in all industries: health and medical, wastewater treatment, construction sector, power generation, and management [94]–[97], [124].

In general, suitable control devices should be used depending on the application type (critical application, health application, etc) and application specification (time response, acquisition frequency, output update time, etc.).

A higher degree of performance, as it is known, comes with higher production costs. For example, unlike processes with relatively high time constants (water flow, heating, etc.), the controller performance increases significantly in the case of high-frequency response control.

In more complex applications, where the PLC unit represents the main control core, special and dedicated devices are mainly used in sub-applications that require special running conditions [98].

In electric drive systems, the maintenance process is a key factor for saving time and money. Real-time monitoring of system health status is an important factor in all applications [99]–[102], [125].

In the case of grid-connected electric machine-based applications, the electromagnetic torque produced by the machine can be used as an information source about the electromechanical system's state of opperation.

BUPT

As presented in [103], considering the specified limitations, the PLC-based systems can be used (with poor results) for grid-connected induction machines' torque estimation.

3.2. Experimental setup - overview

The experimental setup diagram presented in Fig. 3.1 represents the basic schematic diagram used in this chapter for testing the industrial equipment torque estimation performances.

The schematic diagram structure is based on a real setup placed on an industrial platform with large power consumers. The supplying three-phase voltages are highly distorted depending on the grid loading.

The testing bench consists of two coupled induction machines: the grid-connected one with three-pole pair (delta connection), 11kW named the main motor (MM) and the Variable Frequency Converter (VFC) driven one with two-pole pair, and 15kW rated power.

Together with the back-to-back four quadrants VFC, the 15kW induction machine represents the Emulated Load Machine (ELM).

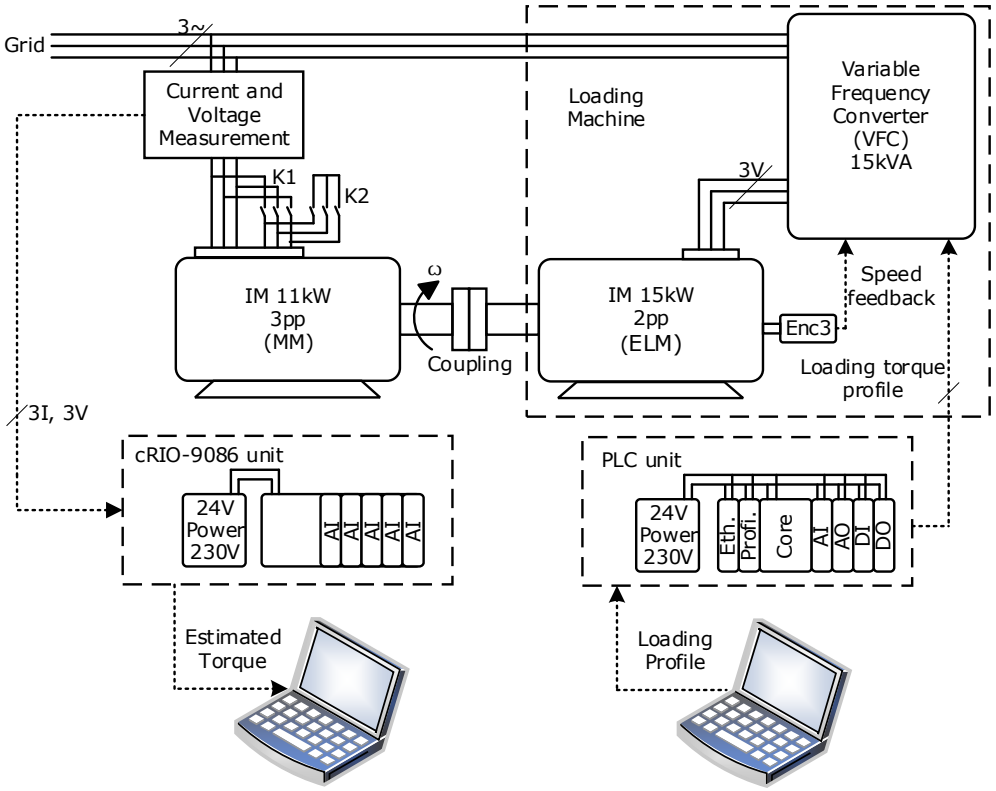

Fig. 3.1 Experimental setup

BUPT

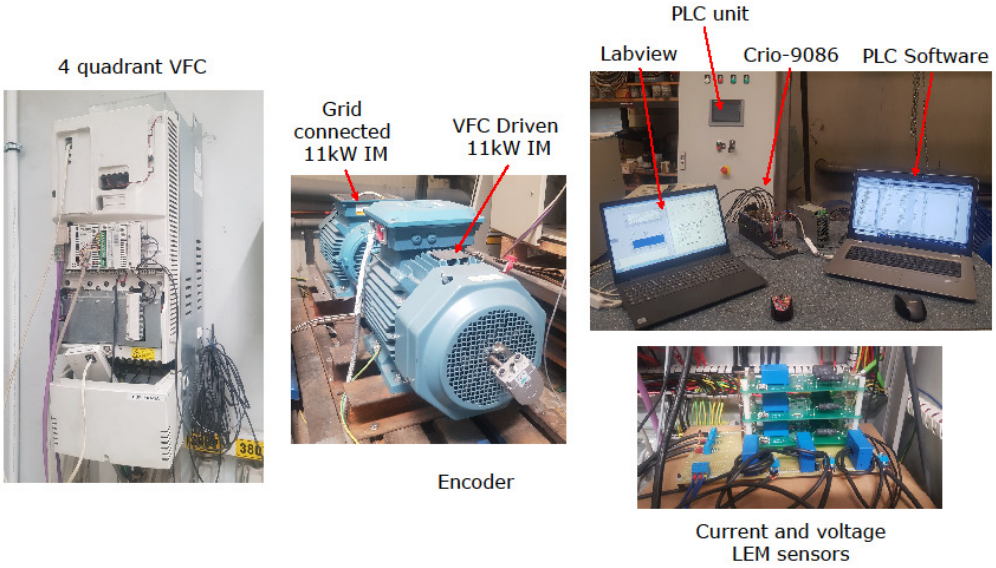

Fig. 3.2 Testing banch

The synchronous system speed is given by a grid-connected machine, while the ELM is Direct Torque Controlled driven.

The test bench has one encoder mounted on the extension of the 15 kW machine shaft used for closed-loop speed for high-precision torque control by the VFC.

The PLC unit is used for real-time control of the loading machine: prescribes the load model to the ELM. The cRIO-9086 platform reads all the necessary electrical data for IM's torque estimation. The torque estimation process can be done offline or online (on FPGA).

In offline mode, the grid-connected IM's electrical measurements (all three voltages and currents) are stored internally in the processor during the test. Then, the saved data are transferred into Matlab&Simulink program and used for flux and torque estimation.

In online mode, the FPGA uses the measured data in real time to internally compute the grid-connected IM's flux and torque.

All the communication protocols are based on industrial standards [126], [127]. The currents and voltages are measured using LEM sensors.

3.3. Induction machine model

A precisely known of the induction machine parameters is requested for torque estimator implementation on industrial control equipment—several methods in the literature deal with induction machine parameter identification [128]–[130]. A good general review of them can be found in [131]. For example, in [132], the author presents a suitable IM parameters identification procedure (with experiments) reporting a robust flux-integration method. Both for parameters identification and loss separation, it is presented below, based on IM's equivalent circuit (Fig. 3.3), the IM's electrical parameters given by the vendor (Table 3.1).

BUPT

Table 3.1 IM's catalog electrical parameters

$I_{rated}(\Omega)$	$\cos\varphi$	η	$R_s(\Omega)$	$R_r(\Omega)$	$R_m(\Omega)$	$X_m(\Omega)$	$\frac{X_s}{X_r}$
22.5	0.79	89.3	0.34	0.33	519	24	0.5526

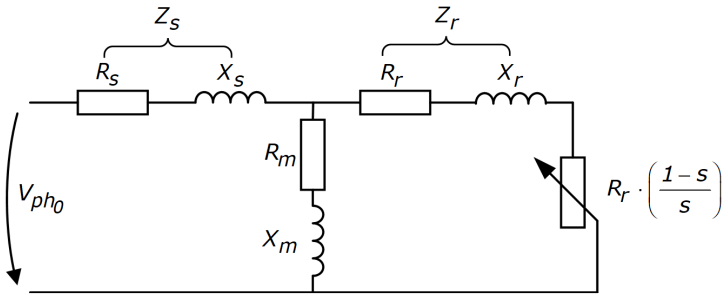

Fig. 3.3 Induction machine equivalent circuit diagram

Where R_s, X_s represent the stator resistance and reactance, R_r, X_r represent the rotor resistance and reactance, R_m, X_m represent the core resistance and reactance, and s represents the slip.

Also, the measurements were obtained from the no-load test (Table 3.2) and the locked-rotor (short-circuited) test (Table 3.3). All measurements were performed with a high-precision power analyzer.

Table 3.2 11kW IM no-load test

No.	Line voltage (V) V_{L_0}	speed (rpm) n	Phase voltage (V) V_{ph_0}	Power (W) P_0	Current (A) I_0
1	445.19	999,8	257.03	546,26	13,367
2	417.77	999,6	241.20	491,60	12,133
3	386.25	999,8	223.00	440,61	11,000
4	367.19	999,8	212.00	394,24	9,967
5	346.64	999,9	200.13	356,52	9,167
6	326.03	999,9	188.23	324,95	8,400
7	300.57	999,9	173.53	290,53	7,667
8	276.49	999,7	159.63	259,49	7,033
9	251.03	999,9	144.93	231,35	6,333
10	226.44	999,9	130.73	205,92	5,700
11	200.80	999,3	115.93	200,08	5,033
12	175.86	999,4	101.53	181,52	4,433
13	151.44	998	87.43	155,45	3,833
14	126.90	997,7	73.27	148,01	3,300
15	101.56	996,4	58.63	130,78	2,800

Table 3.3 11kW IM locked-rotor (short-circuit) test

Line voltage (V) $V_{L_{sc}}$	Phase voltage (V) $V_{ph_{sc}}$	Power (W) P_{sc}	Current (A) I_{sc}
73.71	42.56	933,49	21,53

From Table 3.2, based on (3.1) the mechanical losses, was separated from iron losses in Fig. 3.4

$$P_0 = P_{mech} + P_{iron} + P_{Co1} \tag{3.1}$$

Where: P_0, P_{mech}, P_{iron}, P_{Co1} represent the no-load input power, the mechanical losses, the iron losses, and the losses obtained from the Joule-Lenz effect in stator windings. The total mechanical losses at rated speed are extrapolated from linear interpolation:

$$P_{mech} = 113.68(W) \tag{3.2}$$

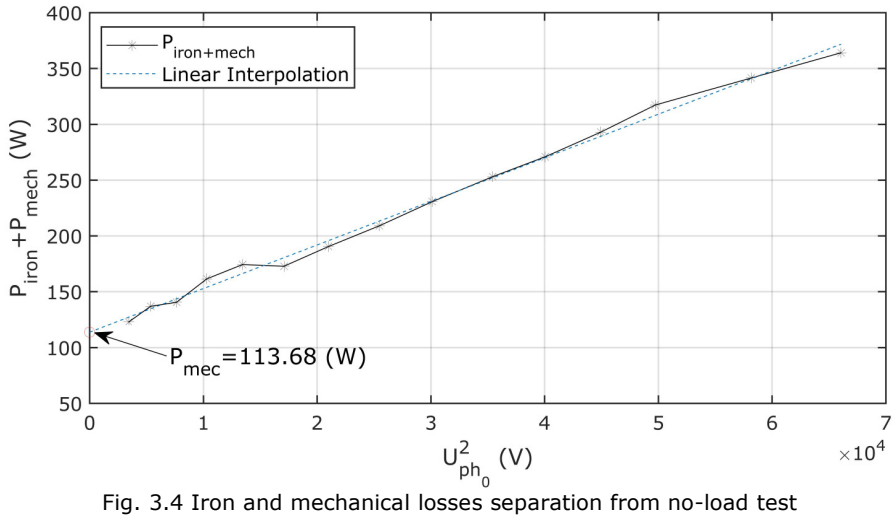

Fig. 3.4 Iron and mechanical losses separation from no-load test

The induction machine DQ-model in stator coordinates used in this chapter is presented in the following equations. One of the first reports of these equations can be found in [133].

$$\dot{\Psi}_{\alpha s} = V_{\alpha s} - a_{11} \cdot \Psi_{\alpha s} + a_{12} \cdot \Psi_{\alpha r} \tag{3.3}$$

$$\dot{\Psi}_{\beta s} = V_{\beta s} - a_{11} \cdot \Psi_{\beta s} + a_{12} \cdot \Psi_{\beta r} \tag{3.4}$$

$$\dot{\Psi}_{\alpha r} = a_{21} \cdot \Psi_{\alpha s} - a_{22} \cdot \Psi_{\alpha r} - p \cdot \omega \cdot \Psi_{\beta r} \tag{3.5}$$

$$\dot{\Psi}_{\beta r} = a_{21} \cdot \Psi_{\beta s} - a_{22} \cdot \Psi_{\beta r} + p \cdot \omega \cdot \Psi_{\alpha r} \tag{3.6}$$

$$I_{\alpha s} = c_1 \cdot \Psi_{\alpha s} + c_2 \cdot \Psi_{\alpha r} \tag{3.7}$$

BUPT

$$I_{\beta s} = c_1 \cdot \Psi_{\beta s} + c_2 \cdot \Psi_{\beta r} \tag{3.8}$$

$$I_{\alpha r} = c_2 \cdot \Psi_{\alpha s} + c_3 \cdot \Psi_{\alpha r} \tag{3.9}$$

$$I_{\beta r} = c_2 \cdot \Psi_{\beta s} + c_3 \cdot \Psi_{\beta r} \tag{3.10}$$

$$\sigma = 1 - \frac{{L_m}^2}{L_s \cdot L_r} \tag{3.11}$$

$$a_{11} = \frac{R_s}{\sigma \cdot L_s} \tag{3.12}$$

$$a_{12} = R_s \cdot \frac{1-\sigma}{\sigma \cdot L_m} \tag{3.13}$$

$$a_{21} = R_r \cdot \frac{1-\sigma}{\sigma \cdot L_m} \tag{3.14}$$

$$a_{22} = \frac{R_r}{\sigma \cdot L_s} \tag{3.15}$$

$$c_1 = \frac{1}{\sigma \cdot L_s} \tag{3.16}$$

$$c_2 = \frac{\sigma - 1}{\sigma \cdot L_m} \tag{3.17}$$

$$c_3 = \frac{1}{\sigma \cdot L_r} \tag{3.18}$$

$$\left.\begin{aligned} \frac{J}{p} \cdot \frac{d\omega_r}{dt} &= T_{elm} - T_{load} \\ \omega_r &= \omega_1 \cdot (1-s) \end{aligned}\right\} \tag{3.19}$$

$$T_{elm} = 1.5 \cdot p \cdot c_2 \cdot \left(\Psi_{\alpha s} \cdot \Psi_{\beta r} - \Psi_{\beta s} \cdot \Psi_{\alpha r}\right) \tag{3.20}$$

$$P_{in} = \frac{3}{2} \cdot \left(V_{\alpha s} \cdot I_{\alpha s} + V_{\beta s} \cdot I_{\beta s}\right) \tag{3.21}$$

$$P_{co1} = \frac{3}{2} \cdot R_s \cdot \left(I_{\alpha s}^2 + I_{\beta s}^2\right) \tag{3.22}$$

$$P_{iron} = \frac{3}{2} \cdot \left[\frac{\left(V_{\alpha s} - R_s \cdot I_{\alpha s}\right)^2}{R_{m_{prl}}} + \frac{\left(V_{\beta s} - R_s \cdot I_{\beta s}\right)^2}{R_{m_{prl}}}\right] \tag{3.23}$$

$$P_{add} = \left(\frac{1}{\frac{s}{\omega_c} + 1}\right) \cdot k_{add} \cdot \left[\frac{3}{2} \cdot \left(I_{\alpha s}^2 + I_{\beta s}^2\right)\right] \tag{3.24}$$

BUPT

$$P_{co2} = \frac{3}{2} \cdot R_r \cdot \left(I_{\alpha r}^2 + I_{\beta r}^2 \right) \tag{3.25}$$

$$P_{mech} = B \cdot \omega_r^2 \tag{3.26}$$

$$\eta = \frac{P_{in} - P_{co1} - P_{co2} - P_{iron} - P_{mech} - P_{add}}{P_{in}} \tag{3.27}$$

where: $\dot{\Psi}_{\alpha s}, \dot{\Psi}_{\beta s}, \dot{\Psi}_{\alpha r}, \dot{\Psi}_{\beta r}$ are stator and rotor α, β-axis time derivatives of orthogonal flux components, $\Psi_{\alpha s}, \Psi_{\alpha r}, \Psi_{\beta s}, \Psi_{\beta r}$ represent the stator and rotor α, β-axis fluxes, $V_{\alpha s}, V_{\beta s}$ are the stator α, β-axis voltage components, $R_s, R_r, R_{m_{prl}}$ are the stator, rotor, and magnetizing resistance (presented below how it is calculated), L_m, L_s, L_r are magnetizing, stator and rotor inductances, $I_{\alpha s}, I_{\beta s}, I_{\alpha r}, I_{\beta r}$ are the stator and rotor α, β-axis estimated current components, ω is the estimated shaft speed, p is the number of pole pairs, $a_{11}, a_{12}, a_{21}, a_{22}, c_1, c_2, c_3, \sigma, k_{add}$ are coefficients, were k_{add} was chosen in such a way that additional losses represent 1.2% of rated power [134]–[139], ω_r is the shaft (rotor) speed, ω_1 is the synchronous speed, T_{elm}, T_{load} are electromagnetic and load torques, ω_c is the cutoff frequency of the low pass filter, s is the slip, $P_{in}, P_{co1}, P_{co2}, P_{iron}, P_{add}, P_{mech}$ are the input power and stator and rotor copper losses, iron, additional and mechanical losses, and η represents the efficiency.

Fig. 3.5 represents the serial and parallel connection of the IM's equivalent circuit without the rotor and shaft.

A good approximation of core resistance in IM's equivalent circuit parallel connection, which is used in the Simulink model for core losses computation, can be obtained (3.28), starting from core resistance and reactance from the series connection of IM's equivalent circuit.

$$R'_{m_{prl}} = \frac{R_{m_{srs}}^2 + X_{m_{srs}}^2}{R_{m_{srs}}} \tag{3.28}$$

From the no-load test, the $R_{m_{srs}}$ can be obtaine as:

$$R_{m_{srs}} = \frac{P_0}{3 \cdot I_0^2} \tag{3.29}$$

The equivalent total reactance from the no-load test can be extracted from the next equation.

$$Z_0^2 = R_0^2 + X_0^2 \tag{3.30}$$

Taking into account (3.31) and considering that the stator reactance can be considered to be half of the total reactance of the locked-rotor test (3.32), we can assume that core reactance in a series connection can be calculated as

$$X_0 = X_s + X_m \tag{3.31}$$

BUPT

$$X_s \simeq \frac{X_{sc}}{2} \tag{3.32}$$

$$X_{sc} = \sqrt{Z_{sc}^2 - R_{sc}^2} \tag{3.33}$$

Where the R_{sc} represents the total resistance of the induction machine from the locked-rotor test ($R_s + R_r$) and Table 3.3, we obtaine the total impedance in short-circuit test:

$$Z_{sc} = \frac{U_{sc}}{I_{sc}} \tag{3.34}$$

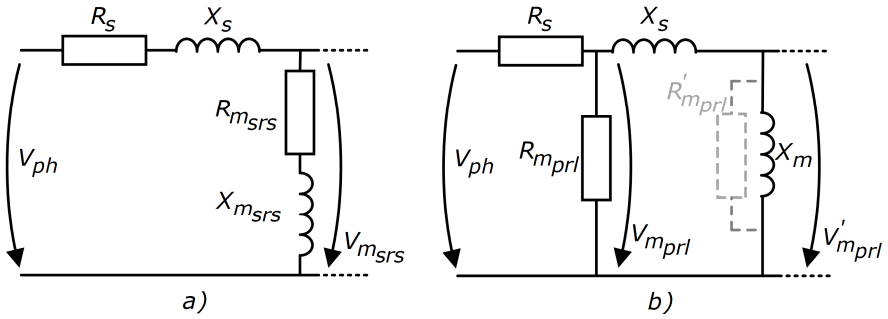

Fig. 3.5 Serial connection a) and parallel connection b) of the IM's equivalent circuit without the rotor and mechanical load

Where: V_{ph} represents the phase voltage, R_s, X_s represent the stator phase resistance and reactance, $R_{m_{srs}}$, $X_{m_{srs}}$ represent the core resistance and reactance in the series connection of the equivalent circuit, $R_{m_{prl}}$, $X_{m_{prl}}$ represent the core resistance and reactance in parallel connection of the equivalent circuit, taking into account the voltage drop on the phase reactance, $R'_{m_{prl}}$ represents the core resistance in parallel connection of the equivalent circuit, without taking into account the voltage drop on the phase reactance, $V_{m_{prl}}$, $V'_{m_{prl}}$ represents the voltage drop on $R_{m_{prl}}$ and $R'_{m_{prl}}$.

In this condition, the magnetizing reactance of the IM's equivalent circuit series connection is calculated as follows:

$$X_{m_{srs}} = X_m = X_0 - X_s \tag{3.35}$$

Considering (3.29) and (3.35) the core resistance in IM's equivalent circuit parallel connection can be calculated with (3.28).

The iron losses in series connection (Fig. 3.5, a) can be estimated as:

$$P_{iron} = \frac{V_{m_{srs}}^2}{R_{m_{srs}}} \tag{3.36}$$

BUPT

The iron losses in parallel connection (Fig. 3.5, b) can be expressed as:

$$P_{iron} = \frac{\left(V'_{m_{prl}}\right)^2}{R'_{m_{prl}}} \tag{3.37}$$

But taking into account also the leakage flux:

$$\frac{V_{m_{prl}}}{V'_{m_{prl}}} \approx \left(\frac{L_m + L_{\sigma s}}{L_m}\right)^2 \tag{3.38}$$

It can be considered that:

$$R_{m_{prl}} = R'_{m_{prl}} \cdot \left(\frac{L_m + L_{\sigma s}}{L_m}\right)^2 \tag{3.39}$$

The induction motor Simulink diagram presented in Fig. 3.6 is based on equations (3.3) - (3.26). The simulation is performed at a fixed step sample rate of $50\mu s$. The IM is supplied with a three-phase voltage system. The $Vabc - V\alpha\beta$ block performs a Clarke transform. Equations (3.3) - (3.6) are used to obtain the α, β stator and rotor time derivatives flux components.

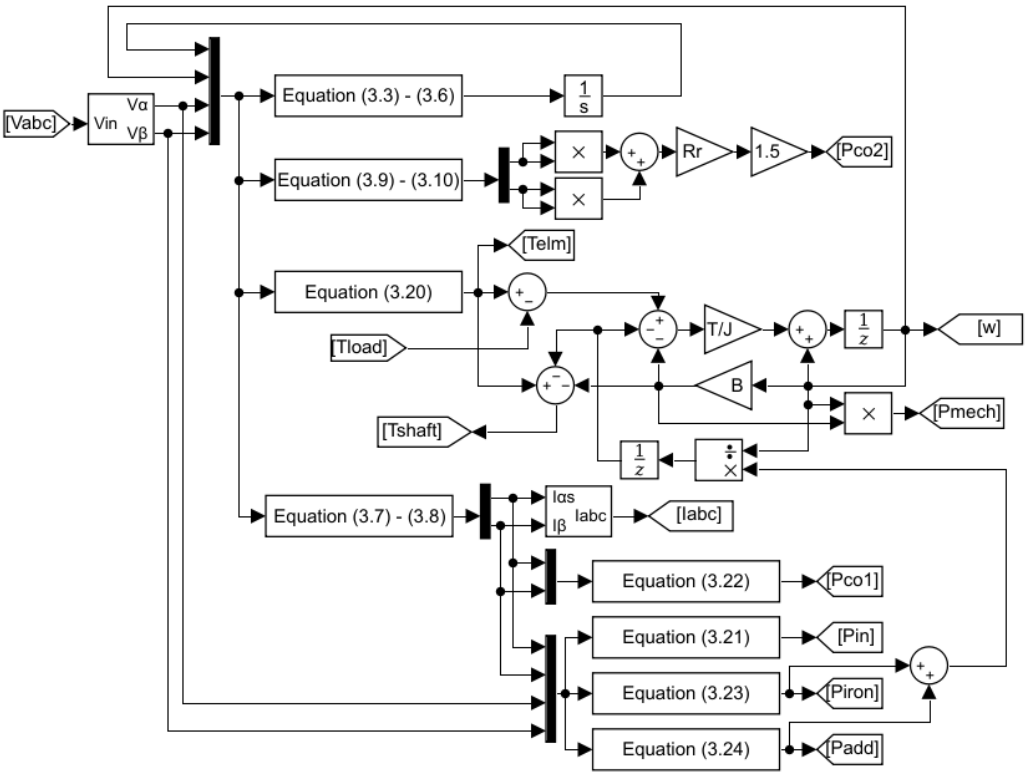

Fig. 3.6 Induction machine – Simulink model

BUPT

The iron losses are approximated separately using a magnetizing equivalent resistance obtained from the parallel equivalent circuit of the induction machine (see (3.28) to (3.39)). The mechanical losses are set so that at rated power, they are equal to those determined from the loss separation test presented in Fig. 2.4, representing the IM load torque.

Additional losses depend on the design of the machine. These can be found even in the stator tooth (caused by the pulsation of the core tooth flux) or in the rotor cage (produced by flux pulsation due to the cage current). In the case of cage rotors, IMs with skewed slots, these additional (stray) losses are also influenced by the interbar currents (caused by the current which flows through the rotor iron core between adjacent bars) [140]. The voltage integration from the equation (3.3) - (3.6) is based on the Backward Euler method. The next subchapter presents a comparative study between Euler and Runge-Kutta no.4 integration method's results. A detailed SCL type PLC software is presented in Appendix 2 (only the main software is given, without the PLC configuration).

3.4. 11kW induction machine model – simulations

Starting with subchapter 3.3, the torque estimators are investigated in ideal and real conditions. First, the ideal conditions are used for estimator calibration. This way, the torque estimators are tested in simulation using data from the simulated 11kW induction machine presented in the previous chapter.

3.4.1. IM's simulations – ideal three-phase voltage source

In ideal conditions, simulations with the IM model use an ideal three-phase voltage source. Next, the main losses, the input power, output power, and the speed and torque are presented for steady-state and no-load (Fig. 3.7) and rated load (Fig. 3.8).

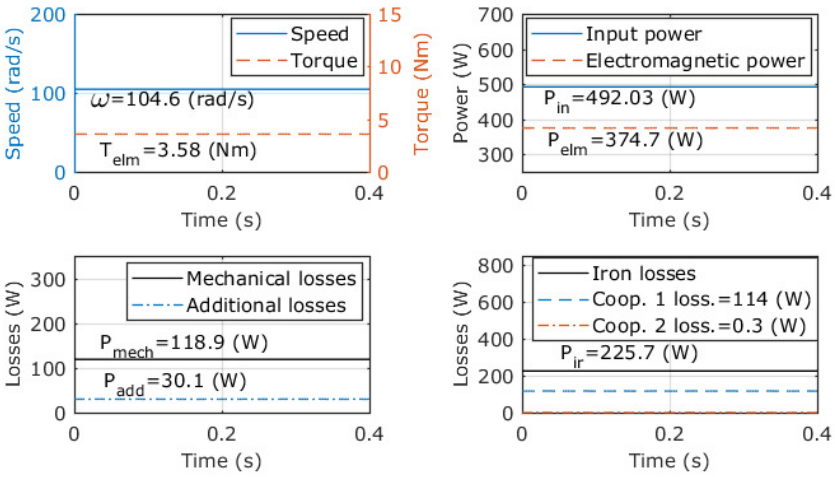

Fig. 3.7 IM measurements at no-load conditions, ideal voltages – simulations

BUPT

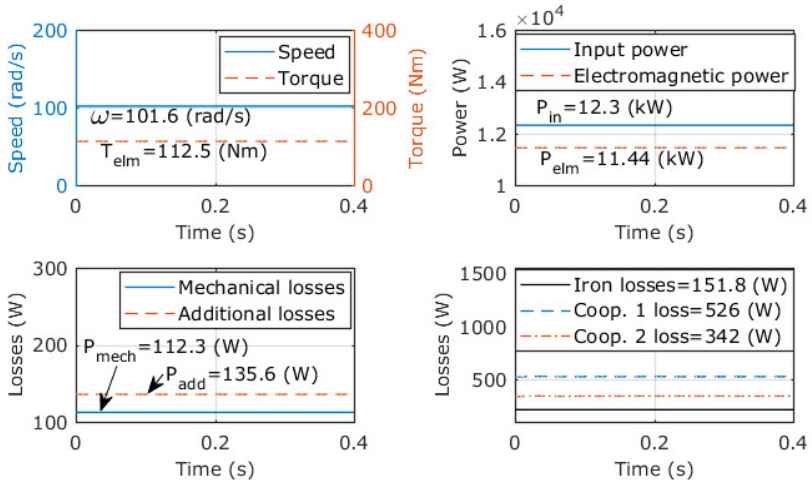

Fig. 3.8 IM measurements at rated power conditions, ideal voltages – simulations

For rate-load conditions, the iron losses represent 1.74% of rated power, the mechanical losses represent 0.91%, and the stray losses are 1.1%. The mechanical losses - as can be seen in, (3.26) depend on the square of the rotor speed.

Fig. 3.9 shows, for different loads, both the real and simulated induction machine efficiency. The best comparison between the graphs is found around the rated value. It has to be considered the fact that the real efficiency curve was obtained in lab conditions, where the IM was tested with an ideal sinusoidal three-phase voltage system.

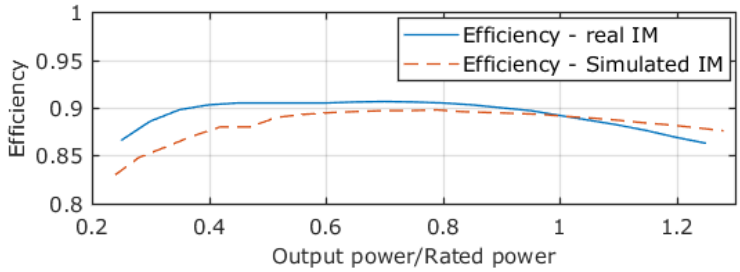

Fig. 3.9 real IM efficiency, simulated IM efficiency

More information related to 11kW IM's performances for rated conditions can be found in Table 3.4, where the simulation results are compared with those obtained from the datasheet/nameplate.

Table 3.4 Real and simulated IM performances in rated-load conditions

No.	Real IM	Simulated IM
1	$P_{Co1} = 516.37\,(W)$	$P_{Co1} = 525.9\,(W)$
2	$P_{Co2} = 316.8\,(W)$	$P_{Co2} = 341.7\,(W)$

BUPT

3	$P_{Ir} = 202.14(W)$	$P_{Ir} = 214.5(W)$
4	$P_{mech} = 114.9(W)$	$P_{mech} = 112.3(W)$
5	$P_{out} = 11(kW)$	$P_{out} = 10.98(kW)$
6	$\eta = 0.892$	$\eta = 0.892$
7	$I_{no-load}/I_{rated} = 0.43$	$I_{no-load}/I_{rated} = 0.47$
8	$n_{rated}/n_{synch} = 0.97$	$n_{rated}/n_{synch} = 0.97$

In the case of the simulated efficiency curve, all the parameters that were used are obtained based on real on-site measurements (in an industrial platform). The measured three-phase voltage system contains harmonics and the inverse (negative) component (unbalanced three-phase system) that does not depend (directly) on the load [141]–[145].

3.4.2. IM's simulations – ideal three-phase voltage source with real characteristics

The previous subchapter 3.4.1 presents the results obtained when the simulated IM was supplied with an ideal three-phase voltage source. The IM is also simulated here, but the three-phase voltage system reproduces the real three-phase voltage characteristics.

In order to achieve a more accurate average of the relative harmonic content and to reproduce the influences of inverse components more accurately, the on-site three-phase voltage system that supplies the real IM has been measured over several days at different times of the day.

Fig. 3.10 shows an example of the frequency spectrum of the measured real voltage. The Fast Fourier Transform (FFT) analysis was performed on 48000 points for a 40kHz acquisition frequency. The frequency bin is 0.83Hz.

The total harmonic content was calculated as in (3.40) and presented in Table 3.5. Here, the average of 20 different measurements, separately for all three phases, of the harmonic content for the first five harmonics components as well as the influence of the inverse component relative to the direct component, is presented.

$$RHC = \frac{\sqrt{\sum_{i=2}^{n} X_i^2}}{X_{1^{st}dc}} \tag{3.40}$$

For the next figure. X_i represents the filtered amplitude of each FFT value, n represents the number of samples, and $X_{1^{st}dc}$ represents the first FFT dc voltage component. The signal was filtered for values smaller than 0.3V.

BUPT

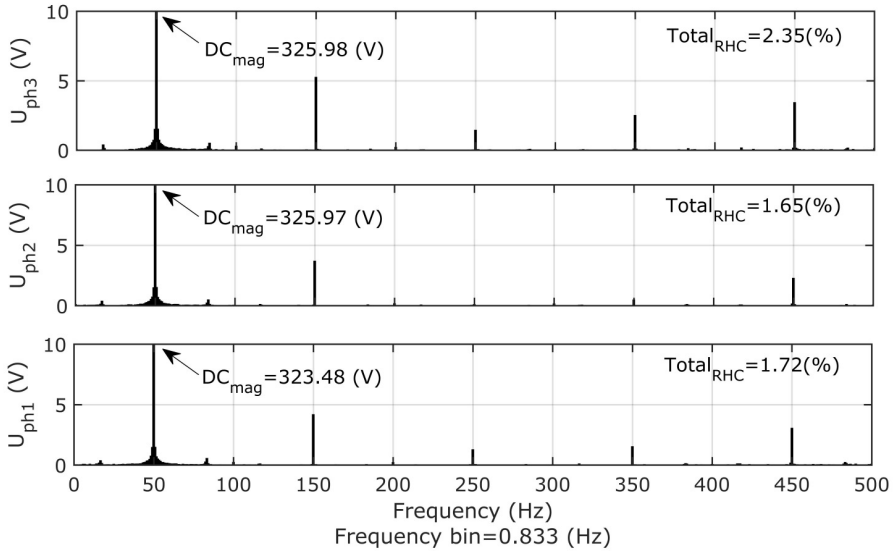

Fig. 3.10 Grid voltages frequency spectrum - example

To determine the inverse (negative) component magnitude in the real three-phase voltage system, the same sets of measurements (used for RHC) are also used here. Fig. 3.11 shows the Simulink graphical method by which the three-phase voltage system's direct and inverse component was determined.

Table 3.5 Mean of 20 measurements - Total and individual Relativ Harmonic Content for all three voltages and the inverse component influences

No.	Measurement	V_{ph1}	V_{ph2}	V_{ph3}
1	$RHC_{Total}\ (\%)$	2.779	2.187	2.2278
2	$RHC_{3^{rd}H}\ (\%)$	1.236	1.096	0.444
3	$RHC_{5^{th}H}\ (\%)$	0.361	0.085	0.489
4	$RHC_{7^{th}H}\ (\%)$	0.461	0.113	0.439
5	$RHC_{9^{th}H}\ (\%)$	0.866	0.634	0.532
6	$RHC_{11^{th}H}\ (\%)$	0.728	0.633	0.315
7	Direct (positive) component (V)	326.026		
8	Inverse (negative) component $(V)\ /\ (\%)$	4.254		1.305

Appendix 3 contains the software used to determine the harmonics influence as well as the inverse component influences over the three-phase voltage system. Other methods for determining these components can be found in the literature, as prescribed in [49] - [52].

BUPT

As was already stated, a more realistic and accurate IMs simulation could be obtained if the simulation's voltages would respect the real voltages' characteristics.

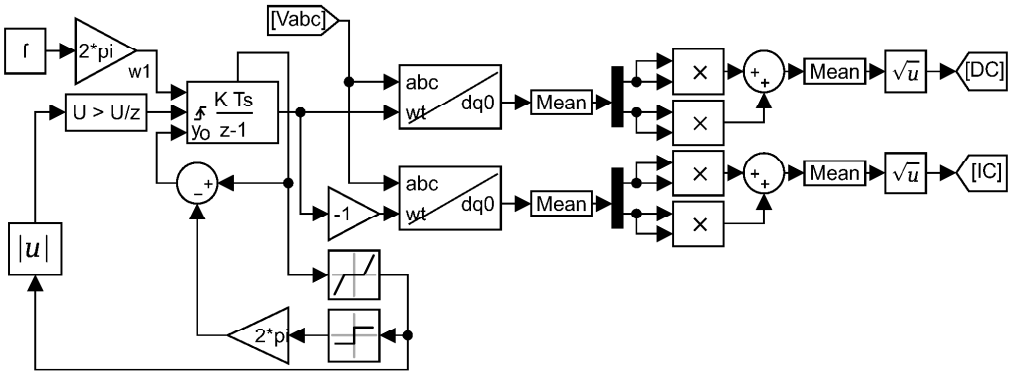

Fig. 3.11 Direct (positive) and inverse (negative) component detection with integrator resetting

This way, the values presented in Table 3.5 and the inverse sequence influence were taken into account in order to obtain more realistic supply voltages.

The below-presented equation system (3.41) represents the ideal three-phase voltage system.

$$\begin{cases} v_{ph1} = V_{ph1} \cdot sin\left(\omega \cdot t + \varphi_{ph1}\right) \\ v_{ph2} = V_{ph2} \cdot sin\left(\omega \cdot t + \varphi_{ph2}\right) \\ v_{ph3} = V_{ph3} \cdot sin\left(\omega \cdot t + \varphi_{ph3}\right) \end{cases} \tag{3.41}$$

where: $v_{ph1}, v_{ph2}, v_{ph3}$ represent the momentary simulated three-phase voltages at the time t, $V_{ph1}, V_{ph2}, V_{ph3}$ represent the maximum values of each momentary voltage, ω represents the pulsation, and $\varphi_{ph1}, \varphi_{ph2}, \varphi_{ph3}$ represent phase shifts.

After adding the individual Relativ Harmonic Content for all three phase voltages, the resulting system contains the first five most important harmonics. Similar applications for voltage harmonics identification and computation can be found in the specialty literature. Also, the (3.42) is partially based on [146]–[150], while (e.g.) in [151], the author finds the grid voltage harmonics using the Kalman filters.

$$\begin{cases} v_{ph1_{rc}} = \sum_{i=1}^{n}\left(V_{(ph1)_i} \cdot sin\left(\omega_{(ph1)_i} \cdot t + \varphi_{(ph1)_i}\right)\right) + v_{ph1_{rc}} \cdot k_{ic} \\ v_{ph2_{rc}} = \sum_{i=1}^{n}\left(V_{(ph2)_i} \cdot sin\left(\omega_{(ph2)_i} \cdot t + \varphi_{(ph2)_i}\right)\right) + v_{ph3_{rc}} \cdot k_{ic} \\ v_{ph3_{rc}} = \sum_{i=1}^{n}\left(V_{(ph3)_i} \cdot sin\left(\omega_{(ph3)_i} \cdot t + \varphi_{(ph3)_i}\right)\right) + v_{ph2_{rc}} \cdot k_{ic} \end{cases} \tag{3.42}$$

BUPT

where: $v_{ph1_{rc}}, v_{ph2_{rc}}, v_{ph3_{rc}}$ represent the ideal three-phase voltage system after the real characteristics (real-measured relative harmonic content and the inverse component influences) were added, i represents the harmonic order, n represents the total number of the harmonics $V_{(ph1)_k}, V_{(ph2)_k}, V_{(ph3)_k}$ represent the amplitudes of the harmonics based on the relative harmonic content from Table 3.5 for each phase, $\omega_{(ph1)_i}, \omega_{(ph2)_i}, \omega_{(ph3)_i}$ and the $\varphi_{(ph1)_i}, \varphi_{(ph2)_i}, \varphi_{(ph3)_i}$ are the frequency and initial phase of each harmonic, and the k_{ic} represents the influence of the inverse component on the three-phase voltage system.

Next, the results obtained from the simulation of the 11kW induction machine are presented in two situations: when the supplying voltage consists of an ideal three-phase voltage system and when the supplying voltage consists of an ideal voltage system with real characteristics (refer to Table 3.5).

At 0s, the IM is considered to be at no-load steady-state operation. At 0.2s, the induction machine is step loaded at rated power. In Fig. 3.12, the currents measured in phase A are presented. Although there is no phase shift between the currents, the current's RMS value in simulation with real voltages seems to be 4% higher than that obtained in the case of simulation with ideal voltages ($RMS(I_A)_{ideal\ votlages} = 22.73(A)$, $RMS(I_A)_{mod\ ified\ votlages} = 23.64(A)$.

Fig. 3.13, Fig. 3.14, Fig. 3.15 present in the same conditions the electromagnetic torque, the rotor speed, and the losses found in the stator.

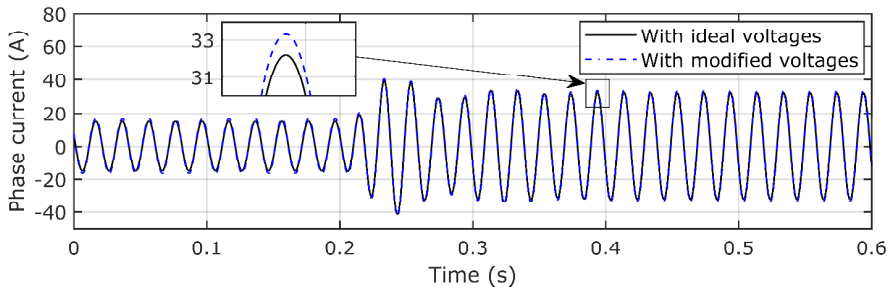

Fig. 3.12 Simulated IM's phase (A) current for no-load to rated power transition with ideal and modified ideal voltages

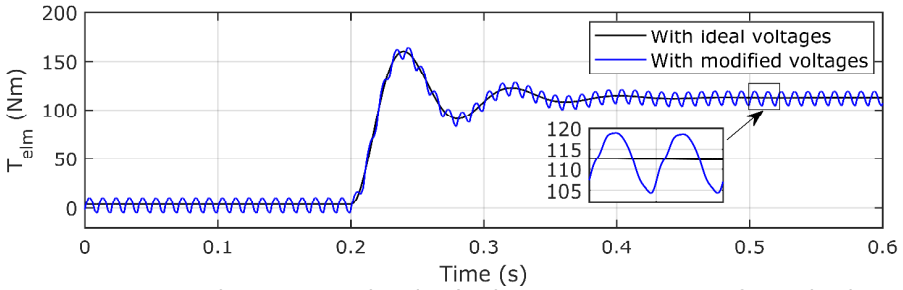

Fig. 3.13 comparison between simulated IM's electromagnetic torque for no-load to rated power transition with ideal and modified ideal voltages

BUPT

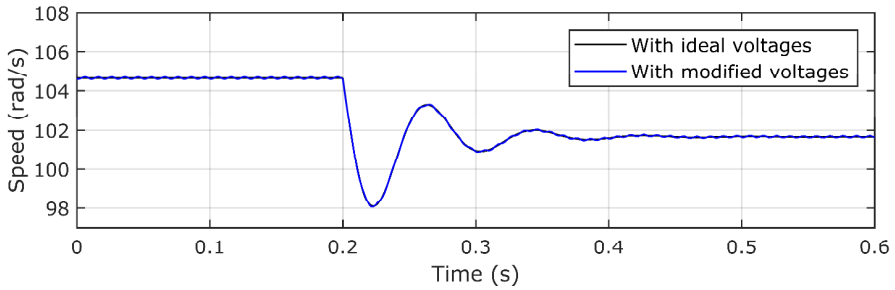

Fig. 3.14 comparison between simulated IM's rotor speed for no-load to rated power transition with ideal and modified ideal voltages

The IM produces a pulsating electromagnetic torque with a modified ideal three-phase voltage system. These pulsations (double the grid frequency) are mainly caused by the influence of the inverse (negative) component in the voltage system.

For the rotor speed, the influences of the grid voltage characteristics do not produce noticeable differences.

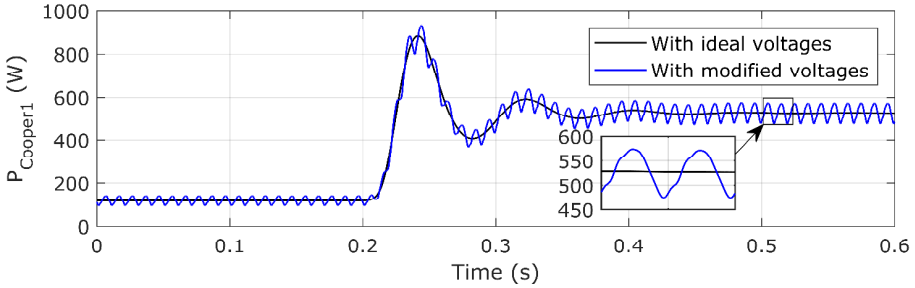

Fig. 3.15 comparison between simulated IM's stator copper losses for no-load to rated power transition with ideal and modified ideal voltages

This is caused, probably, because the IM's inertia being doubled. During the tests, the tested 11kW IM was mechanically coupled with another identical IM with the same inertia. This aspect was taken into account in the IM simulation model.

However, the average copper losses in both the rotor and the stator (Fig. 3.16) and those in the iron (Fig. 3.17) are the same as in the case of IM supplied with the ideal voltages.

Overall, the grid voltage harmonics and the inverse component of the voltage have a direct influence on the IM operation but do not directly affect the efficiency.

This way, e.g., in steady-state operation, at rated load, the electromagnetic torque has almost 12% peak-to-peak oscillation around and regarding the mean value.

BUPT

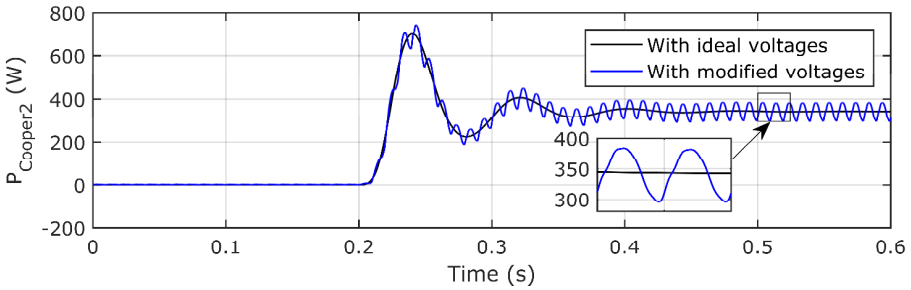

Fig. 3.16 comparison between simulated IM's rotor copper losses for no-load to rated power transition with ideal and modified ideal voltages

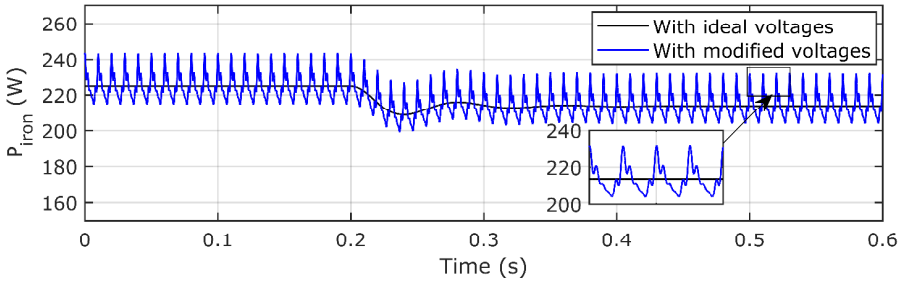

Fig. 3.17 comparison between simulated IM's iron losses for no-load to rated power transition with ideal and modified ideal voltages

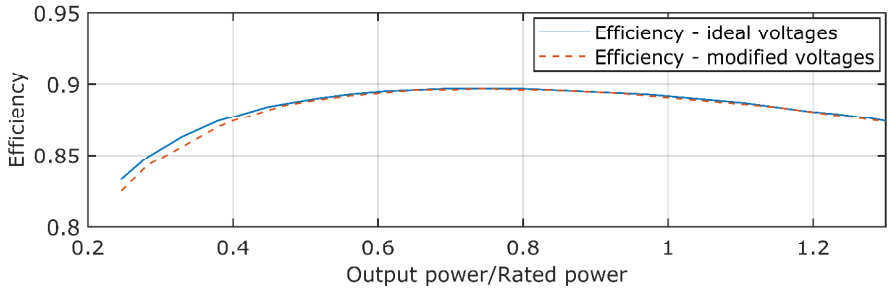

Fig. 3.18 comparison between simulated IM's efficiency with ideal and modified ideal voltages

As already stated in Chapter 2, the acquisition frequency presents a significant influence on the accuracy of IM simulations.

Fig. 3.19 shows the simulated IM's electromagnetic torque when the machine is supplied with a three-phase voltage system without harmonics or inverse components.

However, during the acquisition process, the acquisition frequency was modified randomly (according to the software presented in Appendix 4). Based on acquisition time variations already presented in Chapter 2, even a decent low-cost PLC shows a cyclic time variation greater than 6% of the set time.

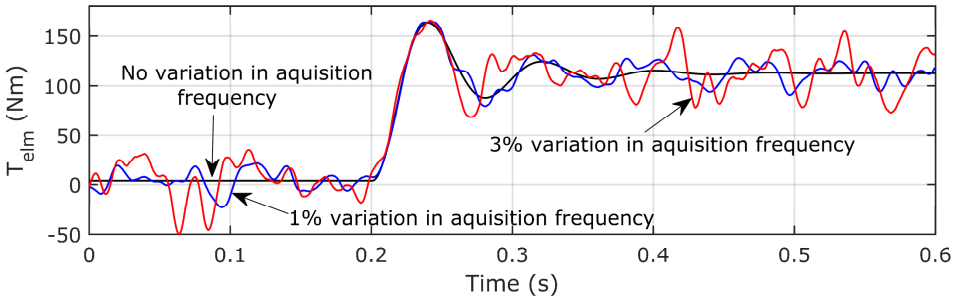

Fig. 3.19 The influences of the acquisition time variations over the IM operation

It can be seen that with only a 1% variation of the acquisition frequency (blue graph) the IM has an unstable operation, while with a 3% variation of the acquisition frequency (red graph), the electromagnetic torque varies in steady-state even by more than 50% of its mean value.

Next, several methods for torque estimation are presented in two different situations: when the estimator measures the voltages and currents used by the simulated induction machine (simulations) and when the estimators are running online on the industrial equipment (experimental).

It has to be highlighted that the experiments are performed in an industrial platform with a weak grid, where the voltages have significant harmonics and invers components.

The simulation principle used in the next subchapters is presented in Fig. 3.20. The "Voltage Modelling" block supplies both the induction machine and the estimator with a 3-phase voltage system, taking into account all the real voltage characteristics, presented above in this chapter.

The "11 kW Induction Machine" block represents the real induction machine and has been described in the previous subchapter. The torque estimator uses both the supply voltages and the currents produced by the induction machine.

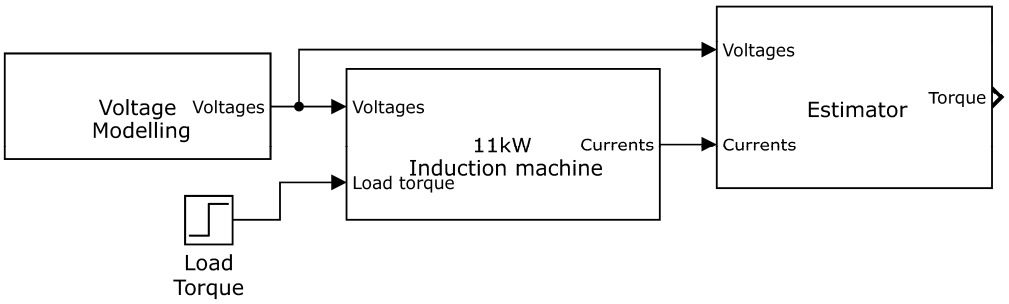

Fig. 3.20 Basic schematic diagram for estimators simulation

The induction machine used for the comparison made in figures Fig. 3.23, Fig. 3.24, Fig. 3.29 - Fig. 3.32 and Fig. 3.38 - Fig. 3.41 is also based on the dynamic model of the machine.

This was simulated in Simulink with a fixed step with the automatic selection of the used Solver.

3.5. Voltage model (VM) based flux estimators

In the last years and now, many high-performance or critical applications have requested AC drives control based on field-oriented or direct torque control (DTC) techniques. Both of these techniques requests an accurate stator flux estimation.

One of the most simple and used methods is based on the stator back-electromotive force (EMF) integration. This method is called the voltage model, which integrates the voltages to obtain the fluxes (voltage model).

In addition to this simple method, the fluxes can also be determined by using the current model (which is not presented here).

The following equations present the flux estimation based on the voltage model:

$$\hat{\Psi}_s = \int \left(u_s - R_s \cdot i_s\right) \tag{3.43}$$

$$\hat{\Psi}_r = \frac{L_r}{L_m} \cdot \hat{\Psi}_s - \sigma \cdot i_s \tag{3.44}$$

$$\sigma = \frac{L_s \cdot L_r - L_m^2}{L_m} \tag{3.45}$$

Where: $\hat{\Psi}_s, \hat{\Psi}_r$ are the stator and rotor fluxes, u_s, i_s, R_s represents the stator voltages, currents, and phase resistance, L_s, L_r, L_m represent the stator, rotor, and magnetizing inductances [152]–[156]. Even if, at first look, the voltage model can be considered for flux estimation due to its simplicity and low implementation costs, one of the significant drawbacks of this estimator is represented by the pure integrator character of the integration method that is being used here.

The presence of the dc offset can lead to unacceptable flux distortion. Several other methods can be used in this case to avoid the dc offset integration [157]–[161]. For instance, in [162], the authors presented an advanced rotor flux estimation method with good simulation and experimental results, where the low-pass filter (LPF) used for integration is followed by a high-pass filter [HPF] to remove the dc-offset without affecting the fluxes. One of the significant drawbacks of the voltage model-based estimators is represented by the poor results for speed values several times lower than the LPF cutoff frequency.

In the following figure, equations (3.43)-(3.45) are structured.

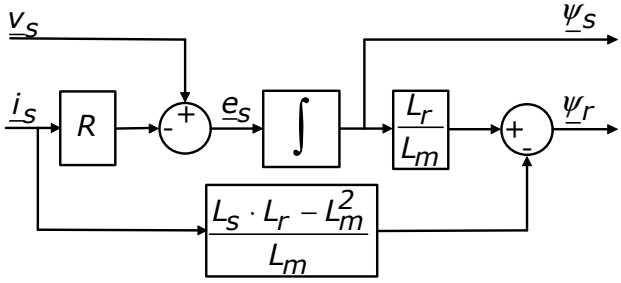

Fig. 3.21 Voltage model estimator structure

BUPT

3.6. The dual reference frame observer – Luenberger observer

A more complex and more performant flux estimator is presented below. Ideally having no phase shift effect, their robustness and accuracy make this type of observer an efficient solution for induction machine fluxes estimation.

Generally, a flux observer consists of a real-time model of the process that follows to be investigated, mentioning that the designer has almost all the freedom to choose its characteristics. In other words, roughly any system can be considered to be an observer [35].

The torque estimation can be problematic due to the high noise content and possible errors. In this presented observer, neither the position nor the rotor speed must be estimated.

$$\hat{\psi}_{r\alpha} = \psi_{s\alpha} \cdot \frac{L_r}{L_m} - i_{s\alpha} \cdot \frac{L_s \cdot L_r}{L_m} \cdot \sigma \tag{3.46}$$

$$\hat{\psi}_{r\beta} = \psi_{s\beta} \cdot \frac{L_r}{L_m} - i_{s\beta} \cdot \frac{L_s \cdot L_r}{L_m} \cdot \sigma \tag{3.47}$$

$$sin(\theta) = \frac{\psi_{r\alpha}}{\sqrt{\psi_{r\alpha}^2 + \psi_{r\beta}^2}} \tag{3.48}$$

$$cos(\theta) = \frac{\psi_{r\beta}}{\sqrt{\psi_{r\alpha}^2 + \psi_{r\beta}^2}} \tag{3.49}$$

$$\hat{i}_{s\alpha} = -\hat{\psi}_{r\alpha} \cdot \frac{L_m}{L_s \cdot L_r \cdot \sigma} + \hat{\psi}_{s\alpha} \cdot \frac{1}{L_s \cdot \sigma} \tag{3.50}$$

$$\hat{i}_{s\beta} = -\hat{\psi}_{r\beta} \cdot \frac{L_m}{L_s \cdot L_r \cdot \sigma} + \hat{\psi}_{s\beta} \cdot \frac{1}{L_s \cdot \sigma} \tag{3.51}$$

$$c_\alpha = \left(i_{s\alpha} - \hat{i}_{s\alpha}\right) \cdot \frac{L_s \cdot T_r \cdot \sigma}{L_m} \tag{3.52}$$

$$c_\beta = \left(i_{s\beta} - \hat{i}_{s\beta}\right) \cdot \frac{L_s \cdot T_r \cdot \sigma}{L_m} \tag{3.53}$$

$$T_{elm} = p \cdot \frac{3}{2} \cdot \frac{(\sigma - 1)}{(\sigma \cdot L_m)} \cdot \left(\psi_{s\alpha} \cdot \psi_{r\beta} - \psi_{s\beta} \cdot \psi_{r\alpha}\right) \tag{3.54}$$

In Fig. 3.22, a structured diagram of a Luenberger-based flux observer is presented. The input voltages used for fluxes are corrected accordingly to the current error.

A low pass filter is applied in the rotor frame. Usually, the K2 constant has to be smaller than 0.

The IM's phase-measured currents and the stator estimate fluxes are indirectly used to perform the Park and Inverse Park transformation.

BUPT

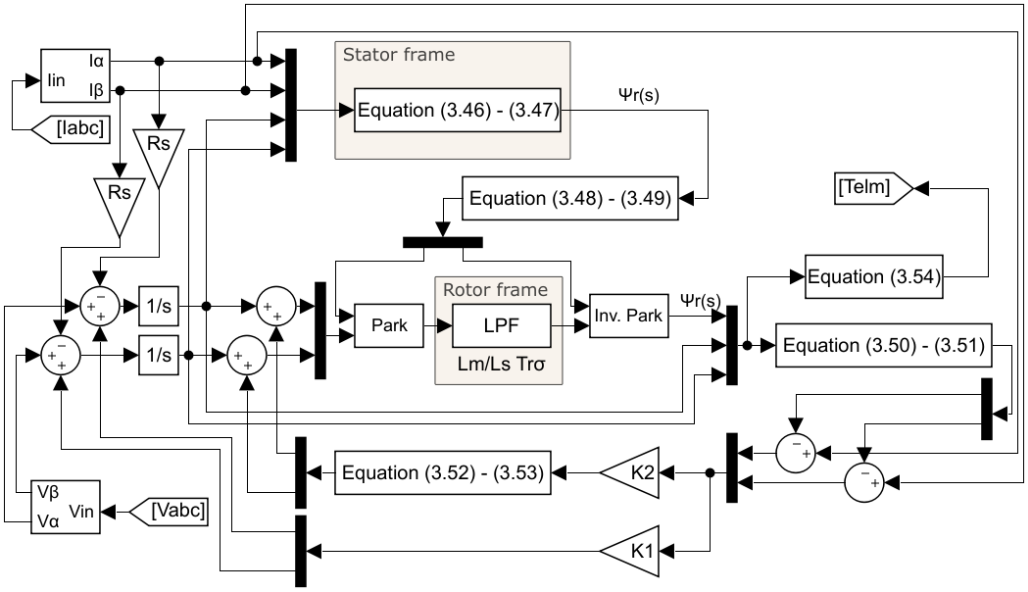

Fig. 3.22 Dual reference frame observer – Luenberger observer Simulink diagram

Next, the author presents two different torque estimators that will be compared to this last presented observer.

3.6.1. Simulations (ideal and real conditions) – Luenberger observer

In Fig. 3.23 and Fig. 3.24, the simulated results obtained from dual frame Leuenberger observer are presented for a no-load to rated-load transition.

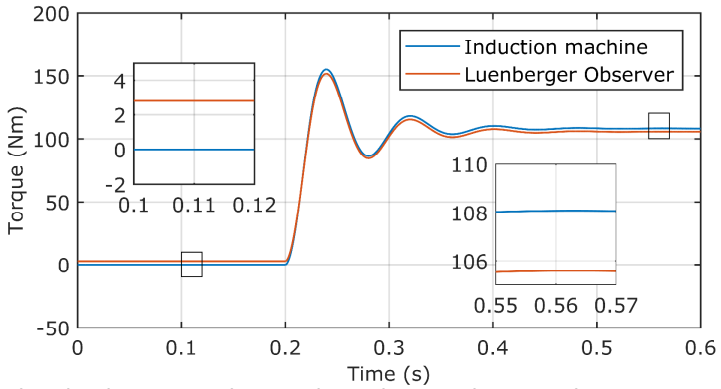

Fig. 3.23 Simulated induction machine and Luenberger observer electromagnetic torque – ideal voltages

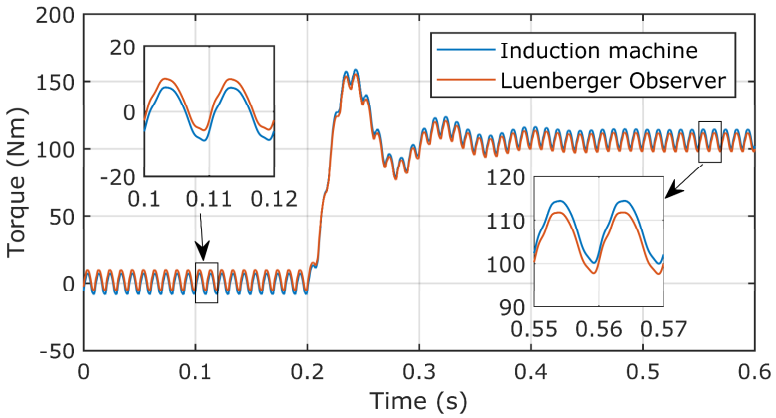

Fig. 3.24 Simulated induction machine and Luenberger observer electromagnetic torque– modified ideal voltages

The results from Fig. 3.23 are obtained with ideal supplying voltages, and the results from Fig. 3.24 are obtained when the supplying voltages contain the harmonics and the inverse component

As it could be seen in ideal conditions, the difference between the simulated induction machine torque and the observer torque appears because the observer does not take into account the mechanical, additional, and iron losses. The significant torque pulsations appear when the inverse component in the supplying voltages increases its magnitude.

3.6.2. Experiments online - Crio-9068 platform – Luenberger observer

All the experiments are performed based on the Crio-9068 chassis, where the observer (and estimators) run on the FPGA in real-time at 20kHz frequency.

More information about the CompactRio setup can be found in Subchapter 3.9. The experiments are presented in three situations: no-load (Fig. 3.25), rated-load (Fig. 3.27), and no-load to rated-load transition (Fig. 3.26).

The actual real estimated torque and its mean value are presented. No voltage or current filtering was used.

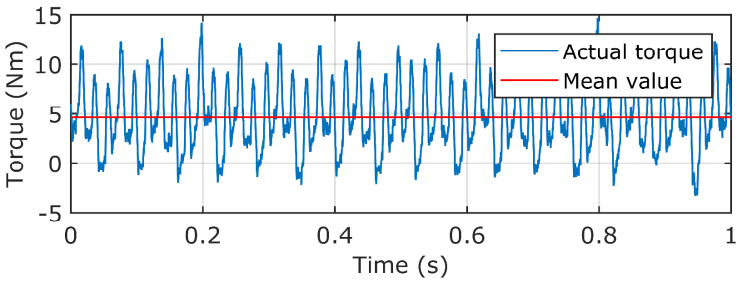

Fig. 3.25 Luenberger observer electromagnetic torque online estimation for no load

BUPT

In no-load conditions, the observer estimated torque should cover the no-load losses of the 11kW IM and also the mechanical losses of the loading induction machine.

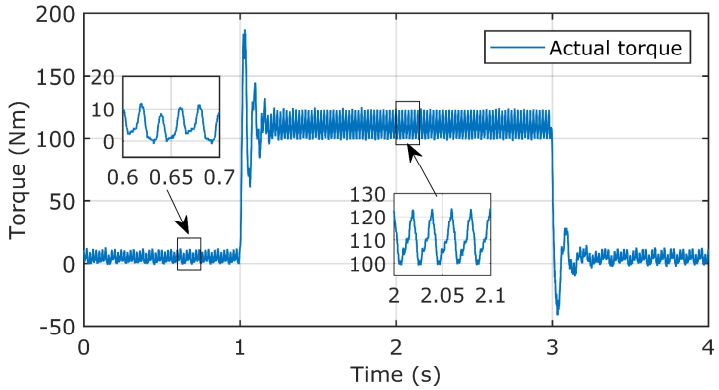

Fig. 3.26 Luenberger observer electromagnetic torque online estimation for 0 to rated load transition

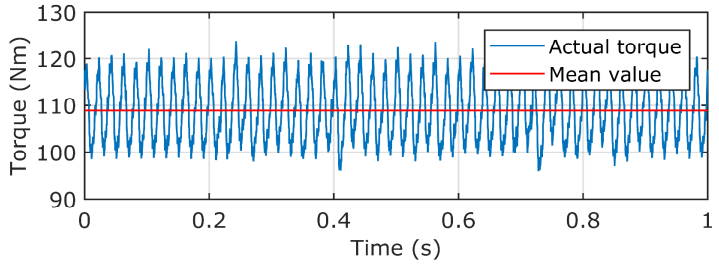

Fig. 3.27 Luenberger observer electromagnetic torque online estimation for the rated load (108 Nm)

3.7. The direct torque computation method

One of the simplest torque estimators presented here is stated as the direct computation method. Even if this estimator is highly sensitive to measured noise, one of the main advantages of using this type of estimator is the ease of implementation.

Depending on the application, the results obtained here may be sufficient, considering the relatively low computing power required for this estimator. This method uses only simple calculations to compute the load torque starting from 3 voltages and three currents. The block diagram of the direct torque estimation method is presented in Fig. 3.28.

$$\left.\begin{aligned} V_\alpha &= \frac{2}{3}\cdot\left(V_a - \frac{1}{2}\cdot V_b - \frac{1}{2}\cdot V_c\right) \\ V_\beta &= \frac{2}{3}\cdot\left(\frac{\sqrt{3}}{2}\cdot V_a - \frac{\sqrt{3}}{2}\cdot V_c\right) \end{aligned}\right\} \tag{3.55}$$

BUPT

$$\left.\begin{aligned} I_\alpha &= \frac{2}{3}\cdot\left(I_a - \frac{1}{2}\cdot I_b - \frac{1}{2}\cdot I_c\right) \\ I_\beta &= \frac{2}{3}\cdot\left(\frac{\sqrt{3}}{2}\cdot I_a - \frac{\sqrt{3}}{2}\cdot I_c\right) \end{aligned}\right\} \tag{3.56}$$

$$P_{in} = \frac{3}{2}\cdot\left(V_\alpha \cdot I_\alpha + V_\beta \cdot I_\beta\right) \tag{3.57}$$

$$P_{co1} = \frac{3}{2}\cdot R_s \cdot \left(I_\alpha^2 + I_\beta^2\right) \tag{3.58}$$

$$P_{iron} = \frac{3}{2}\cdot\left[\frac{\left(V_\alpha^2 - I_\alpha \cdot R_s\right)^2 + \left(V_\beta^2 - I_\beta \cdot R_s\right)^2}{R_{mp}}\right] \tag{3.59}$$

$$P_{add} = \left(\frac{1}{\frac{s}{\omega_c}+1}\right)\cdot k_{add}\cdot\left[\frac{3}{2}\cdot\left(I_\alpha^2 + I_\beta^2\right)\right] \tag{3.60}$$

$$\theta = \int_0^{2\cdot\pi} \omega_1 \cdot dt \tag{3.61}$$

$$\omega_1 = PI_{Ki,Kp}\left[V\alpha \cdot \sin(\theta) - V_\beta \cdot \cos(\theta)\right] \tag{3.62}$$

$$\frac{T_k}{T_n} = \left(\frac{V}{V_n}\right)^2 \tag{3.63}$$

$$\frac{T}{T_k} = \frac{2}{\frac{s}{s_k} + \frac{s_k}{s}} \Rightarrow 2^{nd}\,order\ eq: s^2 \cdot T - s\ \cdot 2\cdot T_k \cdot s_k + s_k^2 \cdot T = 0 \tag{3.64}$$

$$\Rightarrow s = min\left(\frac{-\left(2\cdot T_k \cdot s_k\right) \pm \sqrt{\left(\left(2\cdot T_k \cdot s_k\right)^2 - 4\cdot T^2 \cdot s_k^2\right)}}{4\cdot T}\right) \tag{3.65}$$

$$P_{co2} = P_{elm}\cdot s \tag{3.66}$$

$$P_{mech} = B\cdot\omega_r^2 \tag{3.67}$$

$$\omega_r = (1-s)\cdot\omega_1 \tag{3.68}$$

$$P_{elm} = P_{in} - P_{co1} - P_{iron} - P_{add} \tag{3.69}$$

$$T_{elm} = \frac{P_{elm}}{\omega_1} \tag{3.70}$$

BUPT

$$T_{load} = T_{elm} - T_{mech} \tag{3.71}$$

Where: $V_a, V_b, V_c, I_a, I_b, I_c$ are the three-phase voltages and current, $V_\alpha, V_\beta, I_\alpha, I_\beta$ are the stator α, β-axis voltage and current components, ω_r is the shaft (rotor) speed, ω_1 is the synchronous speed, T_{elm}, T_{load} are electromagnetic and load torques, ω_c is the cutoff frequency of the low pass filter, s is the slip, $P_{in}, P_{elm}, P_{out}, P_{co1}, P_{co2}, P_{iron}, P_{add}, P_{mech}$ are the input, electromagnetic and output power and stator and rotor copper losses, iron, additional and mechanical losses, R_s, R_{mp} are the stator and magnetizing resistance, θ represents the mechanical speed obtained from synchronous speed integration, T_k, T represent the maximum torque and the torque produced at s slip, s_k, s represent the maximum slip and the slip for which the induction machine produces the maximum torque, k_{add} is a filtering coefficient, k_i, k_p are PLL PI integral and proportional coefficients.

The Simulink diagram of the direct torque estimation method (Fig. 3.28) was implemented based on the abovementioned equations.

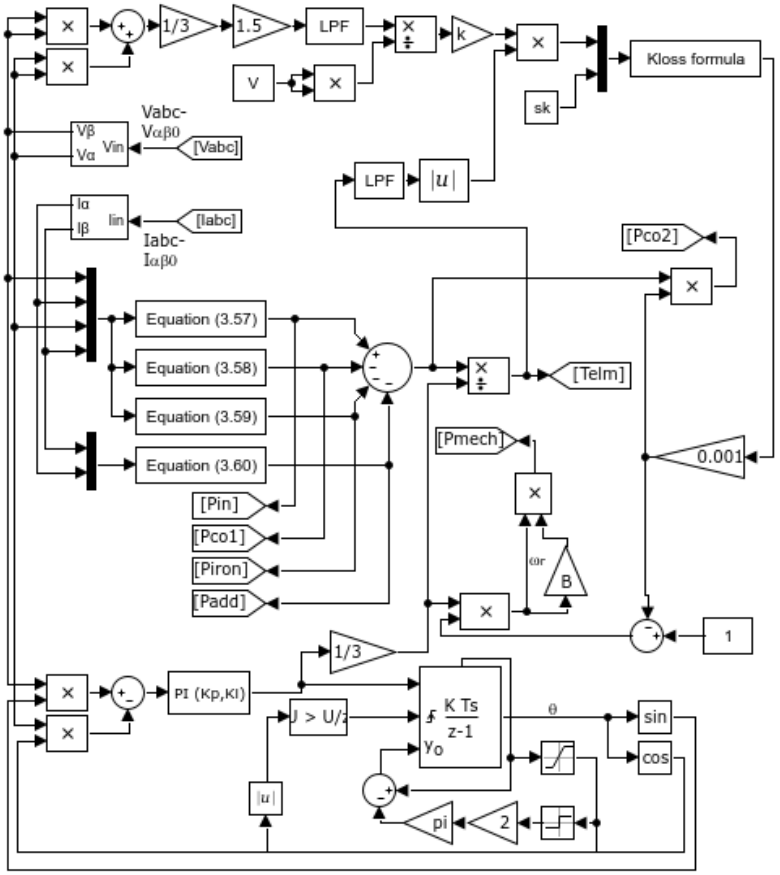

Fig. 3.28 Direct computation method Simulink diagram

BUPT

The input voltage (Vabc) is selected according to the simulated conditions: ideal conditions where three ideal voltage sources synthesize the phase voltage system and real simulation conditions where the ideal voltage is distorted according to the real voltages acquired on the field.

The mechanical torque is calculated as the shaft power and rotor speed ratio. Iron losses are obtained as the ratio between the square of the remaining voltage and the magnetizing resistor.

The synchronous speed is determined using a phase lock loop (PLL) directly from the alpha and beta voltages. The speed integration is performed using a resettable integrator on $[0..2\pi]$ an interval.

Neglecting the stator resistance, an approximation of the slip is made with the help of Kloss's formula.

The maximum torque is corrected according to the actual voltage and the induction machine's actual torque. The rotor copper losses are approximated with the product between the electromagnetic power and the induction machine slip.

3.7.1. Simulations (ideal and real conditions) – direct computation method

Fig. 3.29, Fig. 3.30, Fig. 3.31, and Fig. 3.32 present the torque and speed for the simulated induction machine and the estimator in an ideal three-phase voltage system and distorted ideal voltages.

One of the main disadvantages of this method is sensitivity to noise. However, neither the input quantities nor the torque is filtered.

The estimated torque does not present torque variations in ideal operating conditions (ideal voltage system). As can be seen from Fig 2.31, when ideal characteristics are added to the ideal voltages, the inverse component of the voltages produces these torque ripples.

The differences between the torque of the simulated induction machine and the estimated torque occur because the speed-dependent quantities (rotor copper losses and mechanical losses) vary differently because the estimator cannot estimate the real speed correctly.

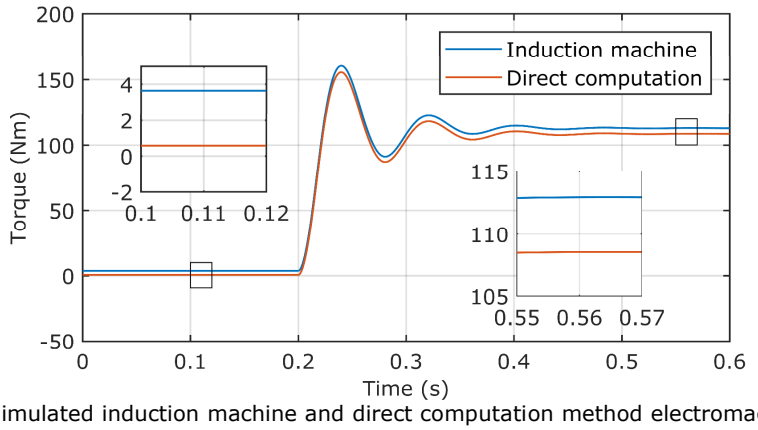

Fig. 3.29 Simulated induction machine and direct computation method electromagnetic torque – ideal voltages

BUPT

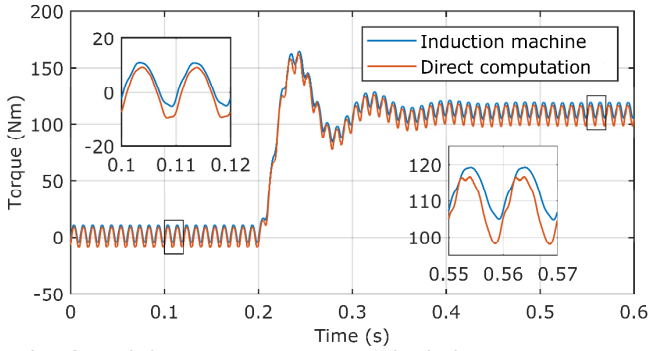

Fig. 3.30 Simulated IM's and direct computation method electromagnetic torque–modified ideal voltages

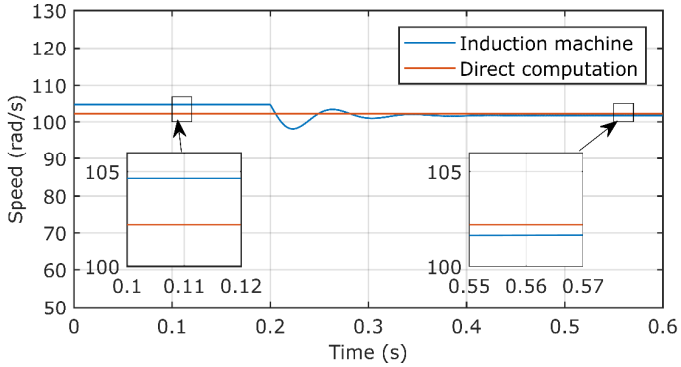

Fig. 3.31 Simulated IM's and direct computation method rotor speed – ideal voltages

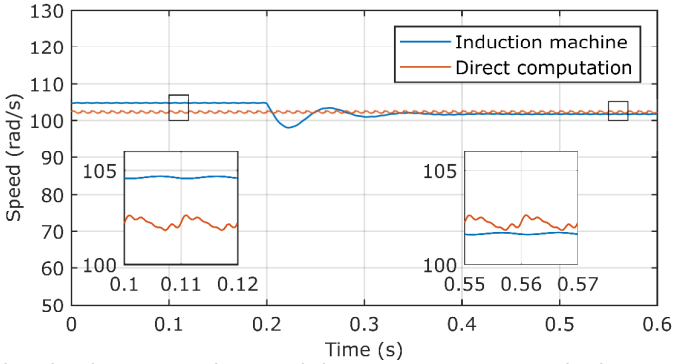

Fig. 3.32 Simulated induction machine and direct computation method rotor speed – modified ideal voltages

3.7.2. Experiments online - Crio-9068 platform – direct computation method

As well as the results presented for the previously presented fluxes observer, the results obtained online on CompactRio for the direct computation

BUPT

method are given below. In Fig. 3.33 the induction machine no-load results are given. The no-load to rated power transition is presented in Fig. 3.34.

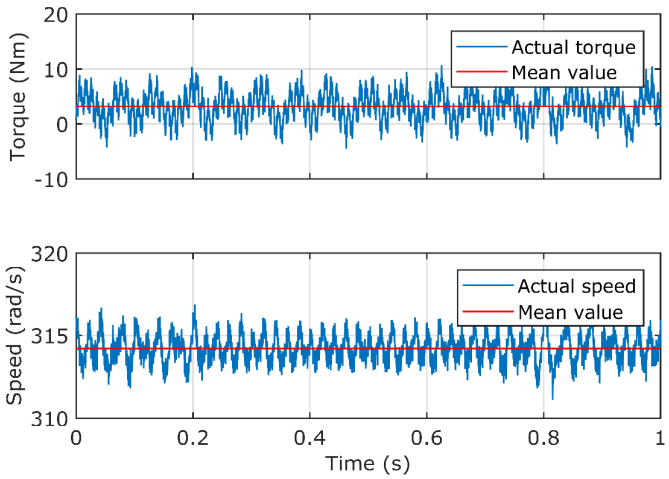

Fig. 3.33 Direct computation method electromagnetic torque and rotor speed online estimation for no load

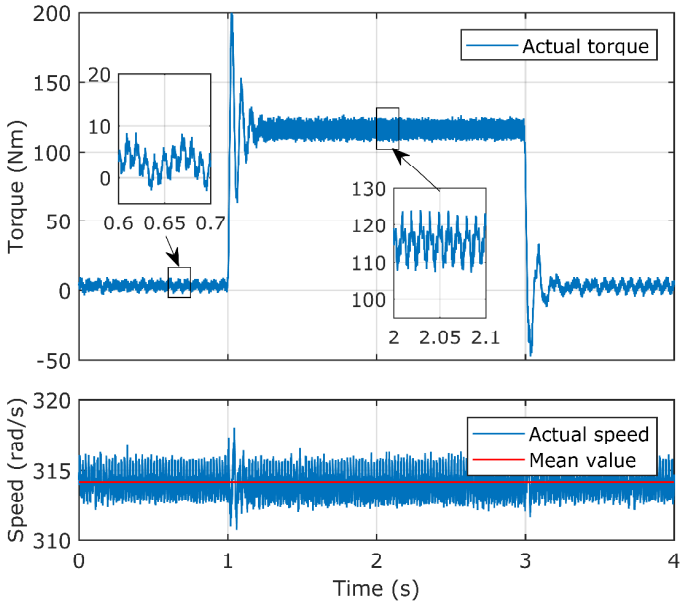

Fig. 3.34 Direct computation method electromagnetic torque and rotor speed online estimation for 0 to rated load transition

In Fig. 3.34, where the no-load to rated load transition is presented, it can be observed that the small changes in the actual speed are caused by the voltage drops when loading. As was already stated, the estimated speed is computed using a phase lock loop directly from measured voltages.

Knowing the electromagnetic power and the slip, the direct computation method can roughly estimate the shaft torque. Although the sensitivity to noise is seen in the high frequencies that appear, the mean value of the torque and the dynamic response of the estimator looks similar to those of the simulated induction machine. In Fig. 3.35, the induction machine was loaded at rated power and the electromagnetic torque and speed are presented.

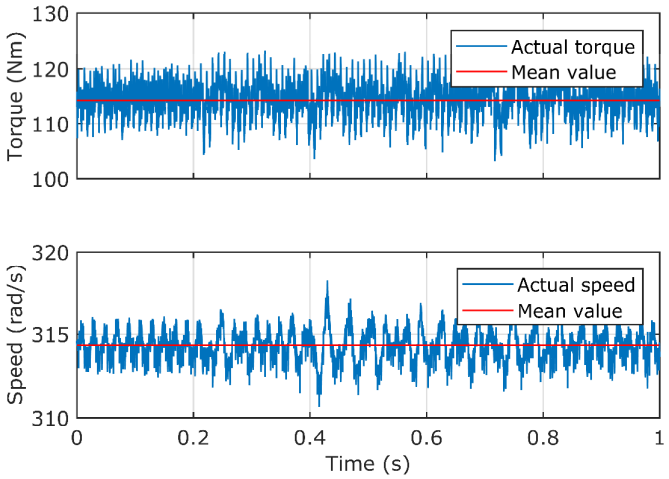

Fig. 3.35 Direct computation method electromagnetic torque and rotor speed online estimation for rated load

3.8. The dynamic mode computation method

The dynamic mode computation method is based on the machine equations presented in subchapter 2.1, where the induction machine is simulated. As the main difference, the adjustment torque used in the motion equation is obtained this time from the estimated stator currents and fluxes and the measured currents. As presented in Fig. 3.36, a PI regulator is used for torque correction. The resulting speed is used for fluxes computation (according to equations (3.3) – (3.18). One of the problematic aspects of the dynamic estimator is represented by performing the voltage integration in order to obtaine the fluxes. Compared to the Euler method, the Runge-Kutta no. 4 integration method (Fig. 3.37) converges faster (in some cases) to the exact solution, making this method more accurate.

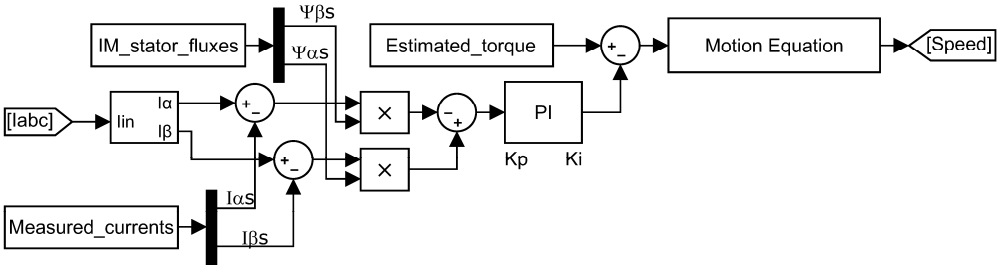

Fig. 3.36 Torque correction for dynamic method torque estimator based on IM's model

BUPT

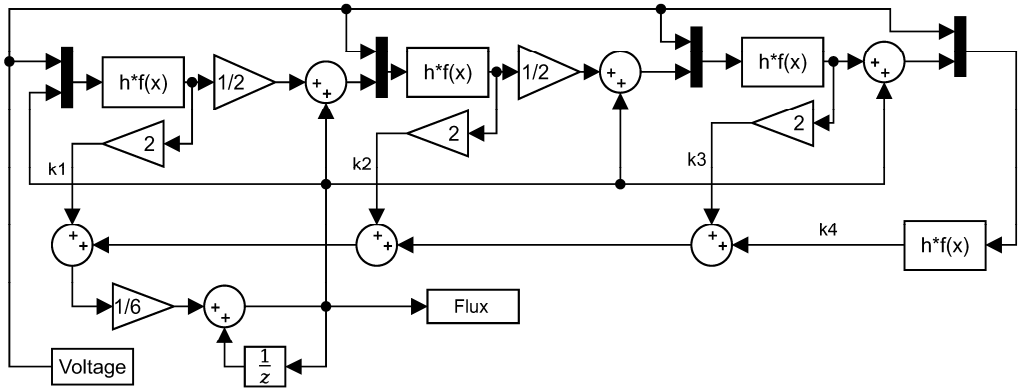

Fig. 3.37 Runge-Kutta no. 4 (RK4) integration method principle

Next equations described the previously presented integration method (RK4):

$$y_n = y_{n-1} + h \cdot \frac{1}{6} \cdot \left(k_1 + 2 \cdot k_2 + 2 \cdot k_3 + k_4\right) \tag{3.72}$$

$$k_1 = f\left(t_{n-1}, y_{n-1}\right) \tag{3.73}$$

$$k_2 = f\left(t_{n-1} + \frac{h}{2}, y_{n-1} + h \cdot \frac{k_1}{2}\right) \tag{3.74}$$

$$k_3 = f\left(t_{n-1} + \frac{h}{2}, y_{n-1} + h \cdot \frac{k_2}{2}\right) \tag{3.75}$$

$$k_4 = f\left(t_{n-1} + h, y_{n-1} + h \cdot k_3\right) \tag{3.76}$$

Where: $t_n = t_{n-1} + h$, k_1, k_2, k_3, k_4 are the slopes in different points from integration interval; k_1 is computed based on Euler's Method, y_n and y_{n-1} is the desired function at moment n, and n-1, h represents the interval and t represents the time, where $n \in \left[0, 1, 2..\right]$.

3.8.1. Simulations (ideal and real conditions) – dynamic mode computation method

Compared to previously presented simulations, in Fig. 3.38 - Fig. 3.40 are presented the simulated IMs results, both obtained from the dynamic model estimator with Euler and RK4 integration method. In this case, the acquisition frequency is 20kHz, so even the Backward Euler integration method produces satisfactory results compared to RK4. So, the RK4 integration method was studied only in simulation, not being used online in experiments.

Although the dynamic method (both for Euler and RK4 integration method) presents a slower time response to the step signal (IM loading) than the other two estimators (direct computation and flux observer), it shows no phase shift for torque pulsations caused by the supply voltage inverse component.

BUPT

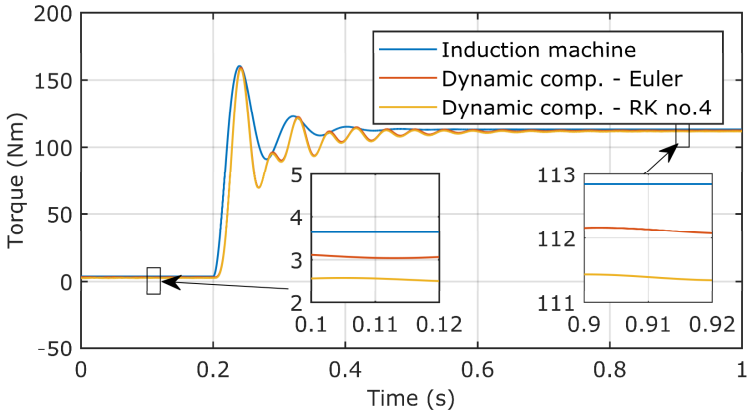

Fig. 3.38 Simulated induction machine and dynamic mode computation method electromagnetic torque–ideal voltages

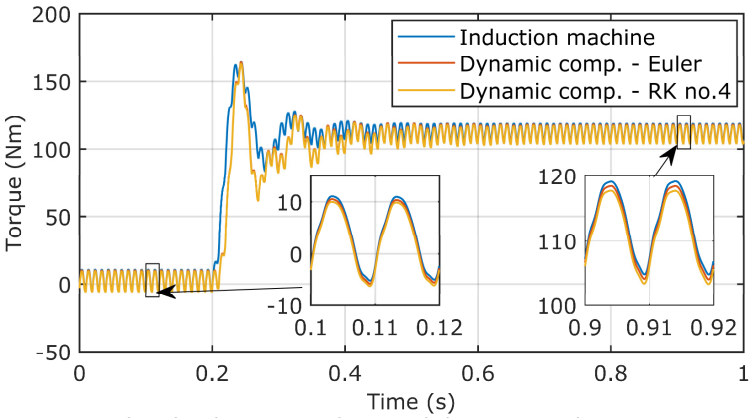

Fig. 3.39 Simulated induction machine and dynamic mode computation method electromagnetic torque–modified ideal voltages

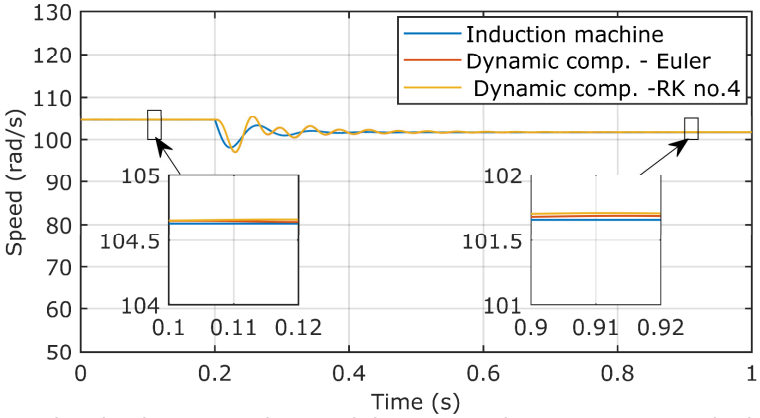

Fig. 3.40 Simulated induction machine and dynamic mode computation method rotor speed – ideal voltages

BUPT

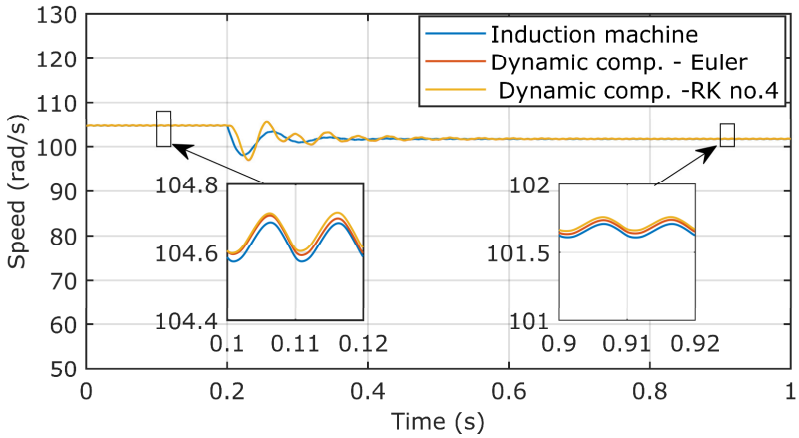

Fig. 3.41 Simulated induction machine and dynamic mode computation method rotor–modified ideal voltages

3.8.2. Experiments online - Crio-9068 platform – dynamic mode computation method

A significant difference between the direct and dynamic computation methods consists of "estimator starting time".

Next, online experiments are presented (Fig. 3.43, Fig. 3.42 and Fig. 3.44). Although it was not captured in these graphs, the dynamic estimator has a significantly higher startup time than the direct estimator (tens of milliseconds).

Similar to simulations, first the no-load results (electromagnetic torque and speed) are presented (Fig. 3.42). The no-load to rated power and vice-versa results are given in Fig. 3.43, where a zoom section is given to presents how does the estimated torque varies around the mean value.

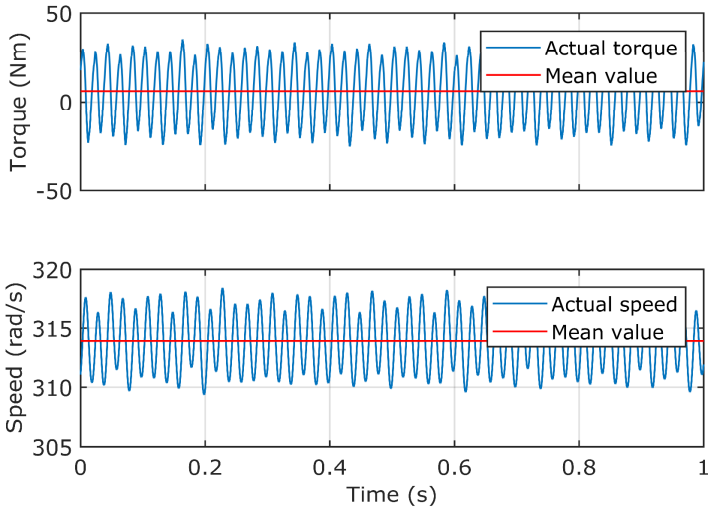

Fig. 3.42 Dynamic computation method electromagnetic torque and rotor speed online estimation for no load

BUPT

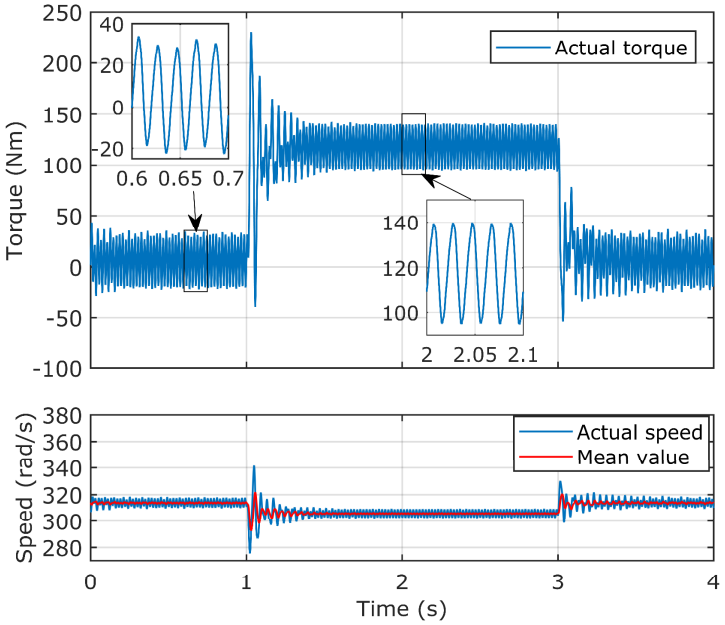

Fig. 3.43 Direct computation method electromagnetic torque and rotor speed online estimation for 0 to rated load transition

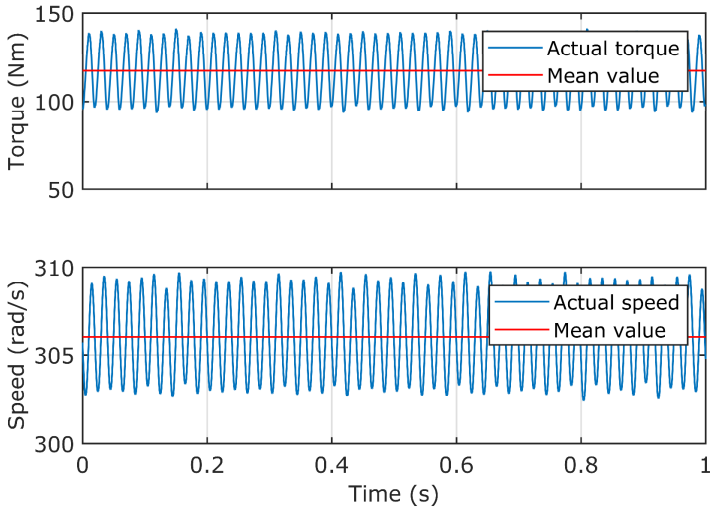

Fig. 3.44 Dynamic computation method electromagnetic torque and rotor speed online estimation for rated load

Although this estimator produces significant steady-state torque pulsations, it can reproduce more accurately - considering the dynamic processes in the machine - the electromagnetic torque during the machine transient regimes. As was already presented, the reason for these torque pulsations is related to the grid voltage spectrum.

BUPT

3.9. Labview and cRIO-9068 setup – short description

The acquisition and processing software was based on the Labview platform, using the cRio-9068 chassis with two NI 9215 Analog Input modules. The software reads, processes, plots, and saves the data in a .csv-type file.

For high-speed data acquisition, the processor was programmed in real-time FPGA mode. Fig. 3.45 and Fig. 3.47 present the diagram block of the Host (RT) and Target (FPGA) software. Fig. 3.46 represents the basic settings in the block diagram for 20kHz data acquisition and processing. The operation principle of the Labview software is relatively simple: the FPGA reads and repeatedly fills up a FIFO (first in, first out) stack function with the read data.

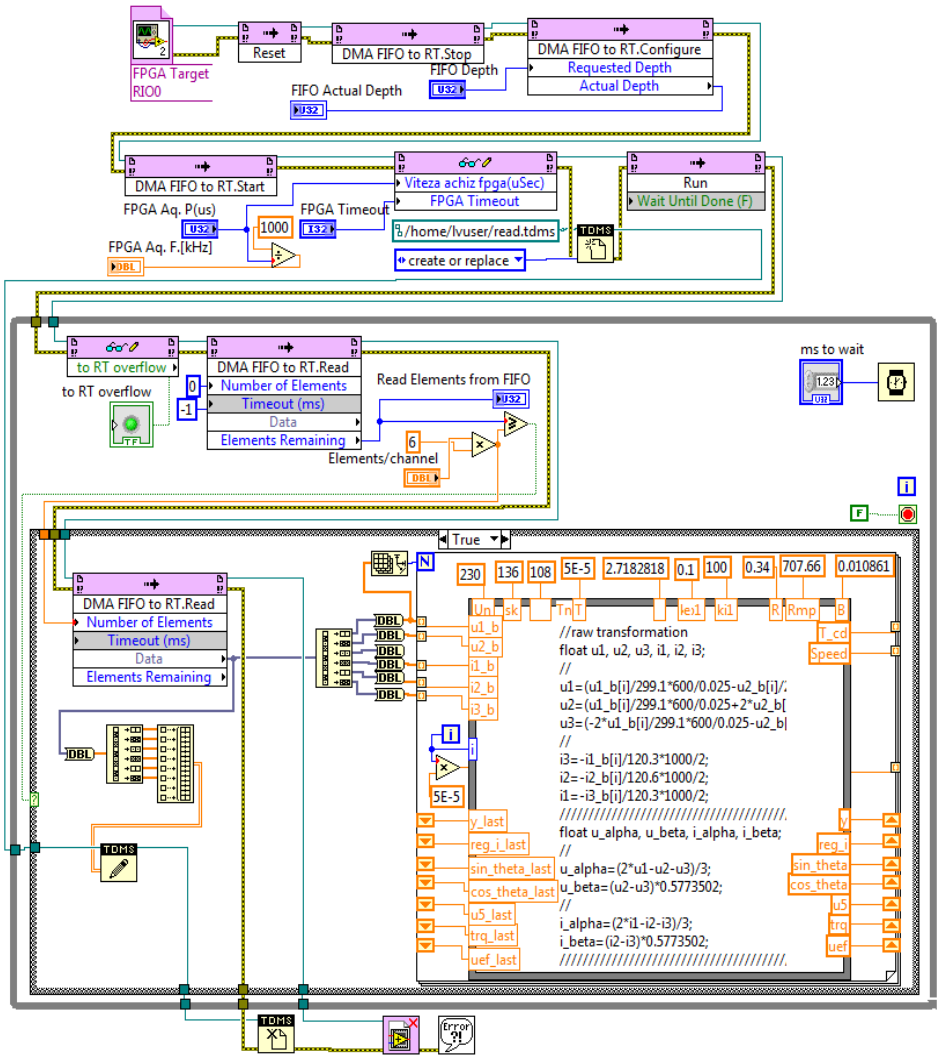

Fig. 3.45 Real Time (RT) HOST block diagram software

On the other hand, simultaneously, the real-time software retrieves the data from this stack and sends them forward for data processing.

It can be seen from Fig. 3.45 that, in order to read the data correctly, the software stops, resets, configures, and then restarts the FIFO stack function once every time the software starts. When enough unread data is available in the FIFO stack, a CASE structure is triggered to read and process the data.

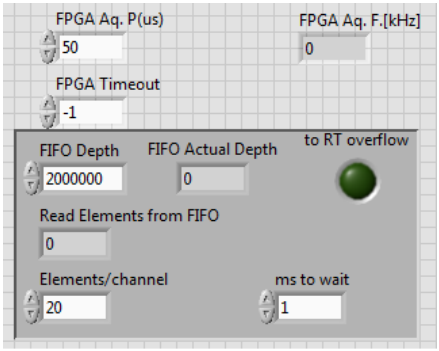

Fig. 3.46 Real Time (RT) HOST front panel software

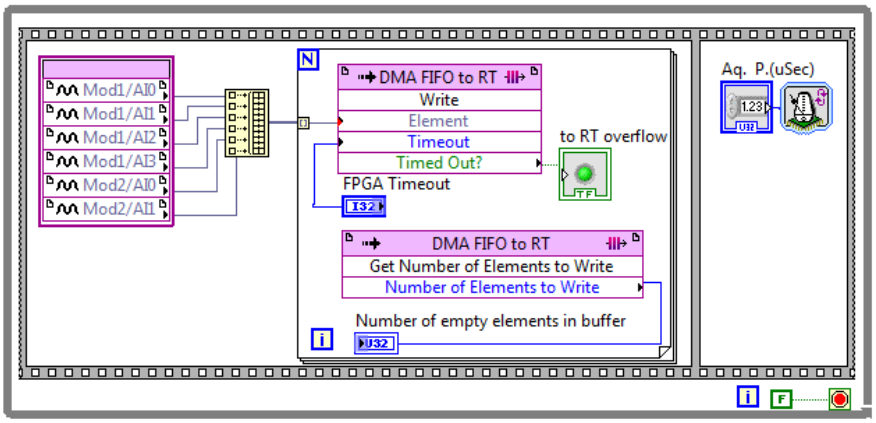

Fig. 3.47 FPGA TARGET block diagram software

The for loop (Fig. 3.45) contains the torque estimator (flux observer) written in a Formula Node. It has to be noticed that, i.e., voltage integration or filtering is possible by using Shift Registers.

The FPGA software reads the data continuously. A Flat Sequence Structure gives the reading frequency. The synchronously read data are concatenated and sent to the FIFO stack in batches.

3.10. Conclusion

Although the IM model presented in this chapter presences better operation around the rated power range, it also presents fairly acceptable operating results all over the power range.

Moreover, the IM model was tested under "real" simulated operating conditions, where the simulated supplying voltages contained the first five harmonics as well as the inverse component of the real three-phase voltage system.

In the second part of the chapter, one flux observer and two torque estimation methods are presented both for offline (Matlab&Simulink) and online calculations.

An application-dedicated FPGA-based processor (CompactRio-9086) reads and computes all the necessary calculus for electromagnetic torque estimation.

The following figure shows the comparative experimental results of the three estimators (flux observer, direct computation method, and dynamic method) in response to a step signal prescribed to the loading machine. At rated load, in steady state, the dynamic method produces a phase-shifted electromagnetic torque compared to the Luenberger observer, while the direct computation method shows the smallest torque ripple despite the speed estimation limitations. No significant differences between estimators are observed during the transient regime.

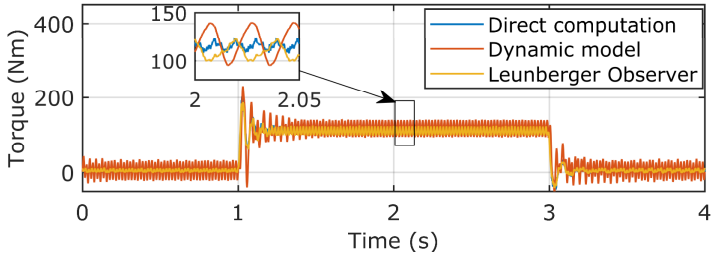

Fig. 3.48 Torque estimators no-load to rated power transition

BUPT

4. PLC-based IM virtual loading

Abstract

This chapter presents an artificial loading method of two induction machines (IM) without mechanical coupling using two dc-link connected variable frequency converters (VFC). Industrial standardized inverters, control equipment, and communication protocols are used.

No structural or internal changes have been made to the VFCs. All control processes are performed via a standardized low-cost programmable logical controller (PLC).

This chapter also discusses the state-of-the-art of artificial loading methods and their references.

Limitations and test possibilities, together with various artificial loading control strategies, are presented in this chapter: open-loop, closed-loop control method, mechanized testing, and thermal testing.

Fast Fourier spectral analysis shows the artificial loading test ac-source current harmonics content and their effects.

Power loss validation is finally shown through Simulink simulations.

4.1. Preliminary aspects

The induction machine is widely utilized all over the world. Induction machines must be tested before being used. It is necessary to ensure performance by finding losses to a prototype or a sample in a batch.

Aside from the rated current at which induction machines are tested, the temperature is an important parameter to be considered. Due to extensive working periods, reaching rated operating temperatures can be difficult. Artificial loading proved to be a useful solution for IM loading at and above rated current, despite induction machine testing challenges.

The following artificial loading approach assumes a rated current IMs loading via fast operating mode switching (motor mode to generator mode and generator mode to motor mode). The overall human resources cost reduction and the lack of mechanical coupling between the induction machines represent the most significant advantages of this procedure. On the other hand, the method requires the employment of two identical machines and two identical dc-connected variable frequency inverters, which is one of the system's most significant drawbacks. Furthermore, testing two machines simultaneously might be considered a time and cost-saving method.

In literature can be found several methods of electric machines' artificial loading. The Ytterberg method is one of the most known artificial loading methods, which requires special equipment for supplying the IM simultaneously with two different frequencies three-phase voltage system [163]–[167].

BUPT

The latest advancement in power converters has made electric machine testing much easier. As a result, the dynamic thermal loading approach can be employed instead of other ways [60], [168]. Either speed-controlled or torque-controlled, the loading methods should produce the rated losses as well as possible. Testing around rated speed ensures the rated mechanical and core losses [138], [169]–[172].

The reference offset in the torque-control technique should cover the machine losses. It is simple to achieve an exact speed offset, amplitude, and oscillating frequency using the speed-control technique. The machine will modify the mean torque value to compensate for the losses.

A solution could be to load one IM artificially utilizing a single unidirectional VFC. Rapid fluctuations in the induction machine's speed result in a potentially dangerous increase in the VFC DC link voltage [173].

The use of a dc-connected chopper can lower oscillation voltage considerably. The energy required to accelerate the machine will be absorbed from the grid, while the energy obtained from IM's braking will be lost as heat, lowering the overall efficiency of the test method. Oversizing the dc-link capacitor can be a solution to increase the IM's loading current, but thus inverters in special construction are needed. In this context, traditional VFC and matrix converter topologies are used for artificial loading [174], [175].

Injecting the oscillating power into the grid could be a feasible option. But a bidirectional ac-dc-ac inverter costs about the same as two unidirectional inverters in the case of conventional industrial inverters. Furthermore, in the case of a weak power grid, high power oscillations from and towards the grid have a negative impact on grid voltage (voltage oscillations causing light flicker or inappropriate functioning of other equipment) [176]–[179].

4.2. Setup configuration

The below-presented figure presents the setup configuration used for the artificial loading test. Two standard industrial dc-connected variable frequency converters are used (VFC1, VFC2). This way, PLC-VFCs communication uses standard industrial protocols. No additional changes were made to the VFCs operation principle.

The dc short-circuit current protection is performed through 2 ultra-fast fuses (F1) mounted between both VFCs' dc-links. One VFC can operate with doubled dc-link capacity by K switch, connecting together both VFC's dc capacitors. Both inverters are fed from the same three-phase ac voltage source. No ac-source filter was added. The IMs generated power can't be injected into the grid due to the unidirectional type of the inverters.

Two identical three-phase induction machines are directly connected to the inverter side of the converters. The VFC1 drives IM1, while IM2 is driven by the VFC2. The induction machines are not mechanically coupled. No position or speed encoders were used in this artificial loading method.

For artificial loading and temperature measurement, a low-cost PLC is used, while for induction machine online torque estimation, a Compact RIO unit is used. The three-phase voltages and currents are measured directly from VFC terminals.

The "Current and Voltage Measurement" block contains three voltage and three current sensors together with the low-pass RC filter.

BUPT

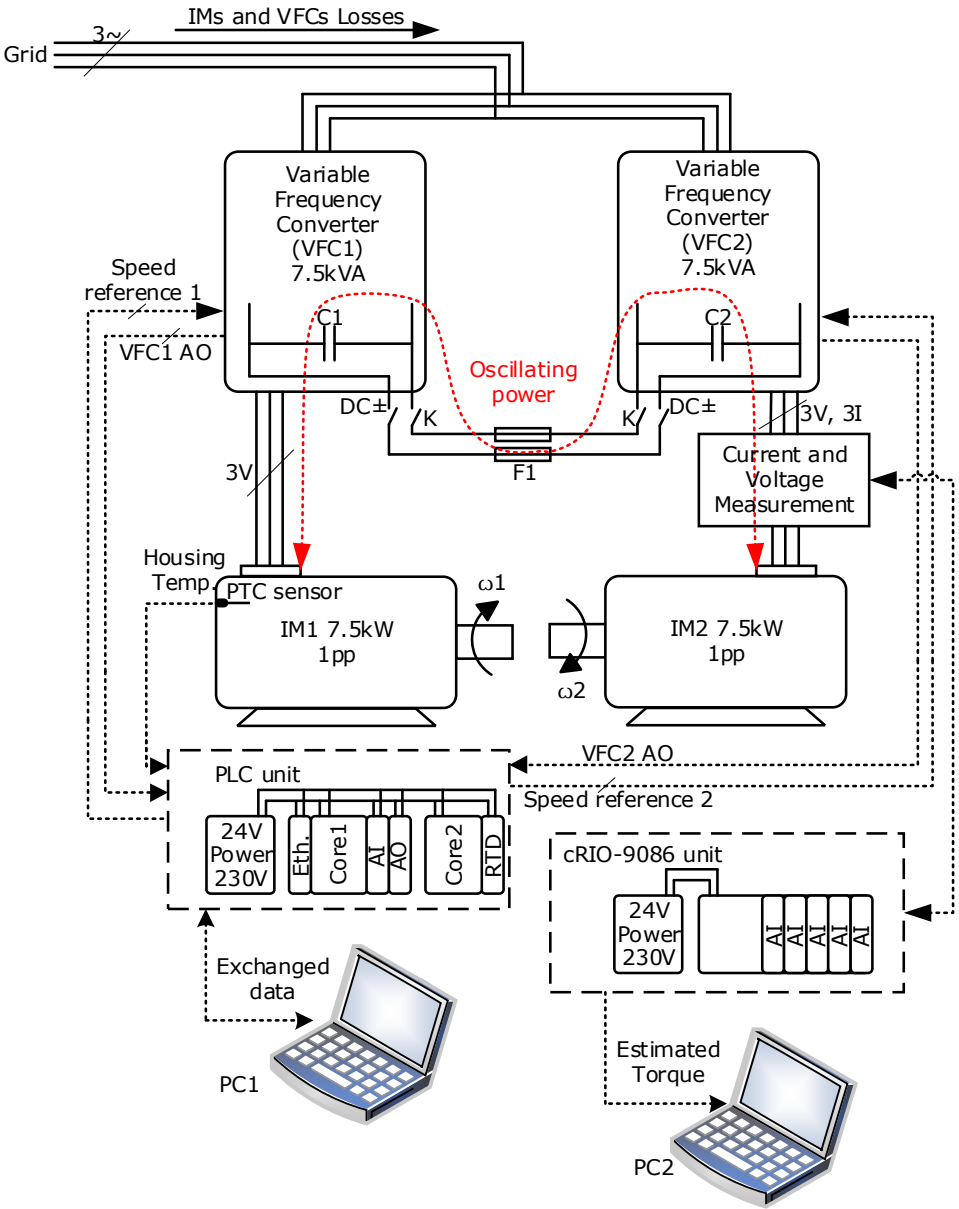

Fig. 4.1 Experimental setup – diagram representation (two induction machines driven by two dc-interconnected variable frequency converters)

In Fig. 4.2 the experimental laboratory setup is shown. The dc link interconnected VFCs, as well as all necessary safety and opperation equipment, are wall mounted in the electrical cabinet. The common dc link connection is performed via a switch. The PC-PLC communication is performed using Ethernet protocols.

BUPT

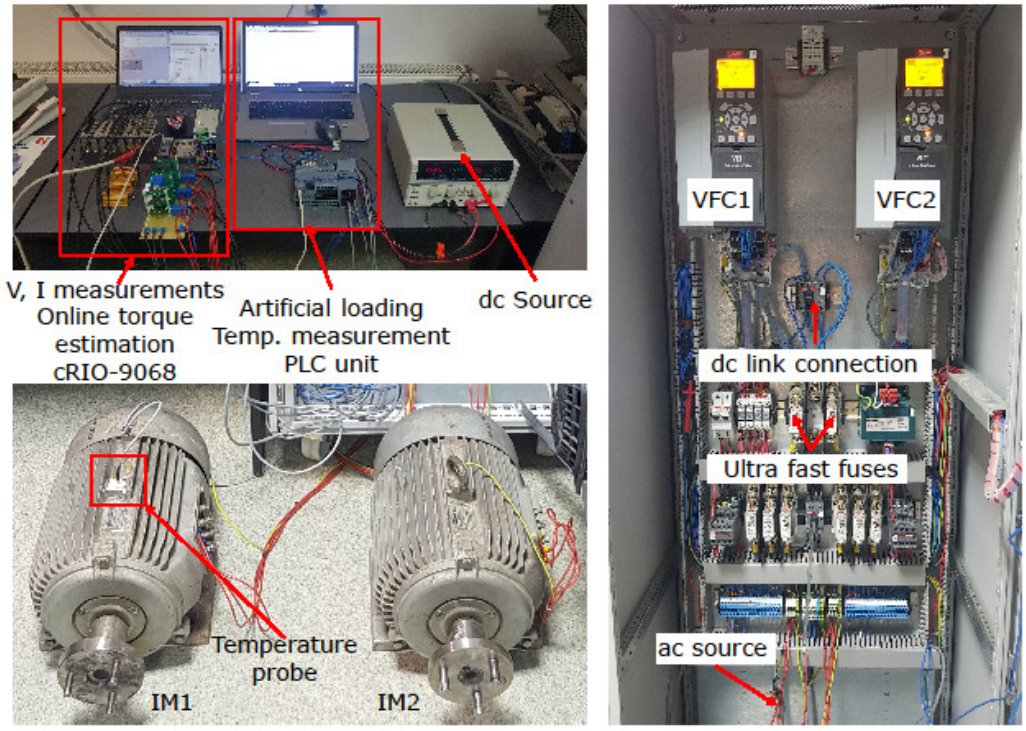

Fig. 4.2 Laboratory experimental setup

For instantaneous (phase currents/voltages, ac-source currents/voltages), a 4-channel oscilloscope is used (left side of the image).

Both 7.5kW induction machines are shown at the bottom of the image. There is no mechanical coupling between the IMs. Both IMs are not even anchored to the ground during the artificial loading operation. In the left-side IM, a temperature probe was inserted into the position of the lifting hook.

The here presented artificial loading method is based on a standard industrial low-cost PLC. The PLC gives the VFCs references as a standardized 4-20mA. The IM's speed, torque, and currents are read from VFCs, in the same manner, as a 4-20mA signal.

A PT100 temperature sensor was inserted in place of one IM's lifting hook. The PLC requires only two analog input ports, two analog output ports, and one RTD module. The PLC-PC communication is performed via ethernet.

The induction machine and variable frequency converters parameters are summarized in Table 4.1.

Table 4.1 Induction machines and variable frequency converters parameters

No.	Induction machines		No.	Variable frequency converters	
1	Voltage (V)	380	1	Voltage In (V)	3~380...500
2	Current (A)	15.4	2	Current In (A)	14.4/13
3	Power (W)	7.5	3	Frequency In (Hz)	48..63
4	Speed (rpm)	2880	4	Voltage Out (V)	3~0..Voltage In

5	cos φ	0.87	5	Current Out (A)	16/14.5
6	Rs (Ω)	0.44	6	Frequency Out (Hz)	0..1000
7	Rr (Ω)	0.6	7	Power (W)	7.5
8	Lm (mH)	90.7	8	-	-
9	Ls (mH)	4.299	9	-	-
10	Lr (mH)	4.299	10	-	-
11	J (kgm^2)	0.015	11	-	-

The here presented artificial loading test is performed at a constant speed (speed reference offset) and an alternating overlapped speed (speed variation amplitude). By means of PC, the artificial loading method (control strategies) is loaded into PLC. The speed reference parameters are changed manually into PLC in manual testing. In automated testing, the speed reference parameters are PLC computed and follows a setpoint. The PLC prescribes the references to the VFCs via a 4-20mA port.

Doubled dc link capacity can be obtained by parallel connection of both VFCs. Further, three different situations are presented: tests with either one VFC and one IM, a doubled dc-link capacitance VFC and one IM, or 2 VFCs (dc-link interconnected) and 2 IMs. However, only the latter is significantly expanded.

The speed reference consists of an offset and alternating component (i.e., sinusoidal, triangle, etc.). One of the most simple and used speed references is presented below: sinusoidal reference.

$$PLC^{*}_{speed\_reference} = DC_{off} \pm A \cdot sin(\omega \cdot t) \tag{4.1}$$

Where: $PLC^{*}_{speed\_reference}$ represents the PLC output speed reference given to the VFCs, DC_{off} represents the offset speed, A represents the amplitude of the sine oscillations, ω represents the pulsation, and t represents the time.

In the case of artificial loading of only one IM, the speed reference is given to a single VFC. On the other hand, artificial loading method of two IMs driven by two dc-link connected VFCs, the speed references have the following form:

$$\left.\begin{aligned} VFC1^{*}_{speed\_ref} &= DC_{off} + A \cdot sin(\omega \cdot t) \\ VFC2^{*}_{speed\_ref} &= DC_{off} - A \cdot sin(\omega \cdot t) \end{aligned}\right\} \tag{4.2}$$

Where: $VFC1^{*}_{speed\_ref}$, $VFC2^{*}_{speed\_ref}$ represents the speed reference given to both inverters.

For simplicity reasons, the dc offset speed references of both VFCs are set internally into inverters. Thus equation (4.2) becomes:

$$\left.\begin{aligned} VFC1^{*}_{speed\_ref} &= A \cdot sin(\omega \cdot t) \\ VFC2^{*}_{speed\_ref} &= -A \cdot sin(\omega \cdot t) \end{aligned}\right\} \tag{4.3}$$

For the artificial loading of two IMs driven by two VFCs, two different PLC's AOs are used. The equation (4.3) is graphically explained in Fig. 4.3.

BUPT

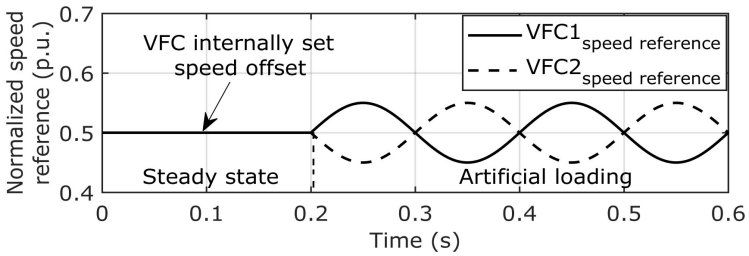

Fig. 4.3 Final VFCs speed references for artificial loading method of two IMs driven by two dc-connected VFCs

Due to the dynamic regime of the artificial loading method, the IMs phase currents read from VFCs have no meaning in terms of IM's loading. To quantify the IMs current, the RMS phase currents are determined inside the PLC (based on the equation (4.4)) using filtered VFC RMS currents.

$$I_{RMS_{PLC}} = \sqrt{\sum_{i=1}^{n/m} \left(\frac{\sum_{k=1}^{m} I_{RMS_{VFC}}^2}{n} \right)} \tag{4.4}$$

Where: $I_{RMS_{PLC}}$ represents the IM RMS phase current determined inside the PLC based on IM RMS phase current read from VFC, $I_{RMS_{VFC}}$ represents the IM RMS current read from VFC, i, k are the sums indexes, n represents the number of samples used for one PLC RMS current, m represents samples number in one subinterval and n/m represents the total number of subintervals. Basically, the n, m values are empirically chosen in order to obtain a stable PLC RMS current ($n = 1000, m = 10$). The number of samples used for one PLC RMS current value (n) should be a multiple of the number of samples used in one subinterval (m).

The PLC control program runs at 1kHz frequency, which means that each 1ms, the VFC speed reference and the IMS VFC read current are updated.

4.3. Artificial loading control strategies

4.3.1. Preliminary results

As was previously discussed, two situations are presented here:

a) Artificial loading of one IM driven by one standard VFC

In this case, the sinusoidal speed reference is given to one single VFC. Even though the sinusoidal speed reference consists of 2500 rpm dc offset (set inside the VFC) and ±200rpm amplitude at 1.8Hz oscillation frequency (given by the PLC), the dc-link voltage variations are extremely high, approaching the maximum permitted dc voltage, as can be seen in Fig. 4.4. The instantaneous ac source current is presented below the dc voltage. The RMS value of the IM's phase current and the

BUPT

RMS value of the ac source current is given in the graph's legend (Fig. 4.4). Both RMS values were computed by the PLC based on the equation (4.4).

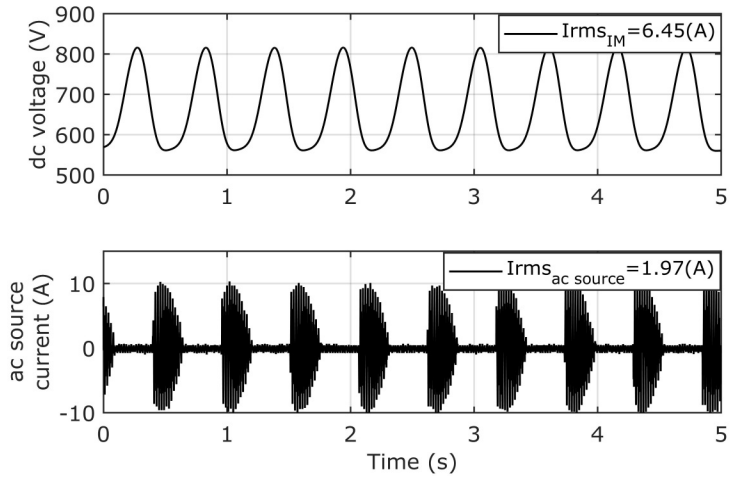

Fig. 4.4 dc-bus voltage and ac source current for artificial loading with 1IM and 1VFC at 2500rpm with ±200rpm amplitude and 1.8Hz oscillation frequency – measured

It can be seen that only 21% increase in the IM's phase RMS current compared to the IM's RMS idle current (5.3A) can cause dangerous values of dc-link voltage. During this experiment, the upper threshold of the VFC dc voltage limit has been reached several times, leading to warnings and faults.

b) Artificial loading of one IM driven by a double dc-link capacitance VFC (parallel connection of both dc links)

Fig. 4.5 presents the results obtained in the same conditions as in Fig. 4.4 (±200rpm amplitude at 1.8Hz speed reference frequency).

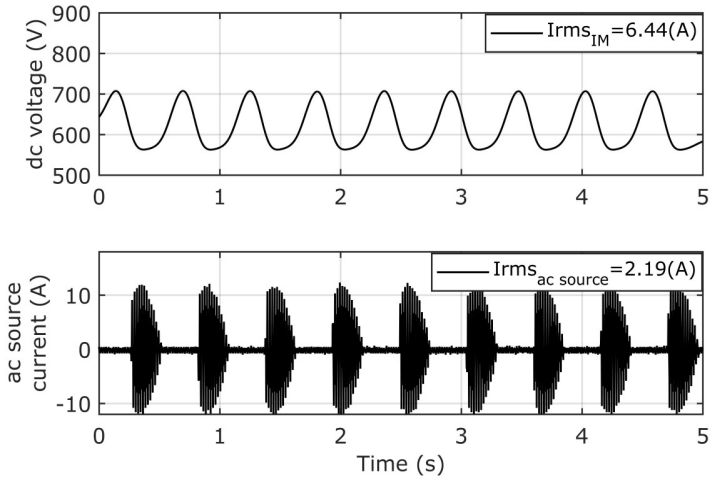

Fig. 4.5 dc-bus voltage and ac source current for artificial loading with 1IM and 1VFC (doubled dc-link capacitance) at 2500rpm with ±200rpm amplitude and 1.8Hz oscillation frequency – measured

BUPT

This way, both VFCs have been connected in parallel by connecting both dc-links. Even though the experiment was carried out with only one IM driven by only one VFC (with doubled dc-link storage capacity).

With doubled dc-link capacitance, the maximum allowable VFC's dc-link voltage limit is easily reached (Fig. 4.6) by increasing the speed reference amplitude with ±90 rpm (at the same oscillations frequency of 1.8Hz).

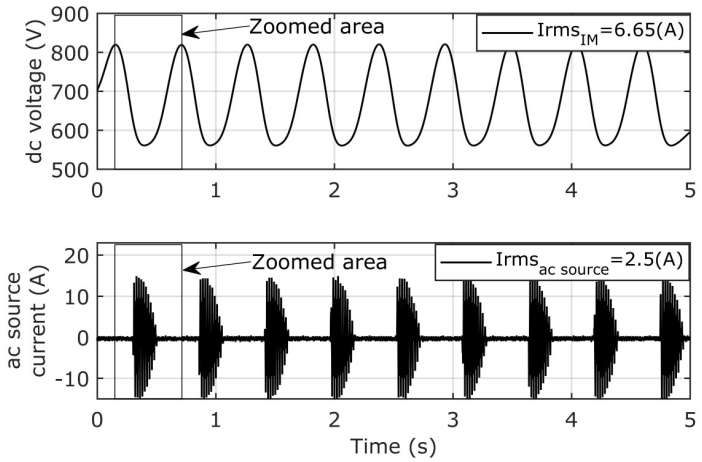

Fig. 4.6 dc-bus voltage and ac source current for artificial loading with 1IM and 1VFC (doubled dc-link capacitance) at 2500rpm with ±290rpm amplitude and 1.8Hz oscillation frequency – measured

Even so, the IM RMS current can not be compared to the IM RMS-rated current. In Fig. 4.7, the zoom area from Fig. 4.6 is presented. The ac source current peaks reached 15A. When the IM accelerates, and the value of the dc voltage tends to fall below the value of the rectified three-phase voltage value (≈565V) the VFC's diode bridge rectifier starts to operate.

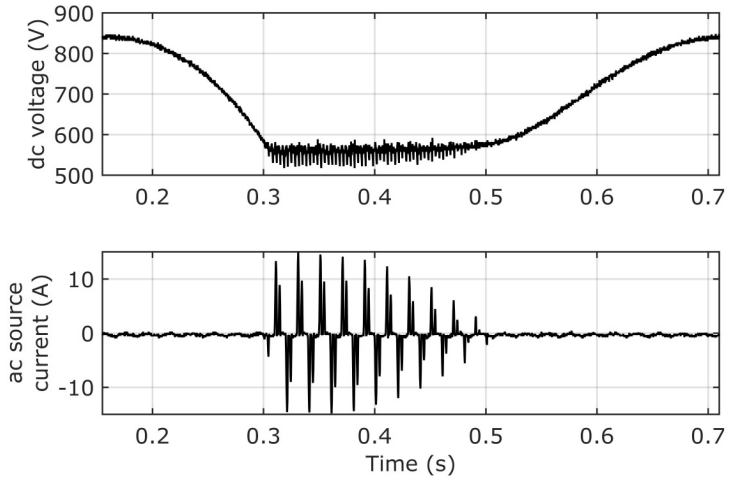

Fig. 4.7 Details on unfiltered dc-bus voltage variations and ac source current presented in Fig. 4.6 – measured

BUPT

The findings reported above (a), b)) serve solely to show the VFC's bad behavior when only one IM is dynamically loaded. The IM RMS current has reached insignificantly compared to the IM RMS-rated current. In both situations, the VFC's dc-link voltage has unacceptable variations.

4.3.2. Open-loop control method

The speed reference amplitude and frequency gradually change until the IM RMS phase current reaches the desired value in the open-loop control method. The major amplitude or frequency sudden changes can cause undesired DC bus over-voltages so during the open-loop artificial loading, the speed reference parameters should be modified slowly.

As the oscillation speed or amplitude increases, the induction machine RMS phase current increases as well, thus, IM's loading increases.

There are several ways to change the IM RMS current: either by speed reference amplitude or speed reference frequency. Fig. 4.8 presents a wide range of possibilities to change the IMs loading. During all these tests, the speed dc offset was set at 2500rpm inside the VFCs. The VFCs current limit is 130% of IM-rated current (about 20.5A).

The red circled point (500rpm speed reference amplitude and 6Hz speed reference frequency) corresponds to the operating point, which was chosen to obtaine the IM RMS-rated current with the artificial loading method. In other words, almost the same results could be obtained if the test was performed at 400rpm speed reference amplitude but 8 Hz speed reference frequency.

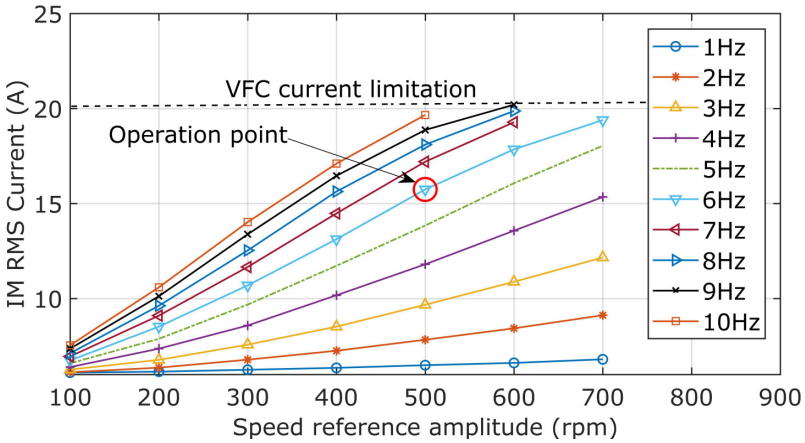

Fig. 4.8 The IM's RMS current variations in artificial loading conditions at different reference amplitude and frequency combinations - measured

To keep as much as possible the rated mechanical losses, the artificial loading test should be performed at a dc offset speed as close as possible to the rated IM speed (2880rpm). To be able to increase the reference amplitude in a wide range and at the same time to keep the mechanical losses as close as possible to rated ones, the dc offset operating point was chosen at 2500 rpm.

At fixed speed reference amplitude, increasing the speed reference frequency the IM inertia filters the speed. Fig. 4.9 shows in two situations (100rpm and 200rpm amplitude) how the IM RMS phase current is limited above a certain

BUPT

oscillating frequency. With 200rpm amplitude, the IM RMS current is 88% of the IM-rated current value, while at 100rpm amplitude, the IM RMS value is about 50% of the IM-rated current value, even if the reference frequency increases up to 30Hz.

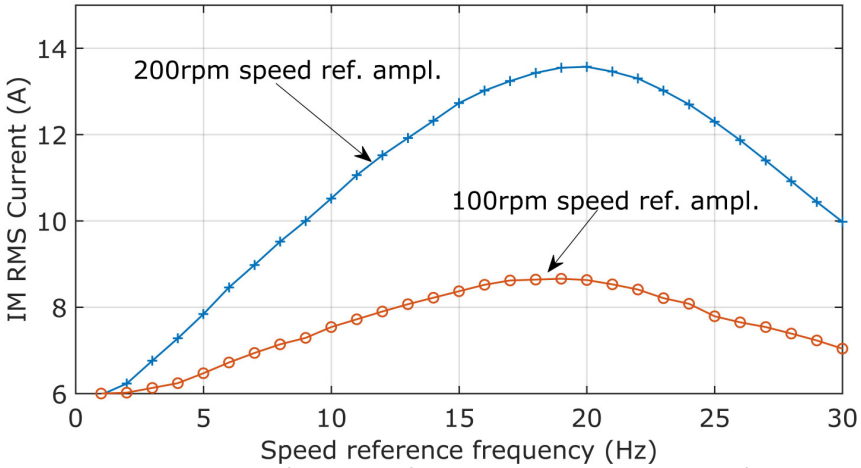

Fig. 4.9 2 IM and 2 VFC IM frequency response – measured

4.3.2.1. 180^0 phase shift speed reference

The following figures present the artificial loading of two identical induction machines without mechanical coupling driven by two identical dc-interconnected standard variable frequency converters.

This method represents the simplest control method of the artificial loading test. The speed reference for both VFCs consists of two identical sinusoidal references 180 degrees phase-shifted between each other (as presented in Fig. 4.3).

In this situation, both VFCs have the dc-link coupled, but each IM is driven by one VFC. The PLC gives two 180-degree phase-shifted sinusoidal references at each inverter.

The total capacitance of the parallel connection of both VFCs is 1000uF. Each inverter has two series-connected 1000uF capacitors.

Fig. 4.10 shows, on the one hand, for each IM, the synchronization between instantaneous currents and the speed reference given to the VFCs, and on the other hand, the time synchronization between both IMs measurements.

While one IM accelerates, the other decelerates. The speed references are given as p.u. values, while the dc offsets speeds are set inside the VFCs. The oscillation speed reference is set at 6Hz, while the oscillation amplitude reaches 500rpm.

BUPT

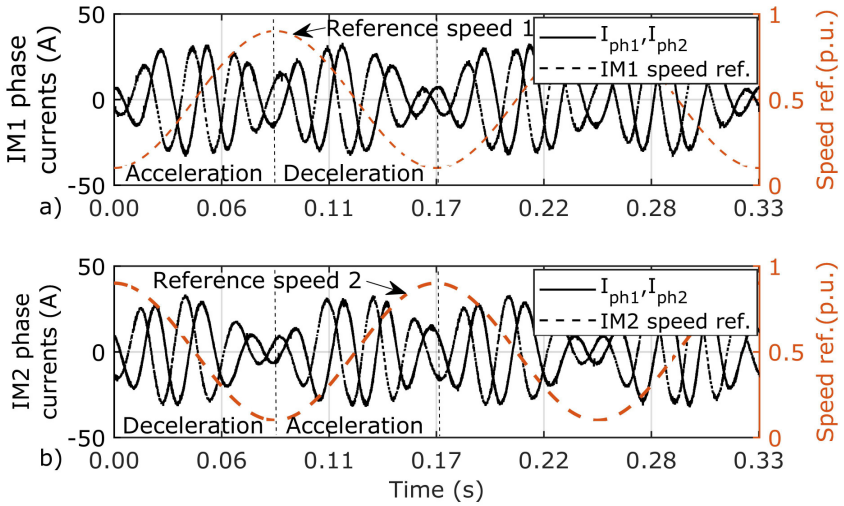

Fig. 4.10 IM1 two instantaneous currents and speed reference, IM2 two instantaneous currents and speed reference – time synchronization - measured

Fig. 3.11 shows the IMs VFCs unfiltered estimated speed and torque values. Here, the measurements are read using the PLC analog input module. The discrete shape graph is due to the VFC's AO module update frequency limit.

Even if the PLC speed reference oscillates between 2000rpm and 3000rpm in artificial loading at IM RMS-rated current conditions, the IM inertia filters the real speed. However, while motoring and generating, the IM torque reaches the VFC's torque limits (160% rated torque while motoring, 120% rated torque while generating).

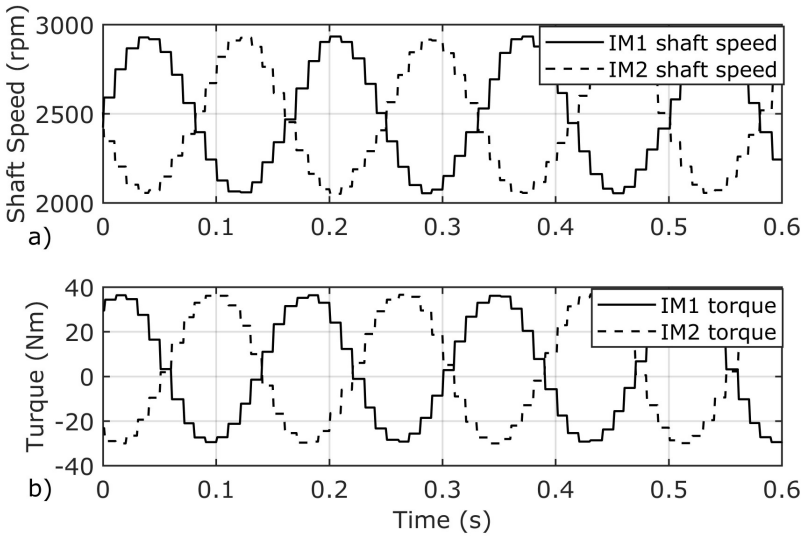

Fig. 4.11 VFC AO values of IMs unfiltered torque shaft and speed in artificial loading conditions of 2 IMs with 2 VFCs at 2500rpm dc offset, ±500rpm amplitude, and 6Hz frequency – measured

BUPT

Fig. 4.12 presents the results obtained from the artificial loading of both IMs at the stator RMS-rated current. When one IM accelerates, the other decelerates. Thus, the power produced by the decelerating machine goes to the accelerating machine through the common dc-bus of the two VFCs.

From Fig. 4.12 and Fig. 4.13 can be observed that in the artificial loading method with 2IMs and two dc bus interconnected VFCs case, no long-term negative impact over the dc bus capacitor lifetime is presented. This is due to the fact that the dc voltage (even at IM RMS-rated current) varies slightly, falling within 10% of the dc voltage-rated value. The power circulation between the IMs can be seen in the instantaneous currents in Fig. 3.13, where both dc voltage and dc current are presented during the artificial loading test.

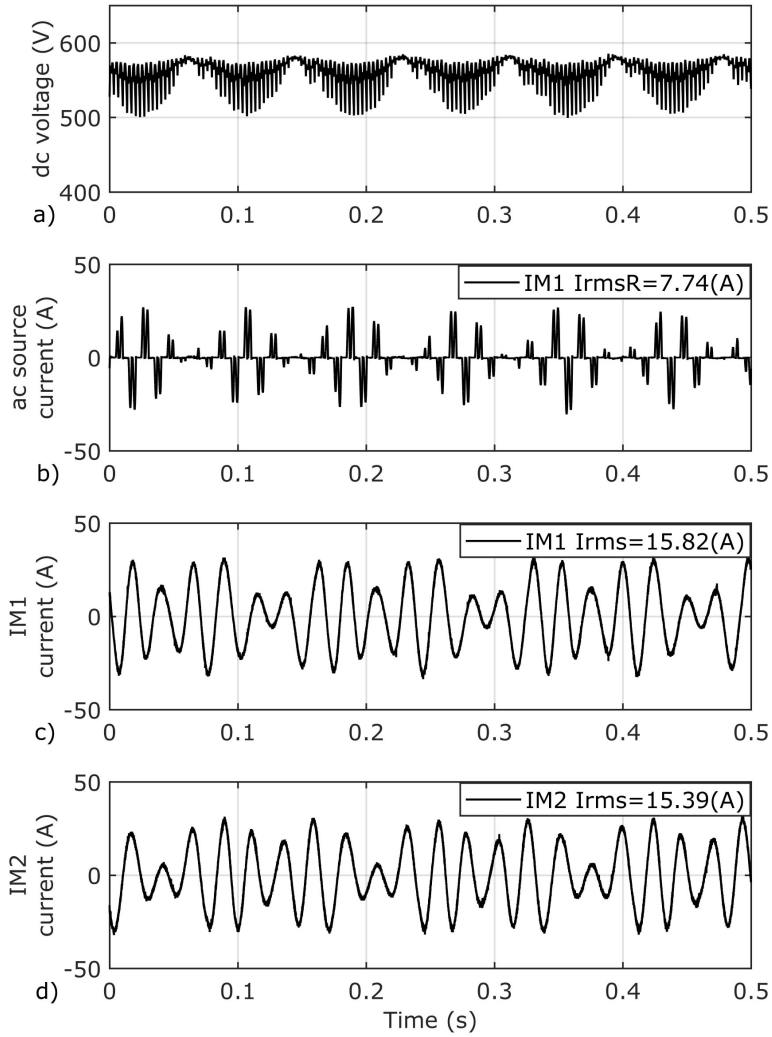

Fig. 4.12 Instantaneous dc-bus voltage, ac source current, IM1 phase current and IM2 phase current for artificial loading with 2IMs and 2VFCs (dc-link interconnected) at 2500rpm with ±500rpm amplitude and 6Hz oscillation frequency – measured

BUPT

The dc-link current varies with the speed reference frequency. Due to the loading principle of two identical IMs, the dc-link voltage varies two times faster than the speed reference frequency.

Starting from Table 4.1, based on the following equation, the IM (computed) losses are ≈1307W.

$$IM_{losses} = \sqrt{3} \cdot V \cdot I \cdot \cos\varphi \tag{4.5}$$

Once accelerated, VFC supplies IM only with the power needed to cover losses. In artificial loading at IM RMS-rated current conditions, the total power absorbed by both VFCs from the ac source is $2787.2(W)$.

Half of it is equal $P_{1VFC\_grid} = 1393.6(W)$ and represents the power absorbed by one single VFC from the grid. At the same time, the measured power consumed by the IM in the same conditions is $P_{IM\_measured} = 1304.8(W)$ (very similar compared to the IM plate computed losses presented above $P_{IM\_plate\_computed} = 1307(W)$).

Thus, the losses of a VFC are:

$$P_{VFC\_losses} = P_{1VFC\_grid} - P_{IM\_measured} = 88.8W \tag{4.6}$$

The voltage and current harmonics investigation is treated in chapter 3.3.4, where more details about frequency spectrum and current circulation are presented.

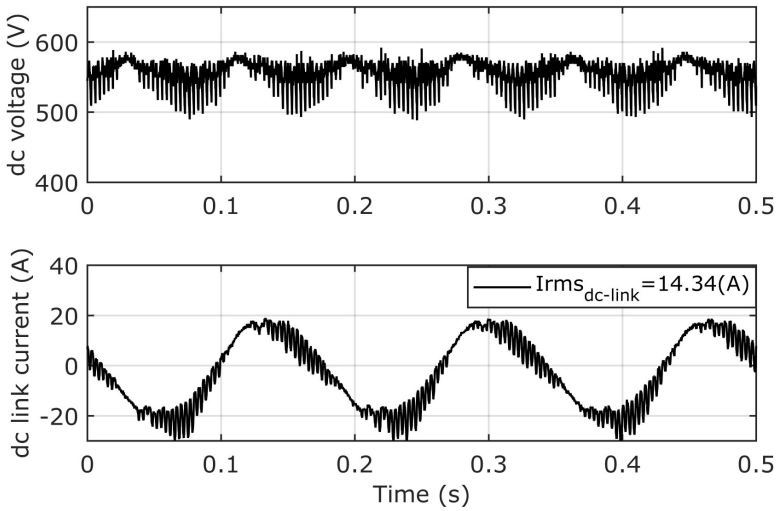

Fig. 4.13 dc voltage and dc current for artificial loading with 2IMs and 2VFCs (dc-link interconnected) at 2500rpm with ±500rpm amplitude and 6Hz oscillation frequency - measured

4.3.2.2. Variable phase shift speed reference

Besides sinusoidal speed reference, next, the artificial loading method was tested with phase-shifted speed reference. The reason for this approach was based on studying the possible side effects of the unsynchronized operation of both machines in terms of dc-link voltages. To validate this assumption, in Fig. 4.14 are presented the phase-shifted references, the dc-buss voltages, and the IM speed.

BUPT

This type of artificial loading referencing requires two different AO ports of PLC. Basically, the phase-shifted sine wave speed reference represents a control topology of the two IMs, in which at each cycle, the IM which starts to accelerate always has a delayed start (with Δt (s)) compared to the IM which starts to decelerate (PLC software on Appendix 5). Thus, changing the Δt, it was studied if the ac-source current was minimized in a context of an IM acceleration with a precharged dc-buss. The PLC performs the phase shift between both references. Due to the relatively low frequency of the PLC program cycle (1kHz), the minimum possible phase shift between the references is 1 ms. However, the time phase shift can be converted into a degree phase shift with the following equation:

$$Phase\_shift = 360 \cdot f \cdot cp_{nbs} \cdot ct \left[^{o} \right] \tag{4.7}$$

Where: f represents the oscillating speed wave frequency and $cp_{nbs} \cdot ct$ represent PLC parameters which represent the total number of cyclic programs (ct ms) uses for shifting and the duration of a program cycle. The phase-shifted test starts with no phase-shifting between the references. Then, after the reference amplitude and frequency were set, the acceleration stage for each IM is gradually delayed according to Δt. Based on (4.7) for a delay corresponding to 15 PLC cyclic programs (of 1ms each) and a 6Hz frequency, the time delay represents $32.4(ms)$.

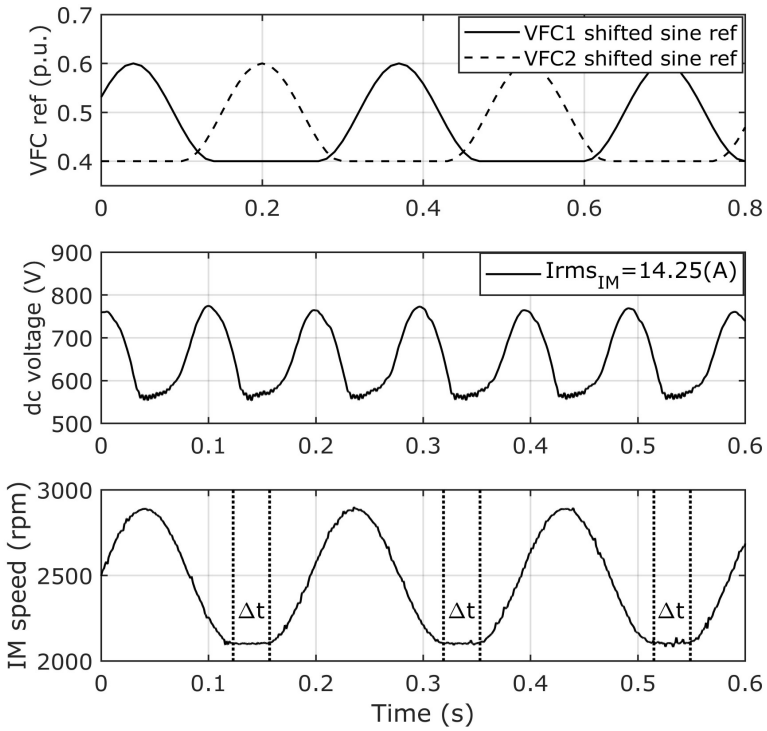

Fig. 4.14 Shifted sine speed reference, dc voltage, and IM real speed for artificial loading of 2IMs and 2VFCs at 2500rpm with ±500rpm amplitude and 6Hz oscillation frequency for IM RMS current value of 14.25(A) – measured

BUPT

That means that, at every speed reference cycle, the motor starts to accelerate delayed with 32.4ms after the generator starts to break. This ensures more power injected into the dc-buss, available for the motor to accelerate. The above-presented results present the maximum speed reference parameters and phase shift delay in terms of maximum allowable dc-bus voltage. However, it was experimentally concluded that over a certain phase shift value, the IM RMS current value decreased while the dc-buss voltage reached undesirable values.

4.3.2.3. Triangle phase shift speed reference

From Fig. 4.15, the dc-buss voltage, the IM speed, and the ac-source current in a triangle-shaped speed reference are presented.

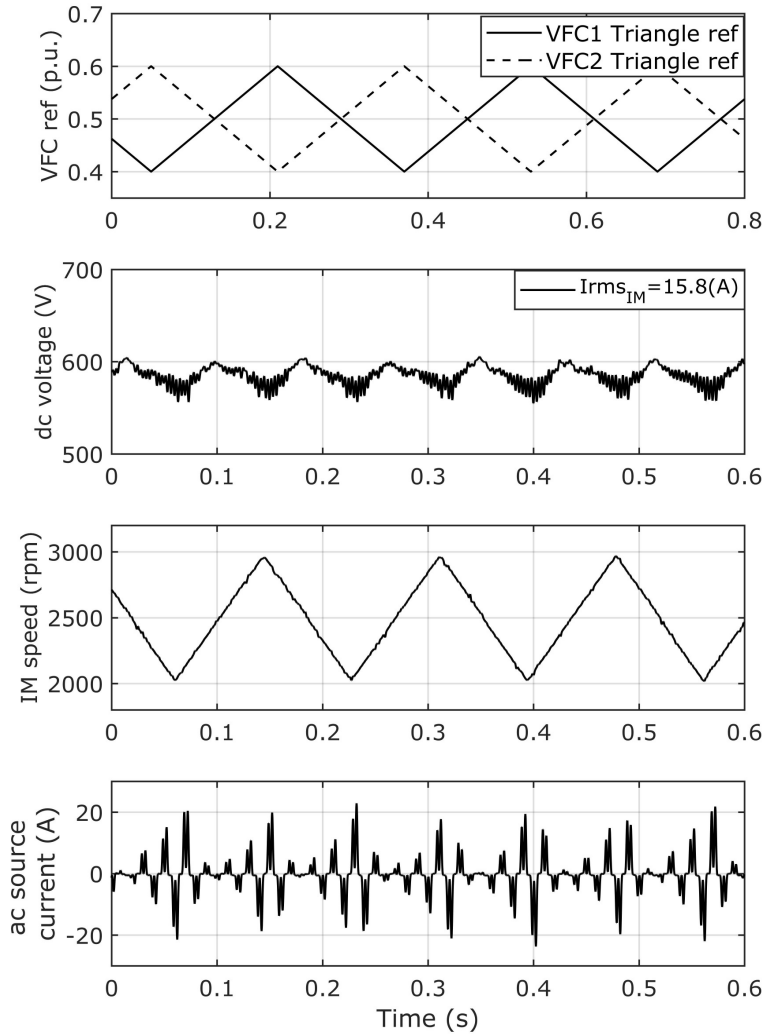

Fig. 4.15 Triangle speed reference, dc voltage, real IM real speed and ac source current for IM RMS value of 15.8(A)

BUPT

In an attempt to limit the ac-source current spikes, and to reduce the dc-buss voltage ripples during the IM artificial loading, the triangle speed reference control method is presented above.

The triangle-shaped speed reference consists (similar to the sinusoidal reference) of an amplitude and a frequency (PLC software given in Appendix 6).
Even if the dc voltage has small variations, the ac source current still has high peaks. Compared with phase-shift results, where the maximum IM RMS current was limited at about 92% of IM-rated current, in this case, the IM loading was performed slightly over the IM RMS current (up to $\approx 103\% \cdot Irms_{IM}$).

In both figures (Fig. 4.14 and Fig. 4.15), the IM speeds read from the VFCs, are unsynchronized with the values read from the oscilloscope (i.e., ac source currents and dc voltages).

4.3.3. The closed-loop control method

The here-presented closed-loop control method was carried out to smoothly modify the speed reference parameters (amplitude and frequency) up to the prescribed value. Here, the PI regulators slowly modify the process values, compared to the open-loop control method, where the parameters were discretely manually changed. The following three equations describe the PLC implementation of the PI regulator:

$$c.v. = \left[\left(I^*_{ref} - I_{VFC}\right) \cdot T\right]_{(n)} + \left[\left(I^*_{ref} - I_{VFC}\right) \cdot T\right]_{(n-1)} \tag{4.8}$$

$$y_1 = c.v.\Big|_{L_{lim}}^{H_{lim}} \cdot k_p \tag{4.9}$$

$$y_2 = sin\left(\left\{\left[\left(c.v. \cdot k_i\right)\Big|_{L_{lim}}^{H_{lim}}\right] \cdot T\right\}_{(n)} + \left\{\left[\left(c.v. \cdot k_i\right)\Big|_{L_{lim}}^{H_{lim}}\right] \cdot T\right\}_{(n-1)}\right) \tag{4.10}$$

$$\left.\begin{aligned} VFC_{ref\,1} &= y_1 \cdot y_2 \\ VFC_{ref\,2} &= y_1 \cdot y_2 \end{aligned}\right\} \tag{4.11}$$

Where: I^*_{ref} represents the prescribed IM RMS current, I_{VFC} represents the IM RMS current read from VFC (computed inside the PLC base on (4.4)), T represents the PLC cyclic program time, $c.v, y_1, y_2$ represent intermediate variables, $n, n-1$ represent the "n" and "n-1" time moment, k_p, k_i represent the PI regulator parameters and H_{lim}, L_{lim} represent the high and low limit necessary for variables limitation. T is set to the PLC minimum cyclic time (1 ms). The high and low limits are used to limit the reference amplitude and frequency to a certain value.
The sin argument range limitation is also performed in order to avoid the PLC stack overflow.

In Fig. 4.16, three different situations of closed-loop operation are presented. The tests were recorded from the no-load current (at idle speed (2500rpm)) until the IM RMS read current reached the prescribed value. The RMS current slope can be modified accordingly to the PI controller parameters.

BUPT

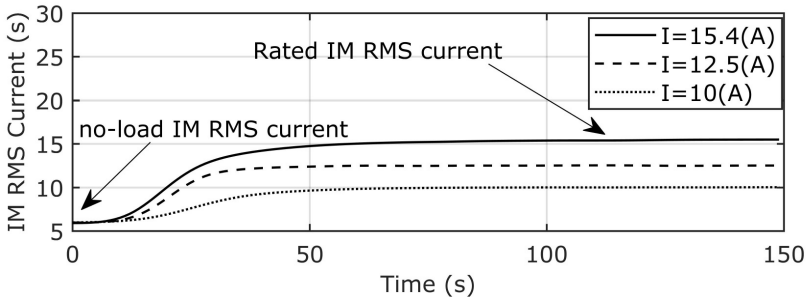

Fig. 4.16 IM RMS current variation in closed-loop control in artificial loading of 2 IMs and 2 VFC conditions – measured

With a closed-loop artificial loading method, an IMs accelerating-loading-decelerating mechanized procedure can be defined.

4.3.3.1. Automated testing

This automatic procedure's main role is limiting both IMs phase currents, and ac source absorbed current in well-defined limits.

Fig. 4.17 shows an automatic acceleration/deceleration procedure of both IMs. The test was performed on 150 seconds time period. The IM's speed and current were read with the PLC.

Sectors 1,2,4,5 represent the accelerating process of both machines. In order to limit the current, each IM starts separately to the dc offset speed (this case, 2500rpm). After the first IM started (sector 1), the second IM started as well (sector 2). In sector 3, the closed-loop artificial loading procedure takes place (i.e. the thermal test presented in Fig. 4.17). In an on-site test operation, this time period could take minutes, hours, or even days, depending on the IM power and test purpose.

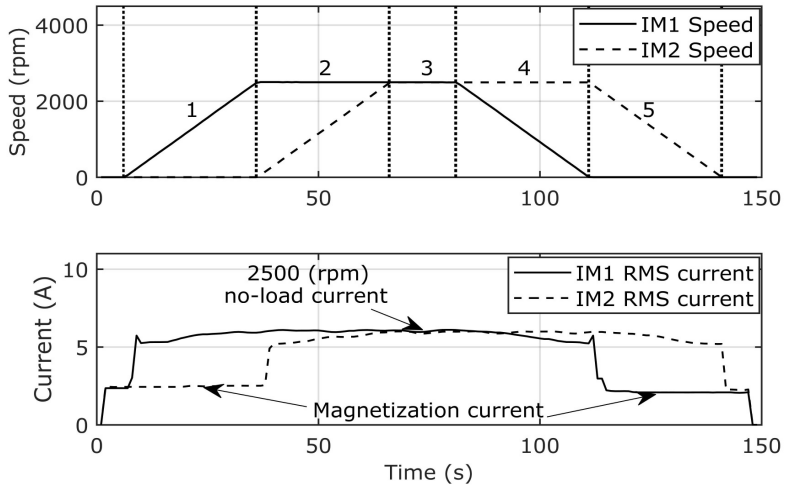

Fig. 4.17 IMs speed and IMs RMS current profile in the closed-loop control method for 0-2500rpm – measured

BUPT

After artificial loading, in sectors 4 and 5 both IMs decelerate at a time, maintaining the current limits. Each acceleration and deceleration sector lasts 30 seconds, with a 15-second steady-state pause in between. During the start-up process, the IMs RMS currents (PLC computed) represent only 40% of the rated IM current. While one IM accelerates or decelerates, the other is only magnetized by the drive. Depending on the application type, the magnetization current limits can be set inside the VFC. Fig. 4.18 presents each sector's ac source current envelope during the closed-loop automated acceleration and deceleration process.

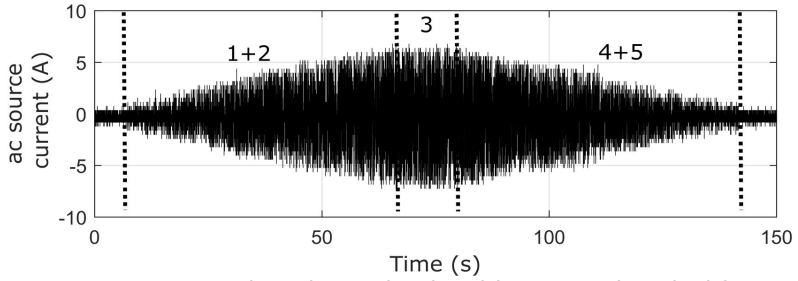

Fig. 4.18 ac source current envelope during the closed-loop control method for 0-2500rpm – measured

4.3.3.2. Thermal testing

The thermal test, presented in Fig. 4.19, represents the practical applicability of the closed-loop automatized start-loading-stop procedure.

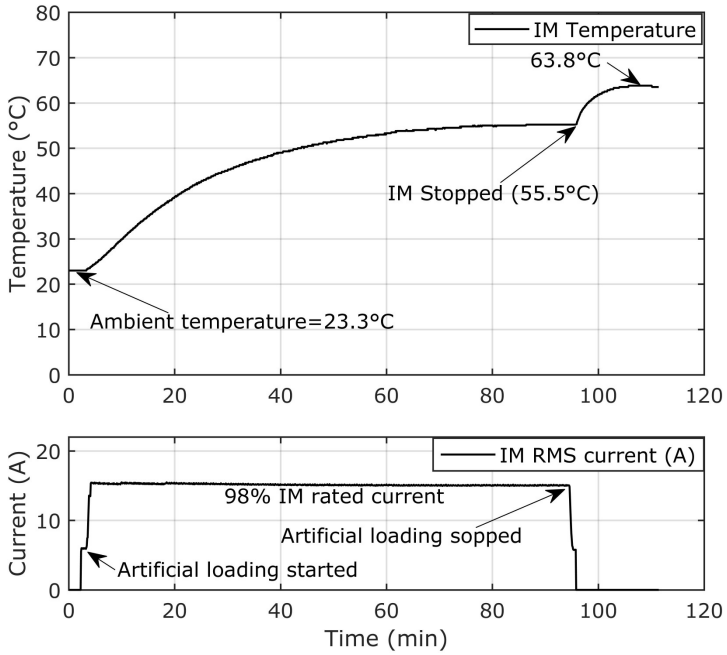

Fig. 4.19 IM temperature (measured in the lifting hook) and the IM RMS current at 2500rpm with ±500rpm amplitude and 6Hz oscillation frequency

BUPT

Twin inverter feed artificial loading of two induction machines can be used to thermal test two IMs simultaneously.

In the previous test, presented in Fig. 4.19, both induction machines were artificially loaded at 0.98 p.u. RMS-rated current, using a sinusoidal speed reference at 2500rpm dc offset with +-500rpm amplitude at 5.8Hz oscillation frequency. The test was performed in 110 minutes. The temperature was measured with a PT100 sensor inserted into the lifting hook (with thermally conductive paste) using an additional PLC module (RTD module). The temperature was read once every 10 seconds. During the test, the IM housing temperature rose from ambient temperature (23degree) to a stabilized temperature of 55.5degree. After the IM stopped (without cooling), the final IM housing temperature reached 63.8degree.

4.3.4. Current harmonics investigation

Next, several measurements were performed and analyzed by Fast Fourier Transform (FFT) to determine the frequency spectrum. The artificial loading conditions were the same for all measurements, for IMs rated phase current value (2500rpm 6Hz and ±500rpm).

In Fig. 4.20, the dc-link voltage and the frequency spectral analysis is presented. The 12 Hz harmonic represents twice of artificial loading frequency (both IMs accelerate/decelerate twice a period). The 300Hz, 600Hz, and 900Hz harmonics are due to the diode bridge rectifier effect.

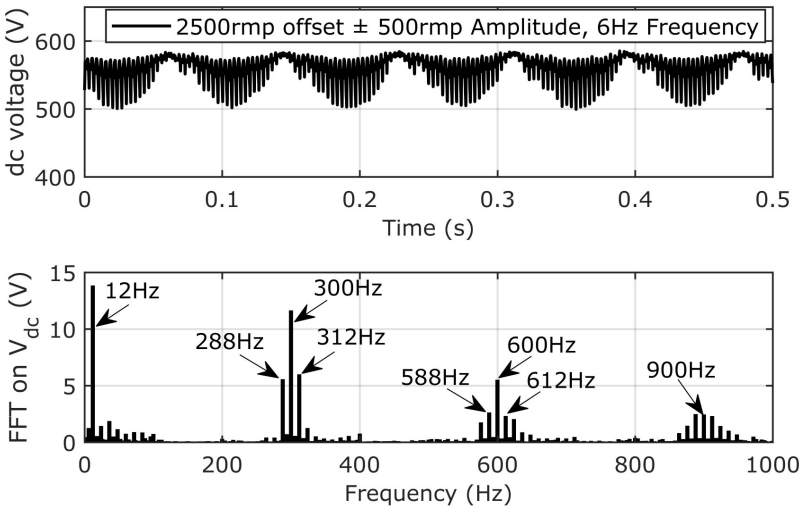

Fig. 4.20 dc-link voltage and and FFT analysis for 2500rpm dc speed offset, 6Hz oscillation frequency and ± 500rpm amplitude – measurements

During the artificial loading, the power flows from one IM to another via the dc-link. The current measured between the inverters $I_{dc\text{-}link}$ (see Fig. 4.1 - the current which flows through F1) and the frequency spectral analysis is presented in Fig. 4.21. Here the speed reference oscillation frequency (6Hz) can be observed as a predominant harmonic. The $I_{dc\text{-}link}$ RMS value ($Irms_{dc\text{-}link}$=13.82(A) represents about 89% of IMs rated RMS current value (15.4(A)), which means that the rest of the power is obtained from the grid.

BUPT

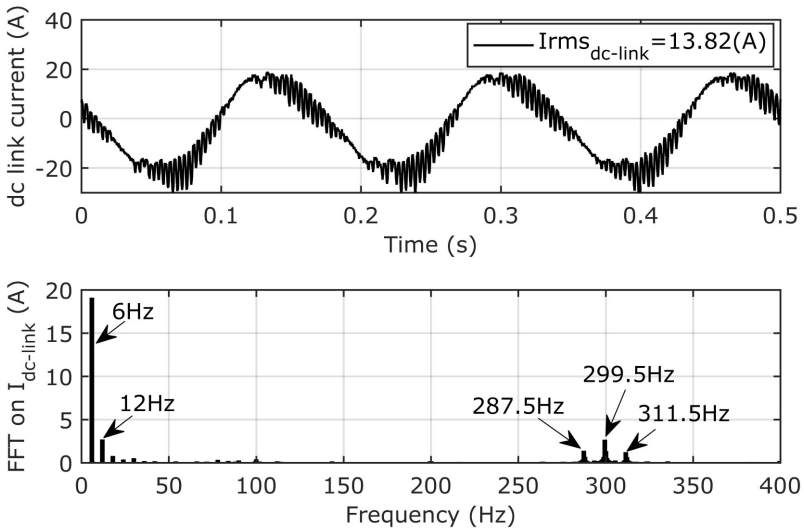

Fig. 4.21 dc-link current and and FFT analysis for 2500rpm dc speed offset, 6Hz oscillation frequency and ± 500rpm amplitude – measurements

In Fig. 4.22, the voltage between the IMs frames was measured.

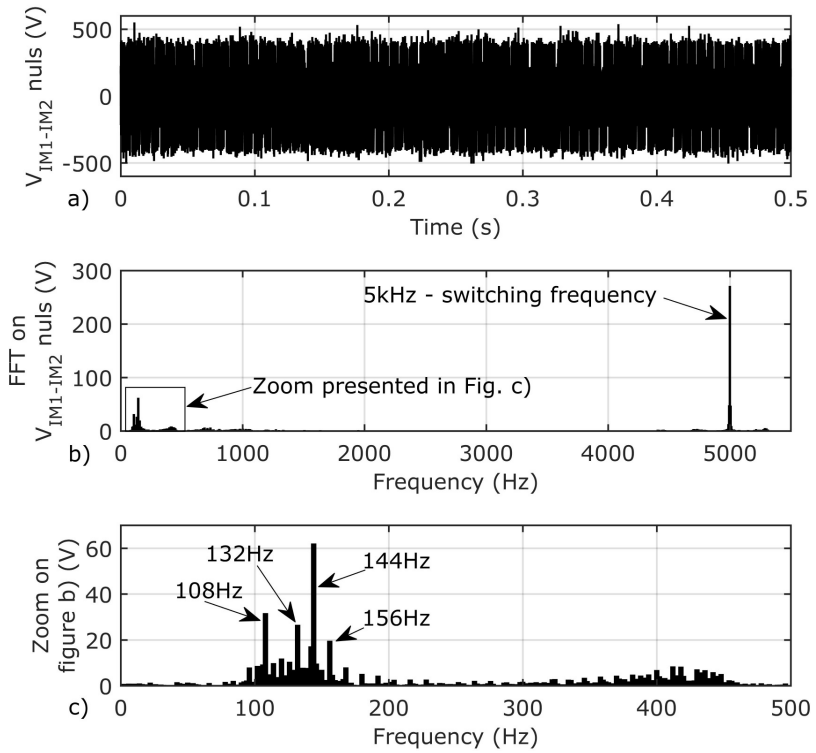

Fig. 4.22 voltage measured between IM's stator winding nulls and FFT analysis for 2500rpm dc speed offset, 6Hz oscillation frequency and ± 500rpm amplitude – measurements

BUPT

Besides the 5kHz VFC switching frequency (Fig. 4.22 b)), the 144Hz (Fig. 4.22 c)) represents the dominant harmonic. 12Hz uniformed distributed less significant harmonics are presented.

Fig. 4.23 presents the voltage measured between the IM's frames and consists of the same voltage spectrum as the voltage measured between IMs' nulls.

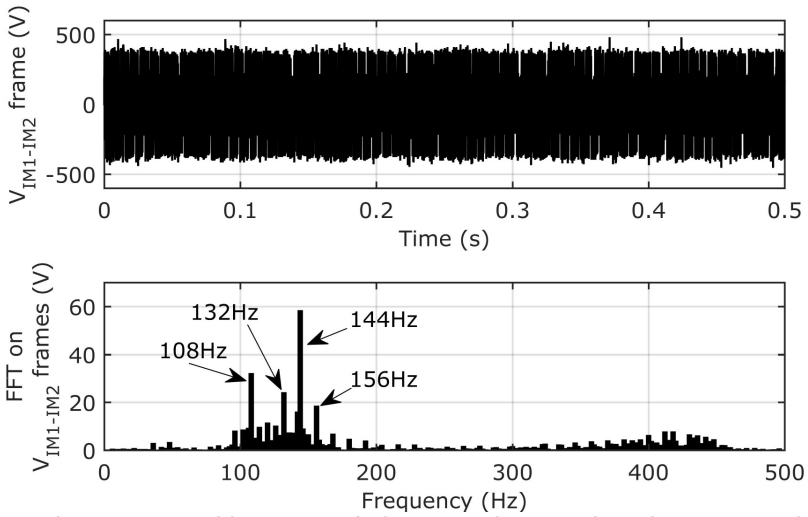

Fig. 4.23 Voltage measured between IM's frames and FFT analysis for 2500rpm dc speed offset, 6Hz oscillation frequency, and ± 500rpm amplitude – measurements

With IM grounding (a common connection between IM frames) there is an insignificant current circulation between induction machines caused by the VFC chopping frequency. This amount of current and the spectral analysis is presented in Fig. 4.24.

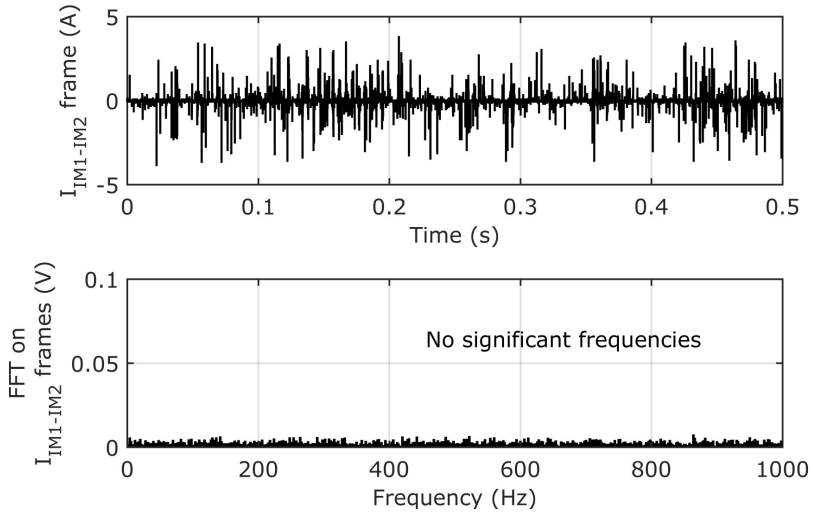

Fig. 4.24 Current measured between IM's frames (with grounding) and FFT analysis for 2500rpm dc speed offset, 6Hz oscillation frequency and ± 500rpm amplitude – measurements

BUPT

In Fig. 4.25, the 50Hz frequency, the 250Hz (5th harmonic), and the 350Hz frequency (7th harmonic) are dominant. All these harmonics have uniformly distributed less significant harmonics.

The 2500rpm speed reference dc speed offset represents the 42Hz frequency. Without a common null connection, the triplen harmonics do not exist.

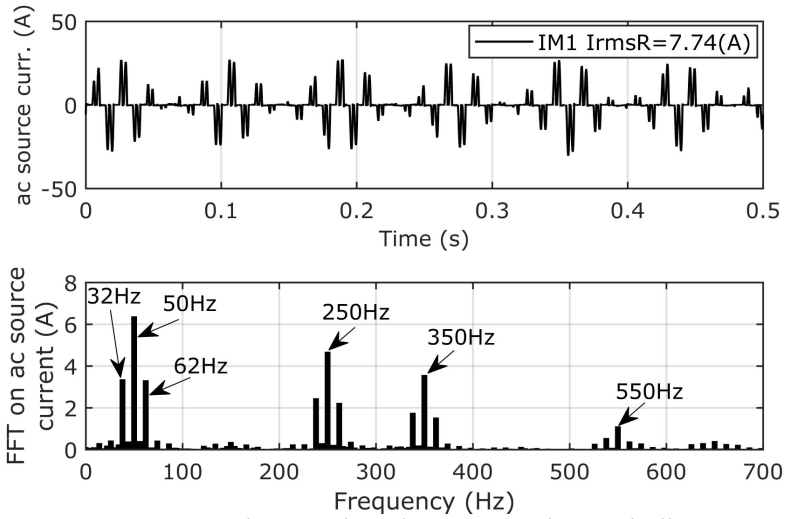

Fig. 4.25 ac source current and FFT analysis for 2500rpm dc speed offset, 6Hz oscillation frequency and ± 500rpm amplitude – measurements

In Fig. 4.26, the IM phase current was investigated. It can be observed that the IM was slightly virtually overloaded (the RMS phase current is 15.82(A)). Over the 66Hz, there are NO significant harmonics. In the zoomed area, the most significant harmonic (120Hz) represents less than 0.01% of the 42Hz component.

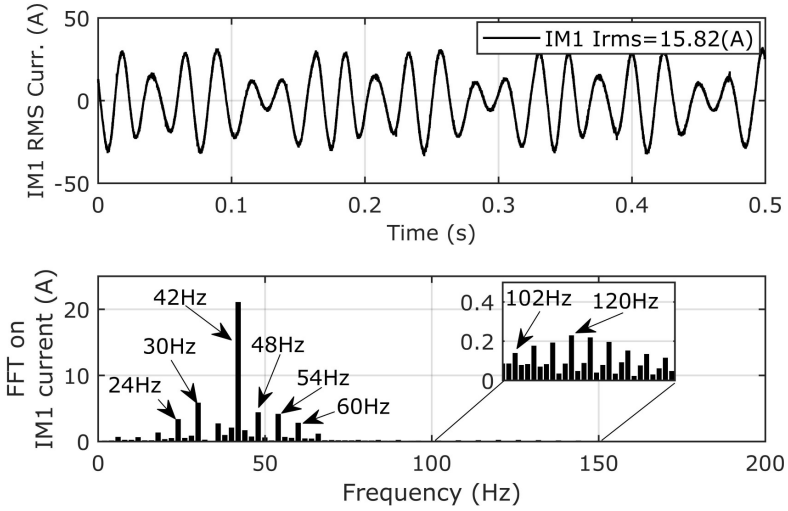

Fig. 4.26 IM phase current and FFT analysis for 2500rpm dc speed offset, 6Hz oscillation frequency and ± 500rpm amplitude – measurements

BUPT

The ac source current is varying with double the speed reference oscillation (6Hz). The high current peak values presented in it are due to the simultaneous IM loss variations. During the acceleration, both IMs have significant losses. At the same time, during the zero-acceleration zones - for sinusoidal speed reference (see Fig. 4.10) the IM's absorbed currents are notably smaller, leading to smaller losses.

As previously explained in here presented artificial loading method, the power flows from one IM to another via the dc-bus. Only the losses are fed from the ac-source. This way, the IMs overall loos variation causes the high peaks of the ac source current.

An asymmetric 2x3 phase winding IM can be used as an additional solution to represent the IM virtual loading without mechanical coupling. The 3rd, 6th, or homopolar current components cannot exist because both IMs have a star connection [180]. On the other hand, improved results in terms of current harmonics minimization can be achieved in non-commercial inverters by applying PWM synchronization techniques [181], [182].

Fig. 3.27 shows all three phase currents for one IM during the rated artificial loading test. The graph is presented for two complete periods of 6Hz. It can be observed that the sum of all three currents is characterized by a dc offset value less than 0.5A, a value that can be considered within the acceptable limits of measurement errors. This way, it can be noticed that no notable circulating currents are presented.

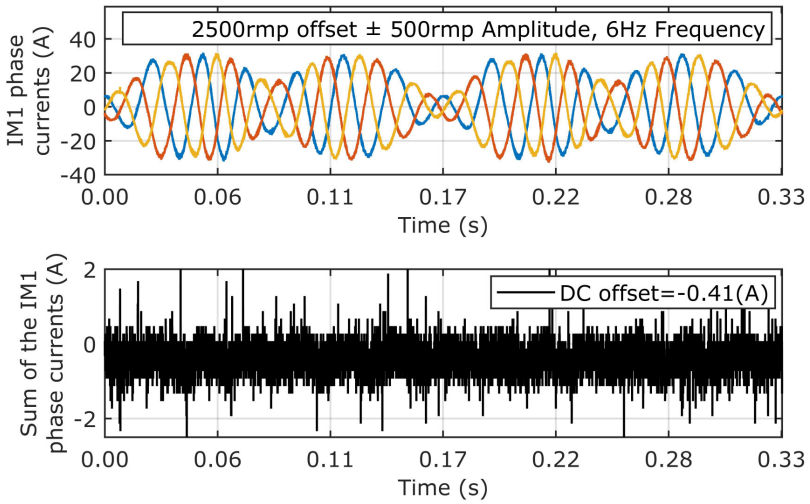

Fig. 4.27 IM's instantaneous phase currents and current sum for 2500rpm dc speed offset, 6Hz oscillation frequency and ± 500rpm amplitude – measurements

4.4. Simulations

All simulated tests were performed in Matlab&Simulink environment.

Two different simulations were performed to validate the method's applicability by studying the induction machine's losses and the test influences on the ac source current:

- simulation with one IM driven by one VFC, mechanically loaded at rated current.

BUPT

- simulation and measurements when two induction machines driven by two variable frequency inverters are artificially loaded at rated current.

The results are compared regarding ac source current effects and power loss validation.

4.4.1. Artificial loading influences on ac source current

To correlate the real measurements obtained from the experiment with those obtaine from simulations for artificial loading conditions, simulations at rated loads are required.

The artificial loading test impact over the ac source current is investigated using the following Simulink diagram.

In Fig. 4.28, the artificial loading impact over the ac source current is investigated. The diagram contains a simplified ac source consisting of a three-phase sinusoidal voltage source, equivalent inductances, and the three-phase diode bridge rectifier (D1, D2, D3, D4, D5, D6). The L1, L2, and L3 are the equivalent grid and VFCs' inductances. The total VFCs dc-link capacitance is represented by the C.

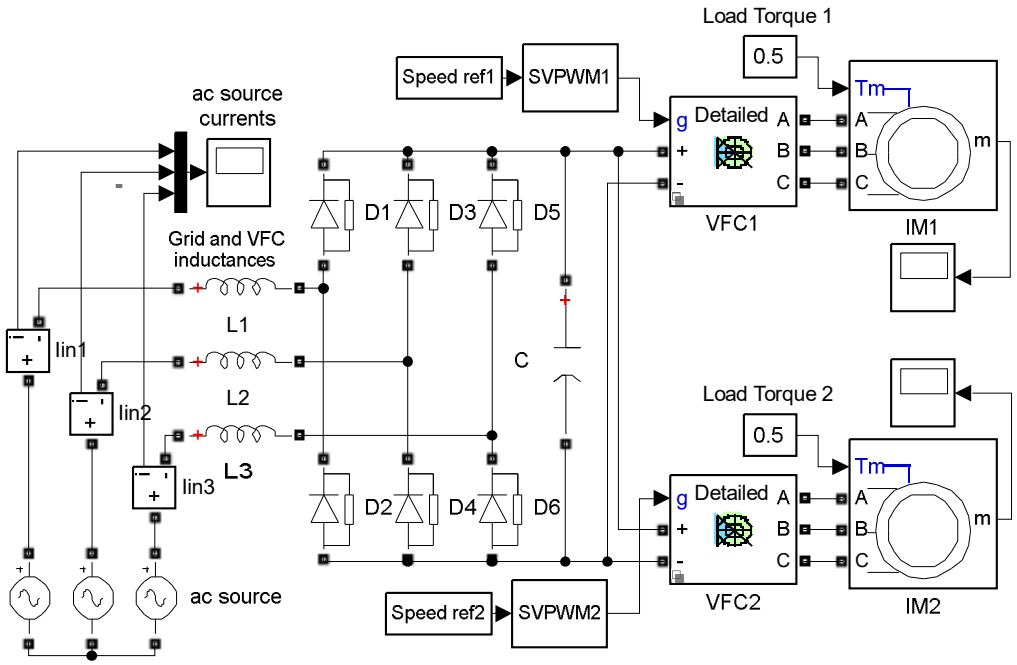

Fig. 4.28 ac source current investigation in artificial loading condition – Simulink implementation

Because only the grid current is investigated at this stage, the induction machines (IM1, IM2) and the variable frequency converters (VFC1, VFC2) are special equipment from the Simulink library. Their parameters are set according to Table 4.1.

BUPT

Both IMs are speed controlled by the drives. The speed reference and the PWM commands are set into Speed ref and SVPWM blocks (Fig. 4.29)

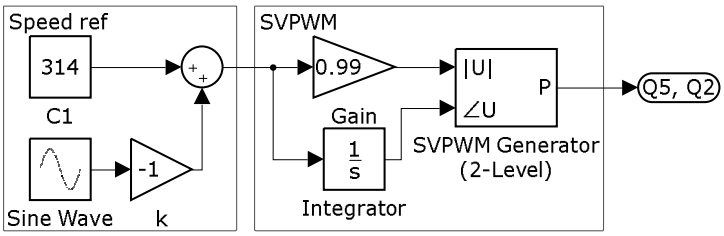

Fig. 4.29 Speed ref and SVPWM blocks explanation (see Fig. 4.28)

With Load Torque blocks, the IM shaft loading torque is set.

Fig. 4.30 and Fig. 4.31 present the diode bridge rectifier current for both real experiments (Measured) and simulation for 2 IMs running at rated speed without shaft loading and for 2 IMs artificially loaded at rated current.

Due to the principle of operation, the IMs used for the artificial loading method assumes a time-variable power loss. Without considering the variable frequency inverter losses, the average total losses are given by twice IM efficiency.

This way, during the artificial loading test, the IM's instantaneous losses vary heavily.

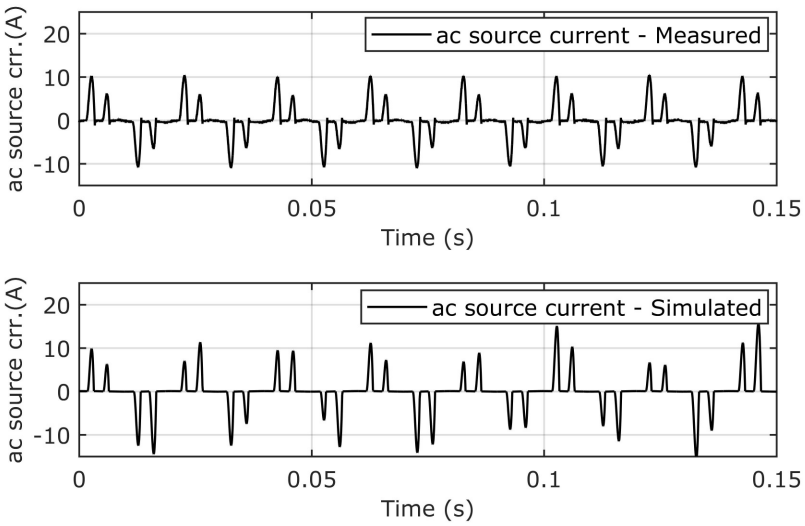

Fig. 4.30 ac source current for two induction machines in no-load and rated speed conditions – real measurements and simulations

As explained in the previous subchapter, during the sine speed reference, the IM losses vary widely due to the unconstant IM stator current.

As it can be observed from previous graphs, the instantaneous modulated peak ac source currents can reach double the IM-rated RMS current. Even so, for rated current artificial loading conditions, the peak value of ac source current is twice smaller as the ac source current peak value obtained for IM-rated shaft loading.

BUPT

The ac source current is limited only by the grid inductances. In many cases, these are very small.

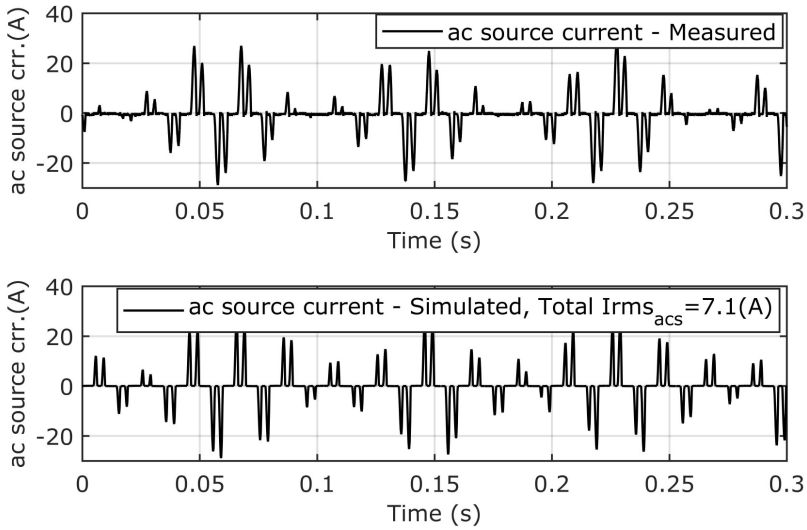

Fig. 4.31 ac source current for two induction machines in artificial loading conditions – real measurements and simulations

The RMS value of the ac source current can be computed as presented in (4.12):

$$I_{RMS_{ac\_source}} = \frac{2 \cdot P_{IM} \cdot k_p \cdot \left(\frac{1}{\eta_{IM} \cdot \eta_{VFC}} - 1 \right)}{\sqrt{3} \cdot V_n} \tag{4.12}$$

Where: $I_{RMS_{ac\_source}}$ represents the RMS value of the ac source current, the P_{IM} represents the induction machine power, which in this formula is taken into account doubled, η_{IM} and η_{VFC} are the IM's and VFC's efficiency, the V_n represents line rated voltage and k_p is a dimensionless factor which refers to the uneven power losses variation during the artificial loading test:

$$k_p = \begin{Bmatrix} 1 - mechanically\ coupled\ IMs \\ 1 + \frac{2}{3} \le 2 - not\ mechanically\ coupled\ IMs \end{Bmatrix}$$

4.4.2. Power loss validation

Considering that experimental shaft-rated loading is not a solution, correlations between simulation are required: first, a relation between artificial loading experiment and simulation needs to be done; second, the shaft loading simulation need to be correlated with artificial loading simulation.

This way, the rated shaft loading simulation of one IM can be tied up by one real IM artificial loading (here, presented method).

BUPT

In Fig. 4.32, the Simulink block diagram for power loss validation in artificial loading conditions is presented. Compared to the previous Simulink diagram (Fig. 3.28), the power losses "inside" the induction machines and variable frequency converters are investigated in this case. The ac source (three-phase voltage source and the diode bridge rectifier) is neglected, considering an ideal rectifier (Ideal Vdc block).

Both IMs are speed controlled, so the simulation is performed by prescribing the speed reference (block Ref. sin.). Like real artificial loading experiments, the speed dc offset is set at 2500rpm, with an ±500rpm and 6Hz oscillation frequency.

The torque reference obtained after the speed and torque regulator block is given to the VFC Control blocks. Reference sinusoidal voltages alpha and beta (obtained from VFC control) and the actual value of the dc-link voltage are given to the SVM blocks. Here, space vector modulation is performed, so both induction machines are fed with a three-phase voltage system in $\alpha\beta\gamma$ reference frame.

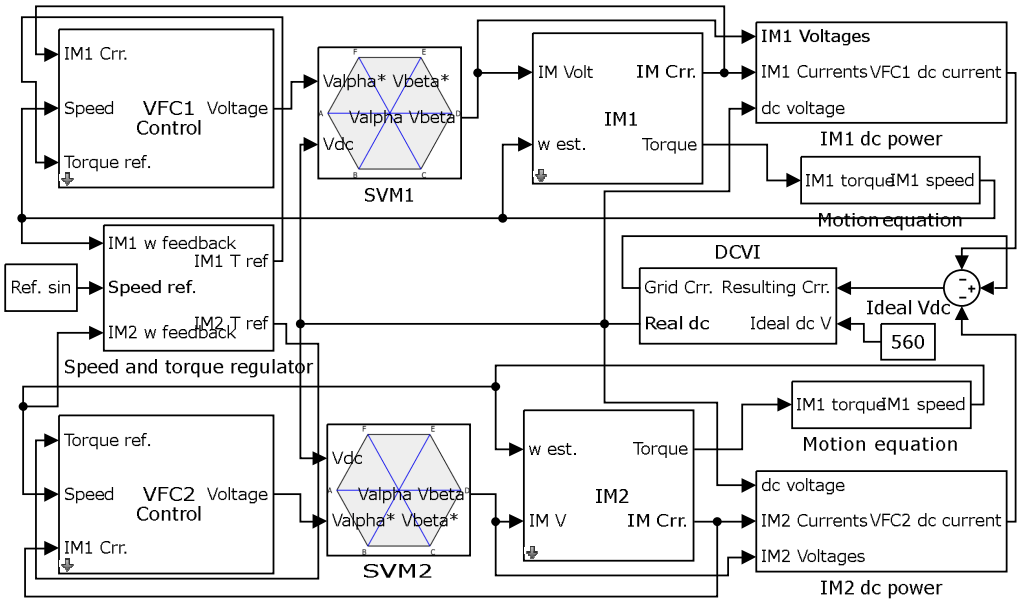

Fig. 4.32 Simulink implementation of artificial loading with two IMs and two VFCs

VFC Control block equations are described below:

Considering a flux weakening of Ψ_r^*:

$$\begin{cases} \omega_{fw} = \dfrac{\Psi_r^* \cdot \omega_b}{\omega}, \left|\omega_{IM}\right| < \omega_b \\ \omega_{fw} = \dfrac{\Psi_r^* \cdot \omega_b}{\omega_b}, \left|\omega_{IM}\right| \geq \omega_b \end{cases} \tag{4.13}$$

$$\omega_b = \frac{n_b \cdot \pi}{30} \tag{4.14}$$

BUPT

$$I_{\alpha\beta} = \frac{2}{3} \cdot \begin{bmatrix} 1 & -\frac{1}{2} & -\frac{1}{2} \\ 0 & \frac{\sqrt{3}}{2} & -\frac{\sqrt{3}}{2} \end{bmatrix} \cdot \begin{bmatrix} I_a \\ I_b \\ I_c \end{bmatrix} \tag{4.15}$$

$$I_{dq} = \begin{bmatrix} \cos(\theta) & \sin(\theta) \\ -\sin(\theta) & \cos(\theta) \end{bmatrix} \cdot \begin{bmatrix} I_\alpha \\ I_\beta \end{bmatrix} \tag{4.16}$$

$$I_d^* = H(s)\left(\frac{\omega_{fw}}{L_m}\right), \quad H(s) = \frac{T_r \cdot s + 1}{0.04 \cdot s + 1} \tag{4.17}$$

$$I_q^* = \frac{2 \cdot L_r \cdot T^*}{3 \cdot p \cdot L_m \cdot \omega_{fw}} \tag{4.18}$$

$$\omega_2^* = \frac{2 \cdot L_r \cdot T^*}{3 \cdot p \cdot T_r \cdot \omega_{fw}^2} \tag{4.19}$$

$$\theta = \int \left(\omega \cdot p + \omega_2^*\right) \tag{4.20}$$

$$V_{d,q}^* = PI_{k_p=10,k_i=0.3} \begin{bmatrix} I_d^* - I_d \\ I_q^* - I_q \end{bmatrix} \tag{4.21}$$

$$V_{\alpha\beta} = \begin{bmatrix} \cos(\theta) & -\sin(\theta) \\ \sin(\theta) & \cos(\theta) \end{bmatrix} \cdot \begin{bmatrix} V_d \\ V_q \end{bmatrix} \tag{4.22}$$

Where: $\omega_{IM}, \omega_b, \omega_{fw}$ represent the IM's rotor speed, the IM's base speed, and the speed after the flux weakening, Ψ_r^* represents the value of the flux weakening after the base speed, n_b represents the base speed in rpm, $I_{\alpha\beta}, I_{abc}, I_{dq}$ represent the $\alpha\beta, abc, dq$ reference frame, I_{dq}^* represents the dq reference current in dq frame, L_m, L_r, T_r are the IM's magnetization and rotor inductances and the rotor time constant, $H(s)$ represents a transfer function used for I_d determination, T^* represents the torque reference obtaine from Speed and torque regulator block, p is the number of pole pairs, ω_2^* .represents the reference rotor speed, θ is the rotor angle, V_{dq}^* represents the dq reference voltage in dq frame, $V_{\alpha\beta}$ represents the $\alpha\beta$ reference voltage prescribed to the Induction Machine.

From Motion equation blocks, the IMs speed (ω) is calculated based on IM's inertia and friction coefficient. With IMs currents and voltages and the resulting dc voltage, the induction machine power and the dc current are computed in IM1 dc power and IM2 dc power blocks. Both VFC powers and the ac source power are mixed in the DCVI block, where the dynamic effect of both inverters is addressed.

BUPT

More than that, the dc link capacitance (C) and the total inductances (L) are considered in this block.

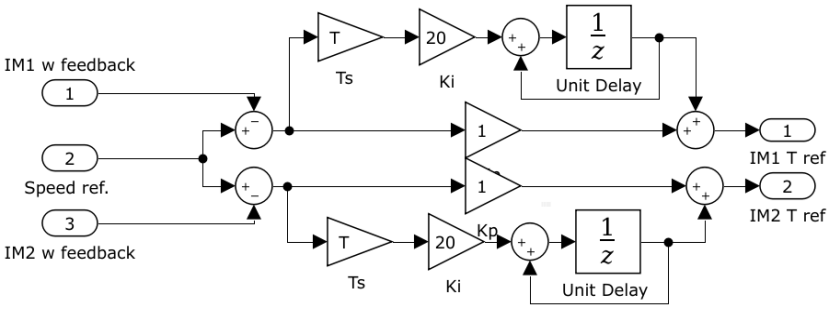

Fig. 4.33 Speed and torque regulator block

The real dc voltage value used for space vector modulation is obtained in the DCVI block from the ac source current and dc currents (from VFCs) and the total capacitance value. The ac source currents are also obtained from the DCVI block using the difference between the real voltage and the ideal one and the total value of the inductances.

The artificial loading results obtained during simulations are presented in Fig. 4.34. Here, the real dc voltage and both IMs phase currents are presented.

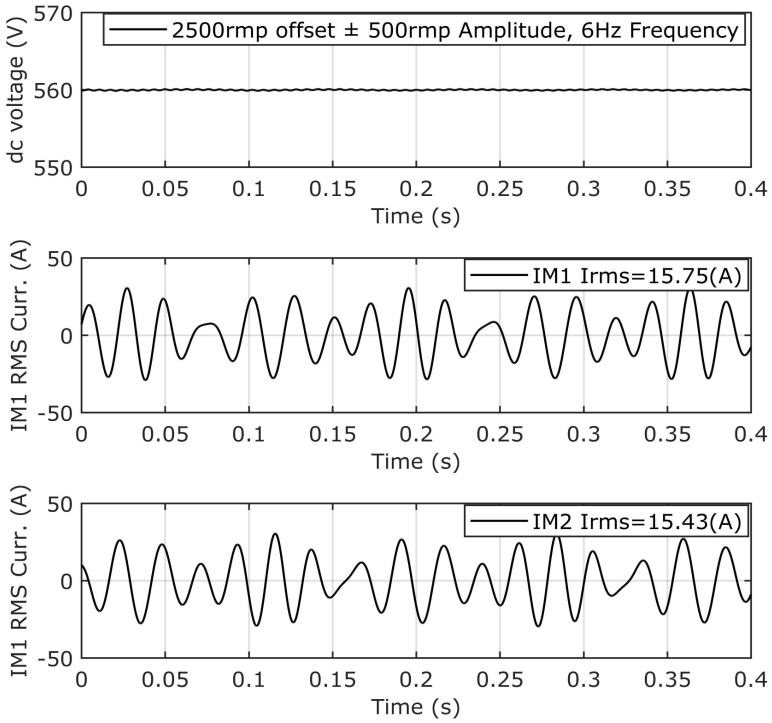

Fig. 4.34 dc voltage and IM's instantaneous phase currents for artificial loading at 2500rpm dc speed offset, 6Hz oscillation frequency and ± 500rpm amplitude – simulations

The induction machine model used in this simulation is based on the same equations set presented in the chapter (Chapter 3).

The real voltage and the ac source current from the DCVI block are obtained accordingly to the next equations:

$$V_{dc\_real} = \frac{1}{C} \cdot \int \left(I_{ac\_source} - I_{dc1} - I_{dc2} \right) \cdot dt \tag{4.23}$$

$$I_{ac\_source} = \frac{1}{L} \cdot \int \left(V_{dc\_real} - V_{dc\_ideal} \right) \cdot dt \tag{4.24}$$

Where: $V_{dc\_real}, V_{dc\_ideal}$ represents the real voltage obtained based on VFCs loading and the ideal dc voltage C, L represent the total dc-link capacitance and the total inductances, $I_{ac\_source}, I_{dc1}, I_{dc2}$ represents the ac source current and the VFCs dc currents.

The IM's losses (both the instantaneous ones and their average) both in the case of artificial loading and in the case of rated shaft torque loading at constant speed are presented in Fig. 4.35 and Fig. 4.36. The loss equivalation can be observed from the sum of all losses presented in the image's description. It can be observed that the artificial loading method can be used as an acceptable method for IM's loss equivalation.

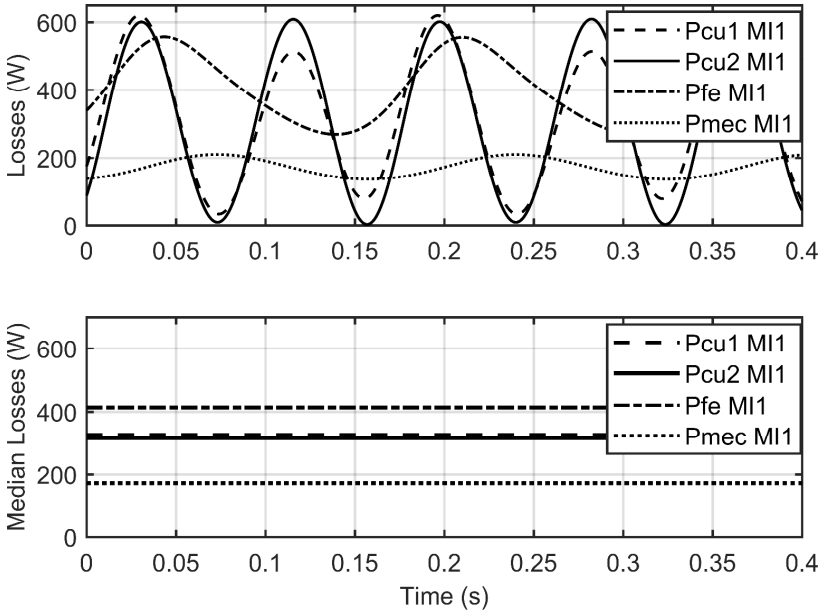

Fig. 4.35 Instantaneous and average values of copper losses, mechanical losses, and iron losses for one IM for artificial loading at rated current at 2500rpm dc speed offset, 6Hz oscillation frequency, and ±500rpm amplitude – simulations. Total median losses= $1228.4(W)$

The next simulation was run at the rated current. The ac current represents the input current of the diode bridge rectifier.

BUPT

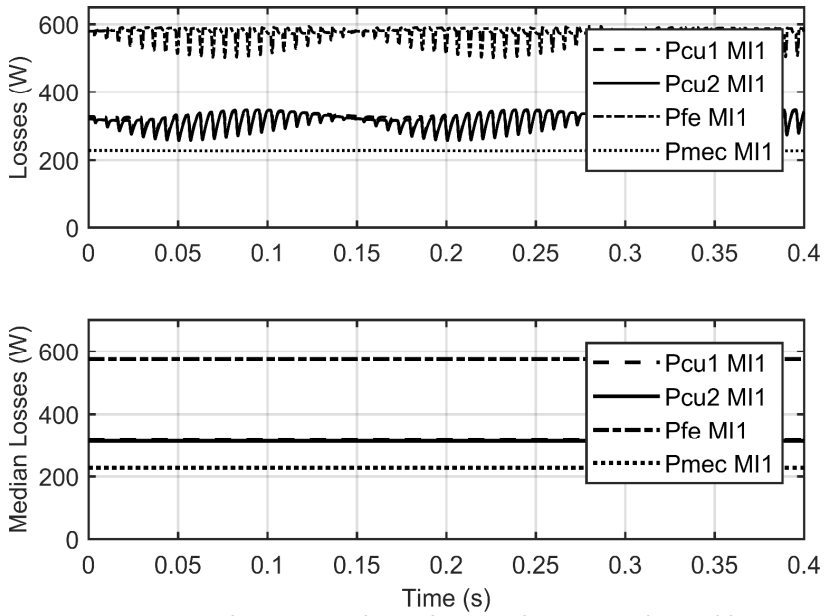

Fig. 4.36 Instantaneous and average values of copper losses, mechanical losses, and iron losses for one IM for shaft loading at rated power – simulations. Total median losses= $1432.1(W)$

Indirectly, this represents the power losses of the two IMs and their VFCs. For simplicity, only the VFC losses are neglected in simulations

In Fig. 4.37, it can be seen that at ±600rpm, regardless of speed offset, the peak-to-peak power of the dc is about 4kW.

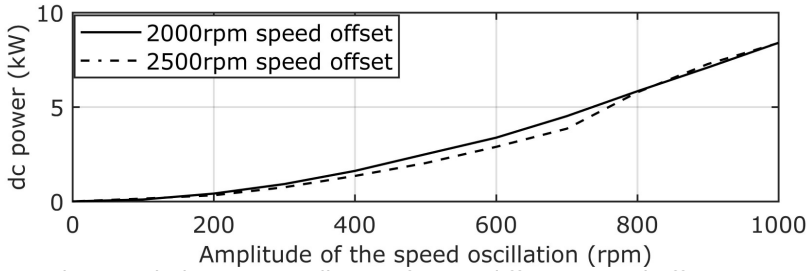

Fig. 4.37 Peak-to-peak dc power oscillations for two different speed offsets: 2000rpm and 2500rpm – simulations.

4.5. IM torque estimation for artificial loading method

In the following, the induction machine torque is online estimated for artificial loading conditions using variable frequencies converter's terminals voltages and currents.

The VFC's switching frequency is 5kHz. For the three-phase VFC output voltages, a low-pass first-order RC filter is used (with 16kHz cutoff frequency), while the phase currents are filtered by the machine.

The torque estimations are based on the estimators presented in Chapter 3 (more details can be found there).

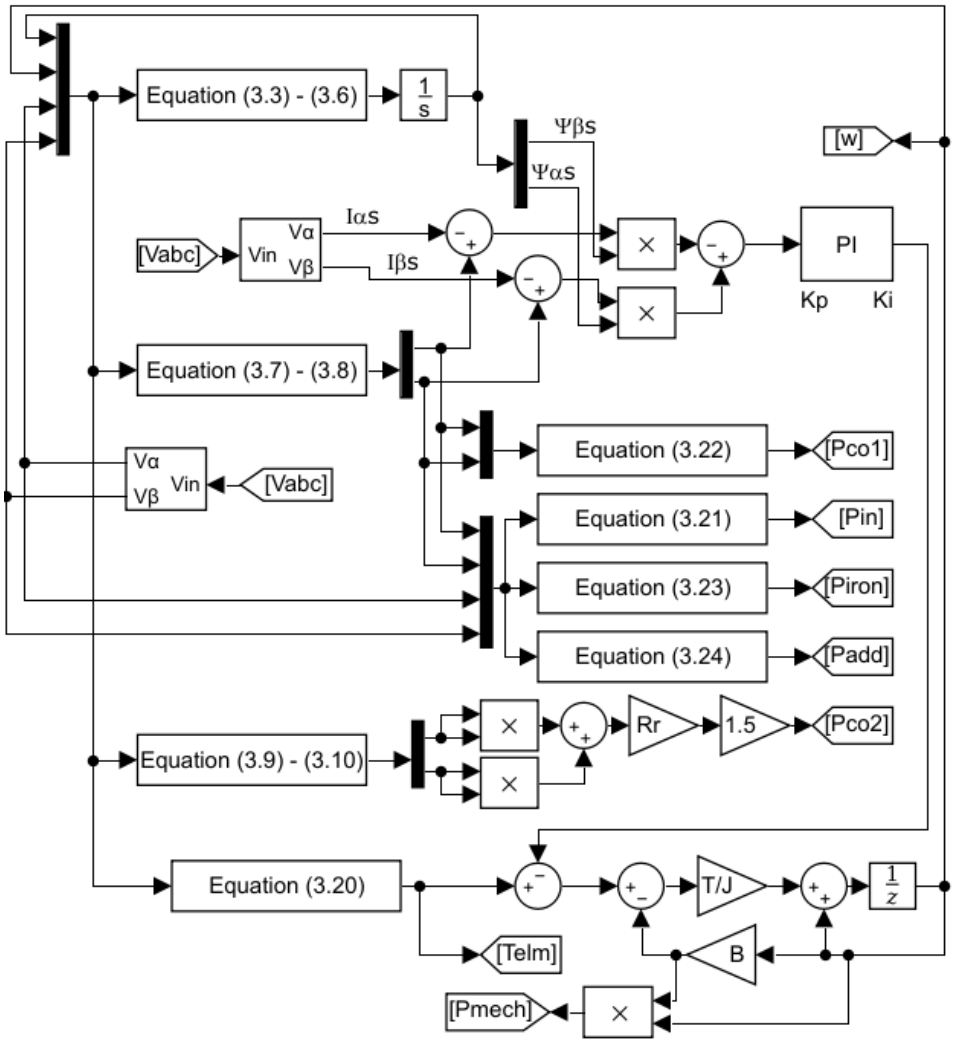

Fig. 4.38 Dynamic mode computation method for online torque estimation

Based on this estimator, the results obtained online during the artificial loading test of both induction machines are presented below. Compared to Fig. 4.35 and Fig. 4.36, where the losses obtained in the simulation are shown (artificial loading Fig. 4.35 and shaft loading Fig. 4.36), Fig. 4.39 presents momentary and mean values of losses obtained online in real-time on cRIO platform during the artificial loading test at rated phase current.

BUPT

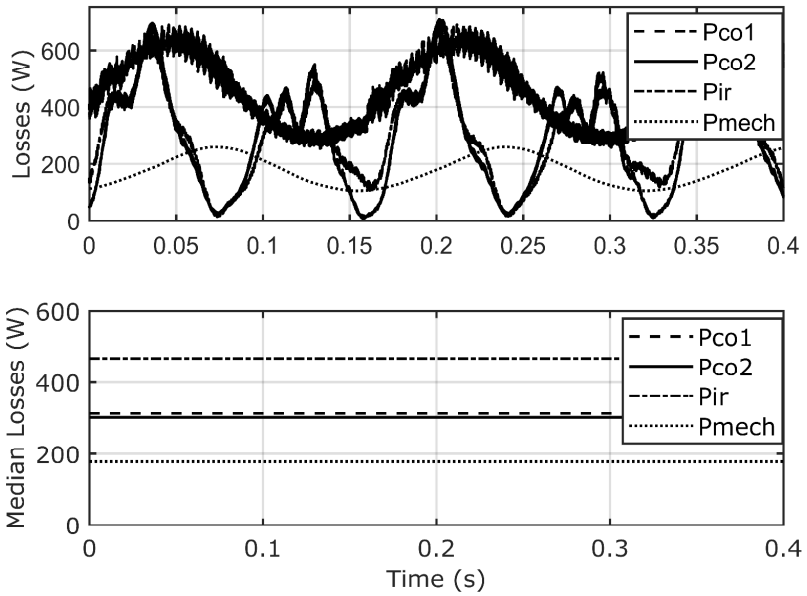

Fig. 4.39 Instantaneous and average values of copper losses, mechanical losses, and iron losses for one IM for artificial loading at rated current at 2500rpm dc speed offset, 6Hz oscillation frequency, and ±500rpm amplitude – online experiments. Total median losses= $1362.3\,(W)$

As can be observed from Fig. 4.35, Fig. 4.36, and Fig. 4.39, the sum of the losses (Pco1, Pco2, Pir, Pmech) online estimated in real-time are included between those obtaine from artificial loading simulation and shaft loading simulation.

It has to be noticed that, compared to online experiments, where the torque estimator runs in real-time on cRIO platform, and the measured voltage represents the 5kHz frequency modulated voltages, in simulations, the IM alpha-beta supply voltages are obtained from an ideal inverter where the output voltages are not modulated.

Based on the dynamic torque estimator model, this leads to a fuzzy iron losses estimation. The iron losses presented in Fig. 4.39 are obtained using alpha-beta 0.5kHz filtered voltages.

In the following figures are presented fairly acceptable comparisons between the losses obtaine in simulation for artificial loading at rated current at 2500rpm dc speed offset, 6Hz oscillation frequency, and ±500rpm amplitude.

The results presented here (without time synchronization) can represent an acceptable validation between the simulation model and the online estimator.

In Fig. 4.40 and Fig. 4.41 are presented the rotor and stator copper losses for online experiments and simulations.

BUPT

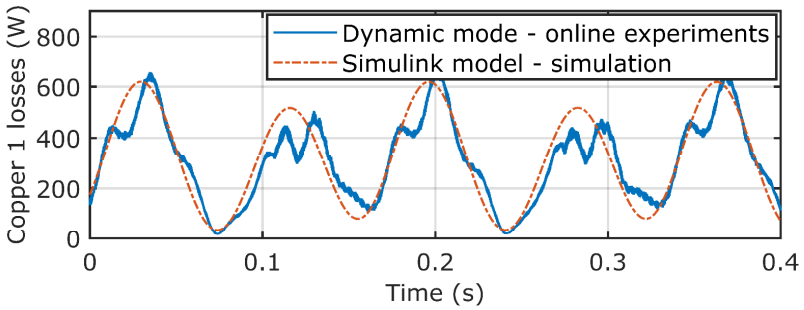

Fig. 4.40 Stator losses for online experiments and simulations for artificial loading at rated current at 2500rpm dc speed offset, 6Hz oscillation frequency, and ±500rpm amplitude

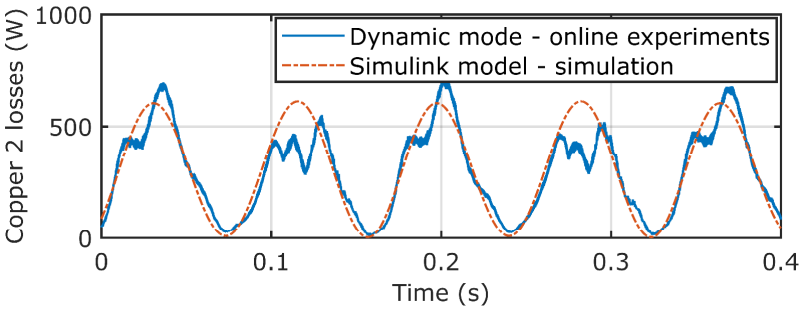

Fig. 4.41 Rotor losses for online experiments and simulations for artificial loading at rated current at 2500rpm dc speed offset, 6Hz oscillation frequency, and ±500rpm amplitude

Both simulated and online experimental results for stator and rotor copper losses follow the same path.

The oscillating frequency is double the speed reference because the machine losses occurred both during the acceleration and deceleration period.

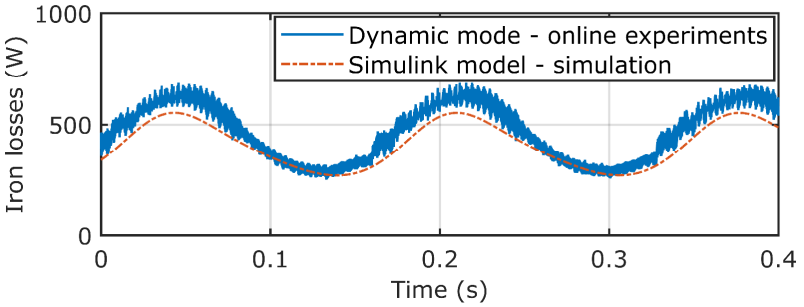

Fig. 4.42 Iron losses for online experiments (with filtered voltages) and simulations for artificial loading at rated current at 2500rpm dc speed offset, 6Hz oscillation frequency, and ±500rpm amplitude

Fig. 4.42 and Fig. 4.43 represent the iron and mechanical losses. The differences between the mechanical losses are caused by the online estimated speed, which varies more than the simulated one.

BUPT

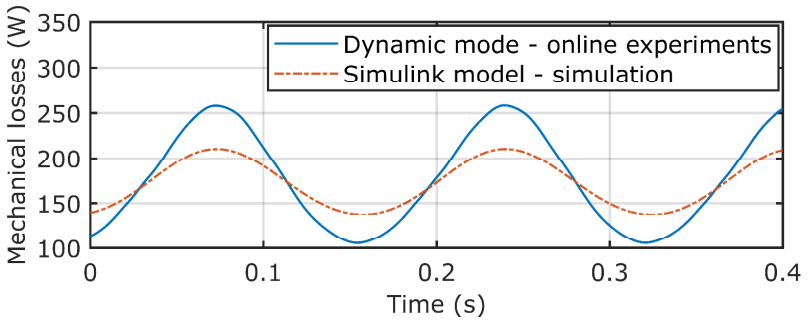

Fig. 4.43 Mechanical losses for online experiments and simulations for artificial loading at rated current at 2500rpm dc speed offset, 6Hz oscillation frequency, and ±500rpm amplitude

Although Chapter 3 has demonstrated that the direct computation method represented a reduced complexity with a good performance solution for IM torque estimation, the modulated VFC's terminal voltages used in this subchapter for torque estimation can not be used by the direct computation method. In this situation, the direct method produces unacceptable results.

Without time synchronization and no filtering in Fig. 3.44 are presented the electromagnetic torque obtained from the dynamic computation method (online experiment), from the Luenberger observer (online experiment), from simulation, and real VFC's estimated torque read from the analog output port.

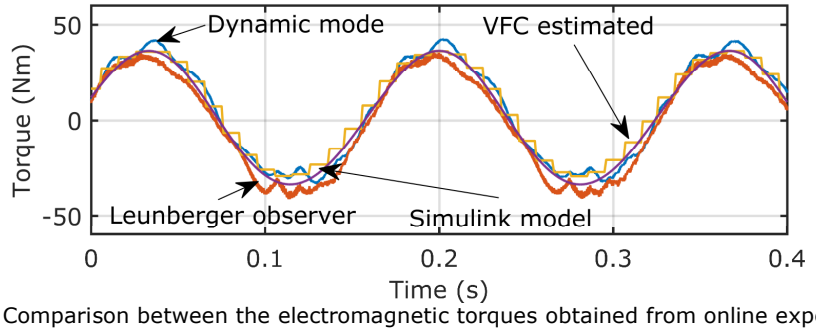

Fig. 4.44 Comparison between the electromagnetic torques obtained from online experimental dynamic mode computation method, online experimental Luenberger observer, simulation and real torque estimated read from VFC's analog output.

4.6. Conclusion

This chapter presents an induction machine artificial loading method in detail. Only industrial/commercial equipment and standardized communication protocols are used for this artificial loading method, where two induction machines without mechanical coupling are tested at rated phase currents. When one IM accelerates, the other one decelerates. The power flows from one IM to another via the common VFCs dc-link.

For ac-source current limitation, different speed references were investigated: 180-degree phase-shifted - where both references were fixed-time shifted, variable phase shift - where the IM in motor mode was delayed from

BUPT

accelerating, and triangle reference - where the IM was forced to change faster the operating regime.

As it was experimentally demonstrated, no circulating current (between the motors via VFCs) does not contain 3k (k=0,1,2,..) harmonics.

More than this, an acceptable Matlab&Simulink simulation is presented, which deals with the artificial loading and shaft loading losses correlation.

Finally, induction machine torque and loss estimation are given for online experiments.

BUPT

5. Active torque pulsation reduction in position-dependent loads

Abstract

For position-dependent loads with pulsating torques, torque pulsation reduction can be achieved in several ways. Passive conventional methods (such as shaft-mounted flywheels) represent a relatively simple method that involves oversizing the shaft/coupling.

In this chapter, an active loading torque pulsation reduction method based on induction machine electromagnetic torque information is presented, both in simulation and experiment. It has to be stated that besides inertia moment, no mechanical parameters (such as coupling backlash or shaft stiffness) are required.

5.1. Introduction

5.1.1. Vibration control and active torque pulsation reduction - overview

The active vibration control (AVC) technique is represented by the use of an external force added into the system, in the opposite manner to the disruptive force (the source of the main vibrations), to reduce partially/totally the unwanted effect of vibrations.

The additionally superimposed force is added to the primary force, leading to vibration minimization. Thus, the effects caused by the loading force are reduced. In many cases, the vibrations are only spread and absorbed by a more elastic part of the system.The need for the AVC technique comes from the need for either safety or comfort. Preponderentely for modern industries, the AVC technique is worldwide spread and used. For example, in recent years, the piezoelectric material (FGPM) [183], [184] and sensors have found an important place for active vibration reduction both in aeronautics/spacecraft [185] and construction [186].

Another modern AVC applicability can be found in robot applications, where vibration-free positioning plays a key role in increased accuracy [187], [188], [189].

As a particularity, in headphones, active noise canceling (ANC), which is - more or less - based on the same principle as AVC, has been adopted by all the major vendors. In this case, active noise canceling (ANC) is pretty similar to AVC because, in this case, the additional force added into the system is replaced by the sound/noise (which should be eliminated) measured outside the headphones and then is reconstructed inside the headphones to eliminate the unwanted distracting background noise [190], [191], [192].

Another active noise cancelation technology is increasingly used nowadays in the automotive industry, where the road noise inside the compartment is reduced by about 5dB [193], [194], [195], [196], [197].

BUPT

In rotary electrical machines, more aspects can be distinguished, depending on the type of torque pulsation source:

- for example, reduced torque ripples (pulsations) caused by the 3rd-order space harmonic in IM can be achieved by voltage regulation (as presented in [198]).
- a different approach for torque pulsation reduction can be found for electrical machines with high anisotropy and permanent magnets (PM). For example, in [199], the authors provide two configurations of flux barriers in PMASynchRM for lower torque pulsation. Another application for torque pulsations minimization in spoke-type PM machines can be achieved, as the author presents in [81], depending on the auxiliary salient poles' position.
- the load type represents another source of torque ripples. The mechanical pulsating/vibrations appear in the system as an effect of the load opperation.

In this last category, more work was carried out in recent years related to reducing the unfavorable/undesired effects of the pulsating loads.

One of the simplest methods for torque pulsation reduction in electromechanical systems with rotating electric machines is represented by the use of passive mechanical methods: flywheels [200]. Based on the configuration, the high inertia of the flywheel is used as a "mechanical filter" for the torque pulsations.

Similarly, with passive vibration reduction methods, centrifugal pendulum vibration absorbers (CPVAs) can also be used, which are designed to reduce only one vibration order torsional fluctuations for rotating shafts. For example, in [201], a centrifugal double pendulum vibration absorber is proposed and analyzed.

Increased performances can be achieved in the case of active online control to minimize the torque pulsations. This method, also called the active torque pulsation reduction method (ATPRM), can be easily implemented in inverter-fed applications where the electrical machine is driven by variable frequency converters (VFC).

For example, in the automotive industry, the internal combustion engine (ICE) torque ripple is reduced with an integrated starter alternator [202], based on an online torque observer and an indirect field-oriented induction machine control

Active torque cancelation for low cylinder count engines using a PMSM and its control strategy is also presented in [203].

Several such methods are presented in the literature, with different control schemes and modulating techniques. In [204], a sensorless FOC control in the inverter-fed electrical machine for large-scale compressors applications is presented. More than that, a rotor flux field oriented control (RFOC) modulation technique used in a proportional-resonant (PR) controller for railway torsional vibration control for inverter-fed electric machines is presented in [205].

In [206], the author presents how the inverter's pulsating torque (caused by the modulation) is propagated to the motor shaft. It is analytically presented that the modulating frequency is more important for the shaft failure than the pulsating torque magnitude.

Another type of loading torque in electromechanical rotary systems is the position-dependent loads (piston-based with crankshaft applications). Compared to the unpredictable and relatively slow in time-varying loads (such as fan, conveyor belts, chopper, rock breaker, etc.), these position-dependent load requires a higher response frequency than standard AVC.

The torque pulsation reduction method presented in this chapter is based on position-dependent loading torques driven by grid-connected induction machines (GCIM).

BUPT

In the case of position-dependent loading torques in which the loads repetitively vary depending on mechanical position, a specific control theory can be applied successfully based on the load's repetitive character. The repetitive control (RC) theory, first introduced by Inoue ([207], [86]), represents a feasible control strategy for active torque pulsation reduction. In recent

With applicability from the last century to the present, repetitive control could be applied in various applications, such as PMSM (torque ripple) and IM (fluctuated loading torque) control ([208], [209]).

5.1.2. Proposed solution

This chapter deals with the torque pulsation reduction methods for position-dependent loads (such as reciprocating compressors) driven by grid-connected induction machines. Compared to the literature presented solutions, the here-presented method is based on an auxiliary motor driven by a VFC, mounted on the same shaft as the load (Fig. 5.1). Moreover, the here-presented torque pulsation reduction method implies a relatively simple control technique compared to the repetitive control (as given in references). As the main difference, the solution is presented as a mechanical parameters-free solution, where only the moment of inertia is required for active torque pulsation damping.

The grid-connected induction machine operation is online and monitored by a high-speed data acquisition and process unit (National Instruments cRIO chassis). The electromagnetic torque and speed are calculated based on three voltages and three currents. **It has to be specified that for real on-site applications, the loading torque is an unknown variable.**

Based on the estimated torque and system position, the cRIO platform calculates and prescribes the torque reference used to the auxiliary induction machine's variable frequency converter to actively reduce the torque pulsations.

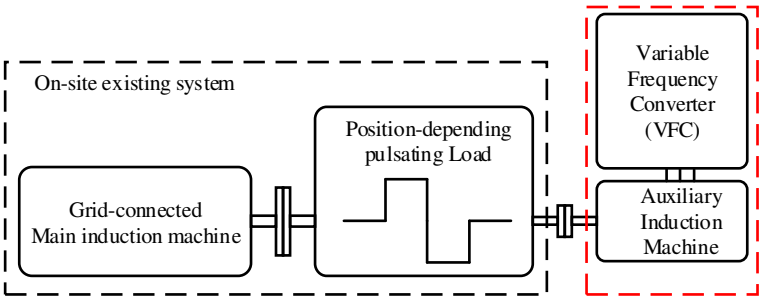

Fig. 5.1 Basic schematic diagram of the proposed operating principle

5.2. Setup configuration

5.2.1. General schematic diagram

The experimental setup (Fig. 5.2) consists of 3 induction machines connected on the same shaft. The loading machine - which produces the position-dependent variable loading torque - is a four-pole pair, 30kW induction machine driven by a 25kVA power frequency converter. A 3 pole pair, 11kW, grid-connected induction machine drives the load.

BUPT

On the same shaft (on the load machine side) a new 2 pole pair, 15kW auxiliary induction machine (compensating machine) driven by a 16kVA variable frequency converter, is added.

One quadrature incremental encoder measures the system speed based. Both variable frequency converters (for the loading and the auxiliary machine) use the encoder speed as the more-accurate feedback speed. It has to be stated that all the variable frequency converters, equipment, and communications, respect industrial standards (no supplementary changes have been made to the inverters' control strategies).

Further, in this chapter, the results obtained both for elastic and rigid couplings are presented.

The loading machine emulates crankshaft-based equipment with position-dependent loading torque.

The system speed is given by the grid-connected induction machine (synchronous speed 1000rpm). Both the loading machine (the emulated compressor) and the auxiliary machine are torque controlled based on the direct torque control (DTC) method.

While the three-pole pair grid-connected induction machine gives the system speed, the sinusoidal torque reference has (theoretically) 16.6Hz frequency.

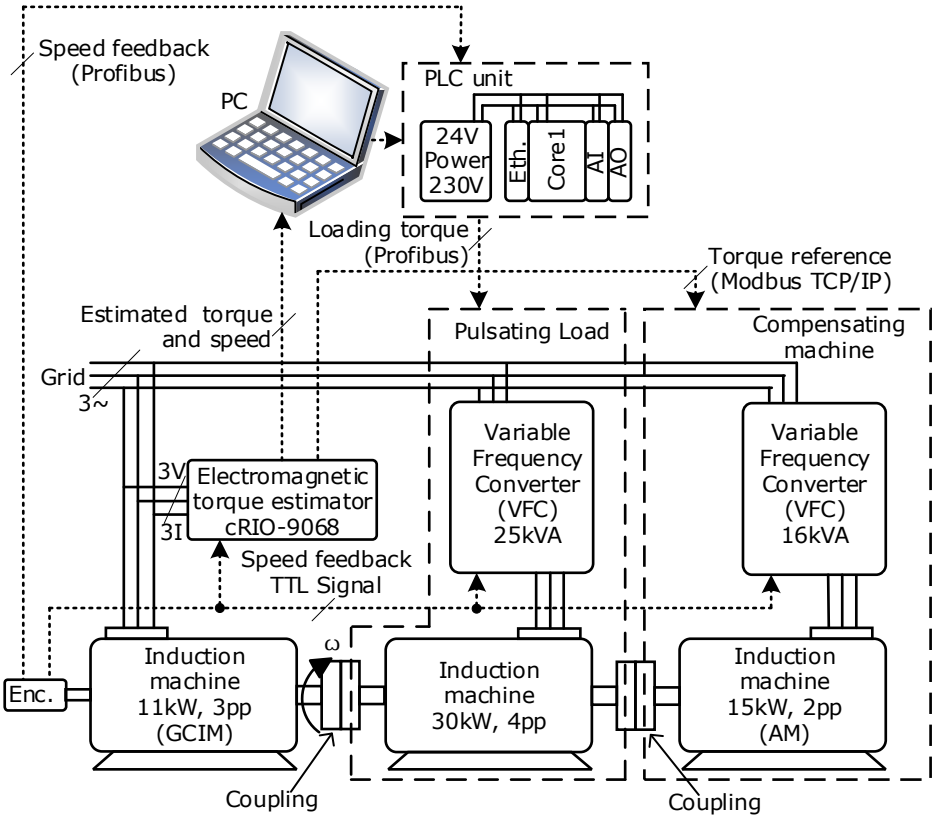

Fig. 5.2 Setup schematic diagram

BUPT

The torque reference is given digitally via industrial protocols: the emulated load machine's converter receives the torque reference via Profibus. In contrast, the auxiliary machine receives the torque reference via Modbus TCP/IP.

A standard industrial programmable controller (PLC), online calculates the position-dependent torque reference (based on (5.1)) for the emulated loading machine. The PLC unit also reads the speed via Profibus.

For online GCIM speed and torque estimation and torque reference generation, a cRIO-9068 chassis with two analog input modules (NI9215) and one 5VTTL signal module (NI9401) is used. The cRIO platform reads three voltages, three currents, and the system speed.

The effects of applying the here presented active torque pulsation reduction method are also investigated from the vibration point of view. 5 accelerometer sensors are used to monitor the vibration spectrum.

For this demonstration, the loading torque profile (the reference given to the Pulsating Load) consists of a sinusoidal component overlapped with a dc component.

The equation (5.1) shows how the torque reference for emulating load is calculated inside the PLC.

$$T_{EL}^{*} = dc + A \cdot sin(\omega t) \tag{5.1}$$

where: T_{EL}^{*} represents the torque reference given to the emulated loading machine, dc and A represent the dc and amplitude component of the torque reference ω represents the pulsation which depends on the system position (read from the encoder via Profibus) and t represents the time. In Fig. 5.3 the testing bench is presented, where all the equipment can be seen.

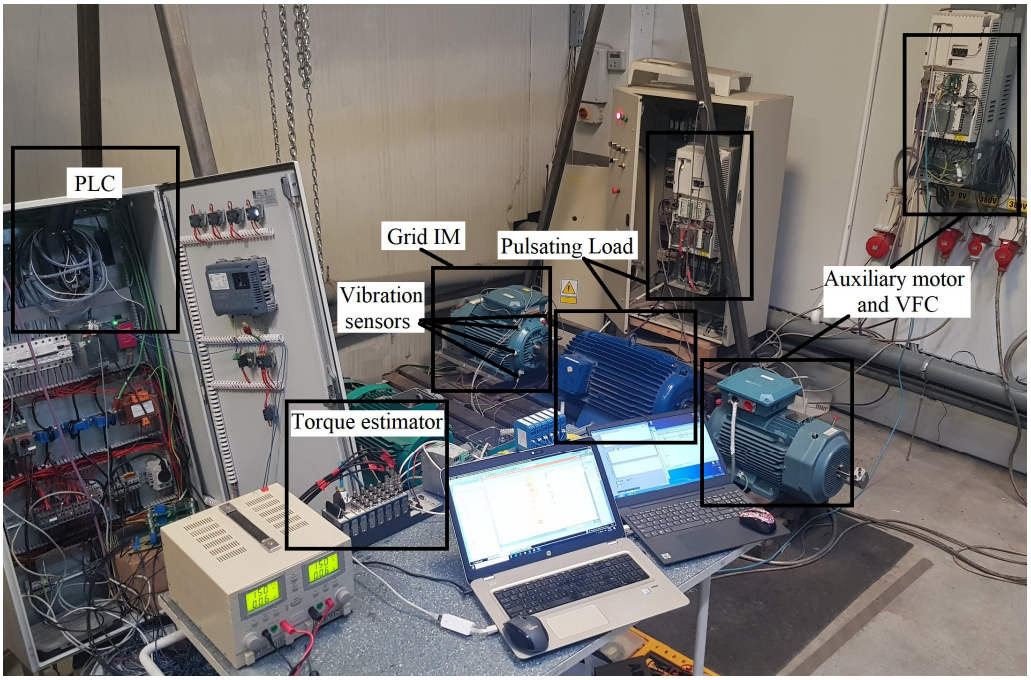

Fig. 5.3 Testing banch

BUPT

5.3. System and control method simulation

All the simulations were performed in the Matlab&Simulink programming environment. The general schematic diagram also simulates the variable frequency converter used for the auxiliary induction machine (its equation is described below). Similar to the results presented in Chapter 3, the simulations are performed in this chapter using real voltages (with the real harmonic components and direct/inverse components). Fig. 4.4 shows the differences between the ideal and real voltages.

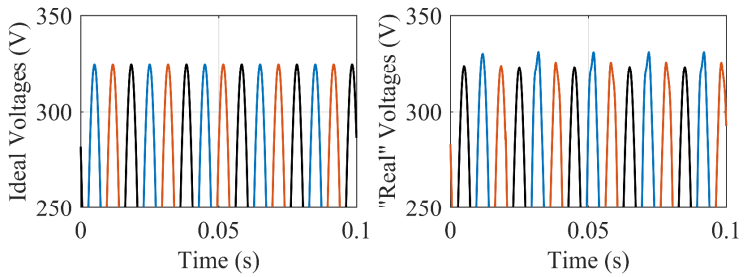

Fig. 5.4 Differences between ideal and "real" voltages – which are further used

5.3.1. General schematic diagram – proposed open-loop method - simulations

The open-loop control method can also be considered to be a principal validation simulation. In Fig. 5.5, the Simulink diagram can be observed. The main elements in this scheme are further used. The grid-connected and auxiliary induction machines are based on the same induction machine equations described in Chapter 2.

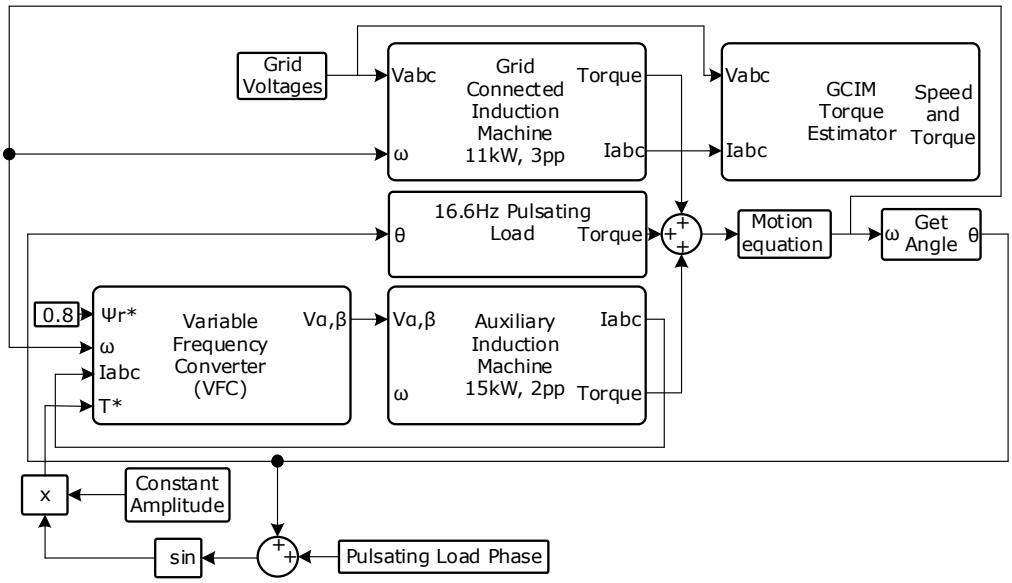

Fig. 5.5 Open-loop control method for torque pulsation reduction

BUPT

More than that, the GCIM performances have also been extensively presented in Chapter 3. The Auxiliary IM's variable frequency converter is described in detail in equations (5.2) to (5.10)**.** The system speed is used for the field weakening implementation. The alpha and beta voltages that supply the IM are obtained as the difference between the estimated and measured currents.

$$\left.\begin{aligned} I_\alpha &= \frac{(2\cdot I_{1m} - I_{2m} - I_{3m})}{3} \\ I_\beta &= \frac{\sqrt{3}}{3}\cdot(I_{2m} - I_{3m}) \end{aligned}\right\} \tag{5.2}$$

$$\left.\begin{aligned} I_d &= I_\alpha \cdot \cos\theta + I_\beta \cdot \sin\theta \\ I_q &= I_\beta \cdot \cos\theta + I_\alpha \cdot \sin\theta \end{aligned}\right\} \tag{5.3}$$

$$\theta = \int \left(\omega_2^* + \omega_m \cdot pp\right) dt \tag{5.4}$$

$$\omega_2^* = \frac{2\cdot L_r \cdot T^*}{3\cdot pp\cdot T_r \cdot \psi_{fw}^2} \tag{5.5}$$

$$\psi_{fw}^2 = \psi_r^* \cdot \frac{\omega_b}{min(\omega_m, \omega_b)} \tag{5.6}$$

$$\left.\begin{aligned} I_d^* &= H_{(s)}\left(\frac{\psi_{fw}}{L_m}\right) \\ I_q^* &= \frac{2\cdot L_r \cdot T^*}{3\cdot pp\cdot L_m \cdot \psi_{fw}} \end{aligned}\right\} \tag{5.7}$$

$$H_{(s)} = \begin{pmatrix} \frac{Tr\cdot s}{0.04s} & \frac{1}{1} \end{pmatrix} \tag{5.8}$$

$$\left.\begin{aligned} \hat{U}_d^* &= PI_{U_d}\left(I_d^* - I_d\right) \\ \hat{U}_q^* &= PI_{U_q}\left(I_q^* - I_q\right) \end{aligned}\right\} \tag{5.9}$$

$$\left.\begin{aligned} \hat{U}_\alpha^* &= \hat{U}_d^* \cdot \cos\theta - \hat{U}_q^* \cdot \sin\theta \\ \hat{U}_\beta^* &= \hat{U}_d^* \cdot \sin\theta + \hat{U}_q^* \cdot \cos\theta \end{aligned}\right\} \tag{5.10}$$

Where: $I_{1m}, I_{2m}, I_{3m}, \omega_m$ represent the GCIM read phase currents and system measured speed, I_α, I_β represent the α, β components of the measured phase currents, I_d, I_q represent the d, q components of the measured phase currents, ω_2^*, pp represent the rotor reference speed and the number of the pole pair,

BUPT

ψ_{fw}, ψ_r^* represent the rotor reference flux after the flux weakening and the rotor maximum flux used for flux weakening, L_r, T^*, T_r, ω_b represent the rotor inductances, the reference prescribed torque, the rotor time constant and the base speed used for flux weakening, I_d^*, I_q^* represents the reference d, q components of the currents used for voltages references, $H_{(s)}$ represents a transfer function, $\hat{U}_d^*, \hat{U}_q^*$ represent the d, q components of the estimated voltage references, $\hat{U}_\alpha^*, \hat{U}_\beta^*$ represent the α, β components of the estimated voltage references. The auxiliary IM parameters which were used in simulations are given in Table 5.1.

Table 5.1 Auxiliary induction machine parameters used in simulations

No.	15kW, 2pp, Induction machine	
1	Rated Voltage (V)	400
2	Rated Current (A)	28.7
3	Rs (Ω)	0.22
4	Rr (Ω)	0.18
5	Lm (mH)	70.028
6	Ls (mH)	1.623
7	Lr (mH)	3.979
8	J (kgm^2)	0.099
9	Tr (s)	0.41115

The mechanical angle is given from the "Get Angle" block, as presented in Fig. 5.6 using a resettable integrator.

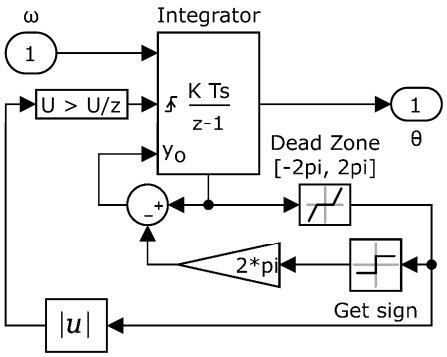

Fig. 5.6 "Get angle" block from Fig. 5.5

The motion equation uses the total system inertia for system speed calculation.

$$J_{total} \cdot \frac{d\omega}{dt} = T_{diff.} + B \tag{5.11}$$

BUPT

where: J_{total} represents the total inertia moment of the system (without couplings), $d\omega / dt$ represents the time derivative component of the speed, T_{diff}, B represent the resulting torque on the system, and the total friction coefficient.

For system calibration, in Fig. 5.7 are presented the load torque (which is a 0 to GCIM rated power step), the GCIM electromagnetic torque, the estimated GCIM electromagnetic torque, the system speed (given by the motion equation), and the estimated speed.

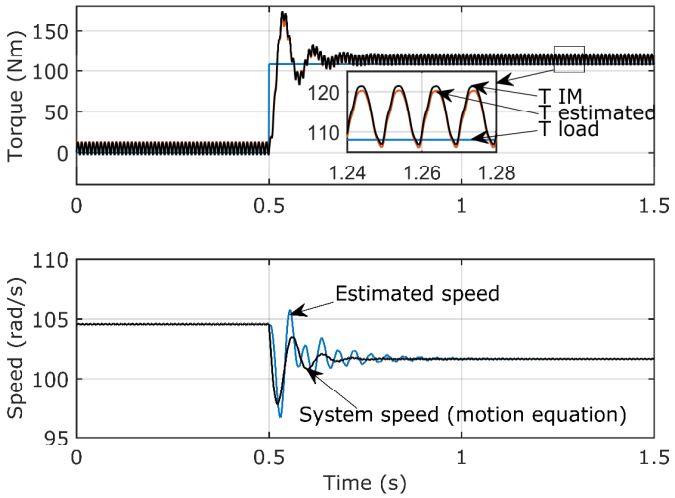

Fig. 5.7 Estimated and GCIM torque and system speed and estimated speed for a 0 to rated load step transition

In Fig. 5.8 the results for different values of the pulsating loading torque are investigated.

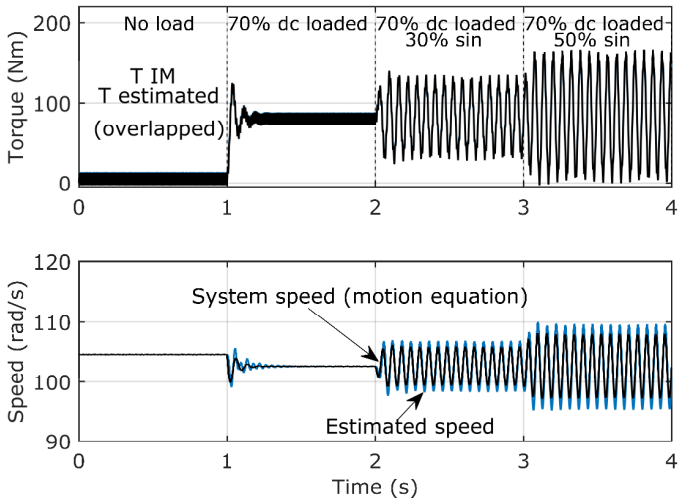

Fig. 5.8 Estimated and real GCIM torque and system speed and estimated speed for dc and sinusoidal loading

BUPT

Fig. 5.8 is divided in 4 sections: 0-1s, the GCIM is not loaded, 1-2s the GCIM is 70% of rated torque loaded (GCIM rated torque = 108Nm), 2-3s a 30% sinusoidal reference is overlapped over the dc component, while in the 3-4s sector, the sinusoidal reference represents 50% of GCIM rated torque.

The simulations use real voltages. The torque pulsations that appear are due to the voltage characteristics (see Fig. 5.4).

The results from the active torque pulsation reduction method (ATPRM) from the open-loop control system are presented in Fig. 5.9. Here, the experiment is divided into five sectors. Between 2s and 5s, the loading torque follows a 70%dc + 30% sinusoidal component (of GCIM-rated power).

Until the ATPRM is applied, the auxiliary machine is only mechanically connected to the system without torque prescription (only inertia moment influences).

From 3s to 5s, the open-loop ATRPM is applied. In sector 3s-4s, the auxiliary machine produces a 180-degree phase-shifted (considering GCIM torque) sinusoidal torque to the respected angle. In sector 3s-4s, the auxiliary machine compensates for 14% of GCIM-rated torque, while in sector 4s-5s, the auxiliary machine compensates for 17% of GCIM-rated torque.

Acceptable results are obtained regarding torque pulsation minimization in the grid-connected induction machine. However, a certain level of torque pulsations appeared in the auxiliary machine.

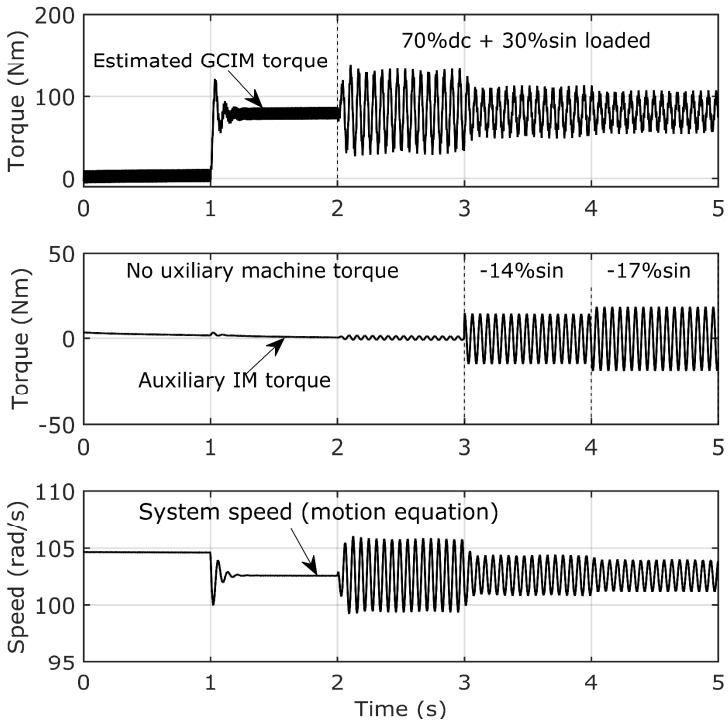

Fig. 5.9 Estimated GCIM torque, auxiliary IM torque, and system speed for open-loop control method with no aux. compensation, with 14% (GCIM-rated power) compensation and 17% (GCIM-rated power) compensation

BUPT

As long as the loading machine is characterized by a position-dependent torque, the auxiliary machine torque phase angle is considered to be constant, without significant variations over time.

It can be observed that with a 30% of GCIM-rated torque sinusoidal component overlapped with a 70% dc component, the speed oscillates with almost 8% of its rated value (Fig. 5.9).

Besides the maximum amplitude that could be compensated, a key role for auxiliary machine sizing is represented by the individual (GCIM and AM) and total power absorbed from the grid.

Fig. 5.10, Fig. 5.11, and Fig. 5.12 demonstrate that the maximum compensated value of the GCIM torque pulsation amplitude could be established considering the total absorbed grid power.

For example, in Fig. 5.10 the minimum grid absorbed power appears when only 34.4% of the pulsating loading torque amplitude is compensated. In this case, a higher level of torque pulsation compensation would be possible, considering a higher energy consumption from the grid.

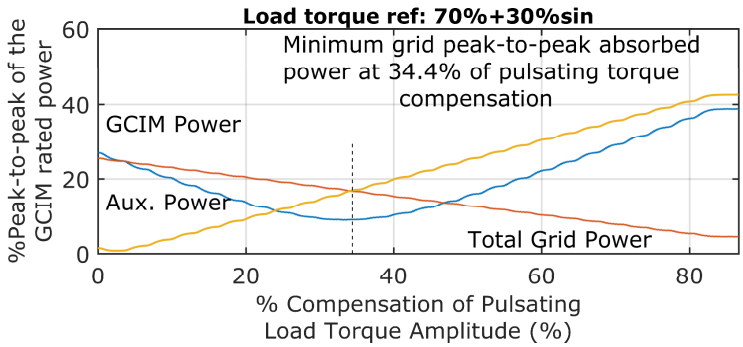

Fig. 5.10 GCIM peak-to-peak power, AM peak-to-peak power, and total peak-to-peak power absorbed from grid different compensation levels for loading torque reference: 70%+30% sin of GCIM rated power.

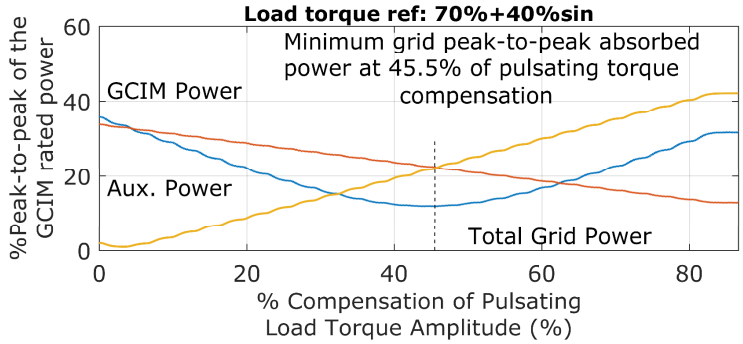

Fig. 5.11 GCIM peak-to-peak power, AM peak-to-peak power, and total peak-to-peak power absorbed from grid different compensation levels for loading torque reference: 70%+40% sin of GCIM rated power.

BUPT

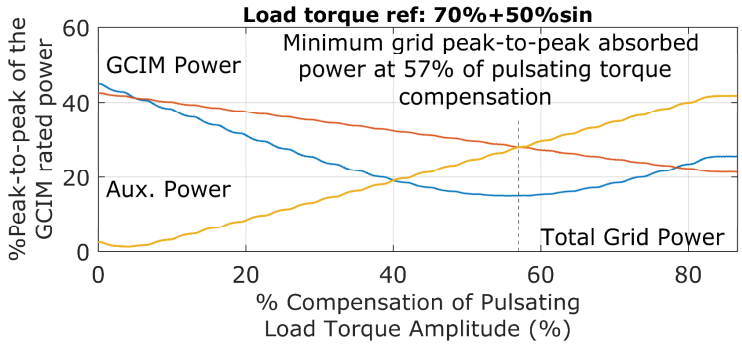

Fig. 5.12 GCIM peak-to-peak power, AM peak-to-peak power, and total peak-to-peak power absorbed from grid different compensation levels for loading torque reference: 70%+50% sin of GCIM rated power.

Fig. 5.13 to Fig. 5.16 present how the GCIM peak-to-peak power amplitude changed depending on the compensating torque phase shift. More than that, four compensating levels are studied (7.5%, 15%, 22.5%, and 30% of GCIM-rated power) considering that the loading torque reference was: 70%+30%sin (of GCIM-rated power).

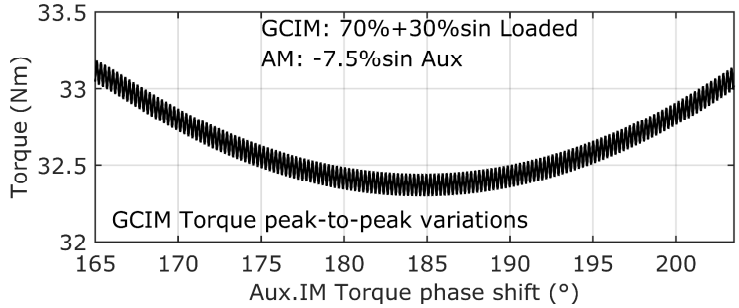

Fig. 5.13 Grid-connected induction machine's peak-to-peak torque variation for torque ref:70%+30%sin (of rated power) with 7.5% (of rated power) compensation for different compensation phase-shift.

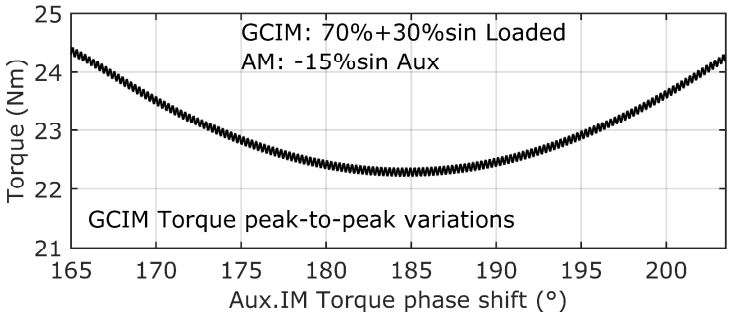

Fig. 5.14 Grid-connected induction machine's peak-to-peak torque variation for torque ref:70%+30%sin (of rated power) with 15% (of rated power) compensation for different compensation phase-shift.

BUPT

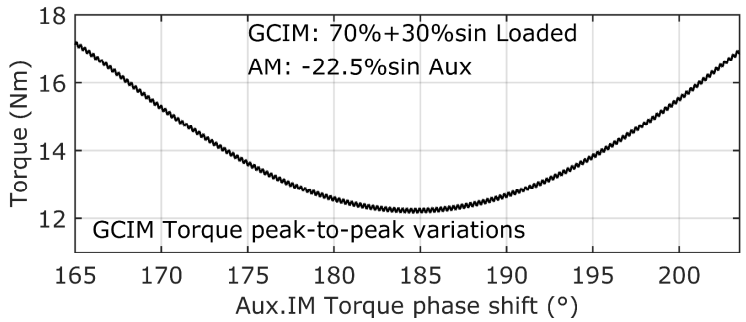

Fig. 5.15 Grid-connected induction machine's peak-to-peak torque variation for torque ref:70%+30%sin (of rated power) with 22.5% (of rated power) compensation for different compensation phase-shift.

The increased auxiliary compensating torque requires more rigorous knowledge of the GCIM torque angle.

However, at compensation torque levels of up to 50% of the pulsating loading torque (Fig. 5.13, Fig. 5.14), a 10degree AM's toque phase-angle deviation around the correct load torque phase angle (where the compensation effect is maximum) leads to a 3% increase of the load torque amplitude of the value obtained at the correct compensation angle.

This result proves that for a closed-loop phase angle detection, a deviation of up to 5 degrees of the compensation angle could be considered to be within acceptable limits.

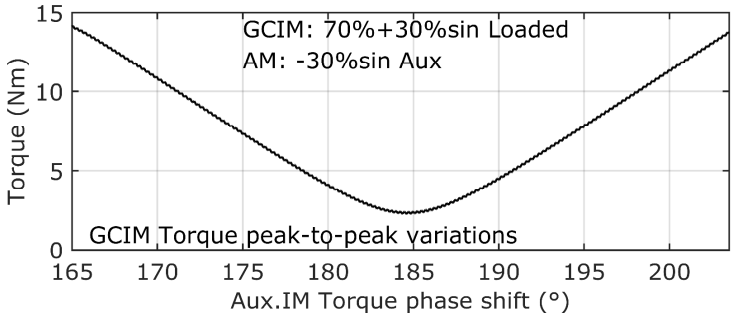

Fig. 5.16 Grid-connected induction machine's peak-to-peak torque variation for torque ref:70%+30%sin (of rated power) with 30% (of rated power) compensation for different compensation phase-shift.

5.3.2. Closed-loop control method 1 - simulations

The closed-loop active torque pulsation reduction method 1 comes with the advantage of an automatic GCIM pulsation amplitude reduction because the auxiliary machine's variable frequency converter torque reference is given from PI output.

Compared with the open-loop method – where the auxiliary machine's VFC torque reference amplitude was manually prescribed – the closed-loop method 1 uses a PI regulator to minimize the GCIM torque pulsation amplitude.

Several high-pass and low-pass filters are used to extract the GCIM regulator feedback value.

BUPT

Fig. 5.17 shows the before-presented open-loop method (dashed part) with the additional added elements for the automatic closed-loop torque pulsation reduction method.

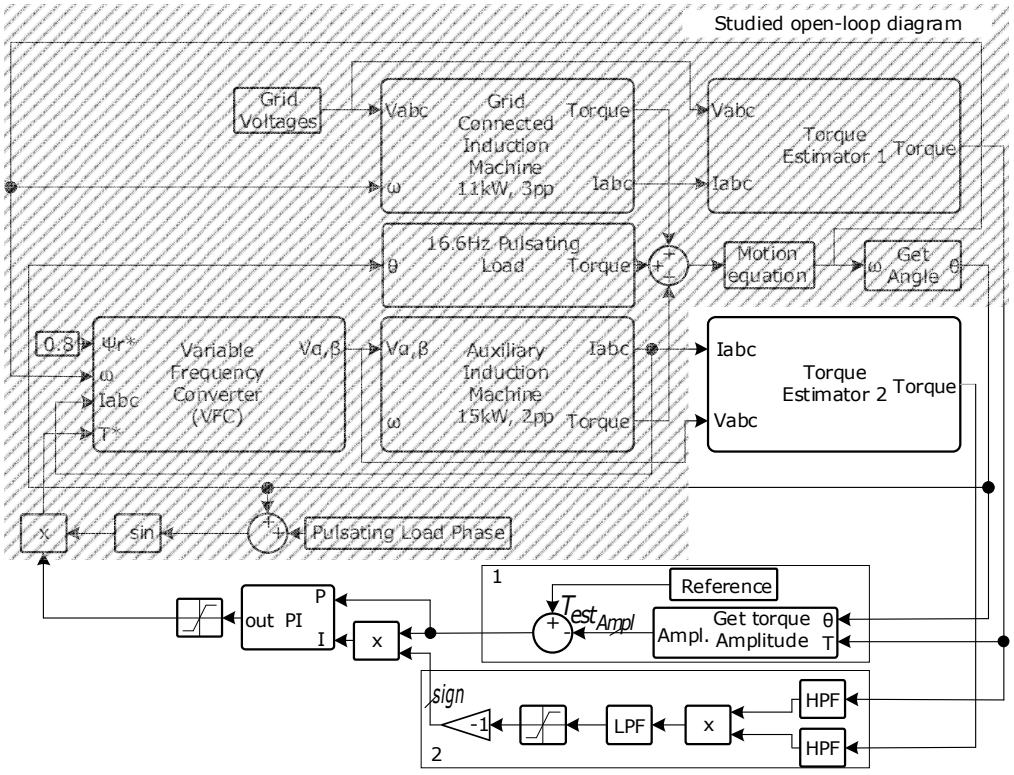

Fig. 5.17 Closed-loop control diagram – simulation

As well as the open-loop method, also the closed-loop method uses a fixed phase-shift angle.

The "Reference" block prescribes the desired GCIM torque pulsation amplitude after the auxiliary machine compensation. In other words, the auxiliary machine reduces the GCIM torque pulsations amplitude to the "References" value.

One main difference is an additional torque estimator used for auxiliary machine torque estimation. The auxiliary machine (AM) torque is needed for the phase-angle detection between the GCIM and AM torques.

The "Get Torque Amplitude" block is presented in Fig. 5.18. The GCIM torque pulsation amplitude is obtained using this block. The equation (5.12) represents the GCIM torque pulsation amplitude obtained from. Fig. 5.18.

The low-pass filters are used to reduce the influences caused by the torque pulsations given by the three-phase voltage system, highlighted in Fig. 5.7.

The second block (noted with "2") from Fig. 5.17 is used to use both the GCIM and AM torque to ensure a safe operation of the ATPDM 1. Therefore, block number 2 prevents the auxiliary machine-produced torque is always used to reduce GCIM torque pulsation amplitude, thus avoiding a phased desynchronization.

BUPT

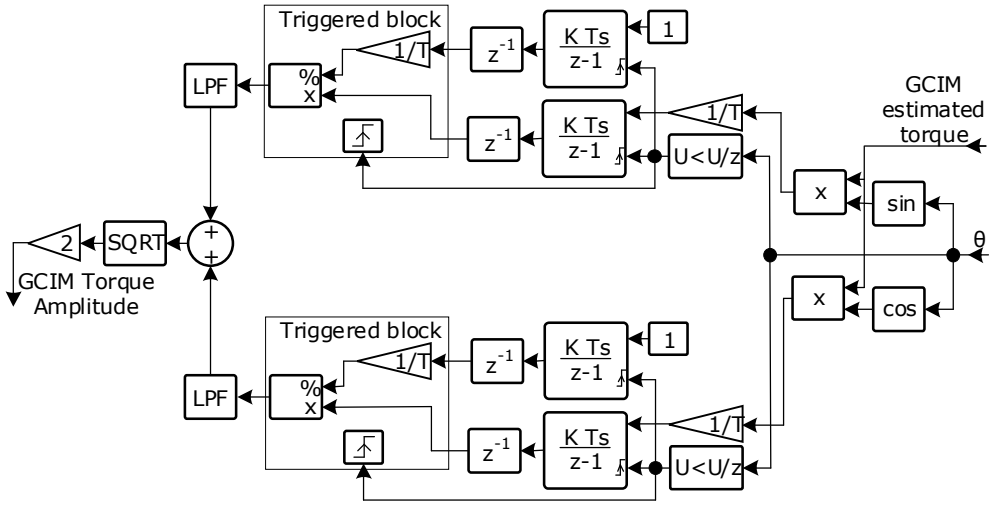

Fig. 5.18 Details for the "Get Torque Amplitude" block from Fig. 5.17

$$\hat{T}_{Ampl} = 2 \cdot \sqrt{\left(LPF\left(\underset{T}{sin\hat{}}\right)\right)^2 + \left(LPF\left(\underset{T}{cos\hat{}}\right)\right)^2} \tag{5.12}$$

$$\left.\begin{aligned} \underset{T}{sin\hat{}} &= Mean\left(\hat{T}_{GCIM}\right) \cdot \int\left(\hat{T} \cdot \sin\theta\right) dt \\ \underset{T}{cos\hat{}} &= Mean\left(\hat{T}_{GCIM}\right) \cdot \int\left(\hat{T} \cdot \cos\theta\right) dt \end{aligned}\right\} \tag{5.13}$$

The high-pass filter eliminates the dc component of the investigated torques.

In contrast, the low-pass filter is used for "sign" detection to separate the torque pulsations produced by the load (16.6 Hz in this case) from those produced by the voltage (higher frequency). Equation (5.14) presents how block two operates.

$$sign = -\left(LPF\left(HPF\left(\hat{T}_{GCIM}\right) \cdot HPF\left(\hat{T}_{Aux}\right)\right)\right) \tag{5.14}$$

The trigonometric interpretation of the above-presented operation of block two from Fig. 5.17 is presented in the equation (5.15). While both torques (the GCIM torque and the AM torque) are in phase, the result will be positive, but on the other hand, when the torques are 180degre phase-shifted, the result turns negative.

$$\left.\begin{aligned} \sin(a) \cdot \sin(b) &= \frac{1}{2} \cdot \left(\cos(a-b) - \cos(a+b)\right) \\ \sin(a) \cdot \left(-\sin(b)\right) &= -\frac{1}{2} \cdot \left(\cos(a-b) - \cos(a+b)\right) \end{aligned}\right\} \tag{5.15}$$

BUPT

A sign correction is performed as long as the auxiliary machine torque has to be in the opposite manner that the GCIM torque (-1).

In Fig. 5.19, the results obtained from closed-loop ATPRM 1 are presented. Similarly, as in the open-loop method, the load has a 70%dc and 30%sinusoidal character.

Also here, the results are presented on different sectors: until 3 seconds, the AM has a 0 torque reference. From 3-5 seconds, the AM automatically decreases the GCIM torque amplitude by 14% (of the GCIM-rated power). From 5-7 seconds, the AM torque reference was increased to 17% amplitude.

Considering the fact that the position-dependent load follows a repetitive path, the PI regulator has a relatively big time constant.

Acceptable oscillations appear during the AM torque reference transition and during the auxiliary machine's full stop (sector 7-9 seconds).

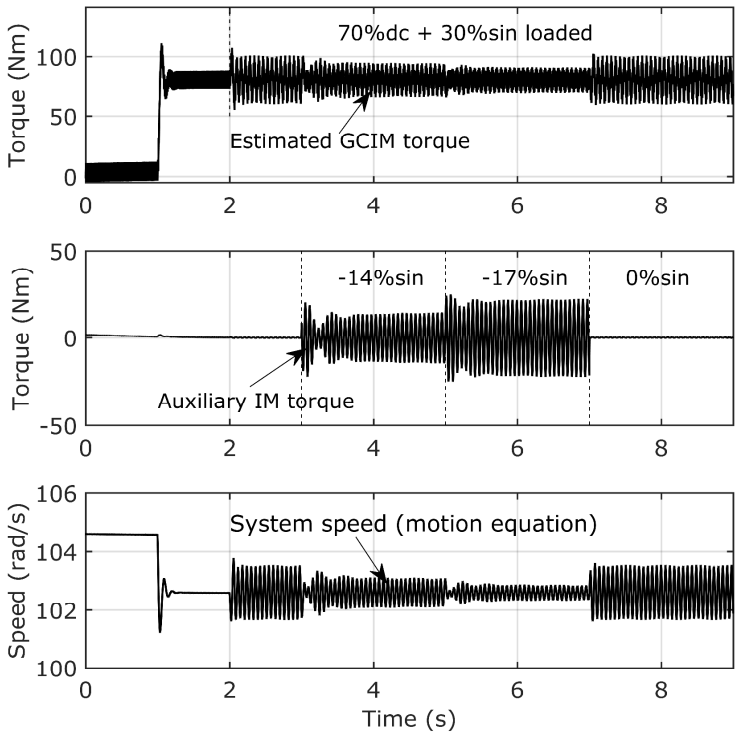

Fig. 5.19 Closed-loop active torque pulsation damping -simulations

In Fig. 5.20, the "Get Amplitude Block" operation is presented for the previously explained test (Fig. 5.19).

For this control method, the correctness of the estimated torque amplitude is a key factor for the torque pulsation reduction method performance.

This GCIM estimated torque amplitude is used as the feedback of the regulation system regarding the torque reference command for the auxiliary VFC. The compensation loop acts only after the start-up period (after 4 seconds in Fig. 5.20).

BUPT

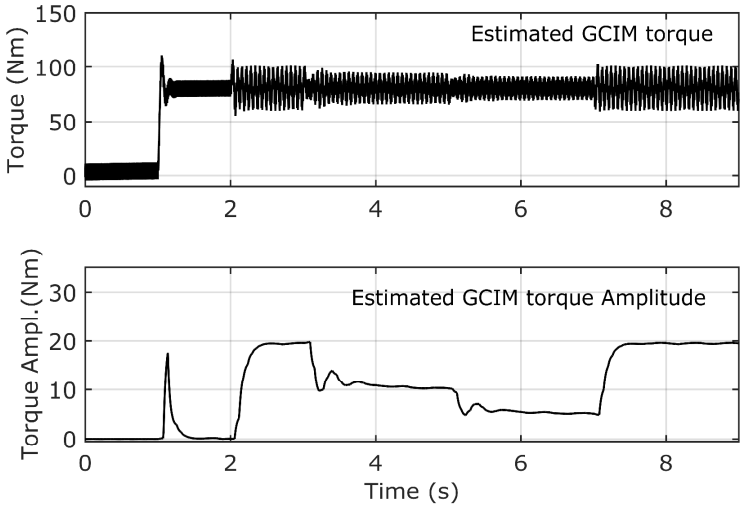

Fig. 5.20 GCIM estimated torque and estimated torque amplitude for the operation described in Fig. 5.19

5.3.3. Closed-loop control method 2 – simulations

Two electromagnetic torques (for GCIM and AM) are required for the closed-loop method 1 to actively reduce the loading torque pulsation. This leads to high complexity of the method.

Even so, the closed-loop method 1 produced acceptable results even with real "simulated" voltages. However, the auxiliary machine's reference prescribed angle was considered known, determined from other electromechanical tests (not presented in this paper).

The here-presented closed-loop method proposes a two-step method for online system inertia and load torque (amplitude and phase) estimation. Moreover, the found loading torque, as a complex number, is then used as a torque reference for the auxiliary machine's VFC. All the simulation results are obtained with the simulation diagram from Fig. 5.5. **All the results (phasors) are given from simulation tests that used "real" simulated voltages.**

5.3.3.1. Moment of inertia and loading torque detection procedure

In the following closed-loop method, both steps are described and explained:

- Step 1:

In order to determine the system's moment of inertia and the loading torque (as a complex number), first, the GCIM is loaded by the loading machine with $\bar{T}_{load}$. To determine the system's total moment of inertia (J), the auxiliary machine should be mechanically connected to the system (with 0 torque reference and magnetized by the inverter). Based on the previous assumption, equation a) from (5.16) can be written. The $\bar{T}_{obs1}$ and $\bar{\Omega}_1$ represent the GCIM estimated electromagnetic torque and measured speed obtained from this first test. The

BUPT

torque resulting from the inertia moment speed variation depends only on the difference between the loading and GCIM torques.

After the first test, the GCIM's amplitude and phase are found by means of the torque estimator. The occurred differences between the real and estimated torque are part of the method's total error.

In Fig. 5.21, the phasor diagram of the first step is given in terms of torque and speed. The small differences that appear between the reference angle and the real angle are due to system errors (such that the GCIM estimated torque and the GCIM real torque are phase-shifted). The loading torque Tload appears at 179.2^{o}. The estimated GCIM torque Tobs1 appears behind the loading torque. In step 2, the auxiliary machine reference torque (Taux (reference)) is given as a 180^{o} phase-shifted Tobs1 torque ($154.5^{o} - 180^{o}$). In this case, the resulting torque Trez1 provided by the $J\frac{d\Omega_1}{dt}$ has large values.

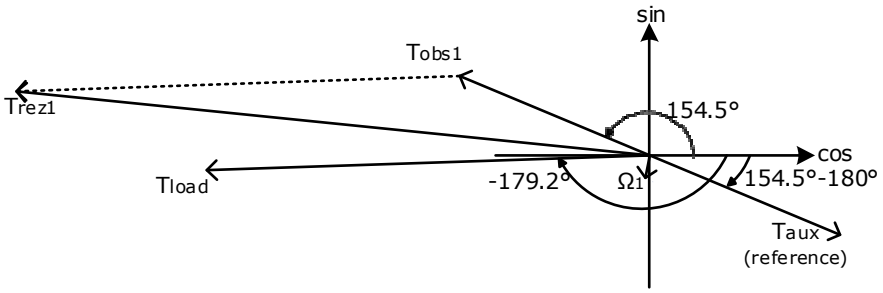

Fig. 5.21 The phasor diagram of the Step 1 test (only loading torque and GCIM torque)

- Step 2:

Step 2 consists of the same loading torque as in the first step, but the torque reference given to the auxiliary machine's VFC consists of the estimated torque amplitude and angle (180 deg phase shifted) found in Step 1. Equation b) from (5.16) explains that for this test (Step 2), the torque resulting from the inertia moment speed variation is given by the interaction between the loading torque $\bar{T}_{load}$, GCIM torque (found by the torque observer in this test $\bar{T}_{obs2}$), and auxiliary machine torque ($\bar{T}_{aux}$ which in this case is none other than $-\bar{T}_{obs1}$. The equation (5.17) explains the mathematical relation between GCIM estimated torque obtained in step 1($\bar{T}_{obs1}$) and the auxiliary machine torque reference used in Step 2.

In Fig. 5.22, the phasor diagram of the step 2 test is given, where the load torque, the GCIM torque as well as the AM torque interact.

In Step 2, the resulting system torque (T_{rez2}) is different than the resulting system torque obtained from Step 1 (T_{rez1}), because of the auxiliary machine influence.

BUPT

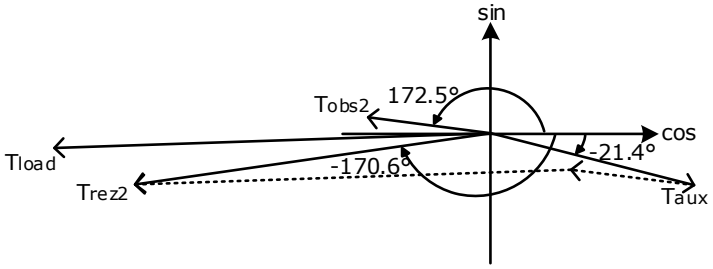

Fig. 5.22 The phasor diagram of the Step 2 test (the loading torque, the GCIM torque, and the AM torque)

It has to be stated that the auxiliary machine torque (Taux) appears at -21.4^{o} (4.1^{o} phase-shifted than the reference – mainly caused by the VFC opperation, but not only). In this case, the system-resulting torque Trez2 (given by the phasor sum of the Tload, Tobs2, and Taux) is notably smaller than the system-resulting torque Trez1 without the AM compensation. The system equations are described in (5.16), where both tests are presented, together with the necessary condition used in Step 2 (5.17):

$$\begin{aligned} &a).\ \bar{T}_{load}+\bar{T}_{obs1}=J\cdot\frac{d\,\bar{\Omega}_1}{dt} \\ &b).\ \bar{T}_{load}+\bar{T}_{obs2}+\bar{T}_{Aux}=J\cdot\frac{d\,\bar{\Omega}_2}{dt} \end{aligned} \tag{5.16}$$

$$\begin{cases} \bar{T}_{aux}=-\bar{T}_{obs1} \\ \bar{T}_{aux_{\sphericalangle}}=\bar{T}_{obs1_{\sphericalangle}}-180^{o} \\ \bar{T}_{aux_{ampl}}=\bar{T}_{obs1_{ampl}} \end{cases} \tag{5.17}$$

By subtracting both equations, we get (5.20) where the only unknown variable is the total moment of inertia J.

$$\left.\begin{cases} \bar{T}_{load}+\bar{T}_{obs1}=J\cdot\dfrac{d\,\bar{\Omega}_1}{dt} \\ \bar{T}_{load}+\bar{T}_{obs2}-\bar{T}_{obs1}=J\cdot\dfrac{d\,\bar{\Omega}_2}{dt} \end{cases}\right| - \tag{5.18}$$

$$\bar{T}_{load}+\bar{T}_{obs1}-\bar{T}_{load}-\bar{T}_{obs2}+\bar{T}_{obs1}=J\cdot\frac{d\,\bar{\Omega}_1}{dt}-J\cdot\frac{d\,\bar{\Omega}_2}{dt} \tag{5.19}$$

$$2\cdot\bar{T}_{obs1}-\bar{T}_{obs2}=J\cdot\left(\frac{d\,\bar{\Omega}_1}{dt}-\frac{d\,\bar{\Omega}_2}{dt}\right) \tag{5.20}$$

BUPT

Where $\bar{T}_{load}$ represent the complex number of the loading torque, $\bar{T}_{obs1}$ $\bar{T}_{obs2}$ represent the GCIM electromagnetic torque given by the torque estimator in Step 1 and Step 2, J represents the total moment of inertia (GCIM, Load, and Auxiliary motor), $\bar{\Omega}_1$ $\bar{\Omega}_2$ represent the complex number of the measured speed from Step 1 and Step 2, $\bar{T}_{aux}$, $\bar{T}_{aux_{\measuredangle}}$, $\bar{T}_{aux_{ampl}}$ represent the auxiliary machine torque in a complex form with its components: angle and magnitude, $\bar{T}_{obs1_{\measuredangle}}$ $\bar{T}_{obs1_{ampl}}$ represent the angle and the amplitude of the GCIM estimated torque obtained from Step 1 and the $\frac{d}{dt}$ represents the time derivative function.

An ideal angle was built based on a fixed-step size, which was used on a limited interval delimited by the $start$ and $stop$ variables.

$$\theta_{ideal} = \Omega_0 \cdot T \cdot (ti - ti_{start}) \tag{5.21}$$

$$\Omega_0 = \frac{1}{Np} \cdot \sum_{i=start}^{stop} \Omega_1 \tag{5.22}$$

$$Np = stop - start + 1 \tag{5.23}$$

where: θ_{ideal} represents the ideal angle based on the elapsed time from simulation, Np represents the total number of elements that were used for calculus (the +1 from its equation depends on the used software – here Matlab Simulink), $start, stop$ represent the indices used for the interval on which the calculations are performed T represents the sample time, ti, ti_{start} represent the total index produced by the simulation, and the index value from where the calculus begins, Ω_0, Ω_1 represent the mean speed from the interest interval, of the simulation measured speed. The complex numbers are given according to the following equations: (5.24) and (5.25).

$$X_{real} = \frac{2}{N_p} \cdot \sum_{i=start}^{stop} \left(cos(h \cdot \theta_{ideal}) \cdot x_i\right) \tag{5.24}$$

$$X_{imag} = \frac{2}{N_p} \cdot \sum_{i=start}^{stop} \left(sin(h \cdot \theta_{ideal}) \cdot x_i\right) \tag{5.25}$$

where the h represents the number of harmonic used (i.e. $h = 1$ fundamental, $h = 2$ first harmonic component, etc). If we consider that:

$$\Omega(t) = \Omega_{1_{real}} \cdot cos(h \cdot \Omega_0 \cdot t) + \Omega_{1_{imag}} \cdot sin(h \cdot \Omega_0 \cdot t) \tag{5.26}$$

and if we derivate it, we can get the derivated real and imaginary components:

$$\dot{\Omega}(t) = \Omega_{1_{real}} \cdot h \cdot \Omega_0 \cdot \left(-sin(\Omega_0 \cdot t)\right) + \Omega_{1_{imag}} \cdot h \cdot \Omega_0 \cdot cos(\Omega_0 \cdot t) \tag{5.27}$$

BUPT

$$\begin{cases} \Omega 1_{real} = \Omega 0 \cdot \Omega 1_{imag} \\ \Omega 1_{imag} = \Omega 0 \cdot \Omega 1_{real} \end{cases} \tag{5.28}$$

Where $\Omega(t)$ represents the momentary speed, $\Omega 1_{real}$ and $\Omega 1_{imag}$ represent the real and imaginary parts of the complex speed, and t represents the time.

So, if we rewrite the (5.20) and divide it into Real and Imaginary components, we get the following:

$$\begin{cases} 2 \cdot T_{obs1_{real}} - T_{obs2_{real}} = J \cdot \Omega 0 \cdot \left(\Omega 1_{imag} - \Omega 2_{imag} \right) \\ 2 \cdot T_{obs1_{imag}} - T_{obs2_{imag}} = J \cdot \Omega 0 \cdot \left(-\Omega 1_{real} - \Omega 2_{real} \right) \end{cases} \tag{5.29}$$

In order to avoid consistent component errors (Real and Imaginary components) around the axes, next we use the amplitude value.Therefore, the equation (5.30) presents the system total inertia equation, extracted from the 2-step method:

$$J = \frac{1}{\Omega 0} \cdot \sqrt{\left(\frac{2 \cdot T_{obs1_{real}} - T_{obs2_{real}}}{\Omega 1_{imag} - \Omega 2_{imag}} \right)^2 + \left(\frac{2 \cdot T_{obs1_{imag}} - T_{obs2_{imag}}}{-\Omega 1_{real} - \Omega 2_{real}} \right)^2} \tag{5.30}$$

Once we have the system's moment of inertia, the load torque is calculated based on the equation (5.17), both for fundamental and harmonics:

$$\bar{T} load_h = J \cdot \frac{d\, \bar{\Omega} 1_h}{dt} - \bar{T} obs1_h \tag{5.31}$$

$$\begin{cases} T load_{real_h} = J \cdot h \cdot \Omega 0 \cdot \Omega 1_{imag_h} - T obs1_{real_h} \\ T load_{imag_h} = -J \cdot h \cdot \Omega 0 \cdot \Omega 1_{real_h} - T obs1_{imag_h} \end{cases} \tag{5.32}$$

Where: all the symbols are explained before, mentioning that the h index represents the component for which the calculation is performed (fundamental or harmonics). Next, the final load torque found through the two-step method is given as the sum between fundamental and harmonics:

$$\bar{T} load_c = \sum_{h=1}^{n} \bar{T} load_h \tag{5.33}$$

where $\bar{T} load_c$ represents the final computed form of the loading torque, n represents the total number of components (harmonics) taken into account, $\bar{T} load_h$ and represents the computed loading torque component.

The results obtained from (5.16)-(5.32) are expressed graphically in Fig. 5.23. First, the two-step method was applied. After both steps, the loading torque was found (amplitude and angle). The resulting torque was then used as the auxiliary machine's VFC torque reference. The angle used is 180deg phase shifted,

BUPT

and the found amplitude was given as 50% and 100% amplitude (even if the 100% compensation level is given only for demonstration purposes).

Based on theory and results, the optimum phase angle used for auxiliary machine VFD torque reference is obtained from the two-step method. The AM's VFC torque reference amplitude can be given as a percentage of found loading torque amplitude. As presented in the following, the observer's parameters variation and the incorrectly calculated loading torque phase shift can lead to a decrease in the efficiency of the torque pulsation compensation method with an auxiliary machine.

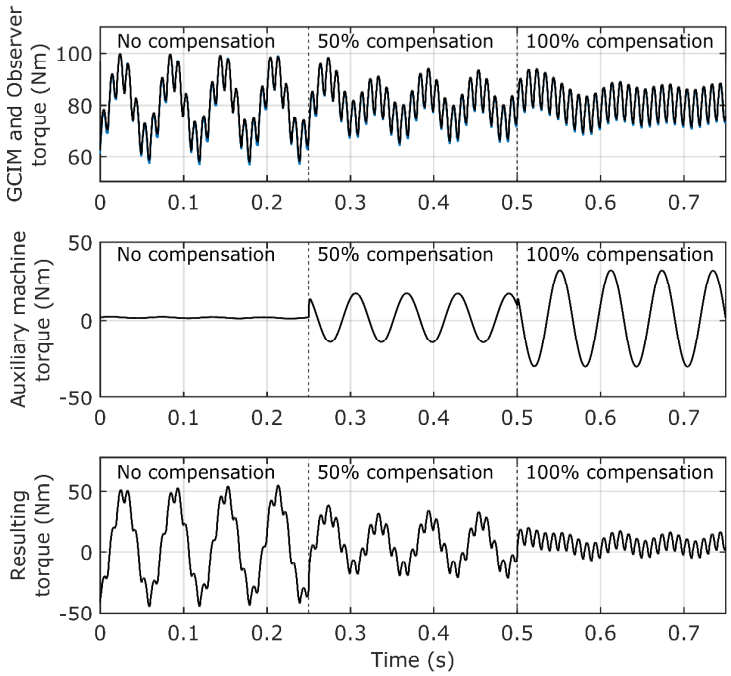

Fig. 5.23 GCIM and Observer torque, auxiliary machine torque, and the system resulting torque for no compensation, 50% loading torque compensation, and 100% loading torque compensation for the phase shift found from the two-step method.

5.3.3.2. Two-step method sensitivity testing

The here-presented two-step method's sensitivity is investigated according to the GCIM torque estimator's parameters variations.

Fig. 5.24, Fig. 5.25, and Fig. 5.26 present how the calculated moment of inertia (5.31) and loading torque (phasor (5.32) varies depending on the estimator's parameter variation.

As long as the errors produced by the magnetizing inductance variation are relatively constant, we can say that the machine saturation should not significantly affect the method's accuracy.

More than that, the errors produced by the rotor and stator resistance variation vary in an opposite manner (when one increases, the other decreases), and considering that both rotor and stator resistance increase or decrease almost simultaneously, it can be considered that the total error variation produced by the rotor and stator resistances variation compensate on each other.

BUPT

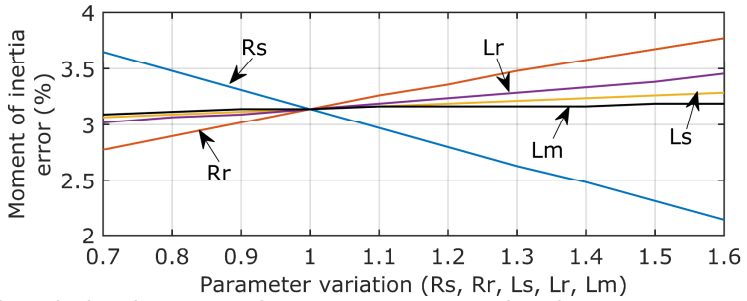

Fig. 5.24 The calculated moment of inertia error respected to the system moment of inertia $J = 0.411(kgm^2)$ depending on the GCIM torque observer parameters variation

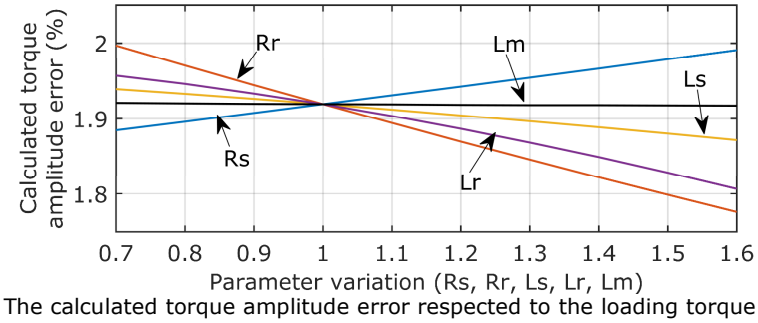

Fig. 5.25 The calculated torque amplitude error respected to the loading torque amplitude depending on the GCIM torque observer parameters variation

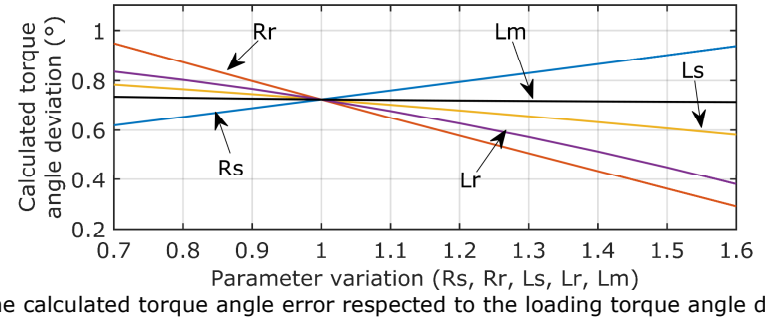

Fig. 5.26 The calculated torque angle error respected to the loading torque angle depending on the GCIM torque observer parameters variation

All the previous calculus and results were given for zero phase shift for the loading torque angle.

Next, the calculated moment of inertia error (Fig. 5.27), the calculated angle deviation (Fig. 5.28), and the calculated loading torque amplitude error (Fig. 5.29) are given for different loading torque angles.

While the most insignificant calculated moment of inertia error can be found around 0deg phase-shifted loading torque (Fig. 5.27), the calculated torque angle deviation (Fig. 5.28) presents the smallest values around $\pm 115^o$.

The positive phase-shifted angles ($0^o - 180^o$) produce smaller errors for the calculated torque amplitude (Fig. 5.29) than the negative ones.

BUPT

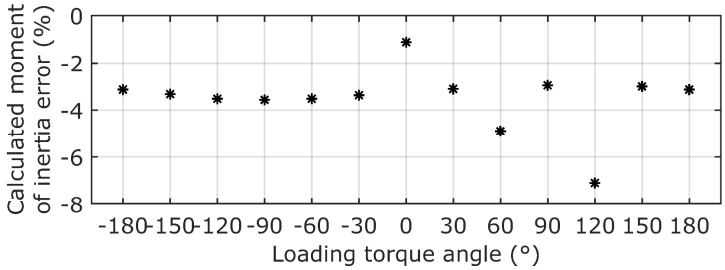

Fig. 5.27 Calculated moment of inertia error depending on the loading torque angle

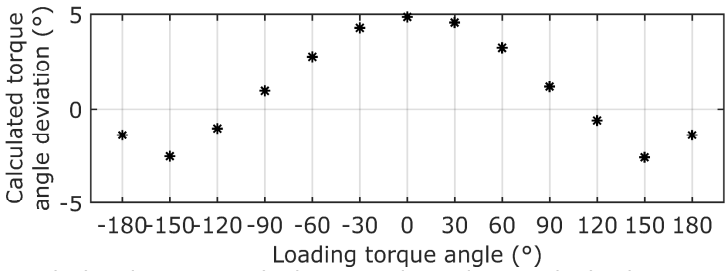

Fig. 5.28 Calculated torque angle deviation depending on the loading torque angle

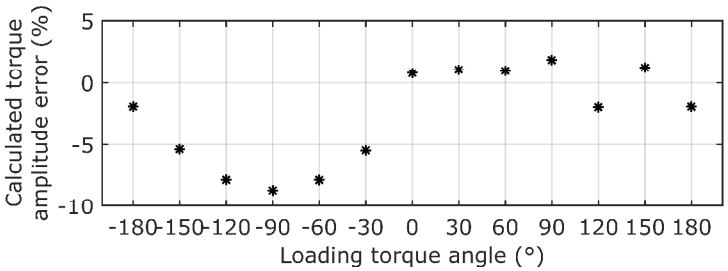

Fig. 5.29 Calculated torque amplitude error depending on the loading torque angle

5.3.3.3. Two-step method testing in real (compressor) loading torque conditions

During previously presented results, the load torque used was synthesized from a sinusoidal waveform.

Another key role in this presented problem is given by the mechanical stress of the mechanical couplings during the operation. To quantify the total torque transmitted between motors and load, the equation (5.34) is used.

In Fig. 5.30, an example of coupling mechanical torque is given. For 5 seconds, the GCIM was loaded with 70%dc components and 30% sinusoidal overlapped components without compensation. From 0.5 seconds, the AM has a 15% sinusoidal torque reference.

$$\left.\begin{aligned} T_{C_1} &= T_{IM} - \frac{d\omega}{dt} \cdot J_{IM} \\ T_{C_2} &= T_{AM} - \frac{d\omega}{dt} \cdot J_{AM} \end{aligned}\right\} \tag{5.34}$$

BUPT

where: T_{C_1}, T_{C_2} represent the torque transmitted through mechanical couplings, T_{IM}, T_{AM} represent the GCIM and AM torque, J_{IM}, J_{AM} represent the inertia moment of the GCIM and AM, and ω represents the system speed.

The GCIM torque appears as an effect of the loading torque, the reason why the mechanical coupling one torque appears in front of the GCIMs torque.

On the other hand, the Auxiliary Machine torque appears at a fixed phase shift (as the VFC drives), while the transmitted torque through mechanical coupling 2 is in phase with the AM's torque.

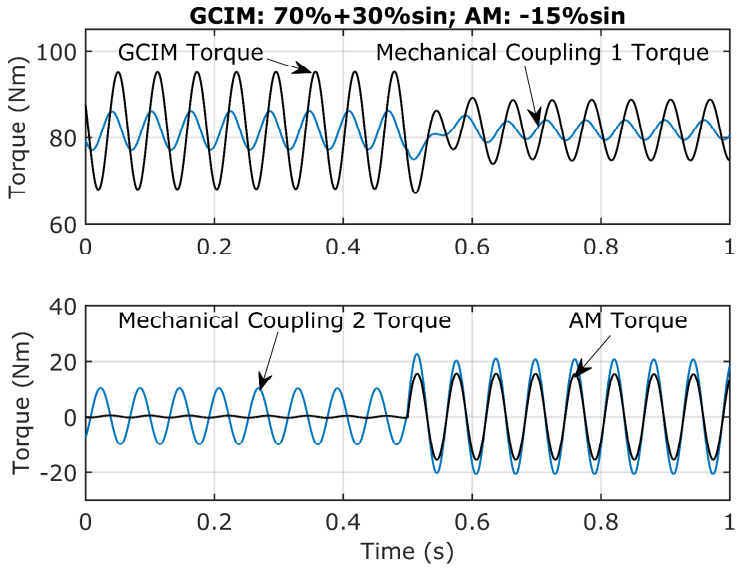

Fig. 5.30 GCIM, AM torques, and transmitted torques between Load and GCIM (mechanical coupling 1) and transmitted torques between AM and Load (mechanical coupling 2)

Next, the two-step method performance is presented when the load torque is given by a reciprocating compressor or a large piston engine.

The next presented loading torque profiles come from the interaction between the torque developed during the cylinder gas compression and the mechanical masses that are reciprocated.

For small powers up to 25kW, single-piston (single-acting or double-acting) reciprocating compressors are used in cars and refrigerator systems [210], [211], [212], [213].

Large 2, 4, or 6 throws -generally double-acting- compressors, are used in the gas and petroleum industry. The reciprocating compressor units can reach up to thousands of kilowatts.

Various examples of double or single-acting, two and four throws compressors with multiple compression stages are given in [214], [215], [216], [217], [218].

In Fig. 5.31, the demand reciprocating compressor torque is given for various compressor types and powers.

The compressor's real torque profiles were given into Simulink using the "Lookup Table" block. The entered values were taken from the real compressor's torque curves.

BUPT

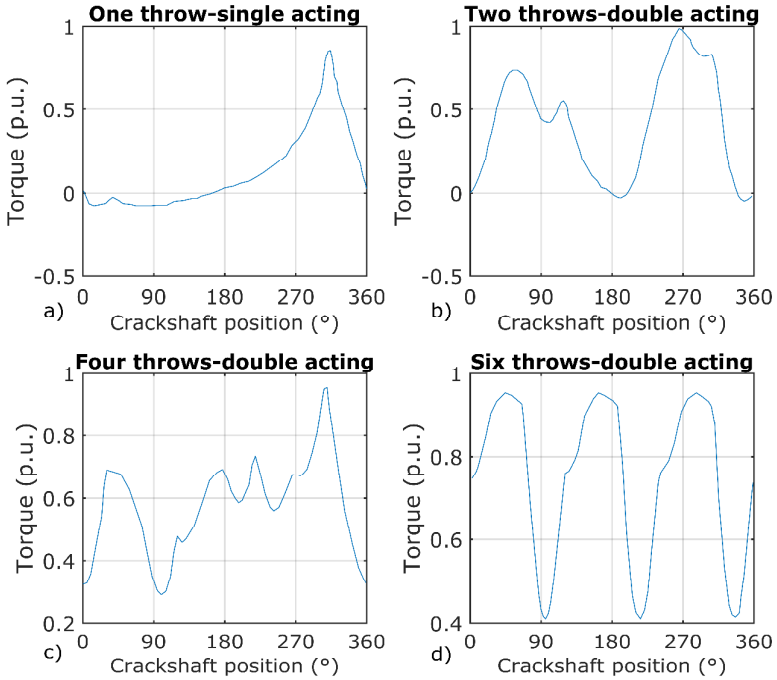

Fig. 5.31 loading torque for different reciprocating compressors: a) single throw - single acting compressor, b) two throws – double acting single stage compressor, c) Four throws – double acting single stage compressor, d) Six throws – double acting single stage compressor

The following results are presented by applying the two-step method, considering the loading torques as the real ones.

In the first step, the moment of inertia is determined (according to the two-step method) only from the 1st harmonic of the loading torque. Compared with the results presented in Chapter 5.3.3.1, where the two-step method was used to determine only the 1st harmonic (fundamental) of the load torque, the second harmonic ($2 \cdot f$) was taken into account for auxiliary machine variable frequency converter torque reference.

In the following figures, the system operation with different real loading torques (refer to Fig. 5.31) is given. In all cases, the system operation is divided into 3 sectors (0s-0.2s: without auxiliary compensation only the loading torque acts; 0.2s-0.4s: with 50% auxiliary motor compensation of the first harmonic; 0.4s-0.7s: with 50% auxiliary motor compensation of the first harmonic and 50% compensation of the second harmonic). The GCIM high-frequency torque is given by the grid voltages.

For a one-throw single-acting compressor, the results are presented in Fig. 5.32. The loading torque also has a negative component. The resulting loading torque decreases when the Auxiliary machine starts to compensate only 50% of the 1st harmonic (0.2s-0.4s). The system speed pulsation does not show substantial changes. When the auxiliary machine reference also contains the 2nd harmonic content, the torque spikes drop even more. Also, the GCIM torque decreases in amplitude with the increase in compensation.

BUPT

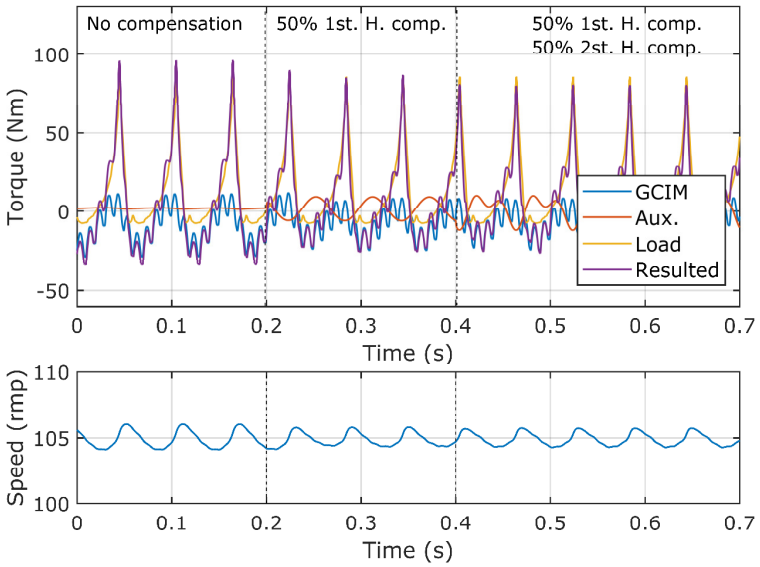

Fig. 5.32 Grid-connected Induction Machine torque, Auxiliary Machine torque, loading torque, the resulting torque, and system speed for the one-throw single-acting reciprocating compressor (Fig. 5.31, a) without pulsating load compensation, with 50% of 1st. harmonic compensation and with 50% 2nd harmonic compensation

In Fig. 5.33, in the 0.4s-0.7s sector, where the auxiliary machine partially compensates for both the first and second harmonics, the mechanical coupling between the auxiliary machine and load is highly stressed.

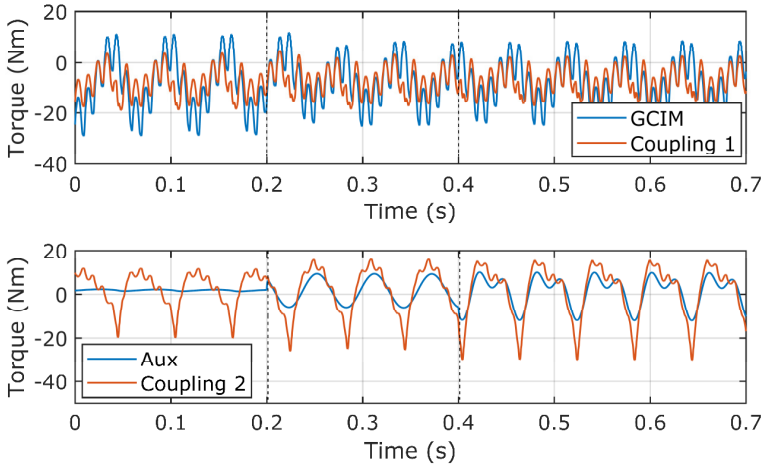

Fig. 5.33 The grid-connected induction machine torque and the torque transferred through the mechanical coupling 1 and the auxiliary machine electromagnetic torque and the torque transferred through mechanical coupling 2 for one-throw single-acting compressor torque reference with and without auxiliary compensation

Even though the auxiliary machine compensating effect does not change substantially the system opperation, the mechanical torque transmitted through

BUPT

couplings is strongly influenced. In the case of a two-throw double-acting compressor loading torque profile (Fig. 5.31, b), the system operation is presented in Fig. 5.34.

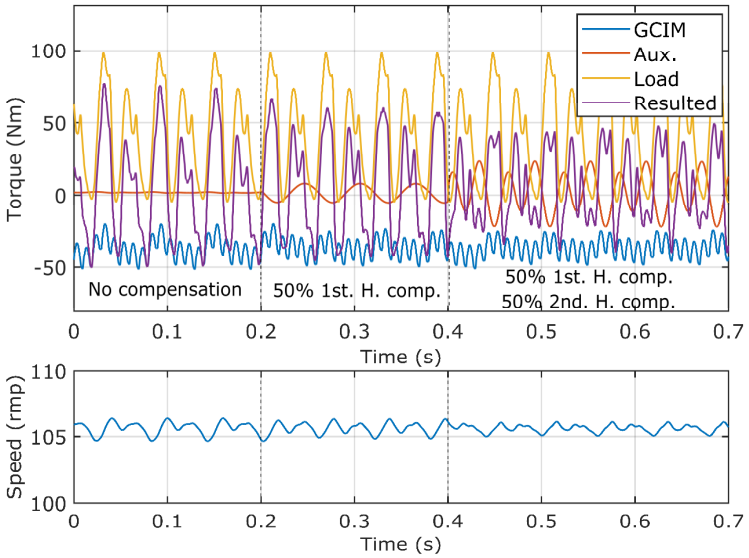

Fig. 5.34 Grid-connected Induction Machine torque, Auxiliary Machine torque, loading torque, the resulting torque, and system speed for the two-throws double-acting reciprocating compressor (Fig. 5.31, b) without pulsating load compensation, with 50% of 1st. harmonic compensation and with 50% 2nd harmonic compensation

Although the 2nd-order harmonic compensation positively affects the GCIM mechanical stress, the torque transmitted through the 2nd coupling presents a substantial increase (Fig. 5.35).

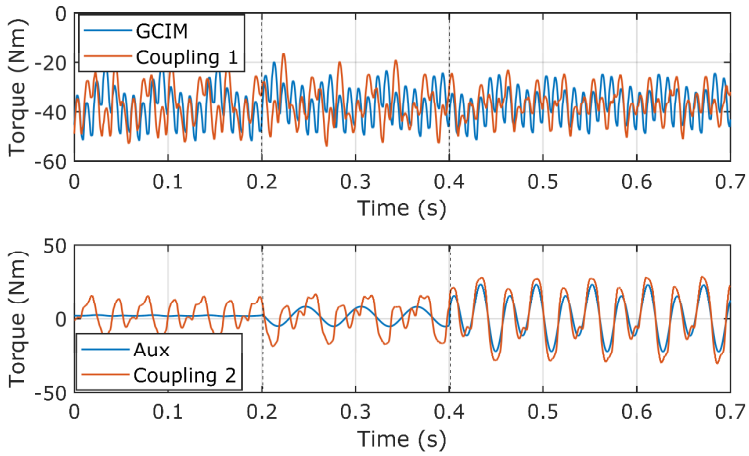

Fig. 5.35 The grid-connected induction machine torque and the torque transferred through the mechanical coupling 1 and the auxiliary machine electromagnetic torque and the torque transferred through mechanical coupling 2 for two-throw double-acting compressor torque reference with and without auxiliary compensation

BUPT

When the Auxiliary Machine VFC's reference contains both the first and second harmonic components, the resulting system torque and the GCIM torque show a substantial decrease in the torque pulsation amplitude. In this case, the second-order harmonic amplitude is almost three times greater than the first harmonic amplitude, which is the reason why the influence of its compensation strongly affects the results.

In the case of the four-throw double-acting compressor torque reference (Fig. 5.36), the second-order harmonic compensation has a small influence over the system's resulting torque. Not even the second-harmonic influence can be neglected; its presence in the auxiliary machine torque conducts to insignificant results of the GCIM torque.

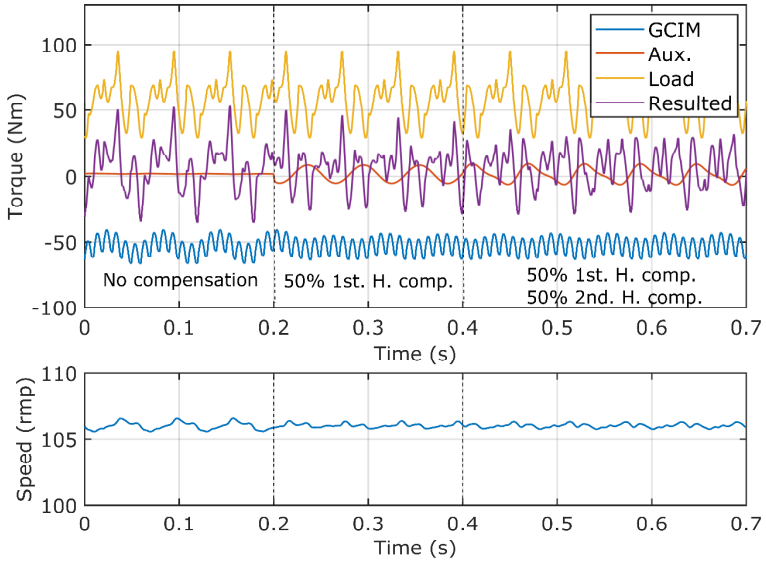

Fig. 5.36 Grid-connected Induction Machine torque, Auxiliary Machine torque, loading torque, the resulting torque, and system speed for the four-throws double-acting reciprocating compressor (Fig. 5.31, c) without pulsating load compensation, with 50% of 1st. harmonic compensation and with 50% 2nd harmonic compensation

However, the partial compensation of second-order harmonic decreases the mechanical stress on coupling 2 (Fig. 5.37).

Thus, it can be considered that in this case, the second-order harmonic compensation can be used to reduce the coupling 2 mechanical stress (peak-to-peak torque).

However, this compensation does not seem to reduce significantly the torque pulsation in GCIM and in its coupling.

In addition to the importance of the load torque profile, with the reduction of peak-to-peak pulsations of the load, the mechanical stress in the coupling between the auxiliary machine and the load also decreases.

In Fig. 5.38, the system operation for the six-throw double-acting compressor torque is presented (Fig. 5.31, d).

BUPT

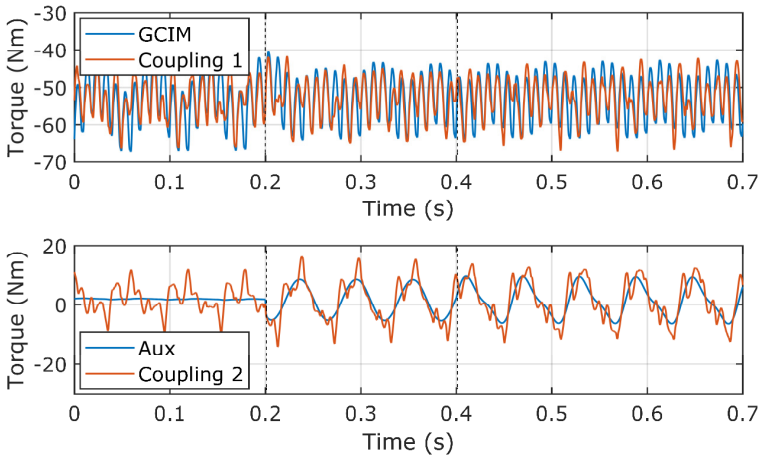

Fig. 5.37 The grid-connected induction machine torque and the torque transferred through the mechanical coupling 1 and the auxiliary machine electromagnetic torque and the torque transferred through mechanical coupling 2 for four-throw double-acting compressor torque reference with and without auxiliary compensation

In this simulation, the system moment of inertia (J=0.422kgm2) filters the speed.

Regarding the load torque, the GCIM torque contains only the dc component. The high frequency is given by the voltages.

No results are obtained from the two-step method for the 1st and 2nd harmonic.

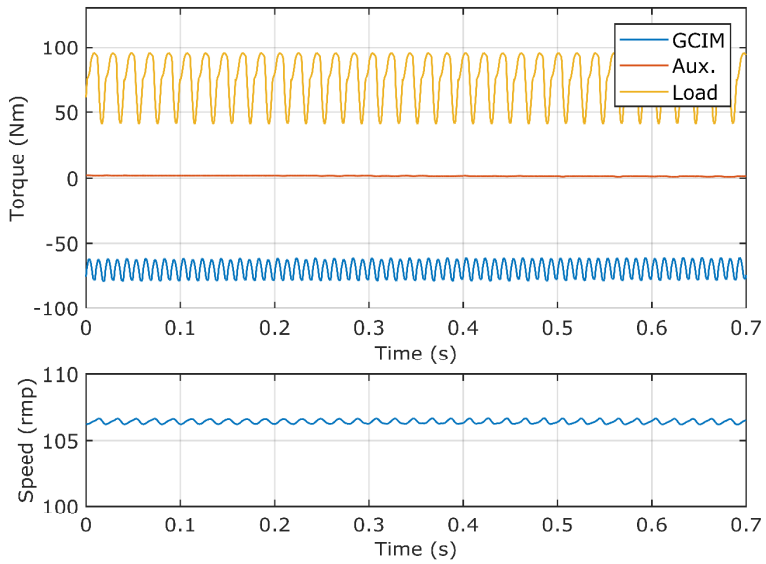

Fig. 5.38 Grid-connected Induction Machine torque, Auxiliary Machine torque, loading torque, the resulting torque, and system speed for the six-throws double-acting reciprocating compressor (refer to Fig. 5.31, d) without pulsating load compensation

The only torque interaction from the auxiliary machine is given by its moment of inertia (Fig. 5.39).

BUPT

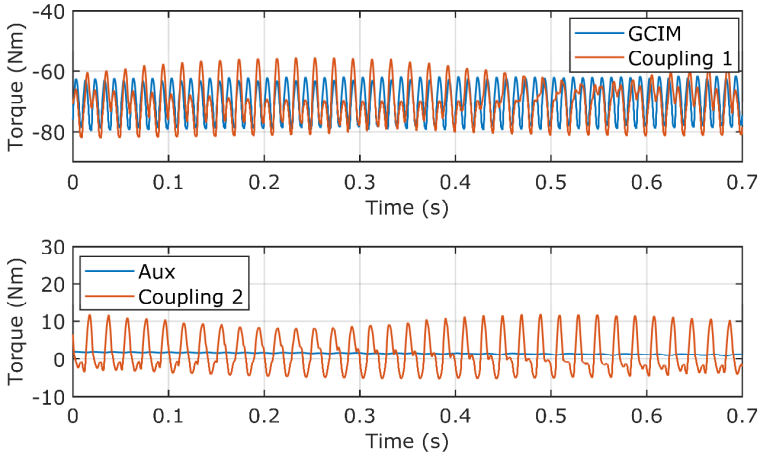

Fig. 5.39 The grid-connected induction machine torque and the torque transferred through the mechanical coupling 1 and the auxiliary machine electromagnetic torque and the torque transferred through mechanical coupling 2 for six-throw double-acting compressor torque reference without compensation

5.4. Experimental validation

The experiments are meant to validate the active torque pulsation reduction simulation methods.

In the following pages, the open-loop and two-step methods are experimentally investigated and discussed. For the open-loop method, the loading torque amplitude and phase are considered to be known, but for the two-step method, the system moment of inertia and the loading torque (amplitude and phase) are determined during the experiments.

As was already presented in the simulation, a key factor is represented by the correct estimation of the pulsating torque to perform an optimum compensation. For closed-loop methods, the pulsating loading torque amplitude and phase angle must be permanently known.

In Fig. 5.40, an elastic spider element, the claw-type coupling, is presented together with and rigid disc-type coupling. All the experiments presented here were obtained with rigid mechanical coupling.

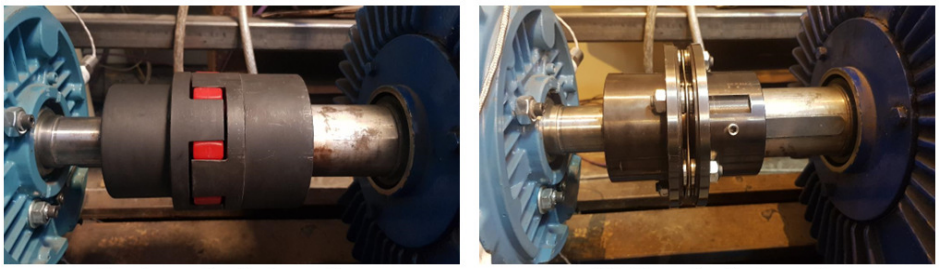

Elastic mechanical coupling Rigid mechanical coupling

Fig. 5.40 Mechanical couplings used in experiments

A high system elasticity could introduce loading torque lags along the shaft and, at the same time, loading torque spectrum filtering. More than that, an elastic

BUPT

coupling between the auxiliary machine and the loading machine could lead to an unpredictable interaction between the auxiliary machine inertia (and compensating torque) and actual loading torque. More information about spider-type and disc-type mechanical couplings can be found in the following references [39]–[43].

In some cases, a wrong application of the compensation torque can lead to unwanted effects of the resulting torque over the mechanical system. The auxiliary machine torque phase is considered a critical value of the active compensation.

The machines' alignment represents another important factor for system safety. As long as the rigid couplings allow a small degree of misalignment between the machines, such an action can lead to mechanical couplings breaking.

In Fig. 5.51, two disks of rigid couplings destroyed during operation can be seen.

The first disc was made of soft steel and was bent due to the machines' misalignment, and the second disc was made of rigid steel and was destroyed due to the wrong compensation of the pulsating torque.

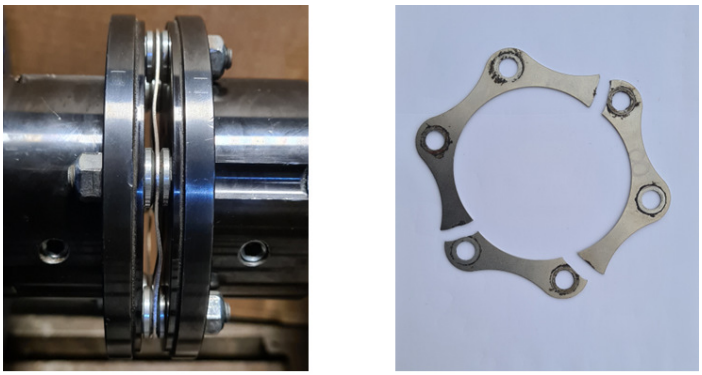

Bent disc - soft steel Broken disc - rigid steel

Fig. 5.41 Destroyed soft steel and rigid steel discs during the tests

5.4.1. Open-loop experimental validation

Similarly, as presented in Chapter 5.3.1, the experiments obtained from the open-loop torque pulsation reduction method are presented below. This situation is meant only to prove the principle of operation: the torque pulsations produced by a position-dependent loading torque can be reduced by an auxiliary superimposed (180-degree phase shifted) torque.

The test (presented in Fig. 5.42) was performed for 20 seconds, with 5 different sectors: 0-4seconds the GCIM was only grid-connected and the AM was not operating; 4-8seconds the GCIM was 70%dc component (of rated torque=108Nm) loaded; 8-12seconds 70%dc component GCIM load was overlapped with a 30%sinusoidal component; 12-16seconds the AM compensates with a 14% sinusoidal component (of the GCIM rated power); 16-20 seconds, the AM compensated with an 18% sinusoidal component of the GCIM rated power.

BUPT

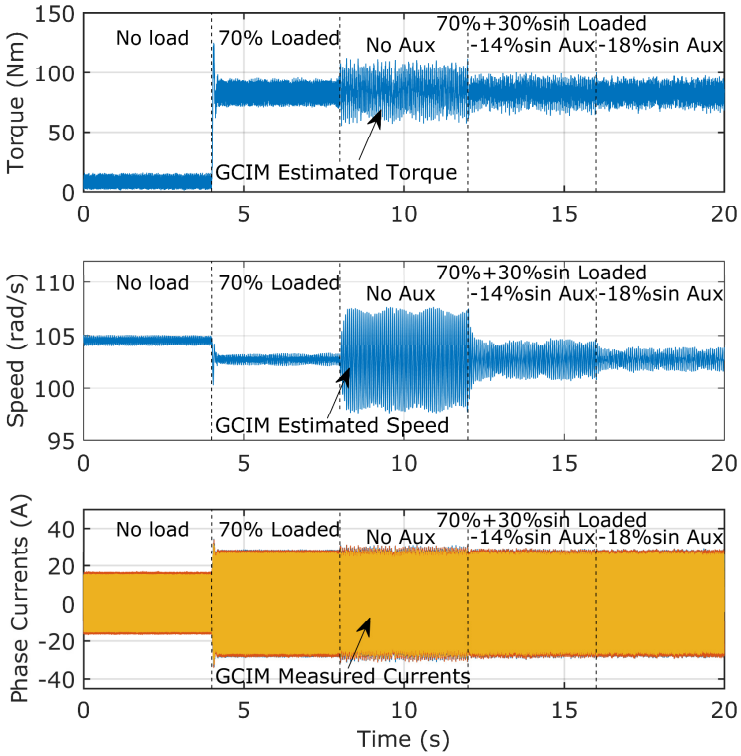

Fig. 5.42 Grid-connected induction machines' s estimated torque, estimated speed, and measured currents for different loads torques and compensation torques – experiments

In Fig. 5.42, the grid-connected induction machine estimated torque, the system estimate speed, and the measured phase currents are presented. It can be observed that in sector three (8-12 seconds) - where the pulsating load is present - the GCIM torque and system speed present a severe pulsating character. As we expected, in the fourth sector, where the AM compensates 14% (of GCIM-rated torque), the pulsations decrease. As the compensation level increases, the system speed and GCIM torque pulsations decrease even more.

In Fig. 5.43, the GCIM estimated electromagnetic torque frequency spectrum is investigated.

Fast Fourier Transform (FFT) analysis is performed for all four situations: no load, with pulsating load, with pulsating load and 14% compensation, and with pulsating load and 18% compensation.

When no loading torque is present, the 16.6Hz harmonic can be neglected. For full-loading torque (without compensation), the 16.6Hz harmonic represents almost 14% of the fundamental harmonic.

For the first level of compensation, the 16.6Hz harmonic decreases by almost 67%, while for the second level of compensation, the 16.6Hz harmonic presents a substantial decrease by more than 80% of its no-compensation situation level.

BUPT

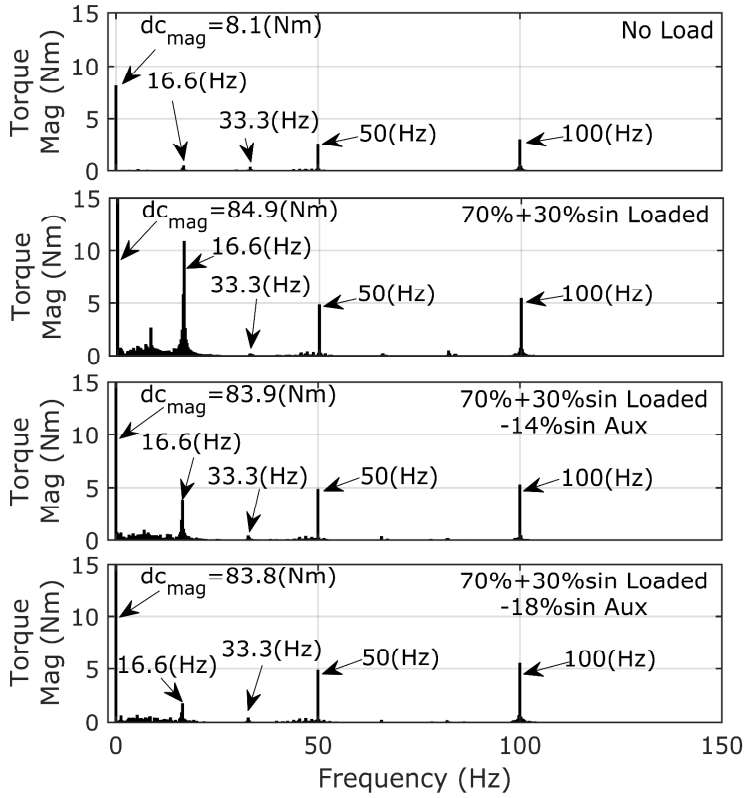

Fig. 5.43 FFT on GCIM's estimated torque for different load torques and compensation torques – experiments

Fig. 5.44 shows the FFT analysis on GCIM phase currents.

The 16A value of the 50Hz harmonic represents the induction machine's no-load current. When the pulsating loading torque is present, the 16.6Hz apart paired harmonics (33.3Hz and 66.6Hz) appear.

These harmonics are given as a result of the phase current harmonics (50Hz and 16.6Hz -caused by the load torque) frequency composition (as it is presented in (5.35))

$$sin(a) \cdot sin(b) = \frac{1}{2} \cdot \left(cos(a-b) - cos(a+b)\right) \tag{5.35}$$

where: a and b represent the 50Hz and 16.6Hz frequencies, and the sin and cos are trigonometric functions.

For the first level of compensation (14% on GCIM-rated torque), the 16.6 Hz apart paired harmonics decrease by more than 62%.

In comparison, for the second level of compensation (18% on GCIM-rated torque), the 33.3Hz and 66.6Hz harmonics decrease by more than 84% from their initial (no-compensation) values.

BUPT

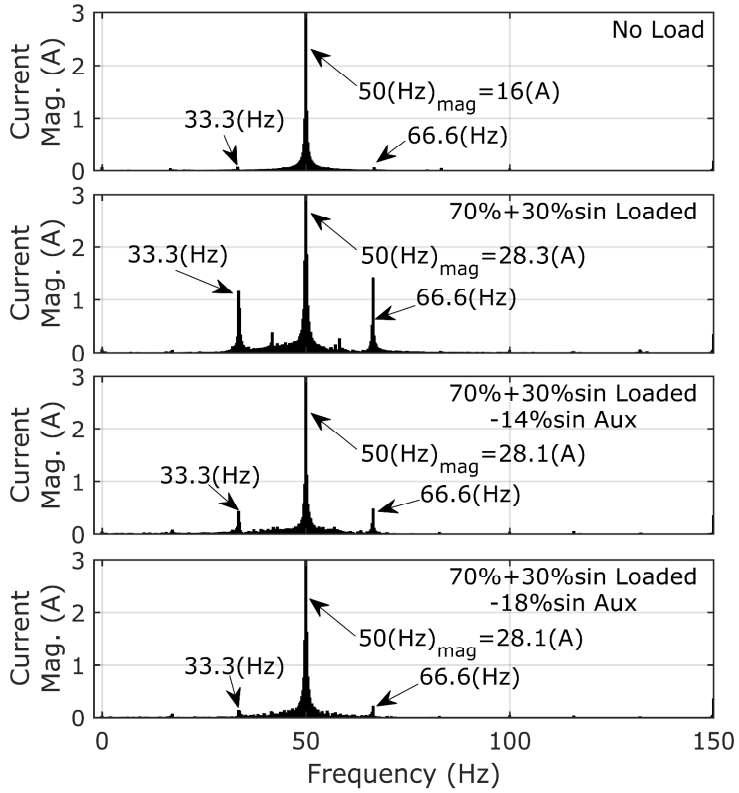

Fig. 5.44 FFT on GCIM's measured phase currents for different load torques and compensation torques – experiments

5.4.2. Two-step method experimental validation – 1st harmonic-based loading torque

All the experiments can be performed using the cRIO chassis.

The existent VFCs (ACS800) communication is limited to Profibus or Modbus RTU or TCP/IP protocol.

The cRIO-9068 chassis has the FPGA capability to operate the Modbus TCP/IP protocol with dedicated Profibus or Modbus modules (which do not exist in the current setup). Otherwise, the Modbus protocol can be implemented into Labview (Fig. 5.45), but with a much lower communication speed performance.

In this case, the cRIO-9068 chassis cannot be used as a unitary equipment for both command and control.

In this way, the cRio-9068 chassis will be used as a flux and torque observer; the two-step method will be implemented on this RT processor. The results obtained fro the two-step method will be used in the PLC to control the auxiliary machine. There is no direct data communication between the real-time cRio-9068 and the PLC.

BUPT

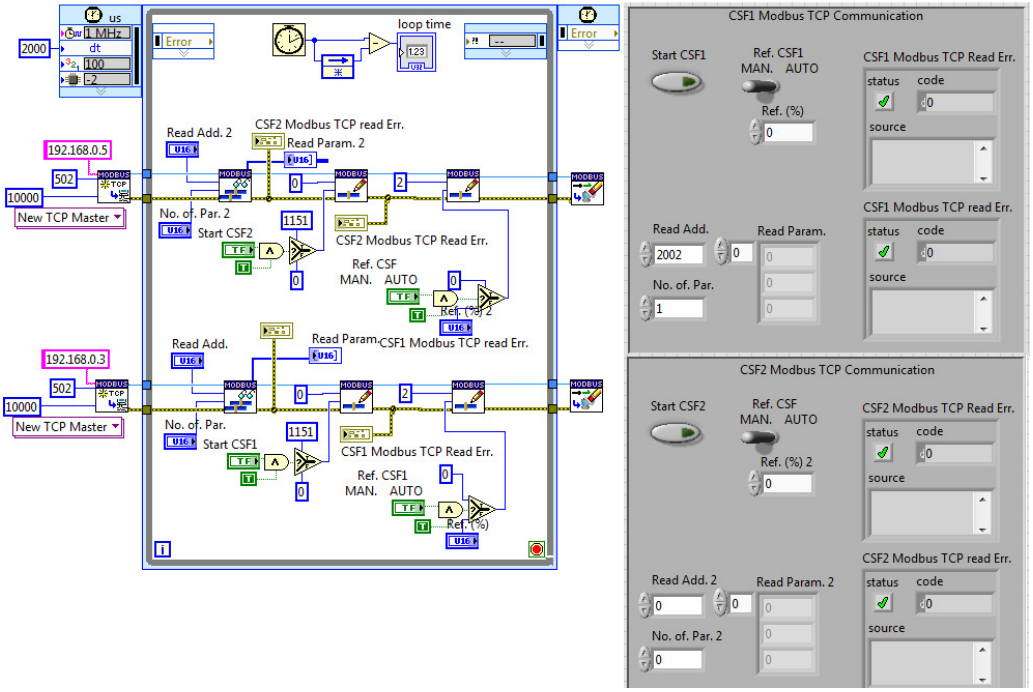

Fig. 5.45 Modbus TCP/IP for two VFCs - Labview implementation

The systems' synchronization (PLC and cRIO) is performed through two encoders mounted on the same shaft (one encoder communicates with the PLC on Profibus, and the other one communicates with cRIO with a 5VTTL signal – see Fig. 5.46).

The processing delay of the encoders was not taken into account directly.

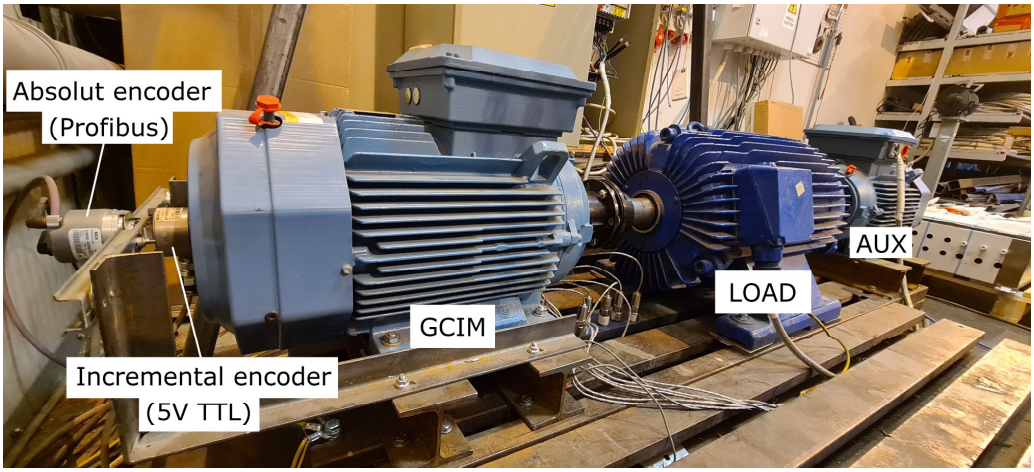

Fig. 5.46 Partial experimental setup (view from encoders)

This limitation leads to a hybrid control and command system (presented in Fig. 5.47). This system uses both a standard commercial PLC with Profibus capability for VFC control and also a cRIO system with high data acquisition frequency modules for data processing.For real applications, where the control system is designed from the beginning, this limitation would not exist.

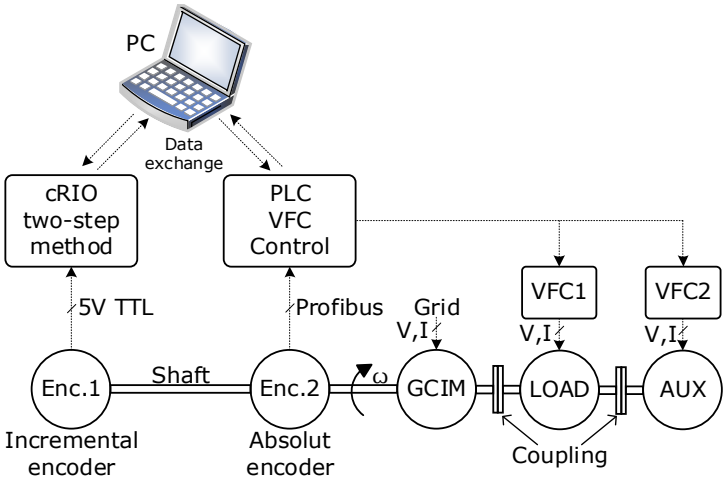

Fig. 5.47 Basic schematic diagram for the hybrid control and command system with PLC and cRIO with two encoders

A more comprehensive understanding of the data transfer on Modbus TCP/IP to the VFCs is described in Fig. 5.48.

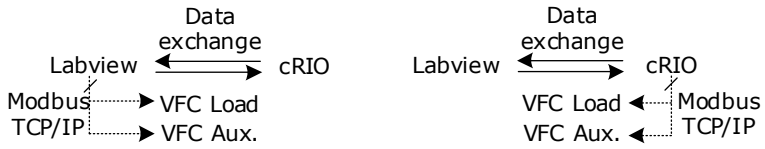

a) Without dedicated module b) With dedicated module

Fig. 5.48 comparison between communication capabilities with and without dedicated modules (Modbus protocol exemplification)

The transition from one reference frame to another, in other words, from cRIO to PLC (or vice versa), is carried out according to Fig. 5.49.

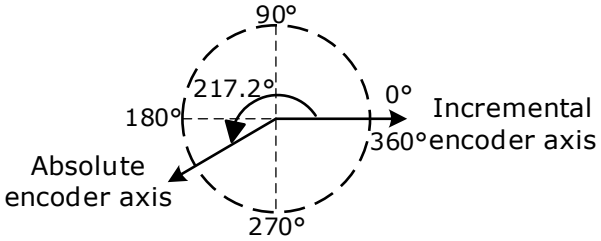

Fig. 5.49 Absolute and incremental encoder axis differences

BUPT

The phase shift between the encoders' axes is 217.2deg and was determined through experiments.

To synchronize the real loading torque estimated by the VFC with the system position measured with the Profibus encoder, the torque reference given to the VFC from the PLC and the VFC received reference was used as a synchronization signal.

In Fig. 5.50, the torque reference and the estimated load torque read from VFC on optical fiber (o.f.) and the torque reference given to the inverter from the PLC on Profibus (prof.) and the system position given by the encoder are presented. Compared to subfigure a), in subfigure b), the 57deg VFC phase shift between the received reference and the estimated real torque is compensated. This way, the experiment can easily be compared with the simulation of the two-step method because, after the 57-degree compensation, the loading torque appears at -180 degrees (as presented in the simulation).

It can be observed that the Profibus communication speed is sometimes limited, so the torque reference sent/received to/by the VFC is strongly altered. Moreover, this produces significant errors in performing the desired loading torque (Fig. 5.50, a, sector between 0.1s and 0.15s).

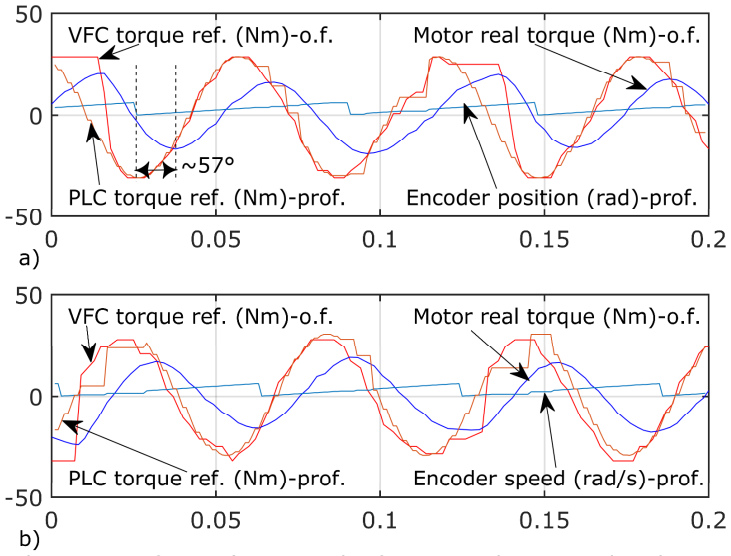

Fig. 5.50 Data synchronization for VFC's received reference and estimated real torque read on optical fiber and PLC's given reference and system position read on Profibus: a) without VFC phase shift compensation, b) with VFC phase shift compensation (57deg)

The two-step method is further described for experimental tests. Similar to what was given in Ch 4.3.3.1, both steps are performed:

- Step 1:

In the first stage, the load operates, thus loading the GCIM. The auxiliary machine is connected to the same shaft.

The Aux. VFC magnetizes the auxiliary machine (the braking torque introduced by the VFC magnetization with 0 torque reference must also be taken into account).

BUPT

In Fig. 5.51, the phasor diagram of the torques that appear in the first step is presented. It has to be noticed that the torque reference given to the Loading Machine (and in the second step also to the AM) has to be around 57 degrees ahead in order to obtaine the desired loading (respectively Auxiliary) torque. In this case, the loading torque (Tload) is given at -180 degrees.

The estimated GCIM loading torque ("Tobs1 incremental enc. reference frame") is being calculated with the cRIO platform in incremental encoder reference frame. 217.2 degree needs to be added to change the reference frame from incremental encoder to absolute encoder reference frame, thus, estimated GCIM loading torque ("Tobs1 absolut enc. Reference frame") can be compared to the loading torque.

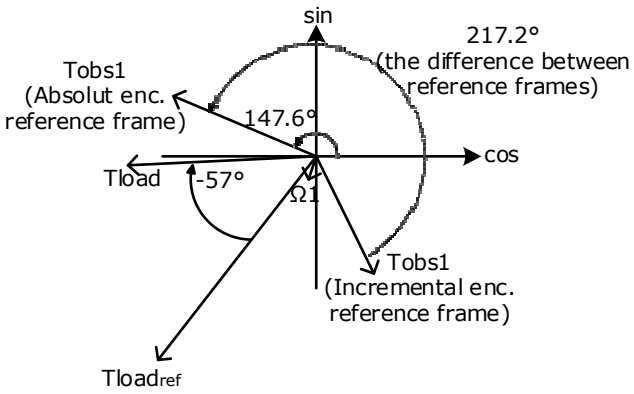

Fig. 5.51 The phasor diagram of Step 1 experimental test (only loading torque and GCIM torque)

- Step 2:

Fig. 5.52 presents the phasor diagram of the Step 2 method, where the Tobs1 (from the First step) is used as information for the Auxiliary machine's VFC torque reference.

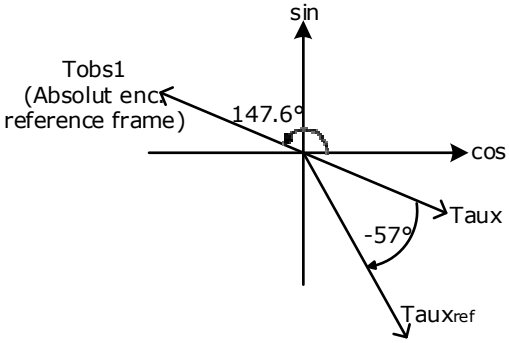

Fig. 5.52 The phasor diagram of Step 2 experimental test (the loading torque, the GCIM torque, and AM torque)

After Step 1 was completed, the "Tobs1 absolut enc. Reference frame" information is known. This way, for this step, the auxiliary machine has to be driven

BUPT

in such a way that its actual torque (Taux) is -180 degree phase shifted than the "Tobs1 absolut enc. Reference frame". This way, the Aux. VFC torque reference is given with about 57 degrees ahead (similarly with Loading Machine).

The two-step method was applied for 11 tests performed for the same loading torque reference angle and amplitude to emphasize the error's unpredictable character. The results are given in Table 5.2.

For each test, both variable frequencies converter were restarted (thus simulating a totally new test). The VFC used for the loading machine was commanded each time with the same data set of parameters (Loading torque parameters). During all tests, the GCIM was connected to the grid. The Profibus communication between PLC and VFC does not guarantee that the VFC always receives exactly the same reference, which can be considered to be the first source of errors.

It can be observed that after the Step 1 test, the torque amplitude and phase of the torque observer are slightly different from each other.

After Step 2, the system moment of inertia, the loading torque amplitude, and the torque angle are calculated. The results are placed in ascending order in the table according to the estimated system moment of inertia.

Table 5.2 Step 1 parameters and Step 2 results after 11 tests for the same loading torque reference angle (180°) and amplitude (30% GCIM rated torque)

Loading torque parameters			Results after Step 1		Results after Step 2		
Amplitude (Nm)		Phase (°)	$T_{obs1_{ampl}}$ (Nm)	$T_{obs1_{angle}}$ (°)	Found Moment of inertia (kgm^2)	Found Loading Amplitude (Nm)	Found Loading Angle (°)
Reference	Real torque						
32.2	18.1	180	10.45	144.91	0.4084	16.31	178.59
			10.73	144.62	0.4183	17.26	179.92
			10.45	144.91	0.4183	17.26	179.32
			10.47	144.93	0.4227	17.15	179.2
			10.77	144.66	0.426	17.19	179.86
			10.69	144.5	0.424	17.33	179.05
			10.67	144.52	0.4248	17.33	179.05
			10.7	145.13	0.4253	17.35	179.04
			10.46	145.6	0.4262	17.17	179.94
			10.42	144.51	0.4295	17.52	179.61
			10.49	144.92	0.4297	17.52	179.61

The moment of inertia in the table is graphically presented in Fig. 5.53. The median and mean values of all measurements are slightly different, with less than 0.3%.

The total differences between the maximum and minimum found moment of inertia values is less than 5% of the real moment of inertia (J=0.422 kgm^2).

BUPT

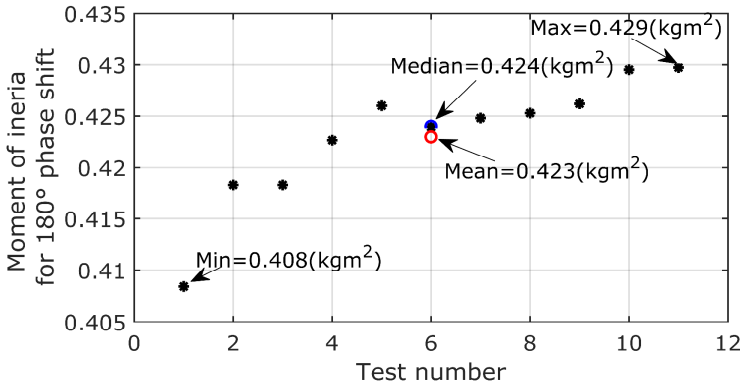

Fig. 5.53 Determined system moment of inertia according to the two-step method for the same loading torque reference angle (180°) and amplitude (30% GCIM rated torque)

After the two-step method was performed, the loading torque found results were used for an effective active torque pulsation reduction. In Fig. 5.54, the GCIM estimated torque, the estimated speed, and the phase currents are presented.

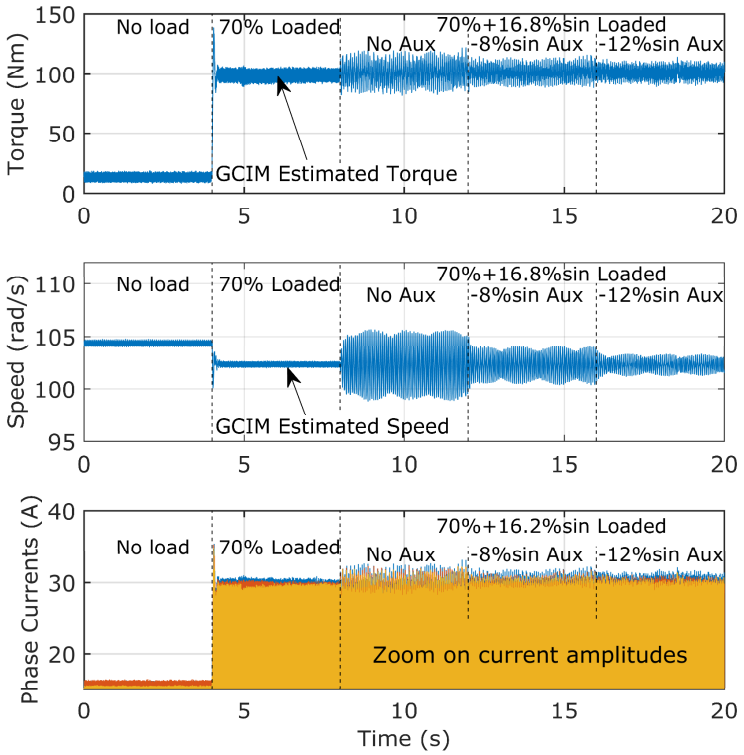

Fig. 5.54 Grid-connected induction machines' estimated torque, estimated speed, and measured currents for auxiliary machine torque reference obtained from two-step method-experiments

BUPT

The graph is divided into 5 different sectors: no load situation, GCIM loaded at 70% of its rated torque ($T_{GCIM_{rated}} = 108(Nm)$), 16.8% sinusoidal reference overlapped with the dc without pulsation compensation, and from 12s to 16 s, the auxiliary machine compensates 8% of GCIM rated torque, and in the last sector, the AM compensates 12% of GCIM rated torque (71% of pulsating real torque)

The following experiment demonstrates the two-step method efficiency for different loading torque angles. According to Fig. 5.55, the loading torque investigated angles change from 60° to 60°.

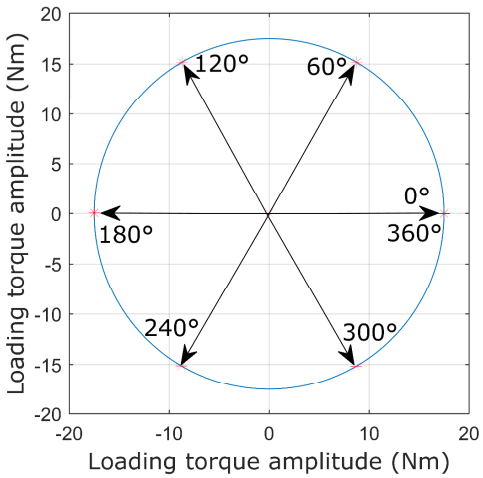

Fig. 5.55 Investigated loading torque reference angle

Fig. 5.56 presents the resulting system moment of inertia error after the two-step method.

Caused, probably, by the incorrect value of the auxiliary VFC torque reference, all the calculated moments of inertia are slightly bigger than the real moment of inertia. The maximum error is reported at 60° but does not exceed 2% of the real moment of inertia.

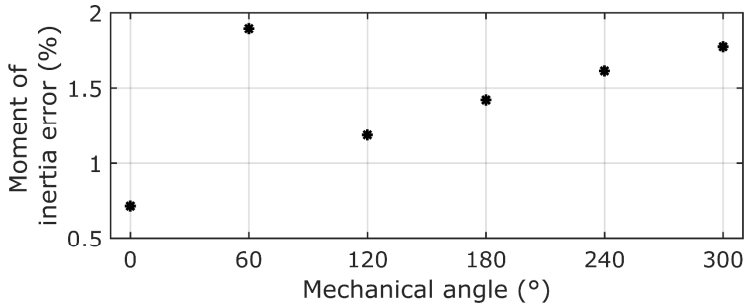

Fig. 5.56 Determined system moment of inertia error according to two-step method for different loading torque reference angle - experiment

Similar to the previous figure, Fig. 5.56 presents the errors between the determined loading torque amplitude and the real loading torque amplitude. Compared to the moment of inertia graph, here, the maximum error is around 6%

BUPT

of the real value, and - as expected- is reported also at 60° loading torque phase shift.

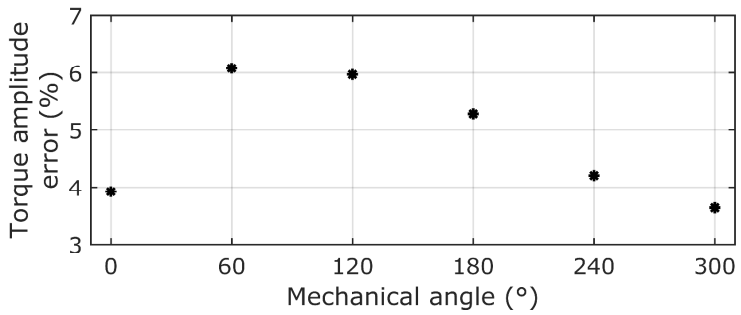

Fig. 5.57 Determined loading torque amplitude error according to the two-step method for different loading torque reference angle - experiment

The estimated torque angle deviations for different loading torque phase shifts are presented in Fig. 5.58.

According to Fig. 5.27 - Fig. 5.29, 2° estimated torque phase-shift deviation has no significant influence over the final results used for the torque pulsation reduction method.

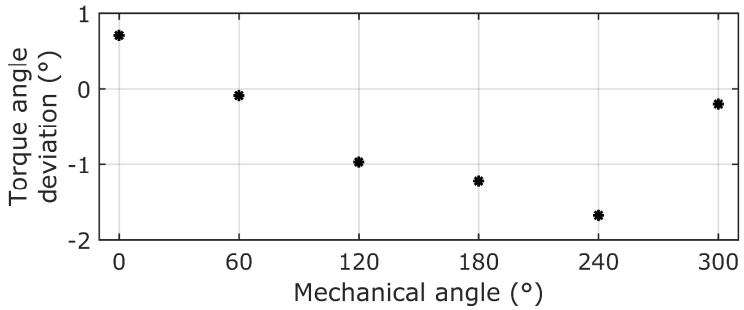

Fig. 5.58 Determined torque angle deviation according to the two-step method for different loading torque reference angle - experiment

5.4.3. Two-step method experimental validation – 1st, 2nd, and 3th harmonic-based loading torque

In the following, the two-step method is experimentally validated for a more complex loading torque profile based on the first three harmonics (fundamental, second, and third harmonic).

The following equation represents the loading torque reference the PLC gave to the VFC via Profibus and the actual torque produced by the loading machine, read from VFC.

As we already know, there is a significant difference between the torque reference given to the VFC and the actual torque produced by the loading machine. No phase shift was added to any harmonic.

BUPT

$$T_{load_{ref}} = 40\%+30\% \cdot cos(\omega_b \cdot t)+60\% \cdot cos(2 \cdot \omega_b \cdot t)+70\% \cdot cos(3 \cdot \omega_b \cdot t) \quad (5.36)$$

Where: the dc component and the amplitudes are related to the rated torque of the GCIM, $\omega_b = 2 \cdot \pi \cdot f_b$ represents the base angular frequency, the f_b represents the system frequency given by the GCIM and t represents the time.

Fig. 5.59 presents the torque reference given by the PLC and the actual loading torque, both read from the variable frequency converter that drives the loading machine. The VFC's limitation and how the actual torque is filtered can be observed.

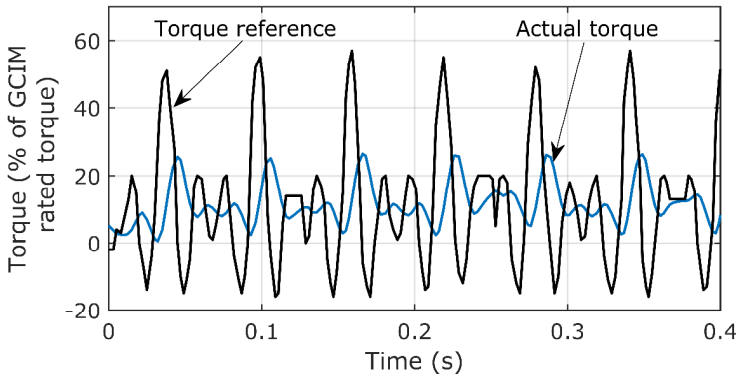

Fig. 5.59 Loading torque reference prescribed by the PLC to the load VFC

As we previously mentioned, inconsistent values appear due to the Profibus communication.

After the two-step method was applied in accordance with its procedure, the resulting loading torque is given in Fig. 5.60. The dc component and other harmonics higher than the 3rd order were not considered.

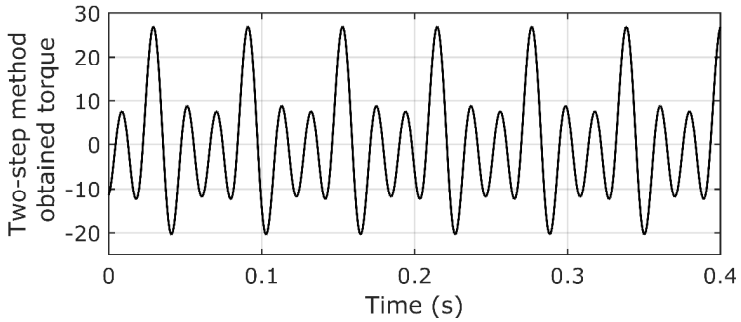

Fig. 5.60 Reconstructed loading torque from the two-step method considering the first three harmonics

Similar results compared to the actual loading torque can be successfully obtained by applying this method for loading torques composed of the first three harmonics.

BUPT

5.5. Conclusion

This chapter presents a practical approach to the well-known Active Torque Pulsation Reduction principle to a novel configuration of an electromechanical system with position-dependent loading torques with an auxiliary machine mounted on the same shaft.

In the first part of the chapter, a comprehensive simulation is given for open-loop principle validation (Fig. 5.9). The simulated open-loop results are validated experimentally. Torque and currents Fast Fourier Transform analysis are given in Fig. 5.42 - Fig. 5.44.

After principle validation, a closed-loop diagram is given with the related results, where the torque pulsations are reduced based on two induction machine torque observers. In this case, the torque pulsation amplitude is monitored and used as feedback in the closed-loop control scheme.

In the second part of the chapter, a two-step method is proposed for the system moment of inertia and loading torque determining. Simulation and experimental results are given for different frequency spectrums of the loading torque. The experimental setup limitations are highlighted for complex loading torques composed of the first three harmonics.

BUPT

6. Conclusion, contribution, and future work

6.1. Conclusions

This thesis had as its main purpose the study of the possibility of extending the classic role of industrial command and control equipment. In this context, using classic industrial equipment, three different applications are presented, simulated, and experimentally validated.

To extend the main traditional role of the Programmable Logic Controllers (PLC), three different low-cost PLCs were extensively investigated to be used as grid-connected induction machine electromagnetic torque observers. It was proven that the main factor that has to be considered for this type of application is not represented by the acquisition frequency but by the variation of the PLC's program cycle. In steady-state, a random 3% variation of the program cycle can lead to more than 50% error in the estimated torque. Not even advanced integration methods (such as Runge Kutta no. 4) produce better results. The low-cost PLCs have a significant limitation, thus producing poor results in terms of electrical machine torque estimators. However, they can be successfully used for frequency analysis considering the well-known Discrete Fourier Transform technique.

In an attempt to precisely estimate online the electromagnetic torque of a grid-connected induction machine, three torque estimators were simulated and implemented in a more-advanced FPGA-based processor. Considering the electrical machine's dynamic effect, the Luenberger-based torque observer produced better results than the presented dynamic computation torque estimator. In contrast with the investigated PLCs, all three torque estimators can run simultaneously on the Real-Time target with data transferred from the FPGA module.

In comparison with the third and fifth harmonics, the grid voltages' inverse component has a significant negative impact on the induction machine operation. Thus, more accurate simulation results are obtained if the real voltage spectrum is considered.

An artificial (synthetic) loading procedure was proposed for two identical induction machines without mechanical coupling driven by two identical dc-link connected, unidirectional variable frequency converters. The phase-rated current loading and thermal test can be performed with industrial standard equipment. No overvoltages occurred even at 120% of the rated current. The experiment revealed that the induction machines' efficiency has a major role as long as the ac source current spikes are given by the machines' losses over a complete period. The grid-absorbed currents are almost twice smaller for here presented method than one induction machine tested at rated power. It was shown that the current that flows between the induction machines during the artificial loading (via variable frequency converters) does not contain the triplens harmonics (3k, k=0,1,2,..) nor the fifth-order harmonic. Besides the open-loop control, a slow close-loop automatized method can be used to improve the total testing time. Acceptable results are obtained by comparing the artificial loading experimental test losses with those obtained from the simulation of one induction machine at rated power.

BUPT

For rotary electromechanical systems, acceptable results can be obtained regarding active torque pulsation reduction for position-dependent loading torque using a novel system configuration with a smaller auxiliary machine mounted on the same shaft. Although this configuration requires a third machine driven by a two-quadrant inverter, the auxiliary machine can successfully smoothen the torque alternating pulsations by producing a 180-degree phase-shifted torque compared to the loading torque. Besides the open-loop, a high-complexity method with two torque observers can be used in a closed-loop configuration to minimize the loading torque pulsation. The method efficiency is also validated by the current and torque Fast Fourier Transform analysis.

It was analytically demonstrated that the same configuration could be used in a two-step method for the system of inertia and loading torque detection. It was experimentally shown that the loading torque phase requires special attention for effective compensation. The two-step method can also be used for complex loading torques with harmonic content and phase shifts different from 0 degrees. The total system moment of inertia gives the loading torque frequency limitation. In this case, the loading machine can only produce the first three harmonics. The two-step method performances are influenced by the system's unknown variable time delay produced by both the communication and also by the internal control logic of the inverters.

6.2. Original contribution

In the following, in the author's opinion, the most relevant original contributions are related to:

- Performing a state-of-the-art regarding the thesis's main investigated fields: state and flux observers, synthetic electrical machine loading and torque pulsation reduction in electromechanical rotary systems.
- Investigation of three different types of low-cost Programmable Logic Controllers in order to extend their classic role.
- Performing the 11kW Induction Machine parameters identification and creating an acceptable simulated induction machine model, also considering the main losses.
- Performing a grid voltage analysis in terms of harmonic content and direct and inverse components.
- The PLC implementation of three different electromagnetic torque estimators and the Discrete Fourier Transform based on the Cooley-Tokey Radix-2 algorithm.
- The simulation, both for ideal data and ideal data with real characteristics, all three torque estimators: the direct computation method, the dynamic torque computation method, and the Luenberger-based torque observer.
- Performing a comprehensive comparison between all three torque estimators.
- Creating a Labview dedicated algorithm (FPGA+RT programming mode) for the cRIO-9086 platform for online investigation of all three torque estimators, including also the Modbus TPC communication procedure and the high-speed reading of the incremental encoder TTL-type signal.

BUPT

- Proposing a new twin un-coupled inverter-fed artificial loading methodology with comprehensive modeling analysis and testing validation.
- Testing multiple control techniques during artificial loading for ac-source current spikes limitation: 180-degree phase shift reference, variable phase shift reference, triangle phase shift reference.
- Performing a closed-loop automatized testing procedure for induction machine thermal testing with phase current feedback.
- Performing a frequency spectrum analysis for grid current as well as for the induction machine circulation current (via common dc link) during the synthetic loading.
- Simulating the artificial loading principle both for ac source current investigation and also for systems behavior analysis.
- Simulating and experimental validating the proposed active torque pulsation reduction method both in theoretical and practical situations.
- Proposing a new high-complexity closed-loop simulation for automatic reduction of torque pulsations based on two torque observers.
- Proposing, testing, and experimental validating of a novel mathematical two-step tool based on the current solution with an auxiliary machine mounted on the same shaft for preliminary system moment of inertia and loading torque detection procedure.
- Performing the two-step method stability analysis for machine parameters variation and extending the two-step method capabilities for more complex loading torques based on the first three harmonics.
- Building the necessary experimental setup for both applications: for artificial loading procedure: two identical induction machines driven by two identical dc link-connected variable frequency converters; for torque pulsation reduction method: with three mechanically coupled induction machines and two variable frequency converters.

6.3. Future work

This work was carried out in a continuously expanding field. Industrial equipment is exponentially growing its need in the market so that, in this context, more future work is needed:

- More research related to find a suitable low-cost with minimum-performance PLC that can be used successfully for torque estimation based on traditional observers is needed.
- Considering using new torque estimators suitable for low-cost processors with small cyclic time variations.
- Improve the torque estimators' stability and optimize them for low-performance equipment.
- Improve the loss estimation for the artificial loading method, also considering the reference speed of the artificial loading procedure (sine, triangle, phase-shifted sine).
- Create a lookup table-like dataset for experimental setup time delays used to reduce the two-step method's errors.
- New torque pulsation reduction strategies can be developed considering the maximum stress on the mechanical couplings also.

BUPT

References

[1] Z. Lv, 'Practical Application of Internet of Things in the Creation of Intelligent Services and Environments', *Front. Internet Things*, vol. 1, 2022, Accessed: Dec. 06, 2022. [Online]. Available: https://www.frontiersin.org/articles/10.3389/friot.2022.912388

[2] D. Pliatsios, P. Sarigiannidis, T. Lagkas, and A. G. Sarigiannidis, 'A Survey on SCADA Systems: Secure Protocols, Incidents, Threats and Tactics', *IEEE Commun. Surv. Tutor.*, vol. 22, no. 3, pp. 1942–1976, 2020, doi: 10.1109/COMST.2020.2987688.

[3] G. Yadav and K. Paul, 'Architecture and security of SCADA systems: A review', *Int. J. Crit. Infrastruct. Prot.*, vol. 34, p. 100433, Sep. 2021, doi: 10.1016/j.ijcip.2021.100433.

[4] A. A. Sallam and O. P. Malik, 'Scada Systems', in *Electric Distribution Systems*, IEEE, 2019, pp. 465–485. doi: 10.1002/9781119509332.ch17.

[5] K. M. Tofani, P. A. Permana, B. B. S. D. A. Harsono, D. R. Jintaka, and K. G. H. Mangunnkusumo, 'SCADA System Implementation for Small System Electricity', in *2020 2nd International Conference on Industrial Electrical and Electronics (ICIEE)*, Oct. 2020, pp. 57–61. doi: 10.1109/ICIEE49813.2020.9277497.

[6] T. S. Tamir *et al.*, 'Developing SCADA Systems to Monitor and Control Liquid and Detergent Factories', in *2020 IEEE 16th International Conference on Automation Science and Engineering (CASE)*, Aug. 2020, pp. 691–696. doi: 10.1109/CASE48305.2020.9217002.

[7] M. F. S. Khan *et al.*, 'PLC Based Energy-Efficient Home Automation System with Smart Task Scheduling', in *2019 IEEE Sustainable Power and Energy Conference (iSPEC)*, Nov. 2019, pp. 35–38. doi: 10.1109/iSPEC48194.2019.8975223.

[8] K. Smerpitak, W. Jearnpanitpong, A. Julsereewong, and T. Thepmanee, 'Multi-PLC Control System Based on Wireless Bridge/Base Stations for Work-in-Process Movements in Corrugated Box Manufacturer', in *2018 18th International Conference on Control, Automation and Systems (ICCAS)*, Oct. 2018, pp. 1175–1180.

[9] S. Howimanporn, S. Chookaew, and W. Sootkaneung, 'Implementation of PSO Based Gain-Scheduled PID and LQR for DC Motor Control Using PLC and SCADA', in *2018 International Conference on Control and Robots (ICCR)*, Sep. 2018, pp. 52–56. doi: 10.1109/ICCR.2018.8534485.

[10] S. Howimanporn, S. Chookaew, and C. Silawatchananai, 'Comparison between PID and Sliding Mode Controllers for Rotary Inverted Pendulum Using PLC', in *2020 4th International Conference on Automation, Control and Robots (ICACR)*, Oct. 2020, pp. 122–126. doi: 10.1109/ICACR51161.2020.9265510.

[11] İ. Köse, S. Öztürk, and M. Kuncan, 'PANTOGRAPHY APPLICATION WITH REAL-TIME PLC BASED ON IMAGE PROCESSING IN GANTRY ROBOT SYSTEM', *Eur. J. Tech. EJT*, vol. 9, no. 2, Art. no. 2, Dec. 2019, doi: 10.36222/ejt.621558.

[12] I. González, A. J. Calderón, and J. M. Portalo, 'Innovative Multi-Layered Architecture for Heterogeneous Automation and Monitoring Systems: Application Case of a Photovoltaic Smart Microgrid', *Sustainability*, vol. 13, no. 4, Art. no. 4, Jan. 2021, doi: 10.3390/su13042234.

[13] W. Zhang, F. Zhang, J. Zhang, J. Zhang, and J. Zhang, 'Application of PLC in Pneumatic Measurement Control System', *IOP Conf. Ser. Mater. Sci. Eng.*, vol. 452, no. 4, p. 042074, Dec. 2018, doi: 10.1088/1757-899X/452/4/042074.

BUPT

[14] R. Mihai, R. Gabriela, F. Constantin, A. Ciprian, and R. M. Simona, 'Design of EV Charging Station Controlled by PLC', in *2020 International Conference and Exposition on Electrical And Power Engineering (EPE)*, Oct. 2020, pp. 189–192. doi: 10.1109/EPE50722.2020.9305523.
[15] H. Zhu, 'Research on PLC DC Motor Speed Control System Based on Quantum Fuzzy Control Algorithm', in *2022 International Conference on Applied Artificial Intelligence and Computing (ICAAIC)*, May 2022, pp. 1672–1675. doi: 10.1109/ICAAIC53929.2022.9793235.
[16] B. Bo, L. Chuang, and C. Meng, 'Based on PLC Fuzzy Control Algorithm in the Application of Level Control', in *2016 International Symposium on Computer, Consumer and Control (IS3C)*, Jul. 2016, pp. 698–701. doi: 10.1109/IS3C.2016.179.
[17] R. Chimatapu, H. Hagras, M. Kern, and G. Owusu, 'Hybrid Deep Learning Type-2 Fuzzy Logic Systems For Explainable AI', in *2020 IEEE International Conference on Fuzzy Systems (FUZZ-IEEE)*, Jul. 2020, pp. 1–6. doi: 10.1109/FUZZ48607.2020.9177817.
[18] H. Leon-Garza, H. Hagras, A. Peña-Rios, A. Conway, and G. Owusu, 'A Big Bang-Big Crunch Type-2 Fuzzy Logic System for Explainable Semantic Segmentation of Trees in Satellite Images using HSV Color Space', in *2020 IEEE International Conference on Fuzzy Systems (FUZZ-IEEE)*, Jul. 2020, pp. 1–7. doi: 10.1109/FUZZ48607.2020.9177611.
[19] D. C. Mazur, B. G. Stewart, H. E. Clark, and R. Paes, 'Analysis of PLC vs. DCS in Industrial Petrochemical Applications', in *2019 IEEE Petroleum and Chemical Industry Committee Conference (PCIC)*, Sep. 2019, pp. 93–102. doi: 10.1109/PCIC30934.2019.9074522.
[20] Y. M. Chung, 'Overview and Characteristics of IoT PLC', in *2020 International Conference on Electronics, Information, and Communication (ICEIC)*, Jan. 2020, pp. 1–3. doi: 10.1109/ICEIC49074.2020.9051002.
[21] L. Ma, K. Liu, Y. Zou, and Y. Li, 'Comprehensive Energy Service - IPv6-based PLC-IoT Technology Enables Converged Multi-Service Transmission', in *2019 IEEE International Conference on Communications, Control, and Computing Technologies for Smart Grids (SmartGridComm)*, Oct. 2019, pp. 1–4. doi: 10.1109/SmartGridComm.2019.8909745.
[22] R. Langmann and M. Stiller, 'The PLC as a Smart Service in Industry 4.0 Production Systems', *Appl. Sci.*, vol. 9, no. 18, Art. no. 18, Jan. 2019, doi: 10.3390/app9183815.
[23] M. A. Ali, A. H. Miry, and T. M. Salman, 'IoT Based Water Tank Level Control System Using PLC', in *2020 International Conference on Computer Science and Software Engineering (CSASE)*, Apr. 2020, pp. 7–12. doi: 10.1109/CSASE48920.2020.9142067.
[24] I. Singh, D. Centea, and M. Elbestawi, 'IoT, IIoT and Cyber-Physical Systems Integration in the SEPT Learning Factory', *Procedia Manuf.*, vol. 31, pp. 116–122, Jan. 2019, doi: 10.1016/j.promfg.2019.03.019.
[25] H. Boyes, B. Hallaq, J. Cunningham, and T. Watson, 'The industrial internet of things (IIoT): An analysis framework', *Comput. Ind.*, vol. 101, pp. 1–12, Oct. 2018, doi: 10.1016/j.compind.2018.04.015.
[26] A. Radke and Z. Gao, 'A survey of state and disturbance observers for practitioners', Jul. 2006, p. 6 pp. doi: 10.1109/ACC.2006.1657545.
[27] K. Schechner and C. M. Hackl, 'Detection of rotational periodic torque deviations in variable-speed wind turbine systems using disturbance observer

BUPT

and phase-locked loop', *J. Phys. Conf. Ser.*, vol. 1037, no. 3, p. 032022, Jun. 2018, doi: 10.1088/1742-6596/1037/3/032022.
[28] D. Tian, R. Xu, E. Sariyildiz, and H. Gao, 'An Adaptive Switching-Gain Sliding-Mode-Assisted Disturbance Observer for High-Precision Servo Control', *IEEE Trans. Ind. Electron.*, vol. 69, no. 2, pp. 1762–1772, Feb. 2022, doi: 10.1109/TIE.2021.3057004.
[29] M. Stender, O. Wallscheid, and J. Böcker, 'Accurate Torque Control for Induction Motors by Utilizing a Globally Optimized Flux Observer', *IEEE Trans. Power Electron.*, vol. 36, no. 11, pp. 13261–13274, Nov. 2021, doi: 10.1109/TPEL.2021.3080129.
[30] A. K. Haridas and K. Vasudevan, 'Design and Analysis of Load Torque Observer for High Precision Position Control of PMSM', in *IECON 2019 - 45th Annual Conference of the IEEE Industrial Electronics Society*, Oct. 2019, vol. 1, pp. 998–1003. doi: 10.1109/IECON.2019.8926616.
[31] R. H. Jaafar and S. S. Saab, 'Approximate Differentiator With Varying Bandwidth for Control Tracking Applications', *IEEE Control Syst. Lett.*, vol. 5, no. 5, pp. 1585–1590, Nov. 2021, doi: 10.1109/LCSYS.2020.3041124.
[32] D. Astolfi, L. Zaccarian, and M. Jungers, 'On the use of low-pass filters in high-gain observers', *Syst. Control Lett.*, vol. 148, p. 104856, Feb. 2021, doi: 10.1016/j.sysconle.2020.104856.
[33] A. Chemori, 'Nonlinear control of parallel manipulators for very high accelerations without velocity measurement: stability analysis and experiments on Par2 parallel manipulator', *Robotica*, vol. 34, Jun. 2014, doi: 10.1017/S0263574714001246.
[34] J. Khan and K. Kim, 'A Performance Evaluation of the Alpha-Beta (α-β) Filter Algorithm with Different Learning Models: DBN, DELM, and SVM', *Appl. Sci.*, vol. 12, no. 19, Art. no. 19, Jan. 2022, doi: 10.3390/app12199429.
[35] D. Luenberger, 'An introduction to observers', *IEEE Trans. Autom. Control*, vol. 16, no. 6, pp. 596–602, Dec. 1971, doi: 10.1109/TAC.1971.1099826.
[36] A. A. Hussein, S. S. Salih, and Y. G. Ghasm, 'Implementation of Proportional-Integral-Observer Techniques for Load Frequency Control of Power System', *Procedia Comput. Sci.*, vol. 109, pp. 754–762, Jan. 2017, doi: 10.1016/j.procs.2017.05.307.
[37] S. BEALE and B. SHAFAI, 'Robust control system design with a proportional integral observer', *Int. J. Control*, vol. 50, no. 1, pp. 97–111, Jul. 1989, doi: 10.1080/00207178908953350.
[38] G. Besançon, 'An Overview on Observer Tools for Nonlinear Systems', in *Nonlinear Observers and Applications*, G. Besançon, Ed. Berlin, Heidelberg: Springer, 2007, pp. 1–33. doi: 10.1007/978-3-540-73503-8_1.
[39] J. Mohd Ali, N. Ha Hoang, M. A. Hussain, and D. Dochain, 'Review and classification of recent observers applied in chemical process systems', *Comput. Chem. Eng.*, vol. 76, pp. 27–41, May 2015, doi: 10.1016/j.compchemeng.2015.01.019.
[40] T. Lacey, 'Tutorial: the Kalman Filter 11.1 Introduction 11.2 Mean Squared Error', 1998. Accessed: Dec. 12, 2022. [Online]. Available: https://www.semanticscholar.org/paper/Tutorial%3A-the-Kalman-Filter-11.1-Introduction-11.2-Lacey/2a4761df17525de463341320bf0458c98e04c654
[41] D. I. Lawrie, P. J. Fleming, G. W. Irwin, and S. R. Jones, 'Kalman filtering: A survey of parallel processing alternatives', *IFAC Proc. Vol.*, vol. 24, no. 7, pp. 49–56, Sep. 1991, doi: 10.1016/B978-0-08-041699-1.50013-6.

BUPT

[42] A. Akca and M. Ö. Efe, 'Multiple Model Kalman and Particle Filters and Applications: A Survey', *IFAC-Pap.*, vol. 52, no. 3, pp. 73–78, Jan. 2019, doi: 10.1016/j.ifacol.2019.06.013.
[43] Y. Kim, H. Bang, Y. Kim, and H. Bang, *Introduction to Kalman Filter and Its Applications*. IntechOpen, 2018. doi: 10.5772/intechopen.80600.
[44] Q. Wang, X. Sun, and C. Wen, 'Design Method for a Higher Order Extended Kalman Filter Based on Maximum Correlation Entropy and a Taylor Network System', *Sensors*, vol. 21, no. 17, Sep. 2021, doi: 10.3390/s21175864.
[45] Q. Zhu, M. Xu, W. Liu, and M. Zheng, 'A state of charge estimation method for lithium-ion batteries based on fractional order adaptive extended kalman filter', *Energy*, vol. 187, p. 115880, Nov. 2019, doi: 10.1016/j.energy.2019.115880.
[46] A. D. Rosaline and U. Somarajan, 'Structured H-Infinity Controller for an Uncertain Deregulated Power System', *IEEE Trans. Ind. Appl.*, vol. 55, no. 1, pp. 892–906, Jan. 2019, doi: 10.1109/TIA.2018.2866560.
[47] W. S. Levine and R. T. Reichert, 'An introduction to H/sub infinity / control system design', in *29th IEEE Conference on Decision and Control*, Dec. 1990, pp. 2966–2974 vol.6. doi: 10.1109/CDC.1990.203329.
[48] W.-H. Chen, J. Yang, L. Guo, and S. Li, 'Disturbance-Observer-Based Control and Related Methods—An Overview', *IEEE Trans. Ind. Electron.*, vol. 63, no. 2, pp. 1083–1095, Feb. 2016, doi: 10.1109/TIE.2015.2478397.
[49] B. R. Andrievsky and I. B. Furtat, 'Disturbance Observers: Methods and Applications. I. Methods', *Autom. Remote Control*, vol. 81, no. 9, pp. 1563–1610, Sep. 2020, doi: 10.1134/S0005117920090015.
[50] S. Ding, W.-H. Chen, K. Mei, and D. J. Murray-Smith, 'Disturbance Observer Design for Nonlinear Systems Represented by Input–Output Models', *IEEE Trans. Ind. Electron.*, vol. 67, no. 2, pp. 1222–1232, Feb. 2020, doi: 10.1109/TIE.2019.2898585.
[51] A. Rahman, X. Lin, and C. Wang, 'Li-Ion Battery Anode State of Charge Estimation and Degradation Monitoring Using Battery Casing via Unknown Input Observer', *Energies*, vol. 15, no. 15, Art. no. 15, Jan. 2022, doi: 10.3390/en15155662.
[52] S.-H. Wang, E. Wang, and P. Dorato, 'Observing the states of systems with unmeasurable disturbances', *IEEE Trans. Autom. Control*, vol. 20, no. 5, pp. 716–717, Oct. 1975, doi: 10.1109/TAC.1975.1101076.
[53] M. Tranninger, H. Niederwieser, R. Seeber, and M. Horn, 'Unknown input observer design for linear time-invariant systems—A unifying framework', *Int. J. Robust Nonlinear Control*, vol. n/a, no. n/a, doi: 10.1002/rnc.6399.
[54] S. J. Kwon and W. K. Chung, Eds., 'Robust performance of the multiloop perturbation compensator', in *Perturbation Compensator based Robust Tracking Control and State Estimation of Mechanical Systems*, Berlin, Heidelberg: Springer, 2004, pp. 41–64. doi: 10.1007/BFb0121386.
[55] S. Kwon and W. K. Chung, 'A discrete-time design and analysis of perturbation observer for motion control applications', *IEEE Trans. Control Syst. Technol.*, vol. 11, no. 3, pp. 399–407, May 2003, doi: 10.1109/TCST.2003.810398.
[56] K. Łakomy and R. Madonski, 'Cascade extended state observer for active disturbance rejection control applications under measurement noise', *ISA Trans.*, vol. 109, pp. 1–10, Mar. 2021, doi: 10.1016/j.isatra.2020.09.007.
[57] I. H. Sarker, 'Deep Learning: A Comprehensive Overview on Techniques, Taxonomy, Applications and Research Directions', *SN Comput. Sci.*, vol. 2, no. 6, p. 420, Aug. 2021, doi: 10.1007/s42979-021-00815-1.

BUPT

[58] S. Zhang, *Artificial Intelligence in Electric Machine Drives: Advances and Trends*. 2021. doi: 10.36227/techrxiv.16782748.
[59] M. Stender, O. Wallscheid, and J. Böcker, 'Accurate Torque Estimation for Induction Motors by Utilizing a Hybrid Machine Learning Approach', in *2021 IEEE 19th International Power Electronics and Motion Control Conference (PEMC)*, Apr. 2021, pp. 390–397. doi: 10.1109/PEMC48073.2021.9432615.
[60] E. Agamloh, A. Cavagnino, and S. Vaschetto, 'Applicability of Superposition Equivalent Loading Method for Induction Machine Temperature Tests', in *IECON 2018 - 44th Annual Conference of the IEEE Industrial Electronics Society*, Oct. 2018, pp. 415–420. doi: 10.1109/IECON.2018.8591721.
[61] 'IEEE Standard Test Procedure for Polyphase Induction Motors and Generators', *IEEE Std 112-2017 Revis. IEEE Std 112-2004*, pp. 1–115, Feb. 2018, doi: 10.1109/IEEESTD.2018.8291810.
[62] A. Meyer and H. W. Lorenzen, 'Two-Frequency Heat Run - A Method of Examination for Three-Phase Induction Motors', *IEEE Trans. Power Appar. Syst.*, vol. PAS-98, no. 6, pp. 2338–2347, Nov. 1979, doi: 10.1109/TPAS.1979.319433.
[63] J. Herman, J. Bojkovski, R. Fišer, and K. Drobnič, 'An Improved Design of Synthetic Loading Method for a Rapid In-Wheel Motor Characterization in Different Operating Points', *IEEE Trans. Transp. Electrification*, vol. 7, no. 4, pp. 2562–2575, Dec. 2021, doi: 10.1109/TTE.2021.3089482.
[64] A. D. Martin, L. N. Tutelea, and I. Boldea, 'Twin Inverter-Fed Induction Machines Artificial Loading Without Mechanical Coupling', *IEEE Trans. Ind. Appl.*, vol. 58, no. 3, pp. 3738–3749, May 2022, doi: 10.1109/TIA.2022.3151320.
[65] Y. Loayza, A. Reinap, and M. Alaküla, 'Performance and efficiency evaluation of FPGA controlled IPMSM under dynamic loading', in *8th IEEE Symposium on Diagnostics for Electrical Machines, Power Electronics & Drives*, Sep. 2011, pp. 550–555. doi: 10.1109/DEMPED.2011.6063677.
[66] F. Barrero and M. J. Duran, 'Recent Advances in the Design, Modeling and Control of Multiphase Machines - Part 1', *IEEE Trans. Ind. Electron.*, May 2015.
[67] A. A. Abduallah, O. Dordevic, and M. Jones, 'Synthetic Loading for Symmetrical and Asymmetrical Six-Phase Machines', in *2018 IEEE 18th International Power Electronics and Motion Control Conference (PEMC)*, Aug. 2018, pp. 617–622. doi: 10.1109/EPEPEMC.2018.8521750.
[68] A. A. Abduallah, O. Dordevic, M. Jones, and E. Levi, 'Synthetic Loading for Symmetrical and Asymmetrical Nine-Phase Machines', in *IECON 2018 - 44th Annual Conference of the IEEE Industrial Electronics Society*, Oct. 2018, pp. 5860–5865. doi: 10.1109/IECON.2018.8592900.
[69] M. Zabaleta Maeztu, E. Levi, and M. Jones, 'A Novel Synthetic Loading Method for Multiple Three-Phase Winding Electric Machines', *IEEE Trans. Energy Convers.*, vol. PP, pp. 1–1, Jun. 2018, doi: 10.1109/TEC.2018.2850976.
[70] K. Shiba, S. Mase, Y. Yabe, and K. Tamura, 'Active/passive vibration control systems for tall buildings', *Smart Mater. Struct.*, vol. 7, no. 5, p. 588, Oct. 1998, doi: 10.1088/0964-1726/7/5/003.
[71] E. Gandelli, D. De Domenico, and V. Quaglini, 'Cyclic engagement of hysteretic steel dampers in braced buildings: a parametric investigation', *Bull. Earthq. Eng.*, vol. 19, no. 12, pp. 5219–5251, Sep. 2021, doi: 10.1007/s10518-021-01156-3.

BUPT

[72] M. Barbieri, S. Ilanko, and F. Pellicano, 'Active vibration control of seismic excitation', *Nonlinear Dyn.*, vol. 93, no. 1, pp. 41–52, Jul. 2018, doi: 10.1007/s11071-017-3853-y.
[73] M. Wang *et al.*, *Active Vibration Suppression Based on Piezoelectric Actuator*. IntechOpen, 2022. doi: 10.5772/intechopen.103725.
[74] A. Hashemi, J. Jang, and S. Hosseini-Hashemi, 'Smart Active Vibration Control System of a Rotary Structure Using Piezoelectric Materials', *Sensors*, vol. 22, no. 15, Art. no. 15, Jan. 2022, doi: 10.3390/s22155691.
[75] T. Kamada *et al.*, 'Active vibration control of frame structures with smart structures using piezoelectric actuators (Vibration control by control of bending moments of columns)', *Smart Mater. Struct.*, vol. 6, no. 4, p. 448, Aug. 1997, doi: 10.1088/0964-1726/6/4/009.
[76] S. Zhang, R. Schmidt, and X. Qin, 'Active vibration control of piezoelectric bonded smart structures using PID algorithm', *Chin. J. Aeronaut.*, vol. 28, no. 1, pp. 305–313, Feb. 2015, doi: 10.1016/j.cja.2014.12.005.
[77] Z. Huang, Y. Mao, A. Dai, M. Han, X. Wang, and F. Chu, 'Active Vibration Control of Piezoelectric Sandwich Plates', *Materials*, vol. 15, no. 11, Art. no. 11, Jan. 2022, doi: 10.3390/ma15113907.
[78] K. Lang and P. Xia, 'Hybrid Active Vibration Control of Helicopter Fuselage Driven by Piezoelectric Stack Actuators', *J. Aircr.*, vol. 56, no. 2, pp. 719–729, 2019, doi: 10.2514/1.C034965.
[79] S. M. Kuo and D. R. Morgan, 'Active noise control: a tutorial review', *Proc. IEEE*, vol. 87, no. 6, pp. 943–973, Jun. 1999, doi: 10.1109/5.763310.
[80] O. Ocak and M. Aydin, 'An Innovative Semi-FEA Based, Variable Magnet-Step-Skew to Minimize Cogging Torque and Torque Pulsations in Permanent Magnet Synchronous Motors', *IEEE Access*, vol. 8, pp. 210775–210783, 2020, doi: 10.1109/ACCESS.2020.3038340.
[81] Q. Chen, G. Xu, F. Zhai, and G. Liu, 'A Novel Spoke-Type PM Motor With Auxiliary Salient Poles for Low Torque Pulsation', *IEEE Trans. Ind. Electron.*, vol. 67, no. 6, pp. 4762–4773, Jun. 2020, doi: 10.1109/TIE.2019.2924864.
[82] S. Leitner, H. Gruebler, and A. Muetze, 'Cogging Torque Minimization and Performance of the Sub-Fractional HP BLDC Claw-Pole Motor', *IEEE Trans. Ind. Appl.*, vol. 55, no. 5, pp. 4653–4664, Sep. 2019, doi: 10.1109/TIA.2019.2923569.
[83] M. Caruso, A. O. Di Tommaso, R. Miceli, and F. Viola, 'A Cogging Torque Minimization Procedure for Interior Permanent Magnet Synchronous Motors Based on a Progressive Modification of the Rotor Lamination Geometry', *Energies*, vol. 15, no. 14, Art. no. 14, Jan. 2022, doi: 10.3390/en15144956.
[84] J. Liu, H. Li, and Y. Deng, 'Torque Ripple Minimization of PMSM Based on Robust ILC Via Adaptive Sliding Mode Control', *IEEE Trans. Power Electron.*, vol. 33, no. 4, pp. 3655–3671, Apr. 2018, doi: 10.1109/TPEL.2017.2711098.
[85] H. W. Yoo, S. Ito, and G. Schitter, 'High speed laser scanning microscopy by iterative learning control of a galvanometer scanner', *Control Eng. Pract.*, vol. 50, pp. 12–21, May 2016, doi: 10.1016/j.conengprac.2016.02.007.
[86] G. Hillerström and K. Walgama, 'Repetitive Control Theory and Applications - A Survey', *IFAC Proc. Vol.*, vol. 29, no. 1, pp. 1446–1451, Jun. 1996, doi: 10.1016/S1474-6670(17)57870-2.
[87] O. da Silva Brandão Jr, L. F. A. Pereira, and J. V. Flores, 'A Systematic Method for Repetitive Controller Design Based on The Process Frequency Response', *J. Control Autom. Electr. Syst.*, vol. 33, no. 5, pp. 1364–1374, Oct. 2022, doi: 10.1007/s40313-021-00873-z.

BUPT

[88] S. Mohanapriya, R. Sakthivel, and D. J. Almakhles, 'Repetitive control design for vehicle lateral dynamics with state-delay', *IET Control Theory Appl.*, vol. 14, no. 12, pp. 1619–1627, 2020, doi: 10.1049/iet-cta.2019.1194.
[89] X. Li, Z. Jiao, Y. Li, and Y. Cao, 'Adaptive Repetitive Control of A Linear Oscillating Motor under Periodic Hydraulic Step Load', *Sensors*, vol. 20, no. 4, Art. no. 4, Jan. 2020, doi: 10.3390/s20041140.
[90] M. Hagemeyer, N. Frohleke, J. Bocker, B. Rödder, L. Aßmann, and B. Völkel, 'Design of a flywheel energy storage system for high current pulsating loads', in *2017 IEEE 12th International Conference on Power Electronics and Drive Systems (PEDS)*, Dec. 2017, p. 1,068-1,073. doi: 10.1109/PEDS.2017.8289157.
[91] Z. Lin, J. Wang, and D. Howe, 'A Hybrid Current Controller for Linear Reciprocating Vapor Compressors', in *2007 IEEE Industry Applications Annual Meeting*, Sep. 2007, pp. 274–280. doi: 10.1109/07IAS.2007.38.
[92] H. Yaodong, F. Yang, L. Du, and M. Ouyang, 'Simulation Research on Engine Speed Fluctuation Suppression Based on Engine Torque Observer by Using a Flywheel ISG', *SAE Tech. Pap.*, Apr. 2019, doi: 10.4271/2019-01-0787.
[93] F. Pasteur, M. Brunelli, A. Fusi, F. Grasso, and A. Ussi, 'Torsional Vibration Analysis of Reciprocating Compressor Trains driven by Induction Motors', *IOP Conf. Ser. Mater. Sci. Eng.*, vol. 90, Aug. 2015, doi: 10.1088/1757-899X/90/1/012021.
[94] T. Sysala, M. Pospichal, and P. Neumann, 'Monitoring and control system for a smart family house controlled via programmable controller', in *2016 17th International Carpathian Control Conference (ICCC)*, May 2016, pp. 706–710. doi: 10.1109/CarpathianCC.2016.7501187.
[95] A. Alaribi, A. Elazhari, and O. A. Zargelin, 'PLC Based a Robust Solution for an Urban Area Water System Dilemma', in *2021 IEEE 11th Annual Computing and Communication Workshop and Conference (CCWC)*, Jan. 2021, pp. 1300–1305. doi: 10.1109/CCWC51732.2021.9375843.
[96] M. A. Sehr *et al.*, 'Programmable Logic Controllers in the Context of Industry 4.0', *IEEE Trans. Ind. Inform.*, vol. 17, no. 5, pp. 3523–3533, May 2021, doi: 10.1109/TII.2020.3007764.
[97] E. B. Priyanka, K. Krishnamurthy, and C. Maheswari, 'Remote monitoring and control of pressure and flow in oil pipelines transport system using PLC based controller', in *2016 Online International Conference on Green Engineering and Technologies (IC-GET)*, Nov. 2016, pp. 1–6. doi: 10.1109/GET.2016.7916754.
[98] L. C. Tasca, E. Pignaton de Freitas, and F. R. Wagner, 'A study on the performance impact of programmable logic controllers based on enhanced architecture and organization', *Microprocess. Microsyst.*, vol. 76, p. 103082, Jul. 2020, doi: 10.1016/j.micpro.2020.103082.
[99] D. Gonzalez-Jimenez, J. del-Olmo, J. Poza, F. Garramiola, and P. Madina, 'Data-Driven Fault Diagnosis for Electric Drives: A Review', *Sensors*, vol. 21, no. 12, Art. no. 12, Jan. 2021, doi: 10.3390/s21124024.
[100] M. Barzegaran *et al.*, 'Fogification of electric drives: An industrial use case', in *2020 25th IEEE International Conference on Emerging Technologies and Factory Automation (ETFA)*, Sep. 2020, vol. 1, pp. 77–84. doi: 10.1109/ETFA46521.2020.9212010.
[101] L. Magadán, F. J. Suárez, J. C. Granda, and D. F. García, 'Real-Time Monitoring of Electric Motors for Detection of Operating Anomalies and Predictive Maintenance', in *Science and Technologies for Smart Cities*, Cham, 2020, pp. 301–311. doi: 10.1007/978-3-030-51005-3_25.

BUPT

[102] L. Magadán, F. J. Suárez, J. C. Granda, and D. F. García, 'Low-cost real-time monitoring of electric motors for the Industry 4.0', *Procedia Manuf.*, vol. 42, pp. 393–398, Jan. 2020, doi: 10.1016/j.promfg.2020.02.057.
[103] A. D. Martin, L. Tutelea, R. Babau, and I. Boldea, 'A novel approach to PLCs based systems utilized in electric drives', in *2019 International Aegean Conference on Electrical Machines and Power Electronics (ACEMP) 2019 International Conference on Optimization of Electrical and Electronic Equipment (OPTIM)*, Aug. 2019, pp. 77–84. doi: 10.1109/ACEMP-OPTIM44294.2019.9007170.
[104] W. Zhong and Z. Li, 'Optimal flight control design in irregular sampled-data control systems', in *2009 IEEE International Conference on Automation and Logistics*, Aug. 2009, pp. 772–777. doi: 10.1109/ICAL.2009.5262820.
[105] C.-W. Hung, C.-T. Lin, and J.-H. Chen, 'A variable sampling PI control with variable sampling torque compensation for BLDC motors', in *2010 5th IEEE Conference on Industrial Electronics and Applications*, Jun. 2010, pp. 1234–1237. doi: 10.1109/ICIEA.2010.5515670.
[106] P. Albertos and A. Crespo, 'Real-time control of non-uniformly sampled systems', *Control Eng. Pract.*, vol. 7, no. 4, pp. 445–458, Apr. 1999, doi: 10.1016/S0967-0661(99)00005-2.
[107] M. Kondratiuk, L. Ambroziak, E. Pawluszewicz, and J. Janczak, 'Discrete PID algorithm with non-uniform sampling – Practical implementation in control system', presented at the 2ND INTERNATIONAL CONFERENCE ON CHEMISTRY, CHEMICAL PROCESS AND ENGINEERING (IC3PE), Yogyakarta, Indonesia, 2018, p. 020029. doi: 10.1063/1.5066491.
[108] H. Feichtinger and K. Gröchenig, 'Theory and Practice of Irregular Sampling', *Wavelets Math. Appl.*, Jan. 1994.
[109] ABB, 'Compact Control Builder AC 800M Product Guide, Version 6.0', p. 150, May 2016.
[110] Siemens, 'Simatic, S7-1500 Cycle and response times', *Siemens AG 2013 - 2014*, p. 31, Feb. 2014.
[111] 'logix-rm002_-en-p.pdf'. Accessed: Jun. 13, 2022. [Online]. Available: https://literature.rockwellautomation.com/idc/groups/literature/documents/rm/logix-rm002_-en-p.pdf
[112] J. W. Cooley, P. A. W. Lewis, and P. D. Welch, 'The Fast Fourier Transform and Its Applications', *IEEE Trans. Educ.*, vol. 12, no. 1, pp. 27–34, Mar. 1969, doi: 10.1109/TE.1969.4320436.
[113] P. Duhamel and M. Vetterli, 'Fast fourier transforms: A tutorial review and a state of the art', *Signal Process.*, vol. 19, no. 4, pp. 259–299, Apr. 1990, doi: 10.1016/0165-1684(90)90158-U.
[114] Z. Wang, 'Fast algorithms for the discrete W transform and for the discrete Fourier transform', *IEEE Trans. Acoust. Speech Signal Process.*, vol. 32, no. 4, pp. 803–816, Aug. 1984, doi: 10.1109/TASSP.1984.1164399.
[115] R. Jaros *et al.*, 'Advanced Signal Processing Methods for Condition Monitoring', *Arch. Comput. Methods Eng.*, Oct. 2022, doi: 10.1007/s11831-022-09834-4.
[116] Y. Lan, Z. Li, J. Qu, J. Wu, and J. Yang, 'A Fast Doppler Parameters Estimation Method for Moving Target Imaging Based ON 2D-FFT', in *IGARSS 2018 - 2018 IEEE International Geoscience and Remote Sensing Symposium*, Jul. 2018, pp. 589–592. doi: 10.1109/IGARSS.2018.8517704.
[117] G. V. Portnova and K. V. Gladun, 'Laugh and Crying Perception in Patients with Severe and Moderate TBI Using FFT Analysis', in *2017 IEEE 30th*

BUPT

International Symposium on Computer-Based Medical Systems (CBMS), Jun. 2017, pp. 123–126. doi: 10.1109/CBMS.2017.11.

[118] S. M. Noor, E. John, and M. Panday, 'Design and Implementation of an Ultralow-Energy FFT ASIC for Processing ECG in Cardiac Pacemakers', *IEEE Trans. Very Large Scale Integr. VLSI Syst.*, vol. 27, no. 4, pp. 983–987, Apr. 2019, doi: 10.1109/TVLSI.2018.2883642.

[119] V. Tutatchikov, 'Application of parallel version two-dimensional fast Fourier transform calculating algorithm with an analogue of the Cooley-Tukey algorithm', in *2020 International Conference on Information Technology and Nanotechnology (ITNT)*, May 2020, pp. 1–6. doi: 10.1109/ITNT49337.2020.9253305.

[120] A. Madanayake *et al.*, 'Fast Radix-32 Approximate DFTs for 1024-Beam Digital RF Beamforming', *IEEE Access*, vol. 8, pp. 96613–96627, 2020, doi: 10.1109/ACCESS.2020.2994550.

[121] A. Bekele, 'Cooley-Tukey FFT Algorithms', p. 4, 2016.

[122] N. Brisebarre, M. Joldeş, J.-M. Muller, A.-M. Naneş, and J. Picot, 'Error Analysis of Some Operations Involved in the Cooley-Tukey Fast Fourier Transform', *ACM Trans. Math. Softw.*, vol. 46, no. 2, p. 11:1-11:27, May 2020, doi: 10.1145/3368619.

[123] P. Heckbert, 'Fourier Transforms and the Fast Fourier Transform (FFT) Algorithm', p. 13.

[124] B. B. Malakanagouda and S. K. Harisha, 'PLC based automation of test rig for brake actuators', in *2017 International Conference on Energy, Communication, Data Analytics and Soft Computing (ICECDS)*, Aug. 2017, pp. 1238–1243. doi: 10.1109/ICECDS.2017.8389639.

[125] B. Klima, L. Buchta, M. Dosedel, Z. Havranek, and P. Blaha, 'Prognosis and Health Management in electric drives applications implemented in existing systems with limited data rate', in *2019 24th IEEE International Conference on Emerging Technologies and Factory Automation (ETFA)*, Sep. 2019, pp. 870–876. doi: 10.1109/ETFA.2019.8869520.

[126] M. Adamiak, D. Baigent, and R. Mackiewicz, 'IEC 61850 Communication Networks and Systems In Substations':, p. 8.

[127] F. M. Tilaro, B. Copy, and M. Gonzalez-Berges, 'IEC 61850 Industrial Communication Standards under Test', p. 4, 2014.

[128] S.-H. Lee, A. Yoo, H.-J. Lee, Y.-D. Yoon, and B.-M. Han, 'Identification of Induction Motor Parameters at Standstill Based on Integral Calculation', *IEEE Trans. Ind. Appl.*, vol. 53, no. 3, pp. 2130–2139, May 2017, doi: 10.1109/TIA.2017.2650141.

[129] M. I. Mossad, M. Azab, and A. Abu-Siada, 'A novel evolutionary technique to estimate induction machine parameters from name plate data', in *2016 XXII International Conference on Electrical Machines (ICEM)*, Sep. 2016, pp. 66–71. doi: 10.1109/ICELMACH.2016.7732507.

[130] D. M. Reed, H. F. Hofmann, and J. Sun, 'Offline Identification of Induction Machine Parameters With Core Loss Estimation Using the Stator Current Locus', *IEEE Trans. Energy Convers.*, vol. 31, no. 4, pp. 1549–1558, Dec. 2016, doi: 10.1109/TEC.2016.2601781.

[131] S. A. Odhano, P. Pescetto, H. A. A. Awan, M. Hinkkanen, G. Pellegrino, and R. Bojoi, 'Parameter Identification and Self-Commissioning in AC Motor Drives: A Technology Status Review', *IEEE Trans. Power Electron.*, vol. 34, no. 4, pp. 3603–3614, Apr. 2019, doi: 10.1109/TPEL.2018.2856589.

BUPT

[132] E. Mölsä, L. Tiitinen, S. Saarakkala, L. Peretti, and M. Hinkkanen, 'Standstill Self-Commissioning of an Induction Motor Drive', in *2020 IEEE Energy Conversion Congress and Exposition (ECCE)*, Oct. 2020, pp. 3044–3050. doi: 10.1109/ECCE44975.2020.9236035.

[133] Y.-S. Lai, 'Modeling and vector control of induction machines-a new unified approach', in *IEEE Power Engineering Society. 1999 Winter Meeting (Cat. No.99CH36233)*, Jan. 1999, vol. 1, pp. 47–52 vol.1. doi: 10.1109/PESW.1999.747424.

[134] S. Lee and J. Yun, 'Influence of electrical steel characteristics on efficiency of industrial induction motors', in *2017 20th International Conference on Electrical Machines and Systems (ICEMS)*, Aug. 2017, pp. 1–4. doi: 10.1109/ICEMS.2017.8056353.

[135] J. Cheaytani, A. Benabou, A. Tounzi, and M. Dessoude, 'Stray Load Losses Analysis of Cage Induction Motor Using 3-D Finite-Element Method With External Circuit Coupling', *IEEE Trans. Magn.*, vol. 53, no. 6, pp. 1–4, Jun. 2017, doi: 10.1109/TMAG.2017.2661878.

[136] S. Yamamoto, H. Hirahara, and B. A. Shantha, 'A Method to Estimate Torque and Stray Load Loss of Induction Motor without Torque Detector', in *2019 IEEE Energy Conversion Congress and Exposition (ECCE)*, Sep. 2019, pp. 2341–2346. doi: 10.1109/ECCE.2019.8913232.

[137] A. Arkkio, S. Cederström, H. A. A. Awan, S. E. Saarakkala, and T. P. Holopainen, 'Additional Losses of Electrical Machines Under Torsional Vibration', *IEEE Trans. Energy Convers.*, vol. 33, no. 1, pp. 245–251, Mar. 2018, doi: 10.1109/TEC.2017.2733546.

[138] L. Aarniovuori, M. Niemelä, J. Pyrhönen, W. Cao, and E. B. Agamloh, 'Loss Components and Performance of Modern Induction Motors', Sep. 2018, pp. 1253–1259. doi: 10.1109/ICELMACH.2018.8507189.

[139] R. S. Kanchan and R. R. Moghaddam, 'Experimental validation of a novel core-loss model including additional harmonic losses for online energy efficient control of induction motors', in *2017 IEEE International Electric Machines and Drives Conference (IEMDC)*, May 2017, pp. 1–6. doi: 10.1109/IEMDC.2017.8002124.

[140] I. Boldea and S. A. Nasar, *The Induction Machines Design Handbook*, 2nd ed. Boca Raton: CRC Press, 2018. doi: 10.1201/9781315222592.

[141] D. Zhang and R. An, 'Effect of Voltage Unbalance and Distortion on the Loss Characteristics of Three Phase Cage Induction Motor', *IET Electr. Power Appl.*, vol. 12, Oct. 2017, doi: 10.1049/iet-epa.2017.0464.

[142] D. Zhang, R. An, and T. Wu, 'Effect of voltage unbalance and distortion on the loss characteristics of three-phase cage induction motor', *IET Electr. Power Appl.*, vol. 12, no. 2, pp. 264–270, 2018, doi: 10.1049/iet-epa.2017.0464.

[143] G. Tanuku and P. Pillay, 'Induction Machine Emulation under Asymmetric Grid Faults', in *2020 IEEE Energy Conversion Congress and Exposition (ECCE)*, Oct. 2020, pp. 2351–2356. doi: 10.1109/ECCE44975.2020.9235830.

[144] F. BABAA and O. BENNIS, 'Steady State Analytical Study of Stator Current Harmonic Spectrum Components on Three-Phase Induction Motor under Unbalanced Supply Voltage', in *2020 International Conference on Control, Automation and Diagnosis (ICCAD)*, Oct. 2020, pp. 1–6. doi: 10.1109/ICCAD49821.2020.9260526.

[145] S. Deleanu, M. Iordache, M. Stanculescu, and D. Niculae, 'The Induction Machine Operating from a Voltage Supply, Unbalanced and Polluted with Harmonics: A Practical Approach', in *2019 15th International Conference on*

BUPT

Engineering of Modern Electric Systems (EMES), Jun. 2019, pp. 181–184. doi: 10.1109/EMES.2019.8795212.

[146] R. Lin, L. Xu, and X. Zheng, 'A Method for Harmonic Sources Detection based on Harmonic Distortion Power Rate', *IOP Conf. Ser. Mater. Sci. Eng.*, vol. 322, p. 072038, Mar. 2018, doi: 10.1088/1757-899X/322/7/072038.

[147] M. J. H. Rawa, D. W. P. Thomas, and M. Sumner, 'Experimental Measurements and Computer Simulations of FL and CFL for Harmonic Studies', in *2014 UKSim-AMSS 16th International Conference on Computer Modelling and Simulation*, Mar. 2014, pp. 335–339. doi: 10.1109/UKSim.2014.13.

[148] P. Jain, A. K. Tiwari, and S. K. Jain, 'Harmonic source identification in distribution system using estimation of signal parameters via rotational invariance technique-total harmonic power method', *Trans. Inst. Meas. Control*, vol. 40, no. 12, pp. 3415–3423, Aug. 2018, doi: 10.1177/0142331217721316.

[149] D. Carta, C. Muscas, P. A. Pegoraro, and S. Sulis, 'Identification and Estimation of Harmonic Sources Based on Compressive Sensing', *IEEE Trans. Instrum. Meas.*, vol. 68, no. 1, pp. 95–104, Jan. 2019, doi: 10.1109/TIM.2018.2838738.

[150] Д. В. Філянін, 'IDENTIFICATION OF HARMONIC DISTORTION SOURCES IN DISTRIBUTION SYSTEMS USING THE DISCRETE FOURIER TRANSFORM ON PERIODS', *POWER Eng. Econ. Tech. Ecol.*, vol. 0, no. 2, pp. 110–119, Oct. 2018, doi: 10.20535/1813-5420.2.2018.147373.

[151] J. Guo, C. Jiang, C. Guan, T. Zhang, and J. Pu, 'Modeling and Simulation of Power Grid Voltage Harmonic Detection Method Based on Adaptive Kalman Filter', in *2021 33rd Chinese Control and Decision Conference (CCDC)*, May 2021, pp. 6166–6172. doi: 10.1109/CCDC52312.2021.9601355.

[152] M. Koteich, 'Flux estimation algorithms for electric drives: a comparative study', in *International Conference on Renewable Energies for Developing countries (REDEC 2016)*, Zouk Mosbeh, Lebanon, Jul. 2016. Accessed: Jun. 27, 2022. [Online]. Available: https://hal.archives-ouvertes.fr/hal-01322795

[153] P. Brandstetter and M. Kuchar, 'Rotor flux estimation using voltage model of induction motor', in *2015 16th International Scientific Conference on Electric Power Engineering (EPE)*, May 2015, pp. 246–250. doi: 10.1109/EPE.2015.7161090.

[154] A. Aliaskari, B. Zarei, S. A. Davari, F. Wang, and R. M. Kennel, 'A Modified Closed-Loop Voltage Model Observer Based on Adaptive Direct Flux Magnitude Estimation in Sensorless Predictive Direct Voltage Control of an Induction Motor', *IEEE Trans. Power Electron.*, vol. 35, no. 1, pp. 630–639, Jan. 2020, doi: 10.1109/TPEL.2019.2912003.

[155] G.-J. Jo and J.-W. Choi, 'Gopinath Model-Based Voltage Model Flux Observer Design for Field-Oriented Control of Induction Motor', *IEEE Trans. Power Electron.*, vol. 34, no. 5, pp. 4581–4592, May 2019, doi: 10.1109/TPEL.2018.2864322.

[156] A. Aliaskari and S. A. Davari, 'A new closed-loop voltage model flux observer for sensorless DTC method', in *2017 8th Power Electronics, Drive Systems & Technologies Conference (PEDSTC)*, Mashhad, Iran, 2017, pp. 143–148. doi: 10.1109/PEDSTC.2017.7910405.

[157] V. Anand, A. Alam, S. Singh, and A. Gautam, 'Hardware Implementation of Real-Time Flux, Torque, Sensorless Speed Estimation of a 3KW Three-Phase Induction Machine using LabVIEW', in *2018 International Conference on Current Trends towards Converging Technologies (ICCTCT)*, Mar. 2018, pp. 1–6. doi: 10.1109/ICCTCT.2018.8550952.

BUPT

[158] S. V. B. S. Reddy, B. Kumar, and D. Swaroop, 'Investigations on Training Algorithms for Neural Networks Based Flux Estimator Used in Speed Estimation of Induction Motor', in *2019 6th International Conference on Signal Processing and Integrated Networks (SPIN)*, Mar. 2019, pp. 1090–1094. doi: 10.1109/SPIN.2019.8711623.

[159] H. Xu, F. Zhao, W. Cong, and W. Peng, 'Study of a New Rotor Flux Estimator for Induction Machine Based on Sliding Mode Control', in *2016 IEEE Vehicle Power and Propulsion Conference (VPPC)*, Oct. 2016, pp. 1–5. doi: 10.1109/VPPC.2016.7791785.

[160] Y. Liu, S. Cheng, B. Ning, and Y. Li, 'Stator flux estimation with vector transforming and signal filtering method for electrical machines', *IET Power Electron.*, vol. 11, no. 2, pp. 357–363, 2018, doi: 10.1049/iet-pel.2017.0331.

[161] G.-J. Jo and J.-W. Choi, 'Rotor Flux Estimator Design With Offset Extractor for Sensorless-Driven Induction Motors', *IEEE Trans. Power Electron.*, vol. 37, no. 4, pp. 4497–4510, Apr. 2022, doi: 10.1109/TPEL.2021.3126331.

[162] A. N. Smith, S. M. Gadoue, and J. W. Finch, 'Improved Rotor Flux Estimation at Low Speeds for Torque MRAS-Based Sensorless Induction Motor Drives', *IEEE Trans. Energy Convers.*, vol. 31, no. 1, pp. 270–282, Mar. 2016, doi: 10.1109/TEC.2015.2480961.

[163] S. Garvey, I. Kolak, and M.T. Wright, 'Aspect of mixed frequency testing for induction machines', *Rec. ICEM-1994D14 Paris Fr.*.

[164] L. Tutelea, I. Boldea, A. E. Ritchie, P. Sandholdt, and F. Blaabjerg, 'Thermal Testing for Inverter-Fed Induction Machines using Mixed Frequency Method', in *Proceedings of International Conference on Electrical Machines, ICEM'98, Istanbul, Turkey, Sept. 1998*, 1998. Accessed: Jul. 29, 2021. [Online]. Available: https://vbn.aau.dk/en/publications/thermal-testing-for-inverter-fed-induction-machines-using-mixed-f

[165] J. Faiz and M. B. B. Sharifian, 'Optimal design of three phase induction motors and their comparison with a typical industrial motor', *Comput. Electr. Eng.*, vol. 27, no. 2, pp. 133–144, May 2001, doi: 10.1016/S0045-7906(00)00010-0.

[166] S. L. Ho and W. N. Fu, 'Analysis of indirect temperature-rise tests of induction machines using time stepping finite element method', *IEEE Trans. Energy Convers.*, vol. 16, no. 1, pp. 55–60, Mar. 2001, doi: 10.1109/60.911404.

[167] S. S. Dessouky, M. Fawzi, B. E. Elnaghi, H. A. Ibrahim, and M. K. Shehata, 'Synthetic loading of three phase induction machines using PWM inverter', in *2017 Nineteenth International Middle East Power Systems Conference (MEPCON)*, Cairo, Dec. 2017, pp. 1044–1047. doi: 10.1109/MEPCON.2017.8301310.

[168] C. Grantham and M. Sheng, 'The synthetic loading of three-phase induction motors using microprocessor controlled power electronics', in *Proceedings of 1995 International Conference on Power Electronics and Drive Systems. PEDS 95*, Feb. 1995, pp. 471–476 vol.1. doi: 10.1109/PEDS.1995.404876.

[169] Y. Ji, P. Giangrande, V. Madonna, W. Zhao, and M. Galea, 'Reliability-Oriented Design of Inverter-Fed Low-Voltage Electrical Machines: Potential Solutions', *Energies*, vol. 14, no. 14, Art. no. 14, Jan. 2021, doi: 10.3390/en14144144.

[170] S.-H. Park, E.-C. Lee, J.-C. Park, S.-W. Hwang, and M.-S. Lim, 'Prediction of Mechanical Loss for High-Power-Density PMSM Considering Eddy Current Loss

BUPT

of PMs and Conductors', *IEEE Trans. Magn.*, vol. 57, no. 2, pp. 1–5, Feb. 2021, doi: 10.1109/TMAG.2020.3007439.
[171] R. Wrobel, G. Vainel, C. Copeland, T. Duda, D. Staton, and P. H. Mellor, 'Investigation of Mechanical Loss Components and Heat Transfer in an Axial-Flux PM Machine', *IEEE Trans. Ind. Appl.*, vol. 51, no. 4, pp. 3000–3011, Jul. 2015, doi: 10.1109/TIA.2015.2405499.
[172] I. Boldea and S. Nasar, *The Induction Machines Design Handbook*. 2018. doi: 10.1201/9781315222592.
[173] A. D. Martin, L. N. Tutelea, and I. Boldea, 'Twin Induction Machines Artificial Loading Without Mechanical Coupling', in *2020 International Conference on Electrical Machines (ICEM)*, Aug. 2020, vol. 1, pp. 352–358. doi: 10.1109/ICEM49940.2020.9270782.
[174] C. Klumpner, I. Boldea, and F. Blaabjerg, 'Artificial loading of the induction motors using a matrix converter', in *2000 Eighth International Conference on Power Electronics and Variable Speed Drives (IEE Conf. Publ. No. 475)*, Sep. 2000, pp. 40–45. doi: 10.1049/cp:20000217.
[175] A. Y. M. Abbas and J. E. Fletcher, 'The Synthetic Loading Technique Applied to the PM Synchronous Machine', *IEEE Trans. Energy Convers.*, vol. 26, no. 1, pp. 83–92, Mar. 2011, doi: 10.1109/TEC.2010.2082543.
[176] K. Li and Y. Wang, 'DC-Link Voltage Fluctuation Reduction of Vector Controlled PMSM Drives with Reduced DC-Link Capacitor', in *2018 IEEE 4th Information Technology and Mechatronics Engineering Conference (ITOEC)*, Dec. 2018, pp. 909–912. doi: 10.1109/ITOEC.2018.8740730.
[177] R. Bertram, 'Flicker Mitigation by Optimization of Voltage Control', in *2019 IEEE Milan PowerTech*, Milan, Italy, Jun. 2019, pp. 1–6. doi: 10.1109/PTC.2019.8810431.
[178] G. Wiczynski, 'Determining location of voltage fluctuation source in radial power grid', *Electr. Power Syst. Res.*, vol. 180, p. 106069, Mar. 2020, doi: 10.1016/j.epsr.2019.106069.
[179] 'On Stability of Voltage Source Inverters in Weak Grids | IEEE Journals & Magazine | IEEE Xplore'. https://ieeexplore.ieee.org/document/8242351 (accessed Nov. 23, 2021).
[180] L. Xu and L. Ye, 'Analysis of a Novel Stator Winding Structure Minimizing Harmonic Current and Torque Ripple for Dual Six-Step Converter-Fed High Power AC Machines', *IEEE Trans. Ind. Appl.*, vol. 31, no. 1, pp. 84–90, Jan. 1995, doi: 10.1109/28.363046.
[181] H. S. Che and W. P. Hew, 'Dual three-phase operation of single neutral symmetrical six-phase machine for improved performance', in *IECON 2015 - 41st Annual Conference of the IEEE Industrial Electronics Society*, Nov. 2015, pp. 001176–001181. doi: 10.1109/IECON.2015.7392259.
[182] D. Hadiouche, H. Razik, and A. Rezzoug, 'On the modeling and design of dual-stator windings to minimize circulating harmonic currents for VSI fed AC machines', *IEEE Trans. Ind. Appl.*, vol. 40, no. 2, pp. 506–515, Mar. 2004, doi: 10.1109/TIA.2004.824511.
[183] M. Li, 'Piezoelectric active vibration control method of rigid flexible hybrid manipulator based on PSO', in *2021 13th International Conference on Measuring Technology and Mechatronics Automation (ICMTMA)*, Jan. 2021, pp. 431–435. doi: 10.1109/ICMTMA52658.2021.00099.
[184] L. Sui, X. Xiong, and G. Shi, 'Piezoelectric Actuator Design and Application on Active Vibration Control', *Phys. Procedia*, vol. 25, pp. 1388–1396, Jan. 2012, doi: 10.1016/j.phpro.2012.03.251.

BUPT

[185] L. DU, L. JI, Y. LUO, S. SHAO, and M. XU, 'Simulation and Experiment of an Active-Passive Isolator for Micro-Vibration Control of Spacecraft', in *2020 15th Symposium on Piezoelectrcity, Acoustic Waves and Device Applications (SPAWDA)*, Apr. 2021, pp. 227–232. doi: 10.1109/SPAWDA51471.2021.9445543.
[186] J. Liu, X. Zhang, C. Wang, and R. Yan, 'Active Vibration Control Technology in China', *IEEE Instrum. Meas. Mag.*, vol. 25, no. 2, pp. 36–44, Apr. 2022, doi: 10.1109/MIM.2022.9756383.
[187] J. Hu, P. Li, and X. Cui, 'Active Vibration Control of a High-Speed Flexible Robot Using Variable Structure Control', in *2012 Fifth International Conference on Intelligent Computation Technology and Automation*, Jan. 2012, pp. 57–60. doi: 10.1109/ICICTA.2012.21.
[188] D. Williams, H. H. Khodaparast, and S. Jiffri, 'Active vibration control of an equipment mounting link for an exploration robot', *Appl. Math. Model.*, vol. 95, pp. 524–540, Jul. 2021, doi: 10.1016/j.apm.2021.02.016.
[189] M. Ozsoy, N. D. Sims, and E. Ozturk, 'Robotically assisted active vibration control in milling: A feasibility study', *Mech. Syst. Signal Process.*, vol. 177, p. 109152, Sep. 2022, doi: 10.1016/j.ymssp.2022.109152.
[190] L. Y. L. Ang, Y. K. Koh, and H. P. Lee, 'The performance of active noise-canceling headphones in different noise environments', *Appl. Acoust.*, vol. 122, pp. 16–22, Jul. 2017, doi: 10.1016/j.apacoust.2017.02.005.
[191] T.-L. Le, T.-T. Huynh, and C.-M. Lin, 'Adaptive filter design for active noise cancellation using recurrent type-2 fuzzy brain emotional learning neural network', *Neural Comput. Appl.*, vol. 32, no. 12, pp. 8725–8734, Jun. 2020, doi: 10.1007/s00521-019-04366-8.
[192] J. Wang, J. Zhang, J. Xu, C. Zheng, and X. Li, 'An optimization framework for designing robust cascade biquad feedback controllers on active noise cancellation headphones', *Appl. Acoust.*, vol. 179, p. 108081, Aug. 2021, doi: 10.1016/j.apacoust.2021.108081.
[193] N. Zafeiropoulos, J. Zollner, and V. Rajan, 'Active Road Noise Cancellation for the Improvement of Sound Quality in the Vehicle', *ATZ Worldw. Springer*, vol. 120, pp. 38–43, Mar. 2018, doi: 10.1007/s38311-018-0003-1.
[194] Z. Jia, X. Zheng, Q. Zhou, Z. Hao, and Y. Qiu, 'A Hybrid Active Noise Control System for the Attenuation of Road Noise Inside a Vehicle Cabin', *Sensors*, vol. 20, no. 24, Art. no. 24, Jan. 2020, doi: 10.3390/s20247190.
[195] G. Reina and G. D. Rose, 'Active vibration absorber for automotive suspensions: a theoretical study', *Int. J. Heavy Veh. Syst.*, vol. 23, no. 1, p. 21, 2016, doi: 10.1504/IJHVS.2016.074625.
[196] Q. Wang, K. Rajashekara, Y. Jia, and J. Sun, 'A Real-Time Vibration Suppression Strategy in Electric Vehicles', *IEEE Trans. Veh. Technol.*, vol. 66, no. 9, pp. 7722–7729, Sep. 2017, doi: 10.1109/TVT.2017.2688416.
[197] S.-K. Lee, S. Lee, J. Back, and T. Shin, 'A New Method for Active Cancellation of Engine Order Noise in a Passenger Car', *Appl. Sci.*, vol. 8, no. 8, Art. no. 8, Aug. 2018, doi: 10.3390/app8081394.
[198] M. Chomat, L. Schreier, and J. Bendl, 'Torque-pulsation reduction in five-phase induction-machine drive', in *2015 17th European Conference on Power Electronics and Applications (EPE'15 ECCE-Europe)*, Sep. 2015, pp. 1–10. doi: 10.1109/EPE.2015.7311682.
[199] H. Ghorbani and M. Moradian, 'Torque pulsation reduction in five-phase PMASyncRMs', *J. Power Electron.*, vol. 22, no. 1, pp. 128–137, Jan. 2022, doi: 10.1007/s43236-021-00329-2.

BUPT

[200] Q. Xu and W. Hong, 'Dynamic performance of reciprocating compressor with capacity regulation system', *Proc. Inst. Mech. Eng. Part E J. Process Mech. Eng.*, vol. 233, no. 3, pp. 526–535, Jun. 2019, doi: 10.1177/0954408918772628.
[201] V. Manchi and C. Sujatha, 'Torsional vibration reduction of rotating shafts for multiple orders using centrifugal double pendulum vibration absorber', *Appl. Acoust.*, vol. 174, p. 107768, Mar. 2021, doi: 10.1016/j.apacoust.2020.107768.
[202] R. I. Davis and R. D. Lorenz, 'Engine torque ripple cancellation with an integrated starter alternator in a hybrid electric vehicle: implementation and control', *IEEE Trans. Ind. Appl.*, vol. 39, no. 6, pp. 1765–1774, Nov. 2003, doi: 10.1109/TIA.2003.818972.
[203] E. Ayana, P. Plahn, K. Wejrzanowski, and N. Mohan, 'Active Torque Cancellation for Transmitted Vibration Reduction of Low Cylinder Count Engines', *IEEE Trans. Veh. Technol.*, vol. 60, no. 7, pp. 2971–2977, Sep. 2011, doi: 10.1109/TVT.2011.2159255.
[204] K. Nagata, H. Nemoto, T. Katayama, and Y. Akita, 'A sensorless control for damping of torsional vibrations with middle voltage induction motor drive for compressor application', in *Proceedings of the 2011 14th European Conference on Power Electronics and Applications*, Aug. 2011, pp. 1–10.
[205] A. Abouzeid, J. Guerrero, I. Vicente, I. Muniategui, A. Endemaño Isasi, and F. Briz, 'Torsional Vibration Suppression in Railway Traction Drives', *IEEE Access*, vol. 10, pp. 1–15, Mar. 2022, doi: 10.1109/ACCESS.2022.3162415.
[206] J. Song-Manguelle, S. Schröder, T. Geyer, G. Ekemb, and J.-M. Nyobe-Yome, 'Prediction of Mechanical Shaft Failures due to Pulsating Torques of Variable Frequency Drives', p. 8.
[207] S. Hara and Y. Yamamoto, 'Stability of repetitive control systems', in *1985 24th IEEE Conference on Decision and Control*, Dec. 1985, pp. 326–327. doi: 10.1109/CDC.1985.268857.
[208] M. Tang, A. Formentini, S. A. Odhano, and P. Zanchetta, 'Torque Ripple Reduction of PMSMs Using a Novel Angle-Based Repetitive Observer', *IEEE Trans. Ind. Electron.*, vol. 67, no. 4, pp. 2689–2699, Apr. 2020, doi: 10.1109/TIE.2019.2912798.
[209] M. Ishida, S. Higuchi, and T. Hori, 'Reduction control of mechanical vibration of an induction motor with fluctuated torque load using repetitive controller', in *Proceedings of 1994 IEEE International Conference on Industrial Technology - ICIT '94*, Dec. 1994, pp. 533–537. doi: 10.1109/ICIT.1994.467074.
[210] A. Vyngra and B. Avdeyev, 'Calculation of the Load of an Electric Drive of a Reciprocating Compressor of a Ship Refrigeration Unit', in *2018 International Multi-Conference on Industrial Engineering and Modern Technologies (FarEastCon)*, Oct. 2018, pp. 1–4. doi: 10.1109/FarEastCon.2018.8602830.
[211] A. Dianov, 'Estimation of the Mechanical Position of Reciprocating Compressor for Silent Stoppage', *IEEE Open J. Power Electron.*, vol. PP, pp. 1–1, Mar. 2020, doi: 10.1109/OJPEL.2020.2978300.
[212] K. T. Ooi and T. T. Wan, 'A Rotaprocating Compressor', p. 9, 2000.
[213] I. Sultan and A. Kalim, 'Improving reciprocating compressor performance using a hybrid two-level optimisation approach', *Eng. Comput. Int J Comput.-Aided Eng.*, vol. 28, pp. 616–636, Jul. 2011, doi: 10.1108/02644401111141046.
[214] F. E. Boru, 'Torsional Vibration Problem in Reciprocating Compressor – Case Study', p. 11.

BUPT

[215] S. Pişirici, E. Çakır, and H. Erol, 'On the Dynamics of a Three Stage Single Acting Reciprocating Compressor', p. 10, 2018.
[216] T. Feese and C. Hill, 'PREVENTION OF TORSIONAL VIBRATION PROBLEMS IN RECIPROCATING MACHINERY', p. 26, 2009.
[217] P. A. Erofeev, O. Kaminskaya, V. A. Kucherenko, V. A. Yemelyanov, and N. S. Logunov, 'Investigation of the Mechanical and Electromechanical Starting Characteristics of an Asynchronous Electric Drive of a Two-Piston Marine Compressor', in *2021 IEEE Conference of Russian Young Researchers in Electrical and Electronic Engineering (ElConRus)*, Jan. 2021, pp. 321–325. doi: 10.1109/ElConRus51938.2021.9396333.
[218] T. Griffith, D. Bogh, and J. Krukowski, 'Applying synchronous motors to reciprocating compressors', in *2012 Petroleum and Chemical Industry Conference (PCIC)*, Sep. 2012, pp. 1–10. doi: 10.1109/PCICON.2012.6549672.

BUPT

Appendices

Appendix 1 – Cooley-Toky Algorithm: Matlab implementation

```
data=xlsread('data_exp2_5.xlsx');
%
start=1200;
stop=2000+start-1;
x=data(start:stop,1);
%
nb_of_points=32;
L=nb_of_points;
x_real=x;
x_imaginary=x.*0;
%
nb_of_cycles=0;
p=0;
N = 2;
while N <= L
      for k = 0:N/8
         w_real(k+1) = cosd(2*180*k/N);
         w_complex(k+1) = sind(2*180*k/N
      end

      ind = 0;
      w_ind = 0;
      span = 1;
      LpN = L/N;
      for k = 0 : L-1
         if w_ind <= N/2
            if w_ind <= N/8
               w_r = w_real(w_ind+1);
               w_c = -w_complex( w_ind+1 );
            elseif w_ind <= N/4
               w_r = w_complex( N/4-w_ind+1 );
               w_c = -w_real( N/4-w_ind+1 );
            elseif w_ind <= 3*N/8
               w_r = -w_complex( w_ind-N/4+1 );
               w_c = -w_real( w_ind-N/4+1 );
            else
               w_r = -w_real( N/2-w_ind+1 );
               w_c = -w_complex( N/2-w_ind+1 );
            end
         else
            if w_ind <= 5*N/8
               w_r = -w_real( w_ind-N/2+1 );
               w_c = w_complex( w_ind-N/2+1 );
            elseif w_ind <= 3*N/4
               w_r = -w_complex( 3*N/4-w_ind+1 );
```

```
            w_c = w_real( 3*N/4-w_ind+1 );
        elseif w_ind <= 7*N/8
            w_r = w_complex( w_ind-3*N/4+1 );
            w_c = w_real( w_ind-3*N/4+1 );
        else
            w_r = w_real( N-w_ind+1 );
            w_c = w_complex( N-w_ind+1 );
        end
    end
    A_r = x_real( ind+1 );
    A_c = x_imaginary( ind+1 );
    B_r = x_real( ind+LpN+1 );
    B_c = x_imaginary( ind+LpN+1 );
    if  k==1 & N==8
        a_r_v=A_r;
        a_c_v=A_c;
        b_r_v=B_r ;
        b_c_v=B_c;
        w_r_v=w_r;
        w_c_v=w_c;
    end
    tmp_real(k+1) = A_r + B_r*w_r - B_c*w_c;
    tmp_complex(k+1) = A_c + B_r*w_c + B_c*w_r;
    if  N==8
        for k = 0:N/8
            w_real_v(k+1) = w_real(k+1);
            w_complex_v(k+1)=w_complex(k+1);
        end
    end
    ind = ind + 1;
    if ind + LpN == L
        ind = 0;
        w_ind = w_ind + 1;
        span  = 1;
    elseif ind + LpN == span*LpN*2
        ind = ind + LpN;
        w_ind = w_ind + 1;
        span = span + 1;
    end

end

N = N*2;
for k = 0:L-1
    x_real(k+1) = tmp_real(k+1);
    x_imaginary(k+1) = tmp_complex(k+1);
    nb_of_cycles=nb_of_cycles+1;
end
stg_1=0;
if N/2==2
    for k = 0:L-1
```

```
            stg_1_real_line(k+1) = tmp_real(k+1);
            stg_1_imag_line(k+1) = tmp_complex(k+1);
            stg_1=1;
        end
    end
    if stg_1==1
        stg_1_real=stg_1_real_line.';
        stg_1_imag=stg_1_imag_line.';
    end
    stg_2=0;
    if N/2==4
        for k = 0:L-1
            stg_2_real_line(k+1) = tmp_real(k+1);
            stg_2_imag_line(k+1) = tmp_complex(k+1);
            stg_2=1;
        end
    end
    if stg_2==1
        stg_2_real=stg_2_real_line.';
        stg_2_imag=stg_2_imag_line.';
    end
    stg_3=0;
    if N/2==8
        for k = 0:L-1
            stg_3_real_line(k+1) = tmp_real(k+1);
            stg_3_imag_line(k+1) = tmp_complex(k+1);
            stg_3=1;
        end
    end
    if stg_3==1
        stg_3_real=stg_3_real_line.';
        stg_3_imag=stg_3_imag_line.';
    end
    stg_4=0;
    if N/2==16
        for k = 0:L-1
            stg_4_real_line(k+1) = tmp_real(k+1);
            stg_4_imag_line(k+1) = tmp_complex(k+1);
            stg_4=1;
        end
    end
    if stg_4==1
        stg_4_real=stg_4_real_line.';
        stg_4_imag=stg_4_imag_line.';
    end
end
x_ct=complex(x_real, x_imaginary);
x_ct=x_ct(1:length(x_ct));
```

Appendix 2 – Runge-Kutta 4-th order integration method

```
IF "mi".start_estimator = true THEN

   IF "mi".gata_primul_calcul = true THEN
      IF "mi".k <= 1200 THEN
       (**)
         "mi".ret_val := RD_SYS_T("mi".datetime);
         "mi".ns := "mi".datetime.NANOSECOND;
         "mi"."t(n)" := "mi".ns / 1000000;
         IF "mi"."t(n)" < "mi"."t(n-1)" THEN
            "mi".delta_t := ((999.9999 + "mi"."t(n)") - "mi"."t(n-1)") / 1000;
         ELSE
            "mi".delta_t := ("mi"."t(n)" - "mi"."t(n-1)") / 1000;
         END_IF;
      (*
      (**)       "mi".excel_delta_t[2] := "mi"."t(n)";
      (**)       "mi".start_estimator := false;
      (**)       "mi".excel_delta_t[3] := "mi"."t(n)" - "mi"."t(n-1)";

         "mi".tensiune1_nefiltrata := ((INT_TO_REAL("v1")) / 2764.8 * 46);
         "mi".tensiune1_calcul := "mi"."tensiune1_calcul(n-1)" * "mi".A_filtru +
"mi".tensiune1_nefiltrata * "mi".B_filtru;
         "mi".tensiune1 := "mi".tensiune1_nefiltrata - "mi".tensiune1_calcul;
         (**)
         "mi".tensiune2_nefiltrata := ((INT_TO_REAL("v2")) / 2764.8 * 46);
         "mi".tensiune2_calcul := "mi"."tensiune2_calcul(n-1)" * "mi".A_filtru +
"mi".tensiune2_nefiltrata * "mi".B_filtru;
         "mi".tensiune2 := "mi".tensiune2_nefiltrata - "mi".tensiune2_calcul;
         (**)
         "mi".tensiune3_nefiltrata := ((INT_TO_REAL("v3")) / 2764.8 * 46);
         "mi".tensiune3_calcul := "mi"."tensiune3_calcul(n-1)" * "mi".A_filtru +
"mi".tensiune3_nefiltrata * "mi".B_filtru;
         "mi".tensiune3 := "mi".tensiune3_nefiltrata - "mi".tensiune3_calcul;
         (**)
         "mi".curent1_nefiltrat := ((INT_TO_REAL("i1")) / 2764.8 / 100 * 2000 / 3);
         "mi".curent1_calcul := "mi"."curent1_calcul(n-1)" * "mi".A_filtru +
"mi".curent1_nefiltrat * "mi".B_filtru;
         "mi".curent1 := "mi".curent1_nefiltrat - "mi".curent1_calcul;
         (**)
         "mi".curent2_nefiltrat := ((INT_TO_REAL("i2")) / 2764.8 / 100 * 2000 / 3);
         "mi".curent2_calcul := "mi"."curent2_calcul(n-1)" * "mi".A_filtru +
"mi".curent2_nefiltrat * "mi".B_filtru;
         "mi".curent2 := "mi".curent2_nefiltrat - "mi".curent2_calcul;
         (**)
         "mi".curent3_nefiltrat := ((INT_TO_REAL("i3")) / 2764.8 / 100 * 2000 / 3);
         "mi".curent3_calcul := "mi"."curent3_calcul(n-1)" * "mi".A_filtru +
"mi".curent3_nefiltrat * "mi".B_filtru;
         "mi".curent3 := "mi".curent3_nefiltrat - "mi".curent3_calcul;
         (**)
```

```
        "mi".u_alpha_m := (2 * "mi".tensiune1 - "mi".tensiune2 - "mi".tensiune3) /
3;
        "mi".u_beta_m := SQRT(3) / 3 * ("mi".tensiune2 - "mi".tensiune3);
        "mi".i_alpha_m := (2 * "mi".curent1 - "mi".curent2 - "mi".curent3) / 3;
        "mi".i_beta_m := SQRT(3) / 3 * ("mi".curent2 - "mi".curent3);
        (**)

        "mi".flux1_k1 := ("mi".u_alpha_m - "mi".a11 * "mi"."flux_s1(n-1)" +
"mi".a12 * "mi"."flux_r1(n-1)") * "mi".delta_t;
        "mi".flux2_k1 := ("mi".u_beta_m - "mi".a11 * "mi"."flux_s2(n-1)" +
"mi".a12 * "mi"."flux_r2(n-1)") * "mi".delta_t;
        "mi".flux3_k1 := ("mi".a21 * "mi"."flux_s1(n-1)" - "mi".a22 *
"mi"."flux_r1(n-1)" - "mi".p * "mi"."w(n-1)" * "mi"."flux_r2(n-1)") * "mi".delta_t;
        "mi".flux4_k1 := ("mi".a21 * "mi"."flux_s2(n-1)" - "mi".a22 *
"mi"."flux_r2(n-1)" + "mi".p * "mi"."w(n-1)" * "mi"."flux_r1(n-1)") * "mi".delta_t;
        "mi".flux1_k1_calcul := "mi"."flux_s1(n-1)" + 0.5 * "mi".flux1_k1;
        "mi".flux2_k1_calcul := "mi"."flux_s2(n-1)" + 0.5 * "mi".flux2_k1;
        "mi".flux3_k1_calcul := "mi"."flux_r1(n-1)" + 0.5 * "mi".flux3_k1;
        "mi".flux4_k1_calcul := "mi"."flux_r2(n-1)" + 0.5 * "mi".flux4_k1;
        (**)
        "mi".flux1_k2 := ("mi".u_alpha_m - "mi".a11 * "mi".flux1_k1_calcul +
"mi".a12 * "mi".flux3_k1_calcul) * "mi".delta_t;
        "mi".flux2_k2 := ("mi".u_beta_m - "mi".a11 * "mi".flux2_k1_calcul +
"mi".a12 * "mi".flux4_k1_calcul) * "mi".delta_t;
        "mi".flux3_k2 := ("mi".a21 * "mi".flux1_k1_calcul - "mi".a22 *
"mi".flux3_k1_calcul - "mi".p * "mi"."w(n-1)" * "mi".flux4_k1_calcul) *
"mi".delta_t;
        "mi".flux4_k2 := ("mi".a21 * "mi".flux2_k1_calcul - "mi".a22 *
"mi".flux4_k1_calcul + "mi".p * "mi"."w(n-1)" * "mi".flux3_k1_calcul) *
"mi".delta_t;
        "mi".flux1_k2_calcul := "mi"."flux_s1(n-1)" + 0.5 * "mi".flux1_k2;
        "mi".flux2_k2_calcul := "mi"."flux_s2(n-1)" + 0.5 * "mi".flux2_k2;
        "mi".flux3_k2_calcul := "mi"."flux_r1(n-1)" + 0.5 * "mi".flux3_k2;
        "mi".flux4_k2_calcul := "mi"."flux_r2(n-1)" + 0.5 * "mi".flux4_k2;
        (**)
        "mi".flux1_k3 := ("mi".u_alpha_m - "mi".a11 * "mi".flux1_k2_calcul +
"mi".a12 * "mi".flux3_k2_calcul) * "mi".delta_t;
        "mi".flux2_k3 := ("mi".u_beta_m - "mi".a11 * "mi".flux2_k2_calcul +
"mi".a12 * "mi".flux4_k2_calcul) * "mi".delta_t;
        "mi".flux3_k3 := ("mi".a21 * "mi".flux1_k2_calcul - "mi".a22 *
"mi".flux3_k2_calcul - "mi".p * "mi"."w(n-1)" * "mi".flux4_k2_calcul) *
"mi".delta_t;
        "mi".flux4_k3 := ("mi".a21 * "mi".flux2_k2_calcul - "mi".a22 *
"mi".flux4_k2_calcul + "mi".p * "mi"."w(n-1)" * "mi".flux3_k2_calcul) *
"mi".delta_t;
        "mi".flux1_k3_calcul := "mi"."flux_s1(n-1)" + "mi".flux1_k3;
        "mi".flux2_k3_calcul := "mi"."flux_s2(n-1)" + "mi".flux2_k3;
        "mi".flux3_k3_calcul := "mi"."flux_r1(n-1)" + "mi".flux3_k3;
        "mi".flux4_k3_calcul := "mi"."flux_r2(n-1)" + "mi".flux4_k3;
        (**)
```

```
        "mi".flux1_k4 := ("mi".u_alpha_m - "mi".a11 * "mi".flux1_k3_calcul +
"mi".a12 * "mi".flux3_k3_calcul) * "mi".delta_t;
        "mi".flux2_k4 := ("mi".u_beta_m - "mi".a11 * "mi".flux2_k3_calcul +
"mi".a12 * "mi".flux4_k3_calcul) * "mi".delta_t;
        "mi".flux3_k4 := ("mi".a21 * "mi".flux1_k3_calcul - "mi".a22 *
"mi".flux3_k3_calcul - "mi".p * "mi"."w(n-1)" * "mi".flux4_k3_calcul) *
"mi".delta_t;
        "mi".flux4_k4 := ("mi".a21 * "mi".flux2_k3_calcul - "mi".a22 *
"mi".flux4_k3_calcul + "mi".p * "mi"."w(n-1)" * "mi".flux3_k3_calcul) *
"mi".delta_t;
        (**)
        "mi".flux_s1 := "mi"."flux_s1(n-1)" + ("mi"."flux1_k1" + 2 *
"mi"."flux1_k2" + 2 * "mi"."flux1_k3" + "mi"."flux1_k4") / 6;
        "mi".flux_s2 := "mi"."flux_s2(n-1)" + ("mi"."flux2_k1" + 2 *
"mi"."flux2_k2" + 2 * "mi"."flux2_k3" + "mi"."flux2_k4") / 6;
        "mi".flux_r1 := "mi"."flux_r1(n-1)" + ("mi"."flux3_k1" + 2 *
"mi"."flux3_k2" + 2 * "mi"."flux3_k3" + "mi"."flux3_k4") / 6;
        "mi".flux_r2 := "mi"."flux_r2(n-1)" + ("mi"."flux4_k1" + 2 *
"mi"."flux4_k2" + 2 * "mi"."flux4_k3" + "mi"."flux4_k4") / 6;
        (**)
        "mi".i_alpha_e := "mi".c1 * "mi"."flux_s1" + "mi".c2 * "mi"."flux_r1";
        "mi".i_beta_e := "mi".c1 * "mi"."flux_s2" + "mi".c2 * "mi"."flux_r2";
        (**)
        "mi".t_elm := 1.5 * "mi".p * "mi".c2 * ("mi"."flux_s1" * "mi"."flux_r2" -
"mi"."flux_s2" * "mi"."flux_r1");
        (**)
        "mi".i_x := "mi".i_alpha_e * "mi".i_beta_m - "mi".i_beta_e *
"mi".i_alpha_m;
        (**)
        "mi".i_x_pid_i := "mi"."i_x_pid_i(n-1)" + "mi".i_x * "mi".delta_t * "mi".ki;
        "mi".i_x_pid := "mi".i_x * "mi".kp + "mi".i_x_pid_i;
        (**)
        "mi"."T_elm-i_x_pid" := "mi".t_elm - "mi".i_x_pid;
        (**)
        "mi".w := (("mi"."T_elm-i_x_pid" - "mi"."w(n-1)" * "mi".B) * "mi".delta_t) /
"mi".J + "mi"."w(n-1)";
        (**)
        (**)
        (**)
        (**)
        (**)
        "mi"."flux_s1(n-1)" := "mi".flux_s1;
        "mi"."flux_s2(n-1)" := "mi".flux_s2;
        "mi"."flux_r1(n-1)" := "mi".flux_r1;
        "mi"."flux_r2(n-1)" := "mi".flux_r2;
        (**)
        "mi"."tensiune1_calcul(n-1)" := "mi".tensiune1_calcul;
        "mi"."tensiune2_calcul(n-1)" := "mi".tensiune2_calcul;
        "mi"."tensiune3_calcul(n-1)" := "mi".tensiune3_calcul;
        "mi"."curent1_calcul(n-1)" := "mi".curent1_calcul;
        "mi"."curent2_calcul(n-1)" := "mi".curent2_calcul;
```

```
    "mi"."curent3_calcul(n-1)" := "mi".curent3_calcul;
    (**)
    "mi"."flux_s1(n-1)" := "mi".flux_s1;
    "mi"."flux_s2(n-1)" := "mi".flux_s2;
    "mi"."flux_r1(n-1)" := "mi".flux_r1;
    "mi"."flux_r2(n-1)" := "mi".flux_r2;
    (**)
    "mi"."flux1_k1(n-1)" := "mi".flux1_k1;
    "mi"."flux2_k1(n-1)" := "mi".flux2_k1;
    "mi"."flux3_k1(n-1)" := "mi".flux3_k1;
    "mi"."flux4_k1(n-1)" := "mi".flux4_k1;
    "mi"."flux1_k2(n-1)" := "mi".flux1_k2;
    "mi"."flux2_k2(n-1)" := "mi".flux2_k2;
    "mi"."flux3_k2(n-1)" := "mi".flux3_k2;
    "mi"."flux4_k2(n-1)" := "mi".flux4_k2;
    "mi"."flux1_k3(n-1)" := "mi".flux1_k3;
    "mi"."flux2_k3(n-1)" := "mi".flux2_k3;
    "mi"."flux3_k3(n-1)" := "mi".flux3_k3;
    "mi"."flux4_k3(n-1)" := "mi".flux4_k3;
    "mi"."flux1_k4(n-1)" := "mi".flux1_k4;
    "mi"."flux2_k4(n-1)" := "mi".flux2_k4;
    "mi"."flux3_k4(n-1)" := "mi".flux3_k4;
    "mi"."flux4_k4(n-1)" := "mi".flux4_k4;
    (**)
    "mi"."i_x_pid_i(n-1)" := "mi".i_x_pid_i;
    (**)
    "mi"."w(n-1)" := "mi".w;
    (**)
    "mi"."t(n-1)" := "mi"."t(n)";
    (**)
    "mi"."delta_t(n-1)" := "mi".delta_t;
    (**)
    "mi".excel_w["mi".k] := "mi".w;
    "mi".excel_tensiune_1["mi".k] := "mi".tensiune1;
    "mi".excel_tensiune_2["mi".k] := "mi".tensiune2;
    "mi".excel_tensiune_3["mi".k] := "mi".tensiune3;
    "mi".excel_curent_1["mi".k] := "mi".curent1;
    "mi".excel_curent_2["mi".k] := "mi".curent2;
    "mi".excel_curent_3["mi".k] := "mi".curent3;
    "mi".excel_u_alpha_m["mi".k] := "mi".u_alpha_m;
    "mi".excel_u_beta_m["mi".k] := "mi".u_beta_m;
    "mi".excel_i_alpha_m["mi".k] := "mi".i_alpha_m;
    "mi".excel_i_beta_m["mi".k] := "mi".i_beta_m;
(**)
    "mi".excel_flux_s1["mi".k] := "mi".flux_s1;
    "mi".excel_flux_s2["mi".k] := "mi".flux_s2;
    "mi".excel_flux_r1["mi".k] := "mi".flux_r1;
    "mi".excel_flux_r2["mi".k] := "mi".flux_r2;
(**)
    "mi".excel_flux1_k1["mi".k] := "mi".flux1_k1;
    "mi".excel_flux2_k1["mi".k] := "mi".flux2_k1;
```

```
      "mi".excel_flux3_k1["mi".k] := "mi".flux3_k1;
      "mi".excel_flux4_k1["mi".k] := "mi".flux4_k1;
      "mi".excel_flux1_k1_calcul["mi".k] := "mi".flux1_k1_calcul;
      "mi".excel_flux2_k1_calcul["mi".k] := "mi".flux2_k1_calcul;
      "mi".excel_flux3_k1_calcul["mi".k] := "mi".flux3_k1_calcul;
      "mi".excel_flux4_k1_calcul["mi".k] := "mi".flux4_k1_calcul;
      "mi".excel_flux1_k2["mi".k] := "mi".flux1_k2;
      "mi".excel_flux2_k2["mi".k] := "mi".flux2_k2;
      "mi".excel_flux3_k2["mi".k] := "mi".flux3_k2;
      "mi".excel_flux4_k2["mi".k] := "mi".flux4_k2;
      "mi".excel_flux1_k2_calcul["mi".k] := "mi".flux1_k2_calcul;
      "mi".excel_flux2_k2_calcul["mi".k] := "mi".flux2_k2_calcul;
      "mi".excel_flux3_k2_calcul["mi".k] := "mi".flux3_k2_calcul;
      "mi".excel_flux4_k2_calcul["mi".k] := "mi".flux4_k2_calcul;
      "mi".excel_flux1_k3["mi".k] := "mi".flux1_k3;
      "mi".excel_flux2_k3["mi".k] := "mi".flux2_k3;
      "mi".excel_flux3_k3["mi".k] := "mi".flux3_k3;
      "mi".excel_flux4_k3["mi".k] := "mi".flux4_k3;
      "mi".excel_flux1_k3_calcul["mi".k] := "mi".flux1_k3_calcul;
      "mi".excel_flux2_k3_calcul["mi".k] := "mi".flux2_k3_calcul;
      "mi".excel_flux3_k3_calcul["mi".k] := "mi".flux3_k3_calcul;
      "mi".excel_flux4_k3_calcul["mi".k] := "mi".flux4_k3_calcul;
      "mi".excel_flux1_k4["mi".k] := "mi".flux1_k4;
      "mi".excel_flux2_k4["mi".k] := "mi".flux2_k4;
      "mi".excel_flux3_k4["mi".k] := "mi".flux3_k4;
      "mi".excel_flux4_k4["mi".k] := "mi".flux4_k4;
   (**)
      "mi".excel_i_alpha_e["mi".k] := "mi".i_alpha_e;
      "mi".excel_i_beta_e["mi".k] := "mi".i_beta_e;
      "mi".excel_t_elm["mi".k] := "mi".t_elm;
   (**)
      "mi".excel_i_x["mi".k] := "mi".i_x;
      "mi".excel_I_x_PID_i["mi".k] := "mi".i_x_pid_i;
      "mi".excel_I_x_PID["mi".k] := "mi".i_x_pid;
      "mi"."excel_t_elm-i_x_pid"["mi".k] := "mi"."T_elm-i_x_pid";
      "mi".excel_diff["mi".k] := "mi".diff_J_B;
      "mi".excel_w["mi".k] := "mi".w;
      "mi".excel_delta_t["mi".k] := "mi".delta_t;
      "mi"."excel_delta_t(n-1)"["mi".k] := "mi"."t(n)";
      "mi".k := "mi".k + 1;

   ELSE
      "mi".k := 1;
      "mi".achizitie_pt_excel := false;
      "mi".start_estimator := false;
      "mi".gata_primul_calcul := false;
      "mi".primul_calcul := true;

   END_IF;

END_IF;
```

```
IF "mi".primul_calcul = true THEN
 "mi".flux1_k1 := 0;
 "mi".flux2_k1 := 0;
 "mi".flux3_k1 := 0;
 "mi".flux4_k1 := 0;
 "mi"."flux1_k1(n-1)" := 0;
 "mi"."flux2_k1(n-1)" := 0;
 "mi"."flux3_k1(n-1)" := 0;
 "mi"."flux4_k1(n-1)" := 0;
 "mi".flux1_k1_calcul := 0;
 "mi".flux2_k1_calcul := 0;
 "mi".flux3_k1_calcul := 0;
 "mi".flux4_k1_calcul := 0;
 (**)
 "mi".flux1_k2 := 0;
 "mi".flux2_k2 := 0;
 "mi".flux3_k2 := 0;
 "mi".flux4_k2 := 0;
 "mi"."flux1_k2(n-1)" := 0;
 "mi"."flux2_k2(n-1)" := 0;
 "mi"."flux3_k2(n-1)" := 0;
 "mi"."flux4_k2(n-1)" := 0;
 "mi".flux1_k2_calcul := 0;
 "mi".flux2_k2_calcul := 0;
 "mi".flux3_k2_calcul := 0;
 "mi".flux4_k2_calcul := 0;
 (**)
 "mi".flux1_k3 := 0;
 "mi".flux2_k3 := 0;
 "mi".flux3_k3 := 0;
 "mi".flux4_k3 := 0;
 "mi"."flux1_k3(n-1)" := 0;
 "mi"."flux2_k3(n-1)" := 0;
 "mi"."flux3_k3(n-1)" := 0;
 "mi"."flux4_k3(n-1)" := 0;
 "mi".flux1_k3_calcul := 0;
 "mi".flux2_k3_calcul := 0;
 "mi".flux3_k3_calcul := 0;
 "mi".flux4_k3_calcul := 0;
 (**)
 "mi".flux1_k4 := 0;
 "mi".flux2_k4 := 0;
 "mi".flux3_k4 := 0;
 "mi".flux4_k4 := 0;
 "mi"."flux1_k4(n-1)" := 0;
 "mi"."flux2_k4(n-1)" := 0;
 "mi"."flux3_k4(n-1)" := 0;
 "mi"."flux4_k4(n-1)" := 0;
 (**)
 "mi".flux_s1 := 0;
 "mi"."flux_s1(n-1)" := 0;
```

```
      "mi".flux_s2 := 0;
      "mi"."flux_s2(n-1)" := 0;
      "mi".flux_r1 := 0;
      "mi"."flux_r1(n-1)" := 0;
      "mi".flux_r2 := 0;
      "mi"."flux_r2(n-1)" := 0;
      "mi".i_alpha_e := 0;
      "mi"."i_alpha_e(n-1)" := 0;
      "mi".i_beta_e := 0;
      "mi"."i_beta_e(n-1)" := 0;
      "mi".t_elm := 0;
      "mi"."t_elm(n-1)" := 0;
      "mi".i_x := 0;
      "mi".i_x_pid := 0;
      "mi".i_x_pid_i := 0;
      "mi"."i_x_pid_i(n-1)" := 0;
      "mi"."T_elm-i_x_pid" := 0;
      "mi".diff_J_B := 0;
      "mi".w := 0;
      "mi"."w(n-1)" := 0;
      (**)
      "mi".delta_t := 0;
      "mi".ret_val := 0;
      "mi"."t(n)" := 0;
      "mi"."t(n-1)" := 0;
      (**)
      "mi".tensiune1 := 0;
      "mi".tensiune2 := 0;
      "mi".tensiune3 := 0;
      "mi".curent1 := 0;
      "mi".curent2 := 0;
      "mi".curent3 := 0;
      "mi"."tensiune1_calcul(n-1)" := 0;
      "mi"."tensiune2_calcul(n-1)" := 0;
      "mi"."tensiune3_calcul(n-1)" := 0;
      "mi"."curent1_calcul(n-1)" := 0;
      "mi"."curent2_calcul(n-1)" := 0;
      "mi"."curent3_calcul(n-1)" := 0;
      (**)
      "mi".ret_val := RD_SYS_T("mi".datetime);
      "mi".ns := "mi".datetime.NANOSECOND;
      "mi"."t(n-1)" := "mi".ns / 1000000;
      (**)
      "mi".primul_calcul := FALSE;
      "mi".gata_primul_calcul := true;
      (*"mi".excel_delta_t[1] := "mi"."t(n-1)";
   END_IF;
ELSE
   "mi".gata_primul_calcul := false;
   "mi".primul_calcul := true;
END_IF;
```

Appendix 3 – Direct and invers component identification

```
freq=20000;
data = csvread('0% csf pornit.csv');
u1_bl=u1_b/299.1*600/0.025;
u2_bl=u2_b/299.1*600/0.025;
u3_bl=u3_b/299.8*600/0.025;
%
u1=(u1_bl-u2_bl)/3;
u2=(u1_bl+2*u2_bl)/3;
u3=(-2*u1_bl-u2_bl)/3;
%
%first 0 crossing detection
i=1;
while i <= length(u1)-1
   i=i+1;
   if u1(i)<0 && u1(i+1)>0
      ind1=i;
      i=length(u1);
   end
end
%last 0 crossing detection
i=length(u1);
while i>=1
   i=i-1;
   if u1(i)>0 && u1(i-1)<0
      ind2=i;
      i=0;
   end
end
%
%refined signals with an integer number of periods
s_u1=u1(ind1+1:ind2-1);
s_u2=u2(ind1+1:ind2-1);
s_u3=u3(ind1+1:ind2-1);
%matrix form
s_u_mtx(1,:)=s_u1;
s_u_mtx(2,:)=s_u2;
s_u_mtx(3,:)=s_u3;
%%%%%%%%%%%%%%%%%%%%%%%%%%%%%%%%%%%%%%%%%%%%%%%%%%%%%%%%%%%%%%%%%%%%%%%%%%%%%%%%
fprintf('Relative Harmonic Content for all three channels\n');
fprintf(1, '\n');
for j=1:3
   i=1;
   fprintf('Ch%d\n',j);
   while i<=11
      fprintf('RHC %dth H = %1.2f',i,h_v(j,i)/h_v(j,1)*100);
      disp('(%)');
      i=i+2;
   end
   fprintf(1, '\n');
```

```
end
fprintf(1, '\n');
fprintf(1, '\n');
fprintf(1, '\n');
fprintf(1, '\n');
%%%%%%%%%%%%%%%%%%%
%                   %
%                   %
%%%%%%%%%%%%%%%%%%%
%Direct(positive) and Invers(Negative) Components Identification
fprintf('Direct(positive) and Invers(Negative) Components\n');
fprintf(1, '\n');
f=50;
a=0;
for i=1:length(u1)
   a=a+f*2*pi*1/freq;
   if a>2*pi
      a=0;
   end
   theta(i)=a;
end
 for i=1:length(u1)
   X(i) = (2*u1(i)-u2(i)-u3(i)) * (1 / 3);
   Y(i) = (u2(i)-u3(i)) * (1 / sqrt(3));
   Z(i) = (u1(i)+u2(i)+u3(i)) * (1 / 3);
    %Direct(positive) component computation
   co_cd(i) = cos(theta(i));
   si_cd(i) = sin(theta(i));
   D_cd(i) = co_cd(i)*X(i) + si_cd(i)*Y(i);
   Q_cd(i) = co_cd(i)*Y(i) - si_cd(i)*X(i);
   %Invers(Negative) component computation
   co_ci(i) = cos(-theta(i));
   si_ci(i) = sin(-theta(i));
   D_ci(i) = co_ci(i)*X(i) + si_ci(i)*Y(i);
   Q_ci(i) = co_ci(i)*Y(i) - si_ci(i)*X(i);
end
%
%Direct(positive) component
%
cd=sqrt((mean(D_cd))^2+(mean(Q_cd))^2);
fprintf('Direct(positive) component=%1.3f',cd);
disp('(V)');
%Invers(Negative) component
ci=sqrt((mean(D_ci))^2+(mean(Q_ci))^2);
fprintf('Inverse(negative) component=%1.3f',ci);
disp('(V)');
fprintf('Inverse(negative) component=%1.3f',ci/cd*100);
disp('(%) of Direct Component');
```

Appendix 4 – Randomly generated acquisition frequency

```
sim_timk=3;%maximum simulation timk
t=0:0.00001:sim_time-0.00001;
Total_points=(sim_time-0.00001)/0.00001;
T=0.0005;
freq_u=50;%Hz
points_on_period_50Hz=length(t)/sim_time*1/freq_u;
points_on_T=length(t)/sim_time*T; %the number of points during the sampling
period.
gama=1;%[%] the percentage of the sampling time variation. it can be only
0%,2%,4%,6%,8%,10%
%
u3=326.6*sin(2*pi*50*t);
u2=326.6*sin(2*pi*50*t+2*pi/3);
u1=326.6*sin(2*pi*50*t-2*pi/3);
%
clear u1_d u2_d u3_d u1_ud u2_ud u3_ud i j vector_i
i=1;
j=1;
k=1;
u1_d=u1(1);
u2_d=u2(1);
u3_d=u3(1);
while i<=Total_points-2*points_on_T;
   i=i+points_on_T+(round(gama*rand)*2)-gama;
   u1_d(j)=u1(i+points_on_T+(round(gama*rand)*2)-gama);
   u2_d(j)=u2(i+points_on_T+(round(gama*rand)*2)-gama);
   u3_d(j)=u3(i+points_on_T+(round(gama*rand)*2)-gama);
   while k*points_on_T<=length(u1)
      u1_ud(k)=u1(k*points_on_T);
      u2_ud(k)=u2(k*points_on_T);
      u3_ud(k)=u3(k*points_on_T);
      k=k+1;
   end
   j=j+1;
end
t_d=0:1:j-2;
```

Appendix 5 – PLC software for variable phase shift speed reference

```
"DB1".w := 2 * "DB1".pi * "DB1".f;
"DB1".defazaj_in_s := "DB1".defazaj_in_cp_ref / 1000; //defazaj in secunde
"DB1".defazaj_in_grd := 360 * "DB1".f * "DB1".defazaj_in_cp_ref / 1000;
//defazaj in grade
IF "DB1".Start_sin = true THEN
   IF "DB1".defazaj_in_cp_ref_setata > 20 THEN //limita superioara
      "DB1".defazaj_in_cp_ref_setata := 20;
```

```
   END_IF;
   IF "DB1".defazaj_in_cp_ref_setata < 0 THEN//limita inferioara
      "DB1".defazaj_in_cp_ref_setata := 0;
   END_IF;
      "DB1".start_verificare := TRUE;
      IF "DB1".defazaj_in_cp_ref_setata > "DB1".defazaj_in_cp_ref AND
"DB1"."ref_out_m1-3" < "DB1"."ref_out_m1-2" AND "DB1"."ref_out_m1-2" <
"DB1"."ref_out_m1-1" (*AND"DB1".k_done_1 = false*)THEN
         "DB1".defazaj_in_cp_ref := "DB1".defazaj_in_cp_ref_setata;
      END_IF;
      IF "DB1".defazaj_in_cp_ref_setata < "DB1".defazaj_in_cp_ref AND
"DB1"."ref_out_m1-2" < "DB1"."ref_out_m1-1" AND "DB1"."ref_out_m2-2" <>
"DB1"."ref_out_m2-1" AND "DB1".k_done_1 = false THEN
         "DB1".defazaj_in_cp_ref := "DB1".defazaj_in_cp_ref_setata;
      END_IF;
      IF "DB1".defazaj_in_cp_ref_initial = "DB1".defazaj_in_cp_ref AND
"DB1".k_revenire_1 = true THEN
         "DB1".k_test_1 := true;
      ELSE
         IF ("DB1".defazaj_in_cp_ref_initial < "DB1".defazaj_in_cp_ref) OR
"DB1".k_defazaj_1 = true THEN
            "DB1".k_test_1 := false;
            "DB1".k_revenire_1 := false;
            "DB1".k_defazaj_1 := true;
            "DB1".defazaj_in_cp_ref_initial := "DB1".defazaj_in_cp_ref_initial + 1;
            IF "DB1".defazaj_in_cp_ref_initial = "DB1".defazaj_in_cp_ref THEN //aici
controlez cate cicluri raman pe stop intre defazaje
               "DB1".k_revenire_1 := true;
               "DB1".k_defazaj_1 := false;
               "DB1".defazaj_in_cp_ref_initial := "DB1".defazaj_in_cp_ref;
            END_IF;
         END_IF;
      END_IF;

      IF "DB1".defazaj_in_cp_ref_initial = "DB1".defazaj_in_cp_ref AND
"DB1".k_revenire_2 = true THEN
         "DB1".k_test_2 := true;
      ELSE
         IF ("DB1".defazaj_in_cp_ref_initial > "DB1".defazaj_in_cp_ref) OR
"DB1".k_defazaj_2 = true THEN
            "DB1".k_test_2 := false;
            "DB1".k_revenire_2 := false;
            "DB1".k_defazaj_2 := true;
            "DB1".defazaj_in_cp_ref_initial := "DB1".defazaj_in_cp_ref_initial - 1;
            IF "DB1".defazaj_in_cp_ref_initial = "DB1".defazaj_in_cp_ref THEN //aici
controlez cate cicluri raman pe stop intre defazaje
               "DB1".k_revenire_2 := true;
               "DB1".k_defazaj_2 := false;
               "DB1".defazaj_in_cp_ref_initial := "DB1".defazaj_in_cp_ref;
            END_IF;
         END_IF;
```

```
      END_IF;
      //ref1
      IF "DB1".k_test_1 = true THEN
         IF "DB1".t1 <= 10 THEN
            IF ((("DB1".ref_out_m1 > (0 - 0.9995 * "DB1".Amp) OR "DB1".kk1 =
true) AND "DB1".k1 = FALSE) OR ("DB1".defazaj_in_cp_ref = 0)) (*OR
"DB1".k_done_1=TRUE*)THEN
               "DB1".t1 := "DB1".t1 + 0.001;
               IF "DB1".ref_out_m1 > (0 - 0.9995 * "DB1".Amp) THEN
                  "DB1".kk1 := false;
               END_IF;
            ELSE
               "DB1".k1 := true;
               "DB1".delta_t1 := "DB1".delta_t1 + 0.001;
               IF "DB1".delta_t1 >= (2 * "DB1".defazaj_in_cp_ref / 1000) - 0.001
THEN
                  "DB1".delta_t1 := 0;
                  "DB1".k1 := false;
                  "DB1".kk1 := true;
                  "DB1".k_test_1 := false;
               END_IF;
            END_IF;
         ELSE
            "DB1".t1 := 0;
         END_IF;
      END_IF;
      //ref2
      IF "DB1".k_test_2 = true THEN
         IF "DB1".t2 <= 10 THEN
            IF ((("DB1".ref_out_m2 ) < (0.999 * "DB1".Amp) OR "DB1".kk2 = true)
AND "DB1".k2 = FALSE) OR ("DB1".defazaj_in_cp_ref = 0) THEN
               "DB1".t2 := "DB1".t2 + 0.001;
               IF ("DB1".ref_out_m2) < (0.999 * "DB1".Amp) THEN
                  "DB1".kk2 := false;
               END_IF;
            ELSE
               "DB1".k2 := true;
               "DB1".test_j := "DB1".test_j + 1;
               "DB1".delta_t2 := "DB1".delta_t2 + 0.001;
               IF "DB1".delta_t2 >= (2 * "DB1".defazaj_in_cp_ref / 1000) - 0.001
THEN
                  "DB1".delta_t2 := 0;
                  "DB1".k2 := false;
                  "DB1".kk2 := true;
                  "DB1".test_j := 0;
                  //END_IF;
               END_IF;
            END_IF;
         ELSE
            "DB1".t2 := 0;
         END_IF;
```

```
      END_IF;
      "DB1"."ref_out_m1-3" := "DB1"."ref_out_m1-2";
      "DB1"."ref_out_m1-2" := "DB1"."ref_out_m1-1";
      "DB1"."ref_out_m1-1" := "DB1".ref_out_m1;
      "DB1".ref_out_m1 := "DB1".Offset + "DB1".Amp * SIN("DB1".w * "DB1".t1);

      "DB1"."ref_out_m2-2" := "DB1"."ref_out_m2-1";
      "DB1"."ref_out_m2-1" := "DB1".ref_out_m2;
      "DB1".ref_out_m2 := "DB1".Offset + "DB1".Amp * SIN("DB1".w * "DB1".t2);
   END_IF;
IF "DB1".Start_sin = false THEN
   "DB1".first_start_ref := true;
   "DB1".t1 := 0;
   "DB1".t2 := 0;
   "DB1".delta_t1 := 0;
   "DB1".delta_t2 := 0;
   "DB1".t := 0;
   "DB1".k1 := FALSE;
   "DB1".k2 := false;
   "DB1".kk1 := false;
   "DB1".kk2 := false;
   "DB1".t_sincronizare := 0;
   "DB1".test_i := 0;
   "DB1".defazaj_in_cp_ref := 0;
   "DB1".ref_out_m1 := 0;
   "DB1".ref_out_m2 := 0;
   "DB1".k_defazaj_1 := false;
   "DB1".k_test_1 := true;
   "DB1".defazaj_in_cp_ref_initial := 0;
   "DB1".k_defazaj_2 := false;
   "DB1".k_test_2 := true;
   "DB1".defazaj_in_cp_ref_setata := 0;
   "DB1".test_j := 0;
   "DB1".k_done_1 := false;
   "DB1".k_revenire_2 := true;
   "DB1".i_val_medie := 0;
   "DB1".suma_val_m1 := 0;
   "DB1".blocare_calc_val_medie := true;
END_IF;
"out_1" := INT_TO_WORD(REAL_TO_INT("DB1".ref_out_m1 * 2764.8)); //
"out_2" := INT_TO_WORD(REAL_TO_INT(0-"DB1".ref_out_m2 * 2764.8)); //
```

Appendix 6 – PLC software for triangle speed reference

```
IF "DB1".Start_sin = true THEN
   "DB1".start_verificare := true;
   "DB1".abatere := 0.1 * "DB1".delta_t;
   //1
   IF "DB1".t >= "DB1".perioada - "DB1".abatere THEN
      "DB1".k_test_1 := true;
```

```
      "DB1".ref_out := 0;
      "DB1".t := 0;
      "DB1".c := false;
      "DB1".d := true;
   END_IF;
   //2
   IF "DB1".k_test_1 = true THEN
      "DB1".perioada := 1 / "DB1".f;
      "DB1".delta_t := 0.001;
      "DB1".delta_h := "DB1".Amp / (("DB1".perioada / 4) / "DB1".delta_t);
      "DB1".t := 0;
      "DB1".k_test_1 := false;
      "DB1".d := false;
   END_IF;
   //3
   IF "DB1".t >= ("DB1".perioada * 3 / 4)+0.001 AND "DB1".t < "DB1".perioada
THEN
      "DB1".ref_out := "DB1".ref_out + "DB1".delta_h;
      "DB1".t := "DB1".t + 0.001;
      "DB1".b := false;
      "DB1".c := true;
   END_IF;
  //4
   IF "DB1".t >= "DB1".perioada / 4 AND "DB1".t < ("DB1".perioada * 3 / 4)+0.001
THEN
      "DB1".ref_out := "DB1".ref_out - "DB1".delta_h;
      "DB1".t := "DB1".t + 0.001;
      "DB1".a := false;
      "DB1".b := true;
   END_IF;
   //5
   IF "DB1".t < "DB1".perioada / 4  THEN
      "DB1".ref_out := "DB1".ref_out + "DB1".delta_h;
      "DB1".t := "DB1".t + 0.001;
      "DB1".a := true;
   END_IF;
ELSE
   "DB1".k_test_1 := true;
   "DB1".t := 0.001;
   "DB1".ref_out := 0;
   "DB1".perioada := 1 / "DB1".f;
   "DB1".delta_t := 0.001;
   "DB1".delta_h := "DB1".Amp / (("DB1".perioada / 4) / "DB1".delta_t);
   "DB1".a := false;
   "DB1".b := false;
   "DB1".c := false;
   "DB1".d := false;
END_IF;
"out_1" := INT_TO_WORD(REAL_TO_INT("DB1".ref_out * 2764.8));
"out_2" := INT_TO_WORD(REAL_TO_INT(0 - "DB1".ref_out * 2764.8));
```

Author's papers

1. **A. D. Martin**, L. N. Tutelea, R. Babau, I. Boldea, "A novel approach to PLCs based systems utilized in electric drives", International Aegean Conference on Electrical Machines and Power Electronics (ACEMP) / International Conference on Optimization of Electrical and Electronic Equipment (OPTIM), Location: Bahcesehir Univ, Istanbul, Turkey, Date: AUG 27-29, 2019, Pages 77.84.
2. 2. **A. D. Martin**, L. N. Tutelea, I. Boldea, "Twin Induction Machines Artificial Loading Without Mechanical Coupling", 2020 International Conference on Electric Machines (ICEM), 23-26 August 2020, Gothenburg, Sweeden (Virtual Conference).
3. 3. **A. D. Martin**, L. N. Tutelea, I. Boldea, "Twin Inverter-Fed Artificial Loading Without Mechanical Coupling", IEEE TRANSACTIONS ON INDUSTRY APPLICATIONS, VOL. 58, NO. 3, MAY/JUNE 2022.
4. **A. D. Martin**, L. N. Tutelea, R. Babau, I. Boldea, "Improved Active Torque Pulsation Reduction Method For Pulsating Loads Driven By Induction Machines", Revue Roumaine des Sciences Techniques, Série Électrotechnique et Énergétique - Romanian Academy – accepted but not published yet
5. 4. **A. D. Martin**, D. L. Vitan, I. Torac, L. N. Tutelea, I. Boldea, "BEGA-biaxial excitation generator – operation for constant diode dc output voltage with 3,6,9 phases for increased redundancy", Optimization of Electrical & Electronic Equipment (OPTIM) Aegean Conference on electrical Machines and Power Electronics (ACEMP), Location: Brasov, 2-3, Septembrie 2021, Online Only.
6. 5. D. L. Vitan, **A. D. Martin**, L. N. Tutelea, I. Boldea, "Supercapacitor City Minibus Propulsion System Simulations, Methodology, and Case Study", Optimization of Electrical & Electronic Equipment (OPTIM) Aegean Conference on electrical Machines and Power Electronics (ACEMP), Location: Brasov, 2-3, Septembrie 2021, Online Only.
7. 6. Ion Boldea, IleanaTorac, **Adrian Martin**, Danut Vitan, Lucian Tutelea, „Axially-Laminated-Anisotropic-rotor Reluctance Synchronous Motorcharacterization: analytical design, key FEM validations and preliminary experiments: 10kW, 2.4-4.8krpm", IEEE-PEMC International Conference Power Electronics and Motion Control 20th Edition (25-28 Septembrie 2022).
8. 6. L.-D. Vitan, **A.-D. Martin**, L. Tutelea, and I. Boldea, "Supercapacitor City Minibus Bonded – NdFeB IPMSM Propulsion System: Design and System Modeling Methodology via a Case Study and Laboratory Experiments," for Special Issue on „Design and Optimization of Electric Motors for Traction Applications", IEEE-IAS

BUPT